ISSN 2188-1456

JAEA R&D Review 2014

Radiation measurement from the sky using the Unmanned Airplane for Radiation Monitoring System

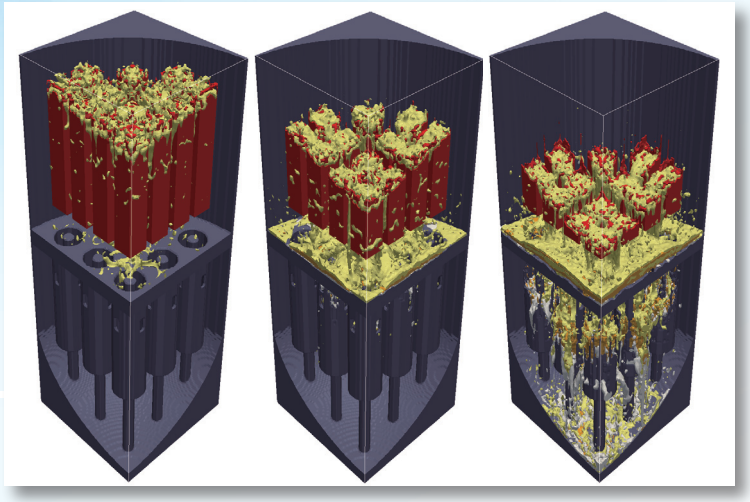

Results of simplified simulations on the relocation behavior of simulated molten materials

Message from the President

松浦祥次郎

President Shojiro MATSUURA

We sincerely thank you for your understanding and continued support of our research and development activities. Since the foundation of the Japan Atomic Energy Agency (JAEA), this publication has been brought out every year with the intention of informing you of the day-to-day accomplishments of the JAEA.

As the only research institute in Japan dedicated to comprehensive nuclear research and development, JAEA has focused on investing efforts toward the recovery from the accident at the Tokyo Electric Power Company, Incorporated (TEPCO) Fukushima Daiichi Nuclear Power Station (NPS) by our scientific and technical expertise.

Furthermore, JAEA could not prevent the occurrence of a series of incidents, such as inadequate maintenance management at the "Monju" and leakages from the Hadron Experimental Facility of Japan Proton Accelerator Research Complex (J-PARC). JAEA is endeavoring to recover the public's trust by improving ourselves. JAEA defined the year beginning October 2013 as an intensive organizational reform period, all JAEA united in an effort to achieve the necessary reform. With strong resolution to recreate ourselves anew, we have made efforts to enhance corporate planning functions, safety management functions, and internal control mechanisms, including reorganizing our research and development framework into six departments. For "Monju," we established an independent management system for the power plant and enhanced the quality assurance system. As part of the J-PARC reforms, we equipped the facilities with safety management systems to guarantee safety.

In April 2014, the "Strategic Energy Plan" was approved by the Cabinet, and the position of nuclear power was designed in the Plan as "a crucial base-load power source, contributing to stability of the energy supply and demand structure" in Japan. In addition, it was expressed in the "Basic Policies for the Economic and Fiscal Management and Reform 2014," approved by the Cabinet in June 2014.

For research and development related to the decommissioning of the TEPCO's Fukushima Daiichi NPS, we have promoted the test on the characterization of the fuel debris, remote decontamination technology, the long-term integrity of the fuel assembly in the spent fuel storage pool for the preparation of its removal, and the treatment and disposal of radioactive waste caused by the accident. We have performed research and development activities towards the quick return of the residents such as radiation monitoring in forests and rivers, migration of radioactive cesium, and calculation of decontamination effects. In addition, we are making efforts to contribute to the recovery from the accident by developing improved decontamination materials, etc.

In the research and development of the fast breeder reactor cycle technology, including "Monju" we aim to collect the research results stipulated in the "Monju Research Plan," and are working towards lifting the security measures put in place by the Nuclear Regulation Authority and complying with the new regulation standards. We are also conducting a research and development activities about reduction and stabilization of radioactive wastes, as well as transmutation technology using accelerators.

Moreover, for the activities on the backend of nuclear energy utilization, which are necessary for advancing our project, we have performed research and development on decommissioning of our own facilities, and the treatment and disposal of radioactive waste. We are also moving forward with the development of technologies related to the processing and disposal of low-level radioactive waste, underground disposal and the light-water reactor fuel cycle.

Regarding nuclear hydrogen and heat application, we are making steady progress in research and development efforts to improve the safety of high-temperature gas-cooled reactors. Furthermore, we aim to conduct trials that connect a High-Temperature engineering Test Reactor (HTTR) with heat utilization facilities (gas turbine power generation, hydrogen production, etc.) as a step toward the practical application of high-temperature gas-cooled reactors. In the research and development aimed at the practical utilization of nuclear fusion energy, we, as a domestic agency/implementing agency of Japan under roles based on the international framework (ITER Project/BA activity) have been promoting our operations using the world's most advanced technologies along the plan that the JAEA prescribed. As part of the research and development on quantum beam science, we have been producing a variety of results in areas ranging from the fundamentals of science and technology to industrial applications, through various quantum beam facility groups owned by the JAEA. Moreover, we have recognized that ensuring nuclear safety is an important step in the use of nuclear power, and we have diligently conducted nuclear safety research for the improvement of safety in the utilization of nuclear energy. In addition, we have promoted a wide variety of engineering research activities, which will serve as the basis in the development of nuclear energy utilization in Japan; these activities have led to many accomplishments.

Hereafter, we are steadily proceeding with structural reforms in accordance with the plan that the JAEA has set forth. With the increased expectations toward the JAEA's role in nuclear technology development after the accident at the TEPCO's Fukushima Daiichi NPS, we are now actively involved in medium-to-long-term human resource development for nuclear technology, industry-academia-government collaborations, promotion of international cooperation with overseas research institutes, and the dissemination of the achievements made in research and development, without failing to prioritize operations.

We are pleased that you will gain further understanding of the accomplishments of the JAEA through this publication, and we thank you for your continued encouragement and guidance in our research and development activities.

JAEA R&D Review 2014

2 Nuclear Safety Research

3 Advanced Science Research

4 Nuclear Science and Engineering Research

5 Quantum Beam Science Research

6 Nuclear Hydrogen and Heat Application Research

7 Research and Development of Advanced Nuclear Systems

8 Research and Development Relating to Nuclear Fuel Cycle Backend and Reprocessing of Spent Nuclear Fuel

9 Nuclear Fusion Research and Development

10 Computational Science and E-Systems Research

11 Development of Science & Technology for Nuclear Nonproliferation

About This Publication and the Outline of Organization of JAEA

This publication introduces our latest research and development (R&D) results in each field. Each chapter presents the activities of one R&D Directorate. As shown in the organization chart, the various R&D Directorates perform their activities through R&D centers or institutes. Some of these centers or institutes consist of only one site, while others are located at two or more sites, depending on the R&D activities. The R&D centers and institutes are located throughout Japan, as shown in the map below. The following brief introduction outlines the research undertaken by each R&D Directorate at various R&D centers and institutes.

1. **The Sector of Fukushima Research and Development** is engaged in R&D to recover from the accident at the Tokyo Electric Power Company, Incorporated Fukushima Daiichi Nuclear Power Station. The Fukushima Decommissioning Technology Center is conducting R&D to restore the nuclear power plant. The Fukushima Environmental Safety Center in the Fukushima prefecture is conducting R&D concerning decontamination technologies to restore the environment, outreach activities concerning radiation, and investigations of internal exposure of the human body. Additionally, the Nuclear Plant Decommissioning Safety Research Establishment is conducting research and analysis of radioactive materials, development of remote-controlled robots, and establishment of research base facilities.
2. **The Nuclear Safety Research Center, Sector of Nuclear Safety Research and Emergency Preparedness,** is in charge of safety research that supports the national nuclear safety regulatory bodies that regulate nuclear power plants, nuclear fuel cycle facilities, and radioactive waste disposal facilities. This work is conducted at the Nuclear Science Research Institute and at the Tsuruga Head Office.
3. **The Advanced Science Research Center, Sector of Nuclear Science Research,** conducts pioneering research in basic fields of nuclear power science mainly through the Nuclear Science Research Institute and the Takasaki Advanced Radiation Research Institute.
4. **The Nuclear Science and Engineering Center, Sector of Nuclear Science Research,** is engaged in key and basic research on various elemental technologies that support nuclear power use. These efforts are carried out at the Nuclear Science Research Institute and the Oarai Research and Development Center.
5. **The Quantum Beam Science Center, Sector of Nuclear Science Research,** is engaged in research using neutrons at the Nuclear Science Research Institute and J-PARC. Work using electron beams, gamma rays, and ion beams is conducted at the Takasaki Advanced Radiation Research Institute. Research using lasers and synchrotron radiation is performed at the Kansai Photon Science Institute.

Japan Atomic Energy Agency -Outline of Organization-

As of December, 2014

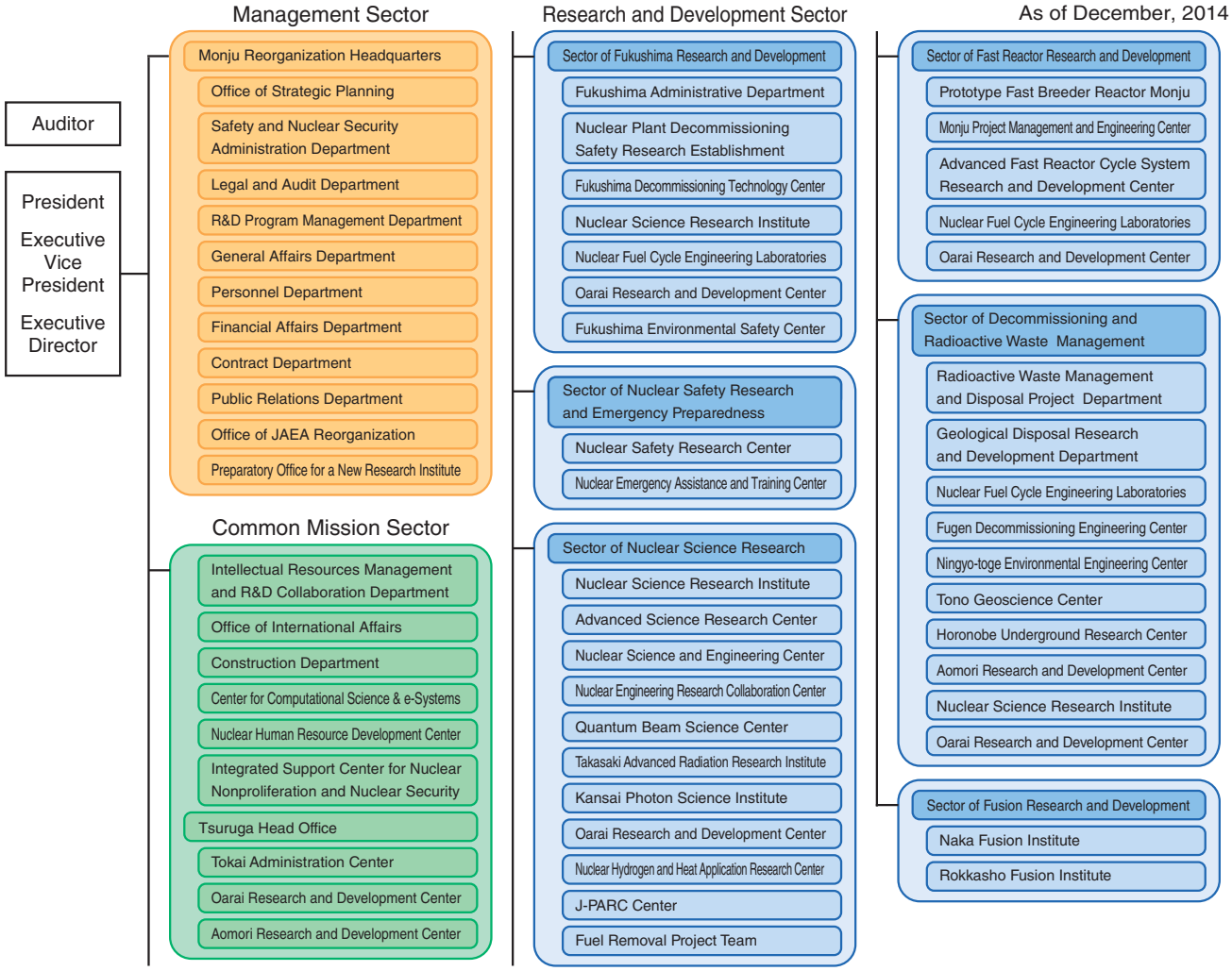

6. **The Nuclear Hydrogen and Heat Application Research Center, Sector of Nuclear Science Research,** conducts R&D on technologies for high temperature gas-cooled reactors (HTGRs) and thermochemical hydrogen production at the Oarai Research and Development Center.

7. **The Sector of Fast Reactor Research and Development** is conducting R&D toward the establishment of fast reactor (FR) cycles to address long-term energy security and global environmental issues. In Tsuruga, staff at the Prototype Fast Breeder Reactor Monju and Monju Project Management and Engineering Center are conducting R&D on "MONJU." R&D activities are also aimed at enhancing the safety of the FR system at the Oarai Research and Development Center, and manufacturing plutonium fuel and reprocessing spent FBR fuel at the Nuclear Fuel Cycle Engineering Laboratories.

8. **The Sector of Decommissioning and Radioactive Waste Management** develops technologies for the safe and rational decommissioning of nuclear power facilities as well as measures for processing and disposing radioactive waste in their R&D centers or institutes. This sector also conducts multidisciplinary R&D aimed at improving the reliability of geological isolation of high-level radioactive waste in Japan. A particular focus involves establishing techniques for investigating the deep geological environment through R&D at the Tono Geoscience Center and the Horonobe Underground Research Center. At the Nuclear Fuel Cycle Engineering Laboratories, the focus is on improving technologies for designing disposal facilities and safety assessment. Additionally, ongoing work is focused on the development of a next-generation knowledge management system based on the above R&D activities. Furthermore, the development of nuclear fuel cycle technology for LWRs is in progress at the Nuclear Fuel Cycle Engineering Laboratories.

9. **The Sector of Fusion Research and Development** is performing fusion R&D as a domestic agency of the International Thermonuclear Experimental Reactor (ITER) project and an implementing agency of Broader Approach (BA) activities. The procurement activity of the ITER project, the upgrade of JT-60 to a superconducting machine as a BA activity, fusion plasma research, and R&D on various element technologies are conducted at the Naka Fusion Institute. Moreover, the International Fusion Energy Research Center project and the Engineering Validation and Engineering Design Activities of the International Fusion Material Irradiation Facility as a BA activity are performed mainly at the Rokkasho Fusion Institute.

10. **The Center for Computational Science & e-Systems** conducts research work on advanced simulation technology and on basic technology in computational science, as well as operation and maintenance of computer systems. These efforts are carried out mainly at the Nuclear Science Research Institute and the Kashiwa Office.

11. **The Integrated Support Center for Nuclear Nonproliferation and Nuclear Security** develops technologies for nuclear nonproliferation and safeguards to ensure peaceful nuclear energy use. These developments are conducted at the Nuclear Science Research Institute and the Techno Community Square Ricotti.

R&D Institutes/Centers of JAEA

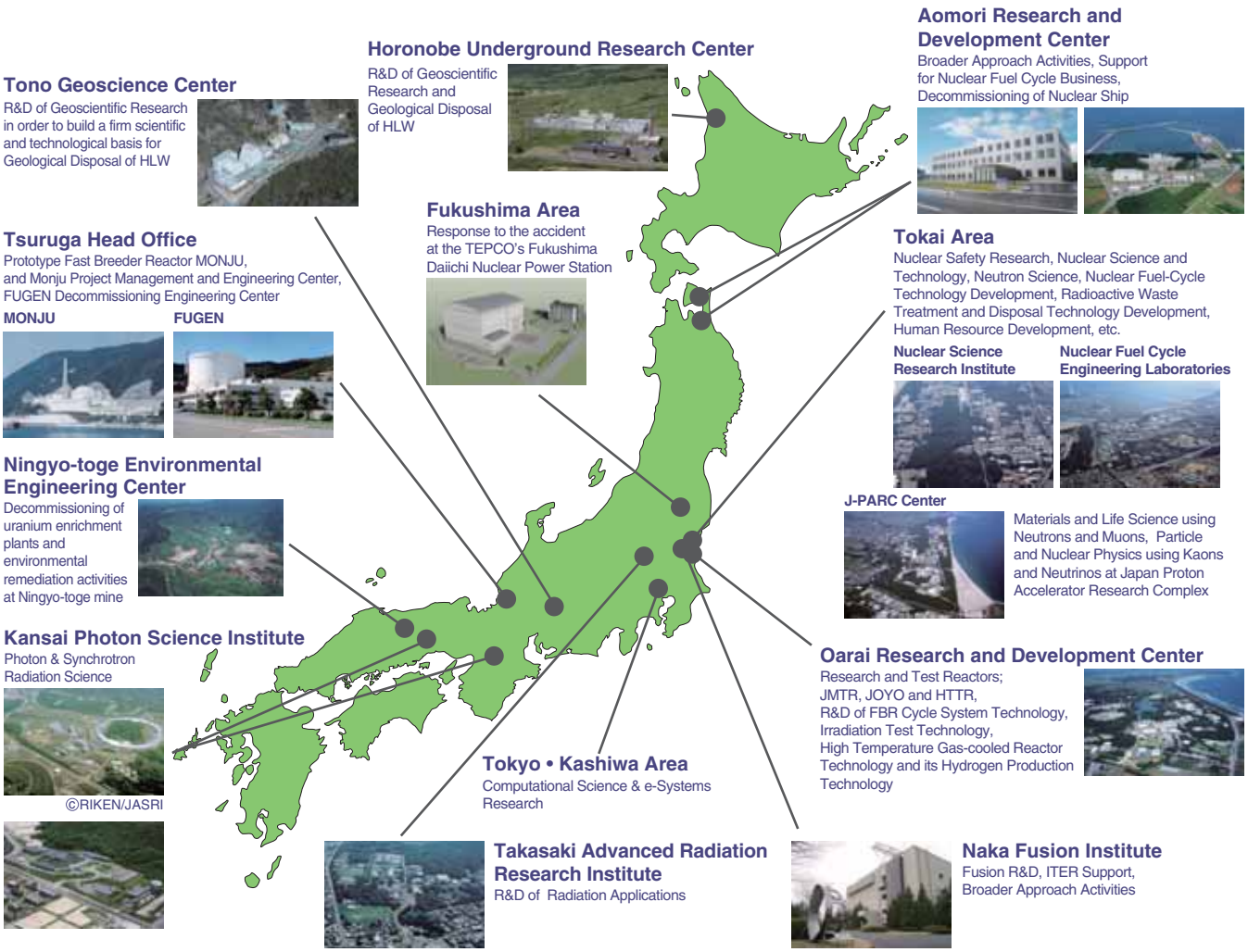

Environmental Remediation and Plant Decommissioning

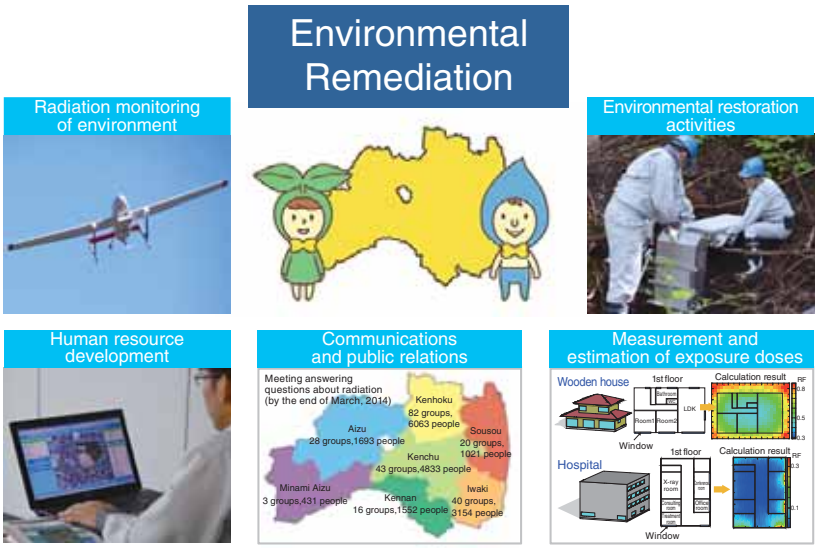

Fig.1-1 JAEA's post-accident efforts at environmental remediation for the recovery of Fukushima
These activities are introduced on the web page of JAEA Sector of Fukushima Research and Development (http://fukushima.jaea.go.jp).

Environmental Remediation

As a designated public institution under the Disaster Countermeasures Basic Act, we started taking action immediately following the Great East Japan Earthquake of March 11, 2011. We have undertaken diverse actions, such as measurement of radiation. A sample of our efforts (described below) are shown in Fig.1-1, and are currently being continued for the recovery of Fukushima.

Radiation Monitoring of the Environment

It is necessary to exactly evaluate the contamination status and radiation dose rates caused by the release of radioactive materials during the accident at the Tokyo Electric Power Company, Incorporated (TEPCO) Fukushima Daiichi Nuclear Power Station (NPS) (1F accident). Thus, the variation of the radioactive iodine distribution in the sea before and after the 1F accident (Topic 1-1) has been investigated. In addition, we have made a map of the contamination by radioactive iodine, based on airborne monitoring data taken just after the 1F accident (Topic 1-2), resulting in an estimate of the spread of radioactive materials in the early stage. Development of a visualization technique for the radiation distribution at the bottom of the storage reservoir (Topic 1-3) and measurement of the soil radioactivity distribution (Topic 1-4) were also performed. Moreover, monitoring data from various measurements were collected and disclosed (Topic 1-5), and information such as monitoring data of the air dose rate measured by local buses in the Fukushima prefecture was uploaded to the web site (http://info-fukushima.jaea.go.jp/joho_en/) on the activities for the recovery of Fukushima.

Environmental Restoration Activities

For the recovery of the environment, performing quick decontamination is important. The portal site "Cleanup navi," which provides the technical information obtained by the decontamination model verification project sponsored by the Cabinet Office, has been established online (http://c-navi.jaea.go.jp/en/index.html). For understanding long-term changes to the distribution of radioactive cesium (Cs) in the environment, a project for researching long-term environmental change in Fukushima is being promoted. The behavior of radioactive Cs in the dam lake (Topic 1-6), the Cs absorption mechanism of clay minerals (Topic 1-7), and the behavior of radioactive Cs in plants (Topic 1-8) were studied. In addition, a simple method for measuring the concentration of radioactive Cs in aqueous solutions (Topic 1-9) was developed. Based on the above activities, studies toward optimization and high efficiency of decontamination for environmental recovery will be continued in the future.

Human Resources Development

We are working to spread knowledge of decontamination by dispatching experts to municipalities to conduct decontamination technology consultation and instruction, field investigation, and briefing session support for local inhabitants. In addition, we are creating guidelines on decontamination, giving advice through one-stop contacts, and cooperating in the development of a municipal decontamination plan based on Japan Atomic Energy Agency's (JAEA's) decontamination support system, "RESET."

Communications and Public Relations

We conduct "meetings answering questions about radiation" for various groups, such as students at nursery schools, kindergartens, elementary schools, and junior high schools in the Fukushima prefecture, to promote greater scientific understanding of radiation. By the end of March, 2014, we had offered such meetings at 232 places, to approximately 18750 people.

Measurement and Estimation of Exposure Doses

We monitored internal radiation exposure using the Tokai Research and Development Center's whole body counter (WBC) and the mobile WBC car for inhabitants of the Fukushima prefecture. By the end of March, 2014, we measured exposure from about 61800 people. In addition, evaluation of the radiation dose reduction in different buildings (Topic 1-10) was performed.

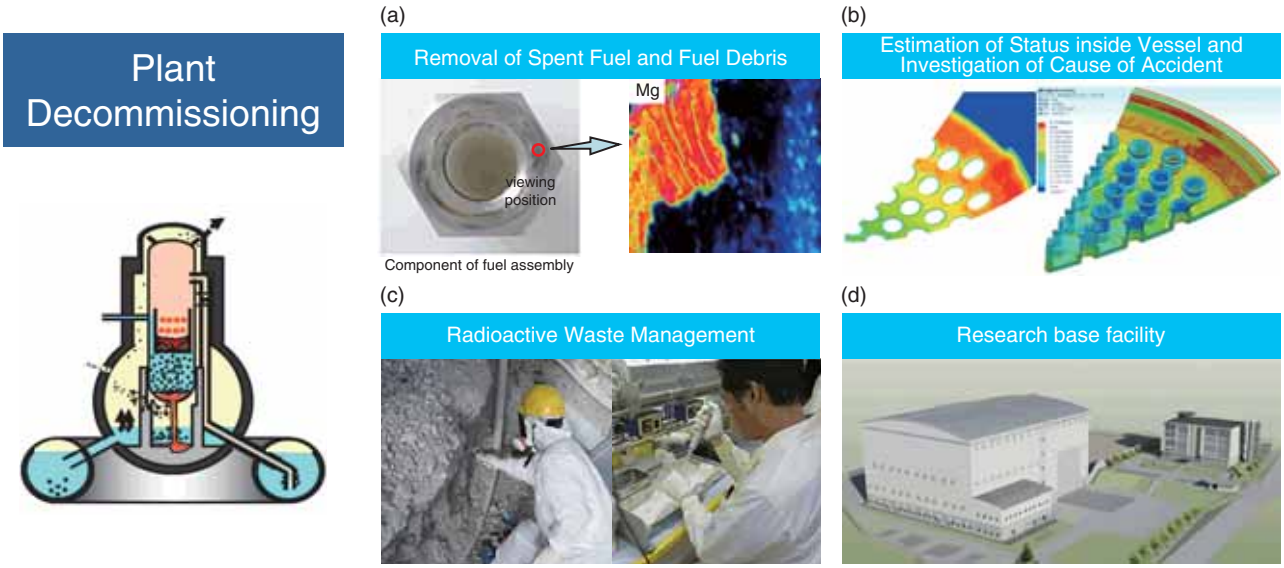

Fig.1-2 Overview of JAEA's Activities toward the Decommissioning of the TEPCO's Fukushima Daiichi NPS
(a) A detailed inspection of samples taken from the unirradiated fuel assembly at 1F4, (b) an example of simulation results for failure of the lower head of the reactor pressure vessel, (c) JAEA staff picking rubble around 1F4 for analysis, and (d) an image of the Remote-controlled Equipment and Device Development Facility.

Plant Decommissioning

Immediately after the accident, we began providing technical advice to the government and TEPCO, and conducting R&D for removal of the molten core materials (the fuel debris), radioactive waste management, and so forth (Fig.1-2).

Removal of Spent Fuel and Fuel Debris

Some of the fuels could have been damaged by falling concrete debris and the like. Hence, we are currently conducting R&D for inspection of the fuel assembly (Topic 1-11).

For defueling the fuel debris in the reactor core, we are researching methods of inspecting the inside of the reactor core (Topic 1-12), as well as developing a cutting and crushing method for extracting the fuel debris (Topic 1-13). Since sea water was injected into reactor vessel for emergency cooling, the possibility of corrosion problems with the structural materials was also considered. We conducted an examination for evaluating this effect (Topic 1-14).

For safe handling, storage, processing, and disposal, it is important to grasp the characteristics of the fuel debris before defueling. We estimated the chemical forms of the fuel debris by a combination of melt-progression analysis and thermodynamic equilibration (Topic 1-15) to investigate the mechanical properties using simulated debris made of U, Zr, and B_4C control blades (Topic 1-16) for the purposes of management of the fuel debris after removal (Topic 1-17).

Estimation of Status inside the Vessel and Investigation of the Cause of the Accident

The fuel in the reactors reached a high temperature and became molten when the core cooling system ceased operation during the station blackout caused by the tsunami. To elucidate the progress of the melting phenomena in the reactor core, we estimated the status in the core by means of severe accident analytical codes, simulated tests, and so forth, contributing to a detailed analysis of the progress of the severe accident.

Radioactive Waste Management

A massive volume of contaminated water has been generated due to the tsunami and the inflow of ground water in the reactor buildings; this contaminated water is temporarily stored at the plant site. We evaluated whether the iodine in the contaminated water could be released in the atmosphere (Topic 1-18), and developed analytical techniques for "difficult-to-measure" radioactive nuclides in the contaminated water (Topic 1-19).

Some water treatment systems are being applied to the removal of radioactive nuclides, e.g., cesium and strontium, from the contaminated water. We are addressing the long-term storage, processing, and disposal of secondary waste produced by treatment of this contaminated water (Topic 1-20).

We collected rubble and trees from 1F, and analyzed their radioactivity concentrations (Topic 1-21).

Research Base Facility

We will construct a Research Base Facility in the Fukushima Prefecture for the purpose of establishing basic technologies and methods (such as remote-controlling systems and analysis of radioactive materials) that are indispensable to the decommissioning of 1F. A Remote-controlled Equipment and Device Development Facility started construction in August, 2014.

1–1 The Migration of Radioactive Iodine in Seawater

— Variation of Iodine-129 Concentration before and after the Accident at the TEPCO's Fukushima Daiichi NPS —

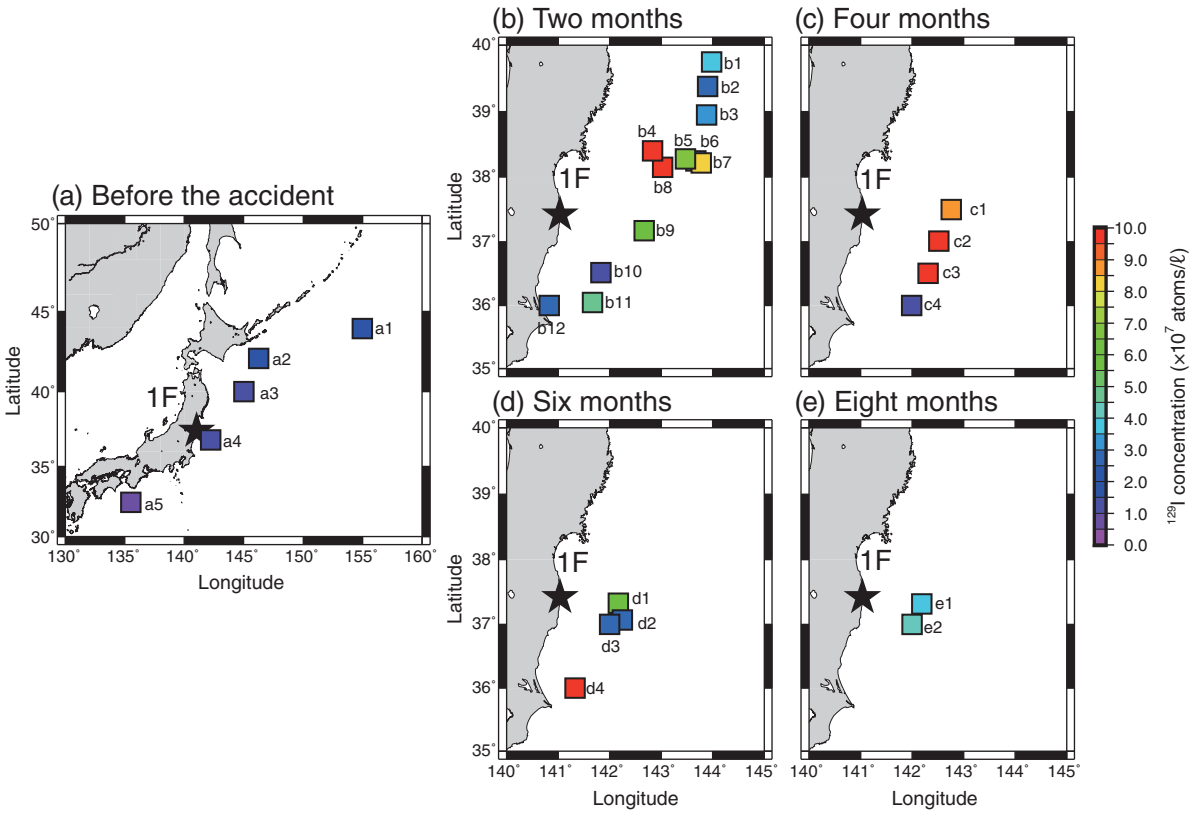

Fig.1-3 Oceanographic stations and concentration of ^{129}I measured in this study
Oceanographic stations and concentrations of ^{129}I before and after the accident are shown. Concentrations over 10^8 atoms/ℓ are shown in red.

If radioactive iodine is accidentally released into the environment from a nuclear facility, it is necessary to survey the migration of this iodine through the environment. We have developed a technique for measuring iodine-129 (^{129}I) in environmental samples using accelerator mass spectrometry (AMS), and we have investigated the background level of ^{129}I to prepare for unexpected accidents. In March 2011, the accident at the TEPCO's Fukushima Daiichi NPS (1F) caused radioactive iodine to be released into the ocean. We have studied the migration of the accident-derived ^{129}I in the sea area around Fukushima using our developed method and background data.

Before the accident, seawater samples had been collected at five stations in the western North Pacific Ocean (Fig.1-3(a)). After the accident, samples were collected at 12 stations after two months (Fig.1-3(b)), four stations after four months (Fig.1-3(c)) and six months (Fig.1-3(d)), and two stations after eight months (Fig.1-3(e)). Concentrations of ^{129}I in the seawater samples were measured using AMS.

The concentrations of ^{129}I in surface seawater around the western North Pacific Ocean before the accident were $(0.94–1.83) \times 10^7$ atoms/ℓ. After the accident, the concentrations of ^{129}I were $(1.08–89.8) \times 10^7$ atoms/ℓ. The maximum value was observed at station c3 four months after the accident, and the minimum was observed at stations b10 and c4 two and four months after the accident, respectively. The maximum was 80 times higher than the background value before the accident. The minimum concentrations were at the same level as the background value before the accident. A wide range of ^{129}I concentrations in surface seawater were observed around the 1F site for several months following the accident. It is believed that this result was induced by the complex flow field with the Oyashio and Kuroshio currents flowing into this region, and the corresponding mesoscale eddies. Since the concentration of ^{129}I in surface seawater after eight months from the accident decreased to the background level, it has been shown that the concentration of accident-derived ^{129}I has been reduced by time.

The findings of this study can be applied to simulation models that predict the distribution of radionuclides in seawater.

Reference

Suzuki, T. et al., Iodine–129 Concentration in Seawater near Fukushima before and after the Accident at the Fukushima Daiichi Nuclear Power Plant, Biogeosciences, vol.10, no.6, 2013, p.3839–3847.

1–2 Ground Deposition Maps of Iodine-131 Obtained Using Airborne Surveys at an Early Stage of the Accident at 1F

— A Joint Study with JAEA and DOE/NNSA —

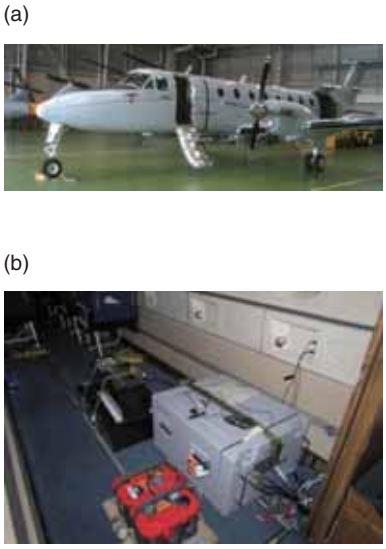

Fig.1-4 Airplane used for the airborne monitoring (a), and the measurement instrument comprising three embedded NaI scintillation detectors (b)
The aerial measuring system installed in the airplane is composed of an array of three 5 cm × 10 cm × 40 cm NaI detectors. Each detector system produces a 1024-channel energy spectrum, once per second with the readout of all the spectrometers synchronized with the time from a GPS receiver.

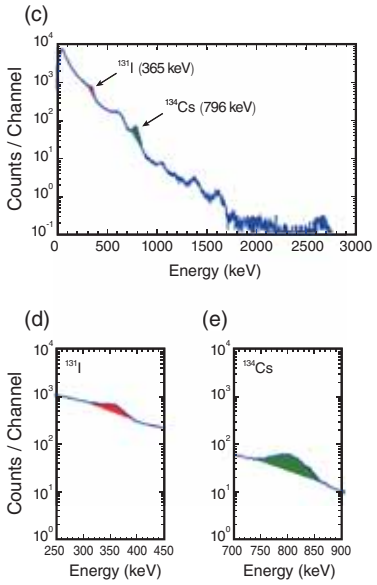

Fig.1-5 Spectral data
Spectral data obtained by airborne monitoring (c), and the extracted energy peak of iodine-131 (^{131}I) (d) and cesium-134 (^{134}Cs) (e) obtained using the Gaussian fitting method.

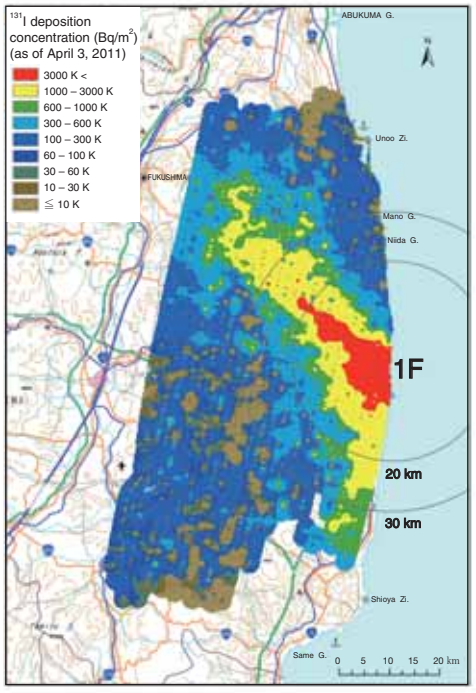

Fig.1-6 ^{131}I deposition distribution (as of April 3, 2011)
(map drawn using map data provided by the Geospatial Information Authority of Japan)
High concentrations of ^{131}I have been deposited to the northwest and south of 1F.

Radioactive substances were spread across a wide area in the aftermath of the accident at the TEPCO's Fukushima Daiichi NPS (1F).

We obtained the airborne monitoring data that was collected by the U.S. Department of Energy National Nuclear Security Administration (DOE/NNSA) at an early stage, March 17 to April 5, 2011 (Fig.1-4), and analyzed the spectral information in a joint research project with DOE/NNSA (Fig.1-5). Within this data, the energy peak corresponding to iodine-131 (^{131}I) was observed. DOE/NNSA and we have developed a new method for analyzing ^{131}I to determine the ground deposition concentrations and create distribution maps.

Our main focus was on three airborne monitoring flights on April 2 and 3, 2011, and the energy peak (365 keV) of ^{131}I (Fig.1-5(d)). The deposition concentrations of ^{131}I were analyzed by developing a method for calculating the response to ground deposited activity at varying aircraft heights. This was conducted using Monte Carlo simulations, which extract the iodine peak and simulate the attenuation of γ-rays in the air.

From this analysis, the ^{131}I deposition distribution was determined, and its maps were created. Fig.1-6 shows the distribution of ^{131}I depositions at varying concentrations, corrected for radioactive decay up to April 3 when monitoring was completed.

Analysis of cesium-134 (^{134}Cs), which has a longer half-life, was conducted using the same method as that for ^{131}I. Consequently, high concentrations of ^{131}I, ^{134}Cs, and cesium-137 (^{137}Cs) were shown to be present to the northwest of 1F. In the area south of 1F, high concentrations were also detected.

To verify the validity of the method, a comparison was performed with the Japanese Ministry of Education, Culture, Sports, Science and Technology (MEXT) Emergency Operation Center's (EOC's) soil sampling data (^{131}I, ^{134}Cs) taken on June 14, 2011. The results from the present analysis were corrected for radioactive decay for the purposes of this comparison. The deposition concentrations of ^{131}I and ^{134}Cs measured on the ground agreed well with the airborne monitoring results. This newly developed method showed the detailed distribution of ^{131}I.

Reference

Torii, T. et al., Enhanced Analysis Methods to Derive the Spatial Distribution of ^{131}I Deposition on the Ground by Airborne Surveys at an Early Stage after the Fukushima Daiichi Nuclear Power Plant Accident, Health Physics, vol.105, no.2, 2013, p.192–200.

1–3 Visualization of the Distribution of Radiocesium Concentration at the Bottom of Irrigation Ponds

— Measurement of Irrigation Ponds Using the Plastic Scintillation Fiber —

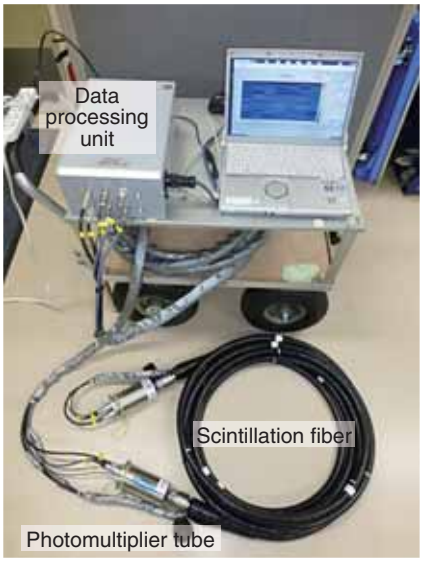

Fig.1-7 A radiation measuring system for the bottoms of water bodies using PSF
15 bundles of PSF with a diameter of 1 mm.

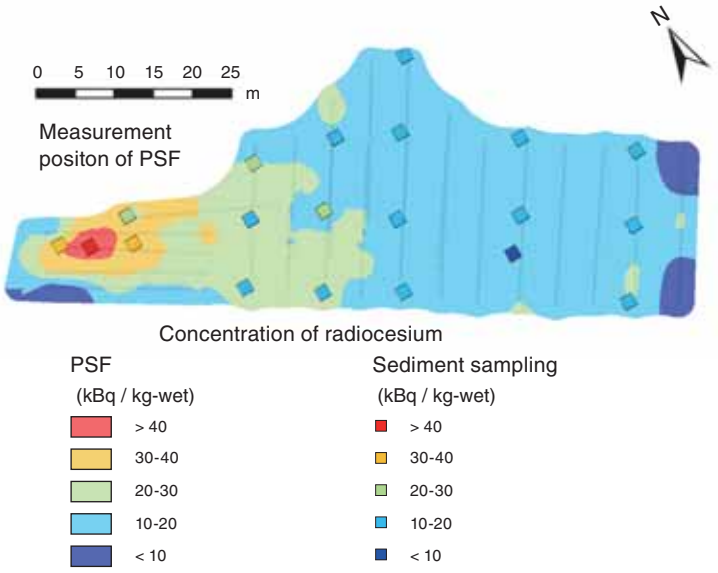

Fig.1-8 Example of a radiocesium distribution map of an irrigation pond in Fukushima Prefecture
PSF measurements were performed at a line spacing of 5 m. The map was created using Kriging, which is an interpolation method. This map accorded with the result of sediment sampling.

There are approximately 3700 irrigation ponds in the Fukushima prefecture. Contamination by radiocesium at the bottom of these ponds has been a concern since the accident at the TEPCO's Fukushima Daiichi NPS (1F). The irrigation ponds collect the water that falls in the catchment area as rain, which is then used for agriculture. In general, the radiocesium concentration in sediment is evaluated by measuring collected samples in a laboratory. The drawback of this method are that the samples become radioactive waste. In addition, the evaluation of the distribution of over the entire irrigation pond is difficult. In Fukushima, a quick and direct technique for measuring a wide area of the bottom of a pond is needed.

We developed the plastic scintillation fiber (PSF) following the accident at 1F. PSF has the following characteristics, (1) a detector is long (max.20 m). (2) the water resistance of the detector is high, and (3) PSF can be put along the measuring object. Therefore, PSF was applied to the measurement of irrigation ponds. A photo of the radiation measurement system based on PSF is shown in Fig.1-7. PSF is an optical fiber with a plastic scintillator at its core. Optical sensors (photomultiplier tubes) were located at both ends of the optical fiber, and the amount of radiation was measured. In addition, the position at which radioactive emission took place was pinpointed based on the difference in the times at which the two sensors counted it. The count rate collected by PSF was used to extrapolate the radiocesium concentration at the bottom of the pond by the results to those taken by waterproof γ-ray spectrometer that was calibrated by Monte Carlo calculation code. The assumption under which the radiocesium concentration was extrapolated was that radiocesium was distributed uniformly over 10 cm from the surface layer of the sediment. There is good agreement between the concentration extrapolated from PSF data and that obtained from sediment core samples. Using this method, measurement of an irrigation pond 1000 m^2 in area took about four days (with five people to each team). An example of a radiocesium distribution map obtained from an irrigation pond in Fukushima is shown in Fig.1-8. The PSF measurements were performed at a line spacing of 5 m. The map was created using the interpolation method known as Kriging. This map accorded with the result obtained by sediment sampling.

We are transferring these techniques to Midori Net Fukushima (http://www.midorinet-fukushima.jp) by making a technical support contract with them. JAEA is going to develop the technology and provide the support that is necessary to utilize these techniques for the measurement of radiocesium in irrigation ponds in Fukushima.

Reference

Sanada, Y. et al., Research and Development of In-Situ Measurement for Radiation Distribution of Waterbed, JAEA-Research 2014-005, 2014, 67p. (in Japanese).

1–4 Why Have Air Dose Rates Decreased with Time?
— Depth Distributions of Radioactive Cesium in Soils —

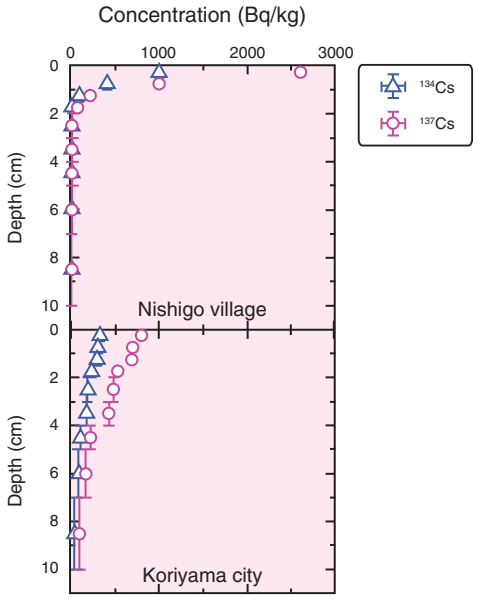

Fig.1-9 Depth distributions of radioactive Cs in the soils
(Sampling method: scraper plate; Implementation period: October 28 to November 29, 2013) A typical depth distribution wherein concentrations of radioactive Cs exponentially decrease with depth.

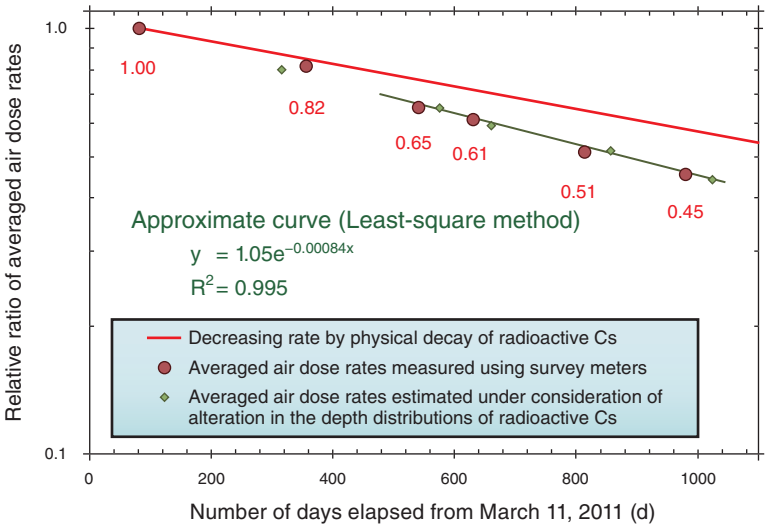

Fig.1-10 Temporal changes in averaged air dose rates above the ground measured using survey meters
The decreasing rate of the physical decay of radioactive Cs, and the temporal changes in the air dose rate estimated under consideration of various depth distributions of radioactive Cs.

With funding from the Ministry of Education, Culture, Sports, Science and Technology of Japan (MEXT) and the Nuclear Regulation Authority (NRA), we have conducted comprehensive large-scale environmental monitoring as a national project since June, 2011, and provided reliable information on the distributions of the air dose rate and the radioactive nuclides deposited in soil on the ground. This has been done to assess the consequences of the accident at the TEPCO's Fukushima Daiichi NPS (1F), and to give basic information for judgment on substantial measures such as decontamination, rearrangement of evacuation zones and so on. As a part of environmental monitoring, depth distributions of radioactive cesium (Cs) in soils have been obtained using a scraper plate method, which can collect soil samples of different depths with minimal cross-contamination.

During the environmental monitoring performed in November, 2013, radioactive Cs deposited in the soils remained within 5 cm of the surface on the whole. Exponential decreases of the concentrations of radioactive Cs with depth (Fig.1-9) were observed in many situations. The depth distribution was found with repeated environmental monitoring to gradually progress deeper into the soil.

The temporal change of the averaged air dose rates was also measured above the ground at various locations around the 1F using survey meters, and the results relative to a first result are shown in Fig.1-10. The reduction rate of the averaged air dose rates was steeper than that caused by the physical decay of radioactive Cs alone. In addition, the results obtained in a migration study performed as a part of the project showed that the horizontal advection of radioactive Cs was negligibly small.

To find the reason for this difference, simulations of the air dose rate as a function of the depth distribution of cesium-137 (^{137}Cs) were conducted with the Particle and Heavy Ion Transport code System (PHITS). The calculation results in the approximated curve (Fig.1-10) were in good agreement with the plots of the averaged air dose rates. The results indicate that the averaged air dose rates have decreased because slight changes in the depth distribution of ^{137}Cs with time have increased the shielding effect of the soil against γ-rays.

The present study was sponsored by the Secretariat of the Nuclear Regulation Authority (NRA).

Reference

Saito, K., Mapping and Modelling of Radionuclide Distribution on the Ground due to the Fukushima Accident, Radiation Protection Dosimetry, vol.160, no.4, 2014, p.283–287.

1–5 Provision of Radionuclide Distribution Data

— The Collection and Quick Provision of Environmental Monitoring Data —

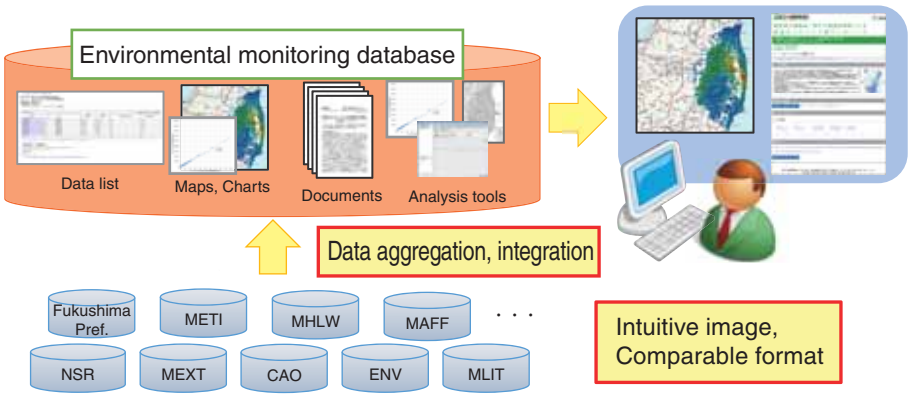

Fig.1-11 An environmental monitoring database system
Integrating many kinds of monitoring data and publishing them in a uniform fashion improves data reusability and comparability.

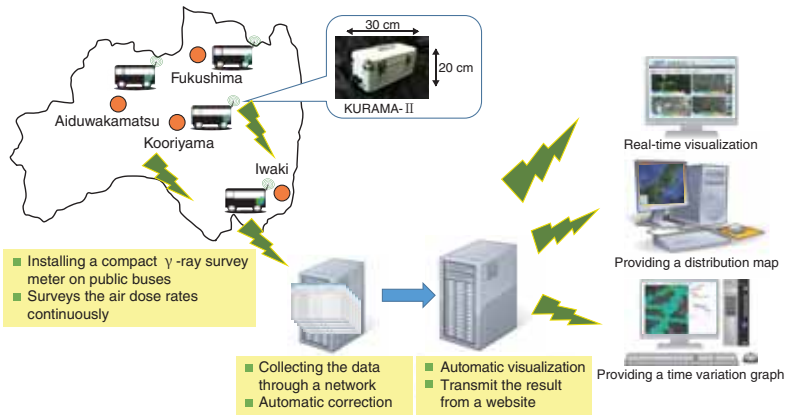

Fig.1-12 A real-time visualization system for the distribution of air dose rates in the Fukushima Prefecture
By installing a compact γ-ray survey system on public buses, survey data will be collected, compensated, visualized automatically, and finally made available to the public.

To estimate the impact of radionuclides emitted by the accident at the TEPCO's Fukushima Daiichi NPS, it was necessary to identify the current distribution of radionuclides and the tendency of this distribution to change in time. We conducted research projects to provide environmental monitoring data, which were essential for these identifications.

One of the research projects was the development of an environmental monitoring database. Many kinds of environmental monitoring data collected by ministries, agencies, and local governments have previously been published in different formats. We republished the data in a uniform fashion by developing a tool to integrate them automatically, thereby improving data usability and compatibility (Fig.1-11). Over 300 million records of data published by 21 organizations were republished. The average number of accessing the new database was 2.5 times larger (about 166 thousand accesses) than the former database, which was developed under a previous MEXT project.

In cooperation with the Fukushima Prefecture and Kyoto University, we conducted another research project that provided real-time visualization of the air dose rate data monitored by the compact γ-ray survey system (KURAMA-II). Because of its limited budget, air dose surveys with KURAMA-II have only been conducted a few times before. The use of public buses that run in residential areas on a daily basis and of servers that collect, compensate, and visualize the data automatically made real-time data provision possible (Fig.1-12). Furthermore, just in case a similar accident occurs, it is expected that this system can provide data in real time. Real-time visualized air dose rate data is now available on a large monitor in the NBF Unix Building near Fukushima Station.

This present study was partly sponsored by the Nuclear Regulation Authority (NRA), and by the Fukushima Prefecture.

Reference

Seki, A. et al., Development of Radionuclide Distribution Database and Map System on the Fukushima Nuclear Accident, Progress in Nuclear Science and Technology, vol.4, 2014, p.47–50.

1–6 Simulating the Migration Behavior of Radioactive Cesium in the Environment
— A Case Study of the Ogaki Dam Reservoir —

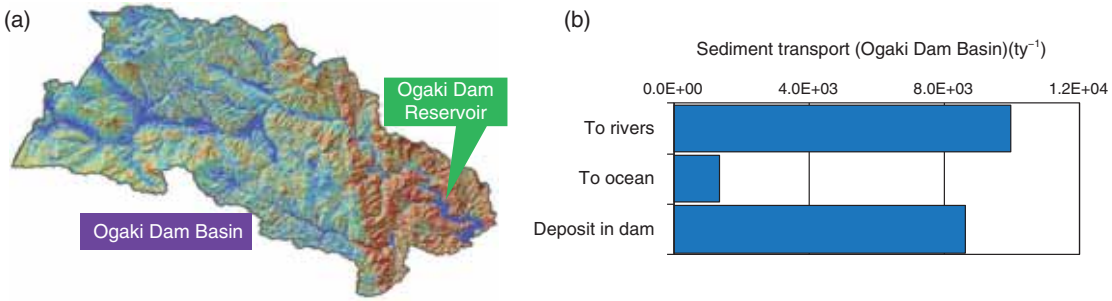

Fig.1-13 (a) The Ogaki Dam Reservoir (map drawn using DEM data provided by the Geophysical Survey Institute) and (b) the simulation results for the amount of sediment movement in the basin
A large amount of soil erodes and moves as sediment during a flood, entering into water systems, such as rivers and reservoirs. Most of the sediment is then deposited on the reservoir bed. The results indicate the importance of the reservoir to Cs migration.

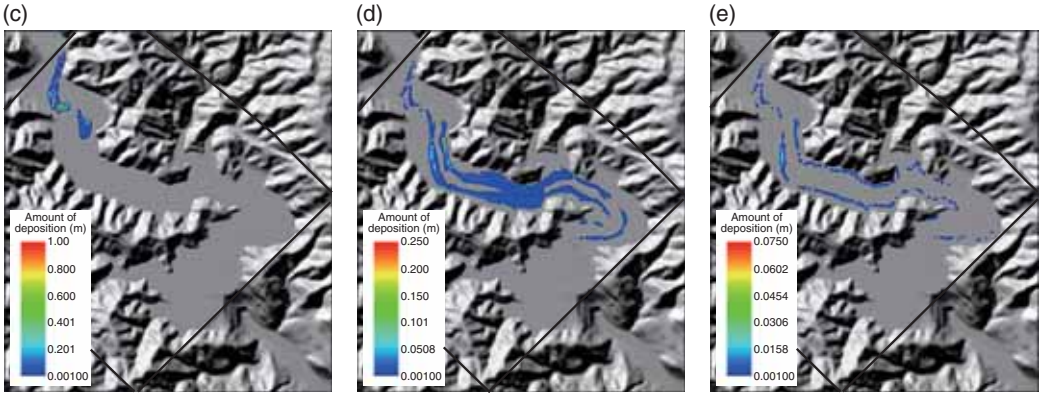

Fig.1-14 Examples of sediment deposition in terms of (c) sand, (d) silt, and (e) clay on the reservoir bed (map drawn using DEM data provided by the Geophysical Survey Institute)
Almost all of the sand and silt are deposited on the reservoir bed, but some clay leaves the reservoir and travels downriver.

Radioactive cesium (Cs), which was deposited on land after the accident at the TEPCO's Fukushima Daiichi NPS (1F), adheres strongly to soils, especially if they are rich in clay. Its migration is mainly caused by soil erosion and sediment transport within surface water during times of widespread flooding. Although the alleviation of all sediment movement is impossible, adequate operation of dam reservoirs may mitigate the dispersion of sediment-absorbed radioactive Cs.

We simulated the movements of sediment and radioactive Cs in the Ogaki Dam Reservoir in Fukushima Prefecture using several simulation models to understand sediment migration behavior during floods. We chose this reservoir because it is located in the middle of the Ukedo river, the river which was most affected in terms of radioactive Cs by the accident at 1F.

Fig.1-13 shows the Ogaki Dam Basin and the simulation results for the amount of sediment that entered into the river system, exported to the ocean, and deposited on the reservoir bed. This simulation was performed using our watershed model, the Soil and Cs Transport model. As can be seen from the figure, almost all of the sediment that entered the upstream part of the river was eventually deposited on the reservoir bed.

Fig.1-14 shows the results for the amounts of sand, silt, and clay that were deposited on the reservoir bed 3 days after a typical flood event. This simulation was performed with the Nays 2D code. Almost all the sand and silt was deposited on the reservoir bed. However, because of the size difference, the locations of the largest deposits of each sediment grade differed. The sand was mainly deposited near the entrance of the reservoir and the silt was deposited almost everywhere under consideration. Clay, on the other hand, remained suspended in the reservoir for longer. More than half of it was eventually deposited on the reservoir bed, while the rest left the reservoir and flowed downriver in our simulation.

In addition, we have simulated the same problem using different water heights within the reservoir. When the water level was lowered, the sand and silt generally behaved in the same manner as above. However, more than half of the clay passed through the reservoir and flowed downstream in a shorter time than it took in the previous case. The results indicate that adjusting the water height in the reservoir may provide a countermeasure against radioactive Cs migration from, or accumulation in, the reservoir. At present, intensive field investigations are ongoing with the goal of validating our simulation results and refining the model as necessary.

Reference

Kitamura, A. et al., Predicting Sediment and Cesium-137 Discharge from Catchments in Eastern Fukushima, Anthropocene, vol.5, 2014, p.22–31.

1–7 Chemical Bonding between Radioactive Cesium and Clay Minerals Revealed by Supercomputer

— First-Principles Calculation Studies of the Chemical Adsorption Form of Cesium on Clay Minerals —

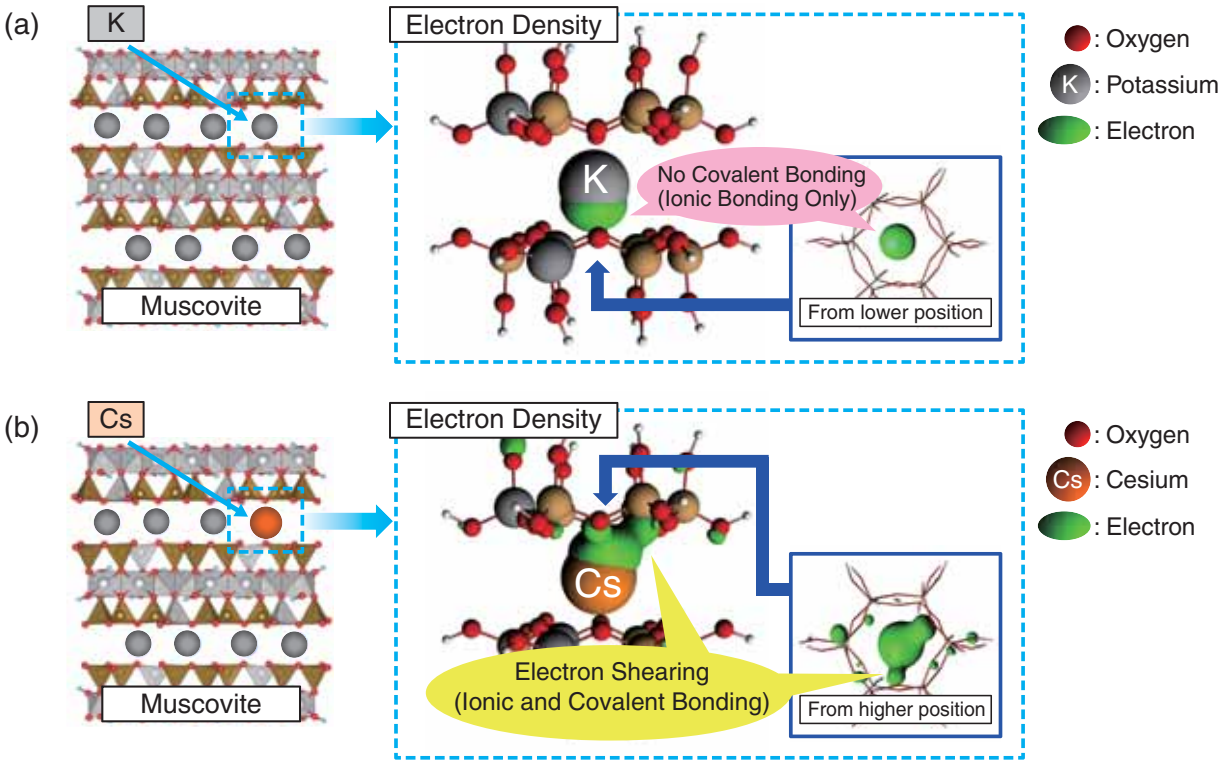

Fig.1-15 Model of clay minerals and electron density
(a) A typical muscovite model and the electron density of K. (b) Cs-adsorbed muscovite and the electron density of Cs.

Large amounts of radioactive nuclides were released into the environment by the accident at the TEPCO's Fukushima Daiichi NPS in 2011. The relatively short-life nuclides like radioactive iodine have almost entirely decayed, but the radioactive cesium (Cs) still remains in the topsoil, and it will remain a primary γ-emitter source for a long time.

It is well-known that Cs is strongly adsorbed onto soil and is difficult to extract from it. At present, the government is operating large-scale decontamination by removal of the contaminated soil and storing it. However, storage sites are extra environmental burden. Therefore, there is a great demand for the development of efficient separation methods of Cs from soil.

To achieve the above purpose, it is important to clarify details of the form of chemical adsorption of the Cs onto the soil, e.g., which ingredient in the soil is essential for adsorption and chemical bonding. If we obtain such information, we can select one of the most efficient decontamination methods based on scientific ideas and approach the final goal at a reasonable speed.

In general, the adsorption process of Cs on topsoil is regarded as follows. First, Cs takes the form of a dissolved ion just before the fallout. Afterwards, the dissolved Cs is selectively and irreversibly adsorbed by micaceous clay minerals through ion exchange with the potassium (K) preoccupied by these minerals. However, the chemical form produced by the adsorption as yet remains unknown. Thus, we studied the form using a numerical technique called a "first-principles calculation method" using a JAEA supercomputer.

We selected muscovite as a target model system in clay minerals and evaluated the electronic states of muscovite together with cations (K and Cs) as shown in Fig.1-15. Consequently, we found that the chemical bond between the oxygen in muscovite and Cs is a combination of ionic and covariant although one between the oxygen and K is only ionic (Fig.1-15). The covalent bonding is caused by the sharing of electrons between bonded atoms. Due to this counterintuitive character, the bonding strength is relatively enhanced. The condition necessary for making a covalent bond is the closeness of energies of the electron orbitals between the bonding atoms. Indeed, we found that the electron orbitals of oxygen and Cs are very close in terms of energy, which is in marked contrast to the clear orbital energy difference between oxygen and K. We are now trying to reveal methods for cutting the special bond between Cs and clay minerals to reduce the volume of waste soils produced by large-scale decontamination efforts in Fukushima.

Reference

Okumura, M. et al., First-Principles Studies on Cesium Adsorption of Clay Minerals; Mechanism and Chemical Bonding, Nippon Genshiryoku Gakkai-Shi, vol.56, no.6, 2014, p.20-25 (in Japanese).

1–8 Translocation of Radioactive Fallout Cesium in Trees

— Analysis of the Distribution of Radioactive Cesium in Plants Using Autoradiography —

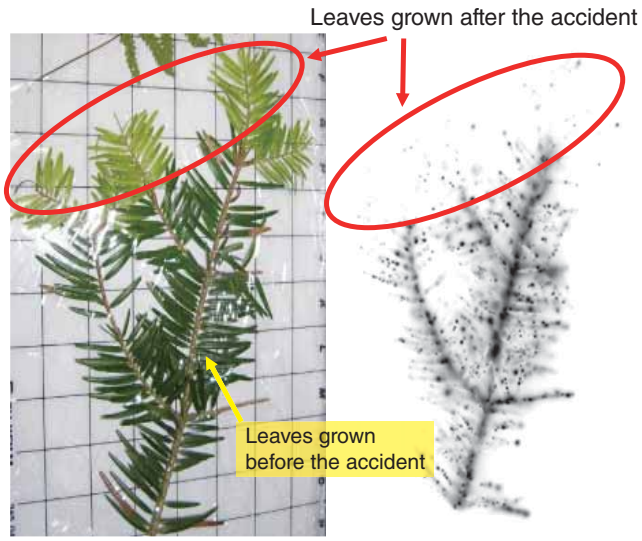

Fig.1-16 Autoradiograph (AR) image of *Torreya nucifera* sampled after 2 months of the accident
(left) Photograph of *T. nucifera*, (right) AR image. Black spots in the AR image show radiation sources in branches and leaves, indicating the presence of radioactive Cs. Red circles indicate the leaves (light green colored leaves in the photo) that grew after the accident. Black spots are practically zero within the red circles, indicating that the radioactive Cs in the old leaves (yellow arrow) was rarely transported into the young leaves.

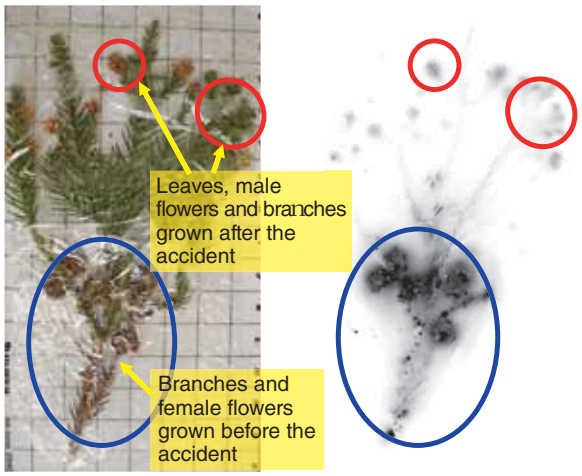

Fig.1-17 AR image of *Cryptomeria japonica* sampled after about 2 years of the accident
(left) Photo of *C. japonica*, (right) AR image. Blue circles indicate the branches, female flowers, and old leaves in the photo (yellow arrows) that grew before the accident. Red circles indicate that male flowers and leaves that emerged after the accident contain some amount of radioactive Cs inside them.

How were radionuclides attached to and transported in forest plants and soil after the fallout from the accident at the TEPCO's Fukushima Daiichi NPS? This question must be resolved to quantify present and future forest contamination. Distributions of radionuclides in plants and soil samples are usually measured by cutting small fractions from the samples. Unfortunately, this technique requires considerable time and effort. Thus, we have applied an autoradiography technique to analyze the distribution of radionuclides within the plants and soil.

We collected *Torreya nucifera* and *Cryptomeria japonica* samples in Iitate-mura, Soma-gun, Fukushima in May 2011 and Okuma-machi, Futaba-gun, Fukushima in December 2012, respectively. We placed the samples on an imaging plate (IP) coated with fluorescent paint that reacts with radiation and photographed the spatial distribution of radionuclides. The distribution of radionuclides in the branches and leaves of *T. nucifera* (Fig.1-16(left)) was analyzed by autoradiograph (AR) images, where many black spots were present (Fig.1-16(right)). These black spots appeared on IP in response to radiation originating from radioactive Cesium (Cs). Note that ^{131}I was decayed out in May. Fig.1-16(left) illustrates dark and light green leaves that grew before (old) and after (young) the accident, respectively. Black spots were present on the dark green leaves but not on the light green leaves, indicating that radionuclides attached to the old leaves were rarely transported to the young leaves. The same result was obtained from analysis of Cryptomeria japonica.

The AR image (Fig.1-17(right)) in *C. japonica* (Fig.1-17(left)) shows many black spots on the branches and the female flowers that emerged before the accident. On the contrary, broadened black areas were observed on the leaves and female flowers that emerged after the accident, indicating that radioactive Cs was translocated from the tree surface to the new branches and leaves. Since the top of the leaves and male flowers are actively growing, and since K ions are known to be accumulated in the active areas, radioactive Cs may have been transported from the old branches to the newer area.

These results clearly show that radioactive Cs deposited on the tree surface is slowly translocated to new growing areas over timescales of the order of years.

Reference

Sakamoto, F., Ohnuki, T. et al., Determination of Local-Area Distribution and Relocation of Radioactive Cesium in Trees from Fukushima Daiichi Nuclear Power Plant by Autoradiography Analysis, Nippon Genshiryoku Gakkai Wabun Ronbunshi, vol.12, no.4, 2013, p.257-266 (in Japanese).

1–9 Easy Monitoring of the Radioactive Cesium Concentration in Water

— A New Assay System Using a Cesium Adsorption Disk and the GM Survey Meter —

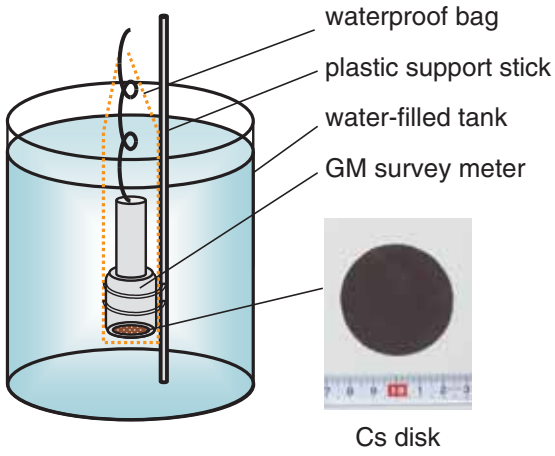

Fig.1-18 A new assay system for monitoring the radioactive Cs concentration in water
Radioactive Cs in water is adsorbed onto a Cs disk, and its radioactivity is measured with a GM survey meter. The Cs disk is then fixed onto the probe of the GM survey meter and sunk in a water-filled tank to decrease the background count rate.

Table 1-1 Application to outdoor school swimming pool water decontamination
Our assay system was applied to the decontamination of an outdoor school swimming pool in Fukushima in July 2011. As a result, it was quickly confirmed at the site of the decontamination that the pool water treated had a radioactive Cs concentration of under ~60 Bq/ℓ, which was below the effluent standard value of 200 Bq/ℓ at that time. This demonstrated the viability of our assay system.

Date (2011)	Cs concentration (Bq/ℓ)	Throughput of pool water (m^3)
July 2	<37	0-65
July 9	48±9	65-131
July 10	56±10	131-183
	62±13	183-235
July 11	<30	235-236

In areas contaminated by the discharge of radioactive cesium (Cs) from the accident at the TEPCO's Fukushima Daiichi NPS, continual monitoring of water and decontamination activities have been conducted. These field operations demand an easy method for monitoring the radioactive Cs concentration in water.

We developed a new assay system using a cesium adsorption disk (Cs disk) and a Geiger-Mueller (GM) survey meter for field operations (Fig.1-18). This assay system comprised (1) the adsorption of radioactive Cs on a Cs disk by filtering of water, (2) the determination of the β count rate of the Cs disk using the GM survey meter, and (3) the calculation of Cs radioactivity on the basis of a calibration factor. The Cs disk (Sumitomo 3M Co. Ltd., Empore™ Cs Rad Disk) contains Cs adsorbent in its matrix.

Some features of our assay system included: high detection sensitivity to β-rays, an easy method of use involving only portable apparatuses, and applicability to water samples contaminated only with ^{134}Cs and ^{137}Cs. In addition, because the calibration factor of ^{137}Cs is larger than that of ^{134}Cs, the use of the former factor led to conservative evaluations.

In the decontamination of an outdoor school swimming pool in Fukushima in July 2011, our assay system was applied to the determination of the radioactive Cs concentration in the pool water. About 100 mℓ of the samples collected from the pool water had a radioactive Cs concentration below ~60 Bq/ℓ. Since this value was below the effluent standard value at that time (200 Bq/ℓ), the decontaminated pool water was pumped out into a nearby river (Table 1-1).

Our assay system is expected to be applied to the monitoring of tap water, because its detection limit reaches 1 Bq after about 10 min of the measuring time.

Reference

Nagano, T. et al., Method for Monitoring Radioactive Cesium Concentration in Water using Cesium Adsorption Disk and GM Survey Meter, Nippon Hoshasen Anzen Kanri Gakkai-Shi (Japanese Journal of Radiation Safety Management), vol.11, no.2, 2012, p.139-145 (in Japanese).

1–10 Assessment of Radiation Dose Reduction of Radioactive Cesium in Buildings
— Numerical Simulation Analysis Using Building Models —

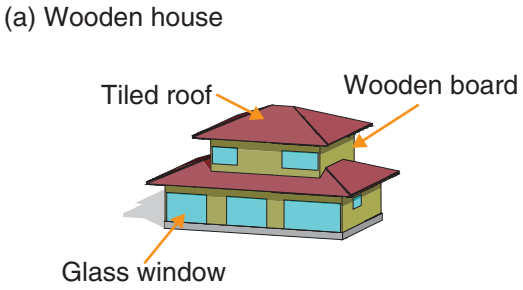

Fig.1-19 Outside appearance of building models
Building models were constructed in three dimensions.

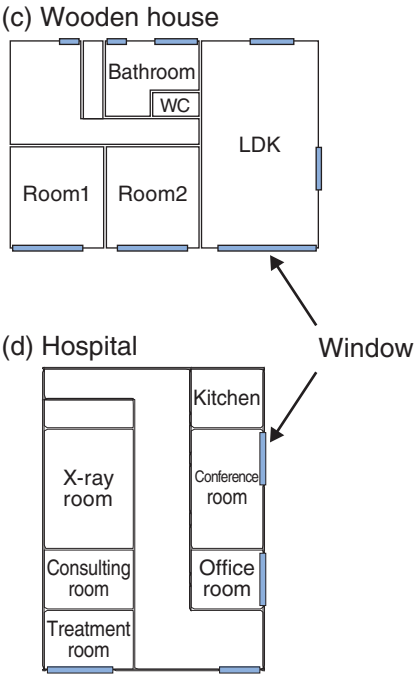

Fig.1-20 1st floor layouts in building models
Building models were constructed accounting for room compartments.

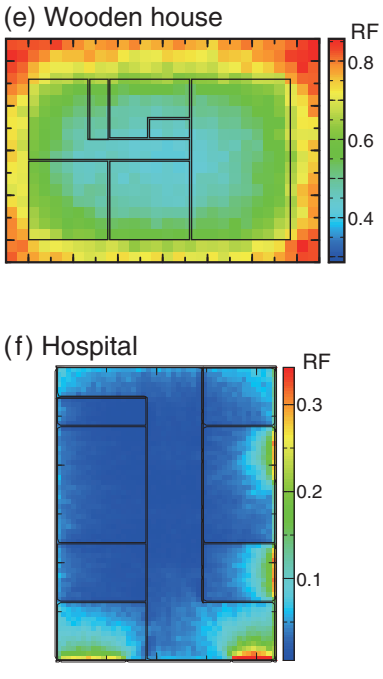

Fig.1-21 Distribution of the radiation dose RF
While RF gradually decreases from the outer walls to the center of wooden houses, γ-ray contributions from windows are essential in concrete buildings.

Radioactive nuclides were discharged by the accident at the TEPCO's Fukushima Daiichi NPS (1F) and radioactive cesium (Cs) still remains in the environment. Precise radiation dose assessment is important for public health and for plans for the return of evacuees. Information about the dose rate measured in the open air has been made available for each area by radiation monitoring, which has been conducted since the accident at 1F. On the other hand, residents spend large amounts of their daily lives inside buildings, where dose rates are reduced compared with their values in open air. Thus, evaluation of dose reduction in various buildings is required for the assessment of external radiation dose exposure accounting for individual lifestyles.

We selected 27 types of buildings based on surveys of buildings in the Fukushima area, and investigated the dose reduction in these buildings by means of numerical simulation analysis. These selected buildings were constructed as three-dimensional models (Fig.1-19) with consideration of their inner structures and compartmentalization of their rooms based on their usages (Fig.1-20). By incorporating the building models into the radiation transport code, PHITS, the behaviors of γ-rays were simulated from radioactive Cs homogenously distributed over the ground surface to inside the buildings. We computed the dose ratios of the inside of the buildings to the outside, the so-called reduction factor (RF), with these simulations. In addition, the distribution inside the buildings was illustrated on top of the layout (Fig.1-21) to analyze the influence of building's configuration on RF.

In wooden houses, the radiation dose decreases towards the center (Fig.1-21(e)) and RF becomes lower for a house with a larger size. This tendency is due to the absence of radioactive Cs beneath the house. In contrast, the dose rates inside concrete buildings are lower than those inside wooden houses because of the high shielding effect of concrete walls. The RF distribution in concrete buildings is largely influenced by the location and size of the windows, which offer little shielding effect (Fig.1-21(f)).

We developed a technique for analyzing the influence of building configuration on dose reduction in various buildings. The obtained data are expected to be useful for dose estimation and reduction countermeasures for returning residents.

Reference

Furuta, T. et al., Analyses of Radiation Shielding and Dose Reduction in Buildings for Gamma-rays Emitted from Radioactive Cesium in Environment Discharged by a Nuclear Accident, JAEA-Research 2014-003, 2014, 100p. (in Japanese).

1–11 Detection of Defects in the Fuel Cladding Tube

— Development of a Defect Detection Technique Using High-Resolution X-ray Computed Tomography —

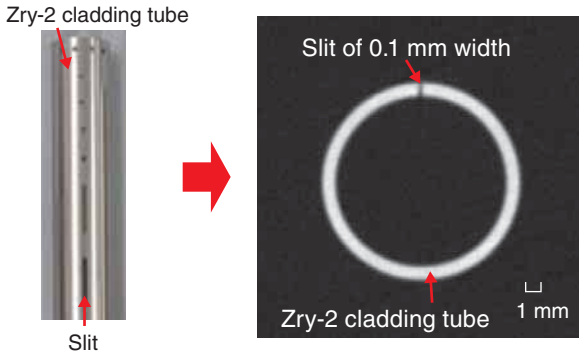

Fig.1-22 X-ray CT image of a zircalloy-2 cladding tube with a slit
A 0.1-mm-wide slit can be observed on the X-ray CT image.

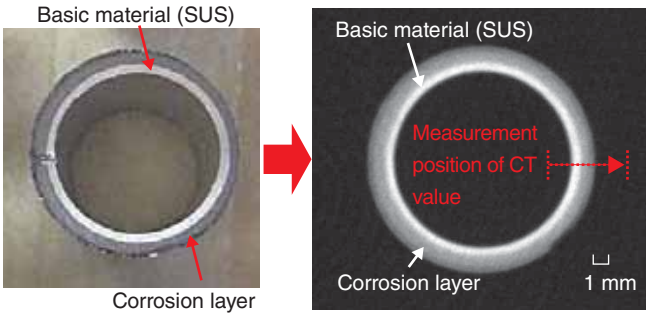

Fig.1-23 X-ray CT image of a SUS tube with a corrosion layer
The corrosion layer could be discriminated from the basic material of a SUS tube.

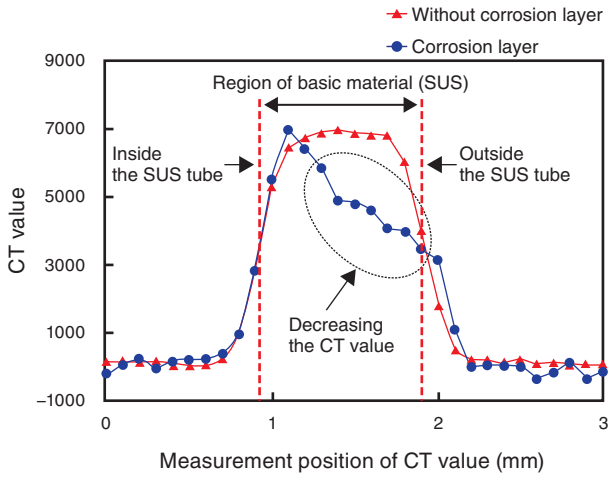

Fig.1-24 CT value distribution of a SUS tube
The CT value decreases with the density. The CT value distribution of the SUS tube with a corrosion layer was lower than that of the SUS tube without the corrosion layer.

The fuel assemblies of the TEPCO's Fukushima Daiichi NPS (1F) will be transported from the spent fuel pool to the shared pool and stored for a long time. In the severe accident of 1F, concrete fragments fell into the spent fuel pool due to the hydrogen explosion, and sea water was temporarily injected to cool the fuel assembly. There is a possibility of defects (the corrosion and the crack) forming on the fuel assembly component materials (cladding tube, tie plate, spacer, support grid, etc.) due to the effects of the concrete fragments and sea water. Thus, it is necessary to evaluate the integrity of the fuel assemblies to safely transport from the spent fuel pool and store in the shared pool.

In this study, we developed a technique for detecting cracks and the corrosion damage on the fuel cladding tube using an X-ray computed tomography (CT) technique, which is the non-destructive way to examine the irradiated fuel assembly.

Zircalloy-2 (Zry-2) cladding tube specimens were manufactured with slits designed to simulate cracks, and an X-ray CT examination was performed on them to obtain data about crack-detection performance with this apparatus. In addition, SUS tube specimens having corrosion layers were manufactured and also subjected to X-ray CT examination to obtain basic data about detection performance on the corrosion layer. The 0.1-mm-wide slit on the Zry-2 cladding tube could be observed on the X-ray CT image in Fig.1-22, and a corrosion layer (gray region) with a thickness of more than 0.35 mm could be discriminated from the basic material (white region) in the X-ray CT image in Fig.1-23. An X-ray CT examination of the Zry-2 cladding tube based on this result has been conducted.

The X-ray CT image is composed of CT values, which depended upon the density. This image analysis technique was developed to evaluate the slit width and the corrosion thickness using the CT value distribution (Fig.1-24). The defect on the fuel cladding tube can be evaluated without dismantling of the fuel assembly by using this image analysis technique. At present, a high performance image analysis technique is being developed to increase the evaluation accuracy.

Reference

Ishimi, A. et al., X-ray CT Basic Data about Inspection of Irradiated Fuel Assembly, JAEA-Data/Code 2014-012, 2014, 72p. (in Japanese).

1–12 Laser Spectroscopic Analysis of Underwater Debris in a Nuclear Reactor Core

— A Contribution to the Decommissioning of the TEPCO's Fukushima Daiichi NPS —

Fig.1-25 Prototype of the transportable LIBS apparatus
This instrument, whose size is 1.2 m (W) × 1.5 m (D) × 0.5 m (H), is composed of lasers, optical fibers, a LIBS probe, and a spectrometer.

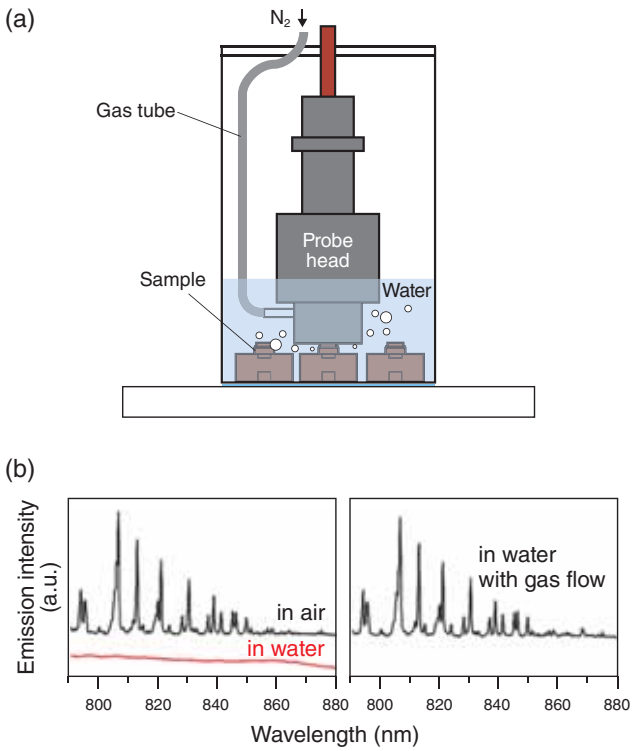

Fig.1-26 Typical experimental set-up and results
(a) Image of the experimental set-up in the LIBS measurement. (b) LIBS emission spectra of zircaloy in air and water (left) and in water with gas flow (right).

To decommission the TEPCO's Fukushima Daiichi NPS (1F), environmental information is needed about the inside of the post-accident reactor core. In 1F, molten fuel debris (a mixture of melted fuel core material, fuel cladding, and construction material) might be submerged in water inside the reactor core. There is not enough space for the direct inspection of the reactor core, because many pipes for water and electricity occupy the inside. Moreover, a high radiation field hinders people's access. Thus, a remote sensing technique that is applicable in narrow spaces is crucial for the inspection of 1F.

For this purpose, we have proposed a combination of a fiber optic transmission system and laser-induced breakdown spectroscopy (LIBS), which is an analysis technique that comprises ablating a material with a focused laser beam and detecting emission from the ablation plasma. A prototype of the transportable LIBS apparatus is shown in Fig.1-25. Among the most pivotal parts was the fiber optics, which needed to have high resistivity against radiation. To test the radiation resistivity, the fiber optics employed in our apparatus were exposed to ^{60}Co γ-rays with a total dose of 1.6 MGy in the Takasaki Institute. Comparing the optical conditions before and after the radiation exposure, we confirmed that the transmissivity of the fiber optics in the infrared region (730–1100 nm) was not degraded by the irradiation, and thus, infrared can be used for the laser and the emission transmission.

In addition to radiation resistivity, the LIBS analysis of underwater debris demands a special technique, since water quickly quenches the plasma emission that is induced by laser ablation. Hence, we attached a gas-flow system to the head of the LIBS probe and performed the LIBS analysis under a quasi-atmospheric environment in water (Fig.1-26(a)). Fig.1-26(b) is the emission spectrum of zircaloy in water using the gas flow system.

Towards *in situ* observation and analysis of the debris, we are improving the system that comprises our LIBS apparatus combined with radiation measurement and image detection through optical fibers.

Reference
Saeki, M. et al., Development of a Fiber-Coupled Laser-Induced Breakdown Spectroscopy Instrument for Analysis of Underwater Debris in a Nuclear Reactor Core, Journal of Nuclear Science and Technology, vol.51, issues 7-8, 2014, p.930-938.

1–13 Melting and Crushing of Fuel Debris with Laser Light as a Heat Source
— Countermeasures to Fuel Debris Characterized by Indefinite Shapes, Higher Hardness, Multi-Ingredients, and Porous Bodies —

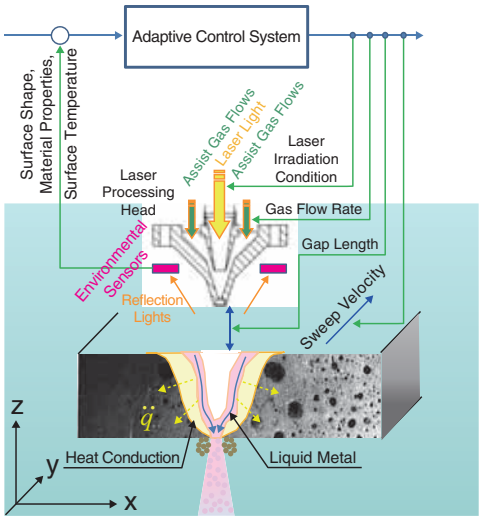

Fig.1-27 An adaptive control system using laser light for melting and crushing fuel debris
The system is adaptively controlled toward suitable laser irradiation conditions through the use of various environmental sensors.

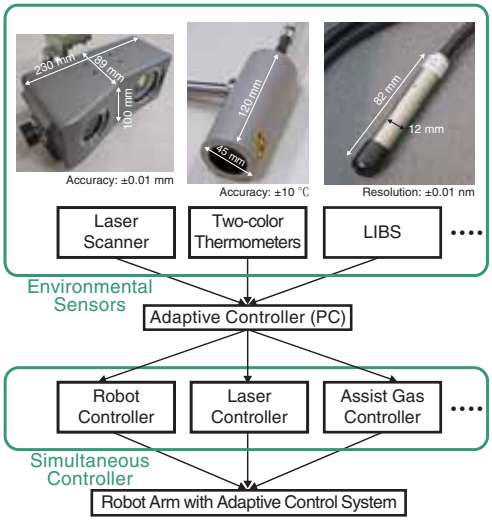

Fig.1-28 Block diagram of the adaptive control system
The system prevents decreases in the melting and crushing performances by simultaneous control of the robot's motion, the laser irradiation, and the assist gas flow.

(a) The establishment of a laser optical path by an assist gas flow

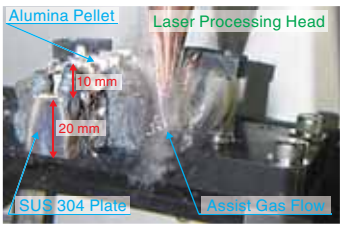

(b) A snapshot of the melting and crushing process in water

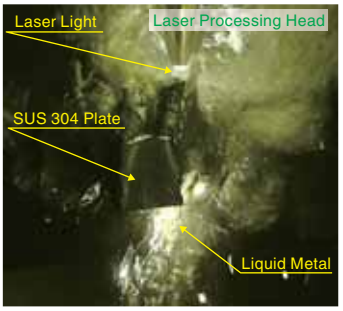

Fig.1-29 A melting and crushing experiment in water
It was confirmed that the system has the potential to melt and crush fuel debris in water.

Laser light is characterized by higher power density, local processability, remote controllability, and so forth, and can be used to melt and crush various materials, such as fuel debris, which do not depend upon fracture toughness.

An adaptive control system for yielding suitable laser irradiation conditions, shown in Fig.1-27, is being developed using various environmental sensors, such as a laser scanner to catch indefinite shapes, a LIBS sensor to identify multi-ingredient materials, and a two-color thermometer to monitor melting conditions in laser irradiated positions for the removal of fuel debris and in-vessel structures from the TEPCO's Fukushima Daiichi NPS (1F).

Fig.1-28 indicates a block diagram of the adaptive control system. The system comprises environmental sensors; a personal computer containing the adaptive control algorithm; and a simultaneous controller for robot motion, laser irradiation, and assist gas flow. While control procedures are employed in the system to obtain suitable laser irradiation conditions, behaviors in the course of the laser melting process are monitored by checking the two-color thermometer signals every time step. Thus, suitable laser irradiation conditions are determined from control rules based on the response surface function.

The adaptive control system was applied to a melting and crushing water experiment using a combined test piece comprising a SUS304 plate (20 mm^{t}) and an alumina pellet (8 $mm^{O.D.}$ × 10 mm^{h}) simulating fuel debris. Fig.1-29 shows experimental photos. A steady-state assist gas flow field of 350 ℓ/min was established as a laser optical path before being used to melt and crush transients (Fig.1-29(a)). In the transient experiments, the SUS304 plate and the alumina pellet of the combined test piece were irradiated by continuous laser light at 6 kW and pulsate laser light over 100 ms, respectively. The sweep velocity of the laser processing head was kept constant at 30 mm/min. As shown in Fig.1-29(b), the combined test piece was melted and crushed well by the use of the adaptive control system.

The results obtained from the water experiment are very encouraging in the sense that the adaptive control system may be used as an efficient tool for removing fuel debris and in-vessel structures from the 1F.

References

Muramatsu, T. et al., Research on Removal Technologies of Fuel Debris and In-Vessel Structures using Laser Light (I) –Research Plan and Research Activities on FY2012–, JAEA-Research 2013-024, 2013, 49p. (in Japanese).
Muramatsu, T. et al., Research on Removal Technologies of Fuel Debris and In-Vessel Structures using Laser Light (II) –Research Activities on FY2013–, JAEA-Research 2014-018, 2014, 41p. (in Japanese).

1–14 Maintaining the Integrity of the Reactor Vessel until the Completion of Fuel Removal

— The Influence of Radiation on the Corrosion of Vessel Steels and Corrosion Measures —

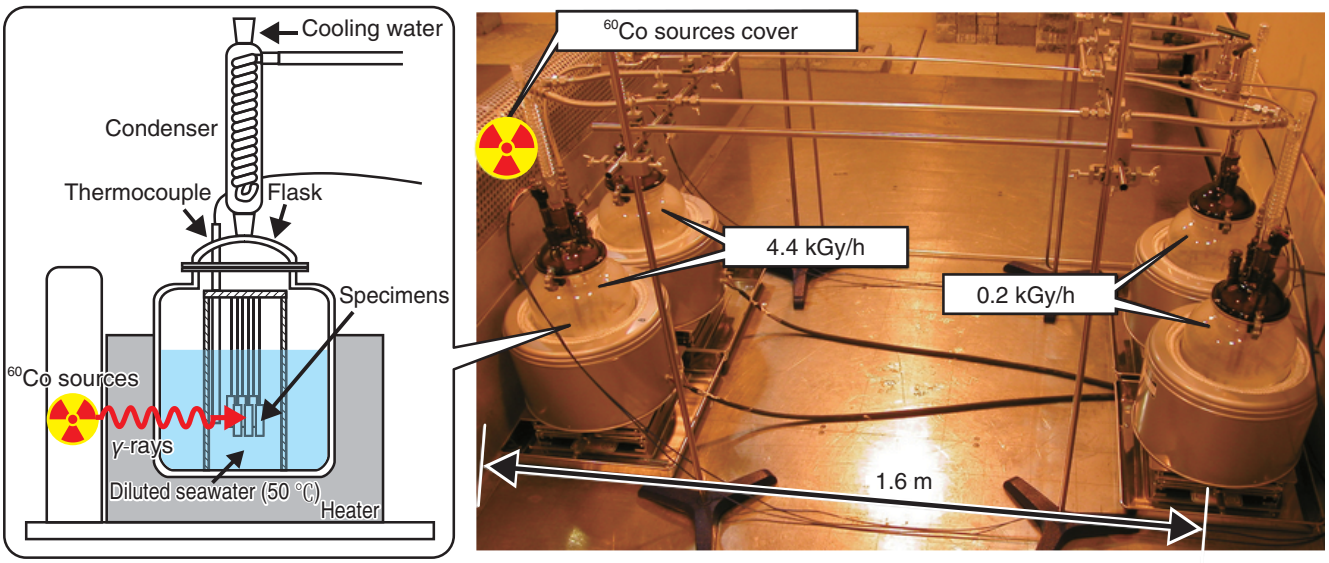

Fig.1-30 Corrosion testing of steel specimens under γ-ray irradiation
To simulate the conditions inside PCVs, corrosion testing of steel specimens in diluted seawater under γ-ray irradiation was conducted.

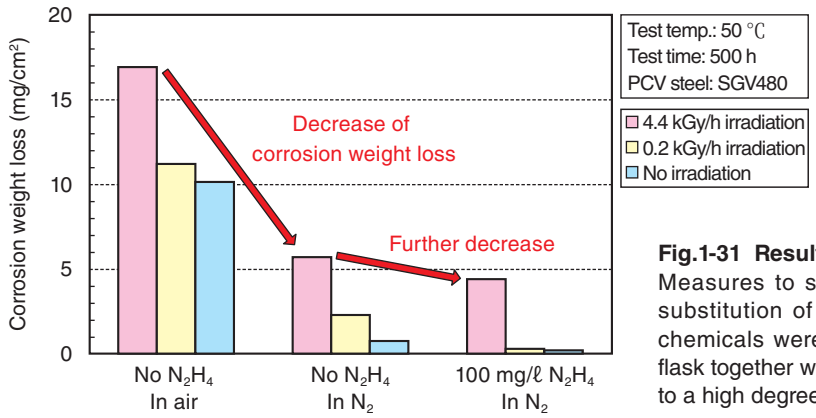

Fig.1-31 Result of the corrosion test of PCV steel
Measures to suppress the corrosion of steel by nitrogen substitution of the gas phase of PCV and the addition of chemicals were examined. The nitrogen substitution in the flask together with hydrazine addition could suppress corrosion to a high degree.

Seawater was poured into reactors 1F1-1F3 after the accident at the TEPCO's Fukushima Daiichi NPS (1F). Therefore, the primary containment vessel (PCV) composed of carbon steel will be corroded by contact with seawater over the long term, and there is a possibility of the loss of structural strength and/or the formation of holes in the vessel. Furthermore, the decomposition of water molecules due to high doses of radiation (i.e., water radiolysis) in the PCV causes the production of chemically active species, such as hydrogen peroxide, which could accelerate the corrosion of the vessel steel. It is, therefore, necessary to predict and control the corrosion of the steel until the completion of the removal of nuclear fuel and debris.

As shown in Fig.1-30, specimens of SGV480 steel–identical to the actual steel used in the PCV–were immersed in diluted artificial seawater and irradiated by γ-rays for 500 h. Fig.1-31 shows the results of the corrosion test under irradiation. "Corrosion weight loss" on the vertical axis is the weight lost by the specimen due to corrosion, and was obtained by removing the rust from the specimen, weighing it, and comparing the result to that obtained before the specimen's immersion. After the accident at 1F, nitrogen gas was enclosed in PCVs for the purposes of preventing hydrogen explosions. Corrosion tests under irradiation in the test flask in which nitrogen gas was enclosed showed a decrease of the weight loss, as shown in Fig.1-31. Since the oxygen partial pressure of the gas phase in the flask decreased through nitrogen substitution, the concentration of dissolved oxygen in the diluted seawater also decreased, and consequently the corrosion rates of specimens decreased as well. Furthermore, the case that used nitrogen substitution together with the addition of hydrazine with the property of removing oxygen from water is shown on the right-hand side of Fig.1-31. From this result, it is believed that the corrosion of PCVs, wherein nitrogen is enclosed and hydrazine has been injected, is still under control at present.

Reference

Nakano, J. et al., Effects of Hydrazine Addition and N_2 Atmosphere on the Corrosion of Reactor Vessel Steels in Diluted Seawater under γ-rays Irradiation, Journal of Nuclear Science and Technology, vol.51, issues 7–8, 2014, p.977–986.

1–15 Estimation of the Chemical Form of Fuel Debris in a Reactor Pressure Vessel
— Estimation with the Help of Thermodynamic Calculation —

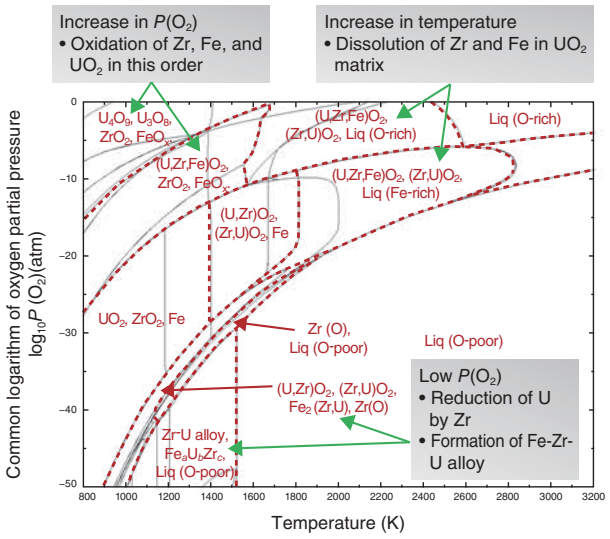

–Details for calculation–
- Composition: 65wt% UO_2; 27wt% Zr; 8wt% Fe
- Software: FactSage6.2 (http://www.factsage.com/)
- Database: TDnucl (http://www.crct.polymtl.ca/fact/documentation/)

Fig.1-32 Calculated phase diagram of temperature vs. oxygen partial pressure ($P(O_2)$) for the UO_2-Zr-Fe system
The chemical form of the fuel debris is expected to change depending upon the temperature and $P(O_2)$ during the melt progression of the BWR core. Oxygen partial pressure as well as temperature is expected to increase with the melt progression.

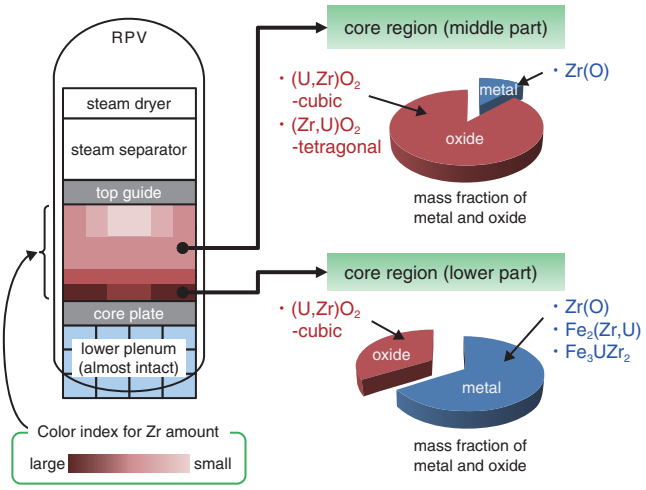

Estimated damage status in RPV after core degradation (The larger the amount of Zr becomes, the darker the cell is indicated)

–Result of thermodynamic calculation–
The mass fraction of metal/oxide and the chemical forms of fuel debris

Fig.1-33 Chemical form estimation for in-vessel fuel debris after core degradation
For 1F2, the spatial distribution of core materials and temperature were evaluated based on the results of melt progression analysis (left side of figure). Based on this information, the phase mass fraction under equilibrium was estimated (right side of figure).

To prepare for the removal of fuel debris at the TEPCO's Fukushima Daiichi NPS (1F), data on the physical properties of fuel debris are necessary. However, the actual situation inside the damaged core of 1F is hardly known. In this study, the chemical forms of fuel debris were estimated through thermodynamic calculation.

As a preliminary evaluation, the effects of temperature and oxygen partial pressure ($P(O_2)$) on the chemical forms of the fuel debris were investigated under constant composition of the core materials (UO_2, Zr, and Fe). As shown in Fig.1-32, at low $P(O_2)$, the metal Zr tends to react with UO_2 and Fe. With an increase in $P(O_2)$, the core materials are oxidized in the order Zr, Fe, and UO_2. Metallic phases, such as Zr(O) and $Fe_2(Zr,U)$, are expected to be formed as long as Zr is not fully oxidized. In addition, an increase in temperature is expected to cause the formation of mixed oxides, such as $(U,Zr)O_2$, and $(U,Zr,Fe)O_2$.

The composition of the core materials in the RPV after core degradation was evaluated from the results of the melt progression analysis conducted by Ishikawa et al (2012 Fall Meeting of the Atomic Energy Society of Japan). Based on this information, a thermodynamic calculation was conducted. Fig.1-33 shows the results of chemical form estimation for 1F Unit 2 (1F2). The middle part of the core region was occupied by mixed oxides, such as $(U,Zr)O_2$, while the lower part near the core plate was rich in metal phases, such as Zr(O) and $Fe_2(Zr,U)$. This trend is consistent with the result of the preliminary evaluation described above. However, if the RPV is severely damaged, the concrete from the pressure containment vessel floor also needs to be considered.

We are accumulating data on mechanical properties such as the hardnesses and fracture toughnesses of the typical phases of fuel debris, including metal phases. Those data will contribute to the appropriate selection of defueling methods and tools.

Reference

Ikeuchi, H. et al., Suggestion of Typical Phases of In-Vessel Fuel-Debris by Thermodynamic Calculation for Decommissioning Technology of Fukushima-Daiichi Nuclear Power Station, Proceedings of International Nuclear Fuel Cycle Conference (GLOBAL 2013), Salt Lake City, Utah, USA, 2013, paper 8174, p.1349-1356., in CD-ROM.

1–16 What Has Formed from the Melted Fuel and Control Blade?

— Investigating the Characteristics of Solidified Core Melt —

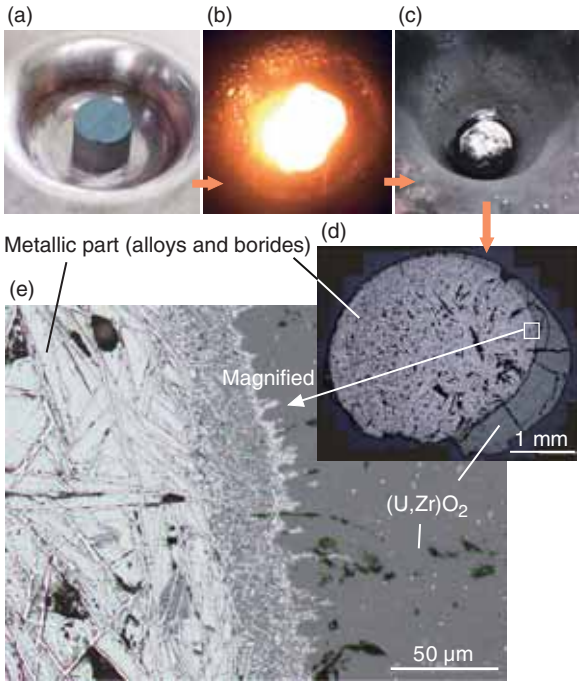

Fig.1-34 The appearance and cross-sectional images of a solidified melt specimens
Photos (a)–(c) show the starting mixture, melted state, and solidified button, respectively. (d) and (e) are the microphotographs of the cross section. The needle-like precipitation of crystalline ZrB_2 is found in the metallic part.

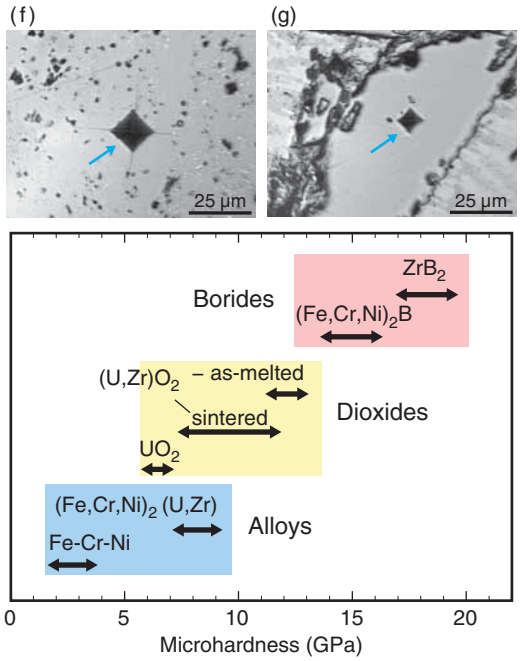

Fig.1-35 Comparison of the microhardnesses of phases in the solidified melt specimens
Photos (f) and (g) show examples of indentation on $(U_{0.5}Zr_{0.5})O_2$ and ZrB_2, respectively. Hardness increases in the order of alloys, dioxides, and borides.

For the decommissioning of the accident at the TEPCO's Fukushima Daiichi NPS (1F), the removal of fuel debris and its appropriate management are imperative missions. Therefore, we have been studying the characteristics of fuel debris using simulated specimens.

The fuel debris formed in the reactor cores mainly comprises materials from the fuel (UO_2 and Zr) and control blade (B_4C and stainless steel). However, the chemical form of boron in the fuel debris has not been well identified.

To simulate the solidified fuel debris in the reactor cores, some pelletized mixtures of B_4C, stainless steel, Zr, and $(U,Zr)O_2$ (a mixed oxide of UO_2 and ZrO_2) were arc-melted under an Ar atmosphere, as shown in photos (a)–(c) of Fig.1-34. The chemical forms in the solidified specimens were analyzed along the cross section (photos (d) and (e)). The specimens likely consist of $(U,Zr)O_2$ ceramic part and metallic part. The latter is found to include the precipitation of borides expressed as ZrB_2 and $(Fe,Cr,Ni)_2B$ in the alloy matrix of Fe-Cr-Ni and $(Fe,Cr,Ni)_2(Zr,U)$ intermetallic.

To examine the influence of oxygen in the atmosphere, the solidified specimens were annealed at 1500 °C in an Ar-0.1%O_2 mixed gas flow for 10 h. Consequently, the Zr and U in the alloy, and the Zr in ZrB_2 were oxidized to form a Zr-rich $(Zr,U)O_2$ layer on the surface. The boron isolated from ZrB_2 alternatively formed $(Fe,Cr,Ni)_2B$ inside the oxide layer.

As a basic mechanical property of fuel debris, the microhardnesses of the phases in the specimen were measured by a Vickers tester (Fig.1-35). It is found that the borides, especially ZrB_2, are extremely hard compounds in all the phases. The dense precipitation of borides in the fuel debris may potentially be a barrier against machining tools for removal operations.

The present study was sponsored by the Agency for Natural Resources and Energy, Ministry of Economy, Trade and Industry of Japan (METI).

Reference

Takano, M. et al., Characterization of Solidified Melt among Materials of UO_2 Fuel and B_4C Control Blade, Journal of Nuclear Science and Technology, vol.51, issues 7–8, 2014, p.859–875.

1–17 Management of Removed Fuel Debris

— A Study of Treatment Scenarios for Fuel Debris after Removal —

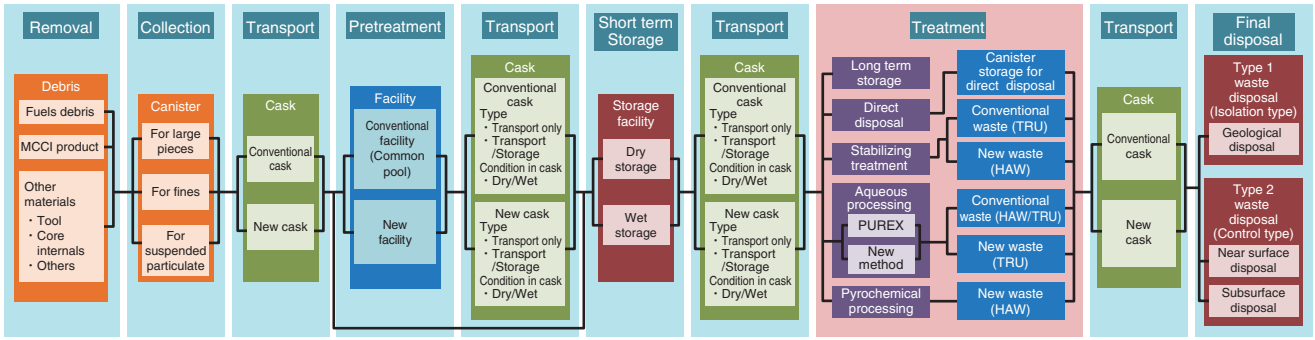

Fig.1-36 Complete scenario ideas from the removal of fuel debris to final disposal
Various options exist from removal to final disposal.

Table 1-2 Characteristics of each treatment scenario idea
The treatment scenario concepts based on several assumed methods are prioritized based on the extent to which they use existing technology.

	Long term storage	Direct disposal	Stabilizing treatment	Aqueous processing		Pyrochemical processing
				PUREX	New method	
Definition	Storage until disposal strategies are defined	Simple treatment for final disposal without U/Pu recovery	Stabilizing treatment for final disposal without U/Pu recovery	Present treatment for final disposal with positive U/Pu recovery		
Base technology	Intermediate storage of spent fuel	Direct disposal of spent fuel	Solidification of high-level waste	Aqueous reprocessing (PUREX)		Pyrochemical reprocessing (Metal electro-refining)
Outline	・Use simple treatment ・Store it after selecting a suitable method from among TMI-2 experiences and short-term storage methods ・Basically postpone the final disposal	・Use simple treatment ・Geological disposal after storage until the decision on the final disposal site is made ・Dispose as just spent fuel was removed or by adding some treatment to it	・Use simple treatment ・Stabilize the waste to reduce its leaching rate assuming it is vitrified ・Avoid dissolution to reduce the generation of secondary waste	Convert into a manageable form of waste based on existing disposal classification when possible		
				・Use simple processing with technical feasibility ・Recover only nuclear material that can be recovered easily	Give priority to the recovery of nuclear material and to the reduction of radioactivity in waste	

The removal of fuel debris from the TEPCO's Fukushima Daiichi NPS is scheduled to begin around 2020. Treatment (processing and disposal) methods for the removed fuel debris are expected to be finalized during the 20–25 year period following December 2011, when the emission of radioactive material and its radiation dose were confirmed to have been significantly inhibited. Therefore, it is necessary to consider an approach of comparative scenario evaluation and obtain fundamental information for selecting treatment methods by the beginning of the removal. In this study, the characteristics and technological problems of each treatment scenario were extracted and put in order, in preparation for comparative scenario evaluation in the future.

Several scenarios for the removal and disposal of fuel debris are shown in Fig.1-36. Among these scenarios, "Treatment" is regarded as a pre-processing step toward the manufacturing of a stable waste form for final disposal.

The selection of treatment methods was implemented for the following policies (Table 1-2).

(1) Storage until disposal strategies are defined
(2) Simple treatment for final disposal without U/Pu recovery
(3) Stabilizing treatment for final disposal without U/Pu recovery
(4) Present treatment for final disposal with positive U/Pu recovery

Elemental technologies for each treatment scenario were evaluated in terms of economy, amount of nuclear waste, and technological difficulties, on the premise that they function in practice. Consequently, it has been found that long-term storage has more advantageous aspects than the other methods, both economically and technologically. Direct disposal, on the other hand, has been found to produce the least amount of waste.

In summary, long term storage and direct disposal are the most advantageous scenarios, though they have some technological problems. The stabilizing treatment, aqueous processing, and pyrochemical processing options are inferior to the rest in terms of economy and the amount of waste.

The present study was sponsored by the Ministry of Economy, Trade and Industry of Japan (METI).

Reference

Fuel Debris Conditioning Technology Development Group, Fukushima Project Team et al., Fuel Debris Characterization and Treatment Technologies Development for TEPCO's Fukushima Daiichi Nuclear Power Station –2012 Annual Research and Development Report–, JAEA-Review 2013-066, 2014, p.83-92 (in Japanese).

1–18 An Exploration of the Reason for Iodine-131 Release after Core Cool Down

— Release of Iodine-131 from Contaminated Water in the Basement of Reactor Buildings —

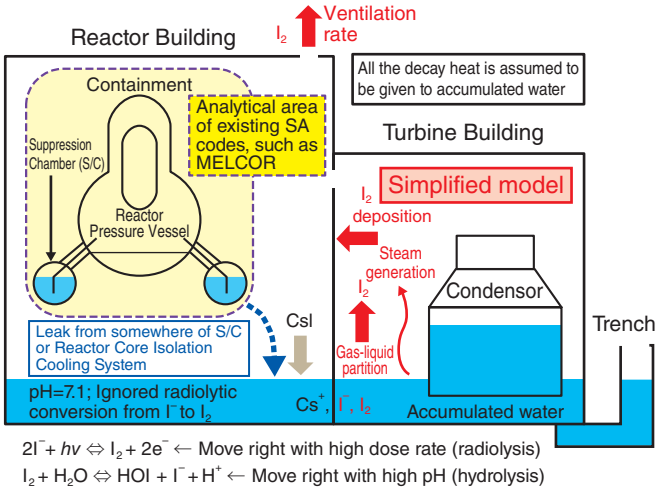

Fig.1-37 Schematic of contaminated water accumulation in the basements of reactor building and turbine building and the release from the accumulated water considered in present simplified model

During the 1F accident, somewhere of the reactor coolant system failed and contaminated water accumulated in the basements of the reactor building. Since the release of ^{131}I from the contaminated water due to gas-liquid partition is not considered to be negligible, a simplified model of the release from the contaminated water was prepared, as indicated in red.

Table 1-3 Estimated fractions of ^{131}I in accumulated water to each core inventory in late March

Unit	^{131}I (%)
1	0.51
2	74
3	26

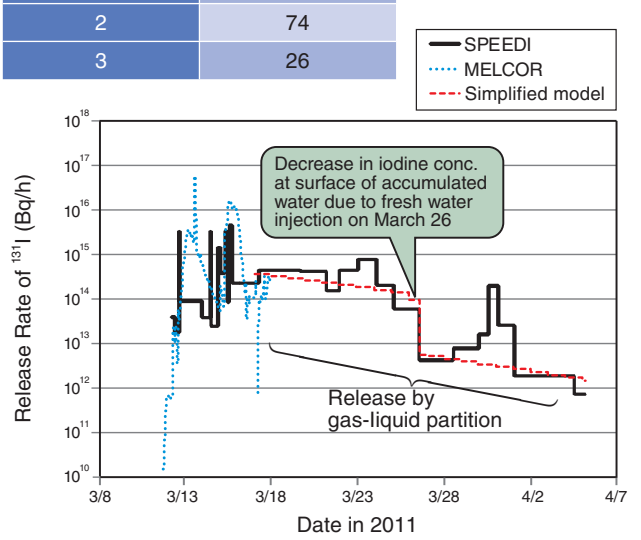

Fig.1-38 A comparison of the ^{131}I release rate between our simplified model and SPEEDI reverse estimation

Although our simplified model did not predict an increase in the release rate on March 23 and 30 due to shortages of cooling water and re-melt, the model mostly reproduced the continuous release from the accumulated water after March 17 and the decrease in the release rate due to fresh water injection on March 26.

During the process of core cooling in the accident at the TEPCO's Fukushima Daiichi NPS (1F), large amounts of contaminated water accumulated in the basements of the reactor buildings (Fig.1-37). The present study estimated the quantity of I-131 (^{131}I) in the water as of late March in 2011 based on the data made available to the press. The estimation showed that a significant fraction of the ^{131}I inventory was dissolved in water (Table 1-3).

Most of ^{131}I released from the fuel would be dissolved as I^- in water, while some of the I^- could become I_2 and be released as a gas phase due to the gas-liquid partition in the case of acidity. This and the ventilation of the reactor buildings result in an increase in the release of ^{131}I into the environment.

Many analyses of ^{131}I release have been attempted, mainly using the two methods. One is reverse estimation using the atmospheric dispersion code SPEEDI combined with the environmental monitoring data. The other is estimation using severe accident analysis codes, such as MELCOR. No large difference was found in the cumulative release to environment between the two methods. However, SPEEDI predicted continuous release for longer than one month, whereas MELCOR predicted that it would stop after March 17 due to the decrease in release from the cooled core (Fig.1-38).

In the present study, we prepared a simplified model of ^{131}I release from the accumulated water, and tried to simulate the continuous ^{131}I release predicted by SPEEDI after March 17.

The pH in the water after March 17 was assumed to be constant at the value of 7.1 measured on March 27. The ventilation rate of the reactor building was determined from the steam generation rate, assuming that all the heat from the decay is given to the water. The decrease in the I_2 release at the time of fresh water injection for core cooling on March 26 was simulated by the stratification of water, due to difference in specific gravity between fresh and sea waters. The simplified model well-reproduced the release baseline predicted by SPEEDI (Fig.1-38).

The present study showed that the ^{131}I release from the accumulated water may explain the release between March 17 and 26. This strongly suggests a need for improvement of the current MELCOR approach, which treats the release only from containment breaks.

We plan to further improve the present simplified model through detailed investigation of the effect of revaporization or resuspension of ^{131}I once-deposited on the wall surface, as well as the stratification of accumulated water at the time of fresh water injection.

Reference

Hidaka, A. et al., Quantities of I-131 and Cs-137 in Accumulated Water in the Basements of Reactor Buildings in Process of Core Cooling at Fukushima Daiichi Nuclear Power Plants Accident and Its Influence on Late Phase Source Terms, Journal of Nuclear Science and Technology, vol.51, issue 4, 2014, p.413–424.

1–19 Safe Storage of Spent Cesium Adsorbent

— Characterization and Evaluation for Hydrogen Production and Corrosion —

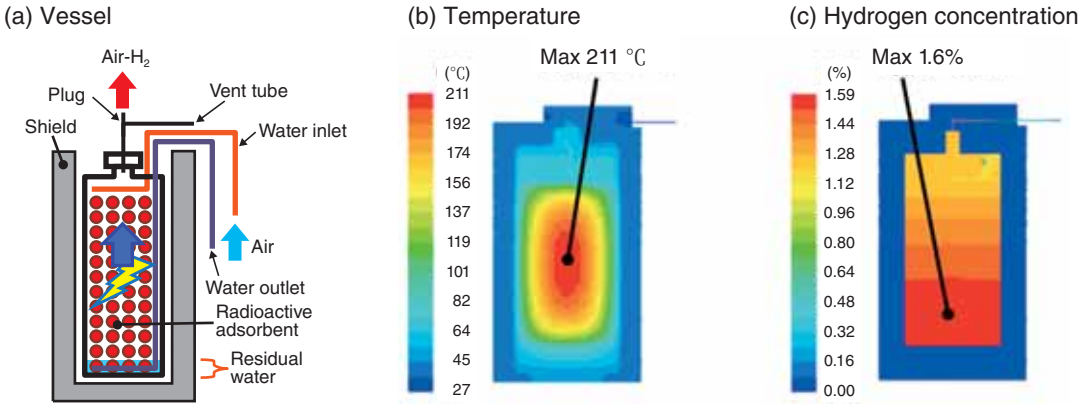

Fig.1-39 An example of the thermal hydraulic analysis of a Cs adsorption vessel with residual water
A reference vessel (decay heat 504 W, water level 24 cm, hydrogen production 20.5 ℓ/d, absorbed dose rate at the bottom 755 Gy/h) was evaluated. Air is introduced by the water inlet and released through the vent plug. The maximum temperature and hydrogen concentration are 211 °C and 1.6%, respectively. The temperature of the residual water is below 47 °C.

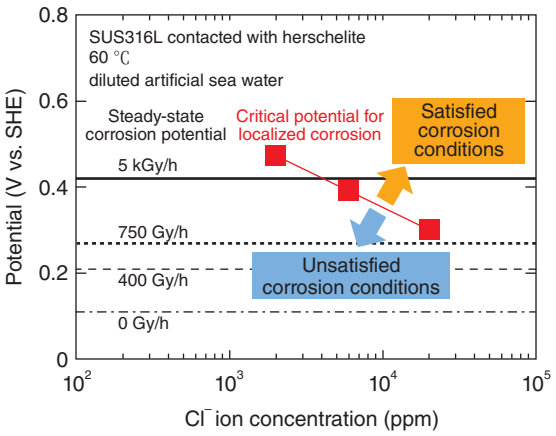

Fig.1-40 Electrochemical corrosion tests of stainless steel SUS316L
The electrochemical potentials of SUS316L in contact with herschelite were measured in diluted sea water to determine its immunity to localized corrosion. The critical potential for localized corrosion decreases as the Cl^- ion concentration increases. Conditions for localized corrosion are satisfied when the critical potential for localized corrosion is lower than the steady-state corrosion potential. Under the conditions of the reference vessel shown in Fig.1-39, the localized corrosion of SUS316L in contact with herschelite would not immediately occur at Cl^- ion concentrations of 20000 ppm.

Stainless steel vessels containing mineral adsorbents (herschelite, etc.), which possess high selectivity toward cesium (Cs), are used for the treatment of radioactive saline water at the accident at the TEPCO's Fukushima Daiichi NPS. The spent vessel is highly radioactive and temporarily stored with the shield (Fig.1-39(a)). For long-term storage, we evaluated the hydrogen production and corrosion of herschelite adsorption vessels.

As fundamental properties of herschelite, we investigated its thermal conductivity, hydrogen production yield, and Cs adsorption coefficients, as well as determined the Cs activity, decay heat, absorbed dose rate, and hydrogen production rate. The hydrogen concentration in a reference vessel of uniform Cs distribution was evaluated based on these fundamental properties. Fig.1-39(b) shows that the maximum temperature is 211 °C, below the self-ignition temperature of hydrogen (500–571 °C). This thermal hydraulic behavior maintains the maximum hydrogen concentration below 1.6% (Fig.1-39(c)) and well below the lower explosive limit of 4%.

An electrochemical method was employed to determine the immunity to localized corrosion. Fig.1-40 shows the potentials of SUS316L in a mixture of herschelite and sea water. The critical potential for localized corrosion decreased as the Cl^- ion concentration increased. The conditions for localized corrosion are satisfied when the critical potential is lower than the steady-state corrosion potential. Therefore, under the conditions (temperature < 60 °C, adsorbed dose rate of 755 Gy/h) shown in Fig.1-39, the localized corrosion of SUS316L in contact with herschelite would not immediately occur at Cl^- ion concentrations of 20000 ppm.

Part of this study was the results of research entrusted to JAEA by the Agency for Natural Resources and Energy, Ministry of Economy, Trade and Industry of Japan (METI).

Reference

Yamagishi, I. et al., Characterization and Storage of Radioactive Zeolite Waste, Journal of Nuclear Science and Technology, vol.51, issues 7–8, 2014, p.1044–1053.

1–20 Development of an Analysis Method for a Hard-To-Measure Nuclide in Wastewater
— Cadmium-113m Analysis Method Using β-ray Measurement —

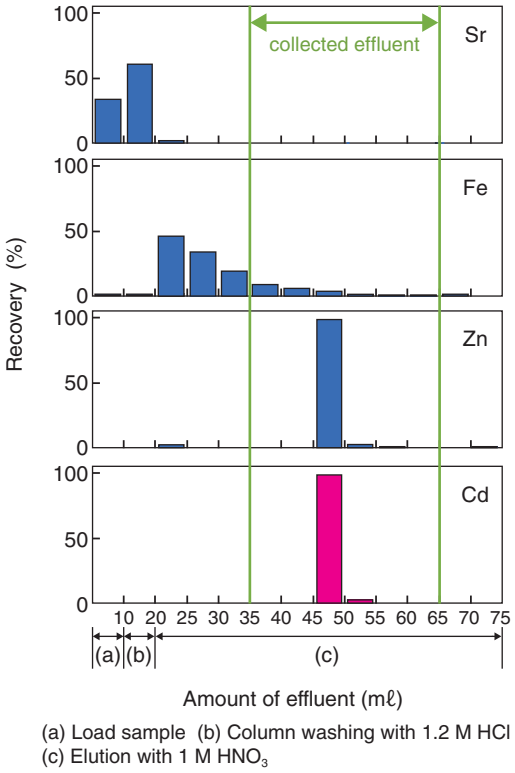

(a) Load sample (b) Column washing with 1.2 M HCl
(c) Elution with 1 M HNO_3

Fig.1-41 Recovery of Cd, Zn, Fe, and Sr as functions of the amount of effluent
Separation condition: The sample is prepared in 10 mℓ of a 2 M HCl solution. (a) The solution is passed through an anion exchange resin. Cd is retained on the resin. (b) The Resin is washed with 10 mℓ of 1.2 M HCl. (c) Cd is eluted from the resin with 55 mℓ of 1 M HNO_3.

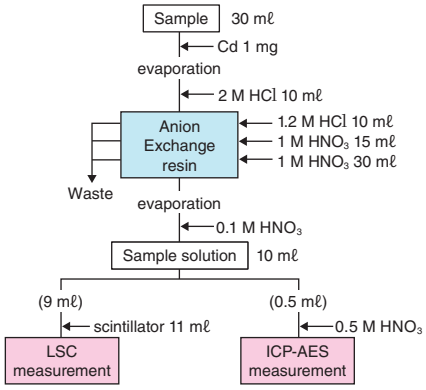

Fig.1-42 Analytical procedure for ^{113m}Cd
Eluate (1 M HNO_3) discards the first 15 mℓ and then collects the next 30 mℓ.

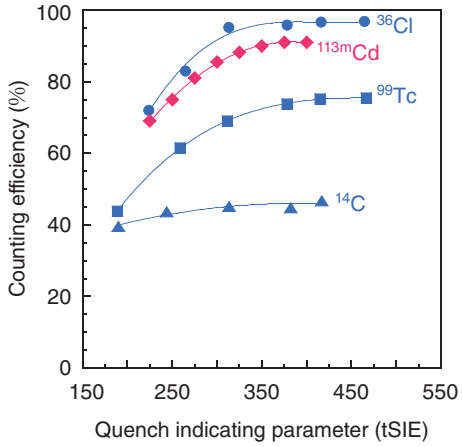

Fig.1-43 Counting efficiency as a function of the quench indicating parameter (tSIE)
The β-ray counting efficiency for ^{113m}Cd was estimated using ^{14}C, ^{99}Tc, and ^{36}Cl standard solutions.

In the TEPCO's Fukushima Daiichi NPS, the wastewater containing radioactive nuclides is treated by water treatment systems. To check the removal performance of radioactive nuclides by the Advanced Liquid Processing System (ALPS) (which is one of the water treatment systems), it is necessary to evaluate the activity concentration of nuclides in water treated by ALPS. Since the γ-ray emission ratio of Cadmium-113m (^{113m}Cd) (which is one of nuclides to be evaluated) is small (0.023%), we cannot apply non-destructive γ-ray measurement. Therefore, a new analysis method that measures β-rays (emission ratio: 99.9%) was examined.

To measure the β-rays of ^{113m}Cd with sufficient accuracy, it was necessary to separate the other nuclides and elements. An anion-exchange procedure was applied to this separation. The examination result of the separation condition of Cd and the other elements is shown in Fig.1-41. Most of the Cd eluted to 45–50 mℓ of effluent. When 35–65 mℓ of effluent was collected, Cd could be efficiently separated and collected from the other elements. The ^{113m}Cd analysis procedure established based on this result is shown in Fig.1-42. β-rays of ^{113m}Cd were measured using a liquid scintillation counter (LSC). Since the counting efficiency of LSC is decreased by quenching phenomena, it is necessary to calibrate its efficiency. However, since a standard solution of ^{113m}Cd was difficult to purchase from vendors, the β-ray counting efficiency of ^{113m}Cd was estimated using other β-ray-emitting nuclides (Fig.1-43).

When the sample, which was a simulation of water treated by ALPS, was analyzed using this established analysis method, more than 97% of Cd was recovered, and a minimum detectable activity of 0.004 Bq/mℓ was obtained. Through the above examination, we contributed to the performance assessment of ALPS.

Reference
Yasuda, M. et al., Determination Method using Liquid Scintillation Counter for ^{113m}Cd in Wastewater in Fukushima-1 Nuclear Power Plant, Bunseki Kagaku, vol.63, no.4, 2014, p.345-350 (in Japanese).

1–21 Toward the Treatment and Subsequent Disposal of the Accident Waste

— An Analysis of Rubble and Trees Collected from the Site of the TEPCO's Fukushima Daiichi NPS —

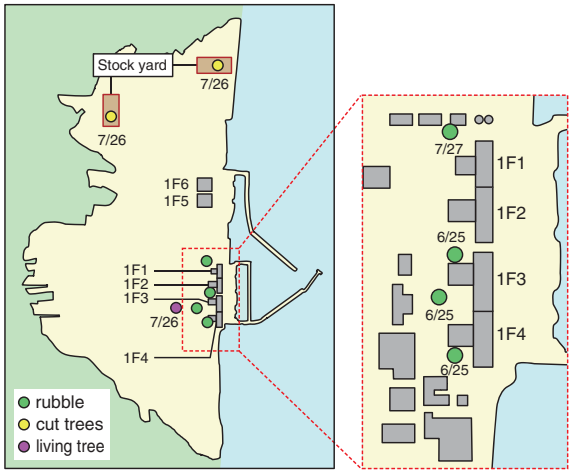

Fig.1-44 Sampling locations of rubble and trees
(Tanaka, K. et al., JNST, vol.51, issues 7-8, 2014, p.1032-1043.)
Rubble around 1F1, 1F3, and 1F4 was collected on June 25 and July 27, 2012. Tree samples were collected on July 26, 2012.

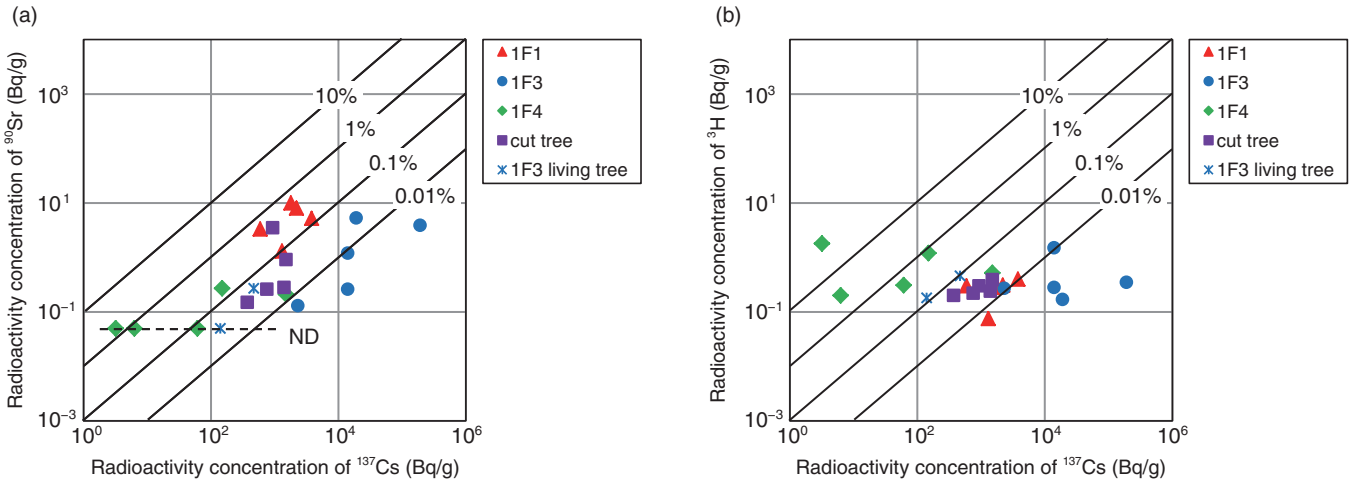

Fig.1-45 Concentrations of ^{3}H and ^{90}Sr as functions of those of ^{137}Cs
(Tanaka, K. et al., JNST, vol.51, issues 7-8, 2014, p.1032-1043.)
These figures show the radioactivity concentrations of (a) ^{90}Sr and (b) ^{3}H as functions of the concentration of ^{137}Cs. It is clarified that the concentrations of ^{90}Sr did depend on those of ^{137}Cs, but those of ^{3}H did not.

After the accident at the TEPCO's Fukushima Daiichi NPS (1F, The "Unit 1-6 at 1F" is abbreviated to "1F1-1F6"), huge quantities of rubble and many trees were contaminated by radionuclides, including ^{137}Cs and ^{131}I, which were generated at the site of 1F. To determine a strategy for the treatment and subsequent disposal of the rubble and trees, it was essential to clarify their radionuclide and radioactivity concentrations. To determine the radionuclides in and on the rubble and trees, samples were collected at the location shown Fig.1-44.

Important radionuclides (including α-ray and β-ray emitting radionuclides, which need chemical analysis) were selected based on a safety assessment of the waste disposal. Analytical methods for the important radionuclides have already been developed by JAEA, and applied to various types of radioactive waste generated by research and industrial and medical facilities. We modified the existing analytical methods and analyzed the rubble and trees.

The ratios of the radioactivity concentrations ^{3}H and ^{90}Sr to those of ^{137}Cs determined in this study are plotted in Fig.1-45. As shown in Fig.1-45, the concentration of ^{3}H did not depend on the sampling location. In contrast, the radioactivity ratios of ^{90}Sr to ^{137}Cs clearly depended on the sampling location. The observed results for ^{90}Sr also implied that the ^{90}Sr/^{137}Cs ratio was different for each Unit of 1F. We are establishing methods for the treatment and disposal of radioactive waste on the basis of this data.

This study was sponsored by the Agency for Ministry of Economy, Trade and Industry of Japan (METI) in the FY 2013 and 2014.

Reference

Tanaka, K. et al., Radiochemical Analysis of Rubble and Trees Collected from Fukushima Daiichi Nuclear Power Station, Journal of Nuclear Science and Technology, vol.51, issues 7–8, 2014, p.1032–1043.

Implementing Continuous Improvements for Safety

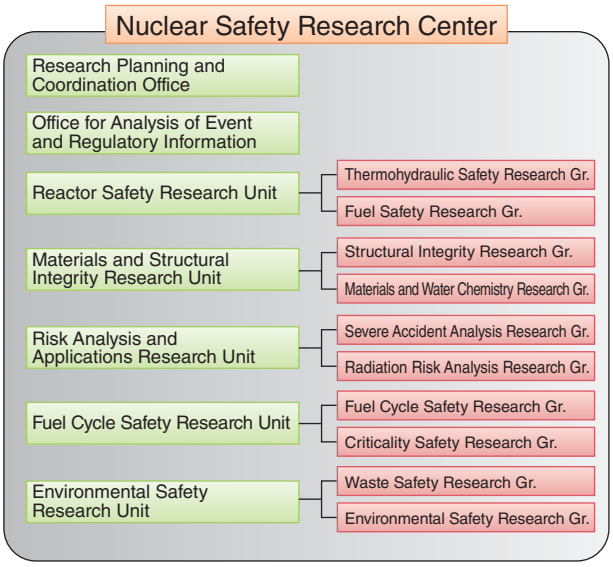

Fig.2-1 Organization of the nuclear safety research center
Starting April 2014, we have been strengthening the organization to promote studies of SAs, including the initiating event, progress of the accident, and the environmental impact, as well as the safety assessment due to the design basis accidents for several nuclear facilities.

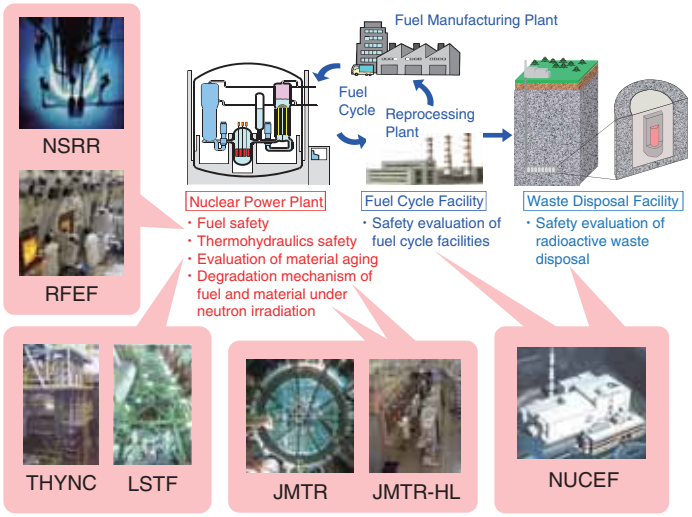

Fig.2-2 Nuclear safety research areas and related JAEA facilities
NSRC acquires experimental data from various Japan Atomic Energy Agency facilities. These data for risk assessment and safety evaluation of nuclear facilities contribute to international efforts to develop evaluation methods and criteria.

To ensure the safe use of current nuclear facilities, the Nuclear Safety Research Center (NSRC) studies the possibility of serious accidents at nuclear installations and their consequences. A massive and severe accident (SA) occurred at the Tokyo Electric Power Company, Incorporated Fukushima Daiichi Nuclear Power Station (1F) as a result of the Great East Japan earthquake and tsunami. NSRC has been collaborating with the Japanese government to institute appropriate emergency response procedures based on research findings and developments. The specialists at NSRC regret that they were unable to prevent the accident.

Continuous efforts should be made to avoid serious damage while we utilize nuclear energy. A proper understanding of the situation and continuous improvement of current technologies are important for making the best and safest use of these technologies. In fact, the International Atomic Energy Agency, which investigated the accident at 1F, highlighted the importance of "continuous improvement." To contribute to "continuous improvement aimed at the highest level of safety," we strengthened the organization to promote studies of SA prevention and evaluation to reduce the risk of accidents at nuclear facilities and to improve nuclear disaster prevention using analyses such as environmental impact assessments (Fig.2-1).

We are committed to safety research and have devoted to this cause the various facilities shown in Fig.2-2. These special facilities allow the handling of radionuclides and the simulation of accident conditions.

This chapter presents the results of recent safety research on the following topics: simulation of fuel-cladding failure (Topic 2-1), effect of neutron irradiation on fracture properties of stainless overlay cladding for reactor pressure vessel (Topic 2-2), development of probabilistic structural assessment code for nuclear components with long-term operation (Topic 2-3), analytical techniques of gas inflow during loss of coolant accidents at pressurized water reactors (Topic 2-4), study on applicability of compacted clays to waste-disposal facility (Topic 2-5), and SA evaluation regarding loss of cooling function of highly active liquid waste in reprocessing plant (Topic 2-6).

The following Topics solicited by NSRC and related to the accident at 1F are described in Chapter 1: release of I-131 from contaminated water in the basement of the reactor building (Topic 1-18).

2–1 Fuel Failure Processes Revealed by Numerical Approach
— Simulation of Fracture Behavior Using Damage Mechanics Model —

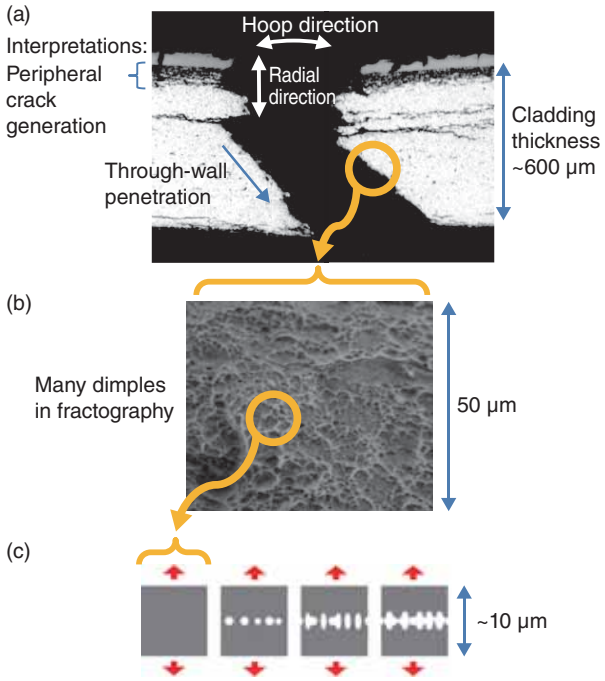

Fig.2-3 Failure of long-term used fuel cladding and modelling
(a) We anticipated that peripheral cracks are at the origin of the observed cladding failure. (b) Many dimples indicate that fracture occurred in a ductile manner. (c) The cladding was modeled as an assembly of elements that break upon finite deformation.

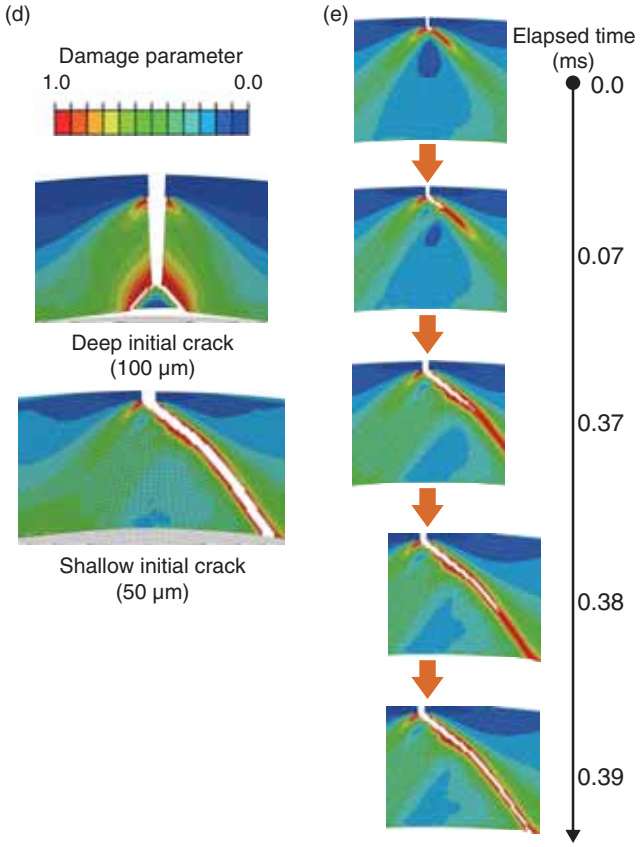

Fig.2-4 Simulation results
(d) Fracture appearance depends on initial crack length.
(e) Penetration through the wall with very small increment in time (and strain).

Reactivity initiated accident (RIA), a power excursion caused by control rod ejection, is one of the accidents assumed to confirm safety design of nuclear reactors. In Japan, the failure limit of long-term used fuels for RIA is postulated to be lower than that of fresh fuels, based on RIA-simulated tests conducted at the Nuclear Safety Research Reactor. Although the lower failure limit was considered to be caused by through-wall penetration of cracks which were generated in the cladding peripheral region with hydrogen absorbed and accumulated during reactor operation (Fig.2-3(a)), directly observing a phenomenon as rapid as fuel failure inside the reactor is not possible. Thus, the anticipated mechanism was not confirmed and the detailed processes remain unknown.

To overcome this difficulty, we developed a numerical model of fuel cladding to simulate a RIA. The cladding was modeled as an assembly of elements (Fig.2-3(c)), each about 10 μm in size. This element was designed to break upon finite deformation, as determined independently of the RIA tests. We then simulated the failure of the virtual cladding under RIA conditions, which is quite a new approach in this field, realized on the basis of accumulated test data and simulation techniques.

The simulation well reproduced the observations: fractures characterized by a predominant ductile shear in the shallow-crack case and straight-crack propagation in the deep-crack case (Fig.2-4(d)), and penetration through the wall that occurs in a very short time (<1 ms) (Fig.2-4(e)). This result strongly supports the aforementioned hypothesis and reveals that predominant ductile shear (Fig.2-3(a)) occurs when a softened region extends along the strain field around the crack tip and collapses simultaneously at a certain deformation. A sensitivity analysis using the model provides information on the influence of the loading state and temperature distribution inside the cladding on the failure limit, which supports the ongoing development of methods for safety evaluation that can accurately predict the failure limit of long-term used fuels.

Reference
Udagawa, Y. et al., Simulation of the Fracture Behavior of Zircaloy-4 Cladding under Reactivity-Initiated Accident Conditions with a Damage Mechanics Model Combined with Fuel Performance Codes FEMAXI-7 and RANNS, Journal of Nuclear Science and Technology, vol.51, issue 2, 2014, p.208-219.

2–2 Improving Structural Integrity Assessment of Reactor Pressure Vessels

— Effect of Neutron Irradiation on Fracture Properties of Stainless Overlay Cladding for Reactor Pressure Vessel —

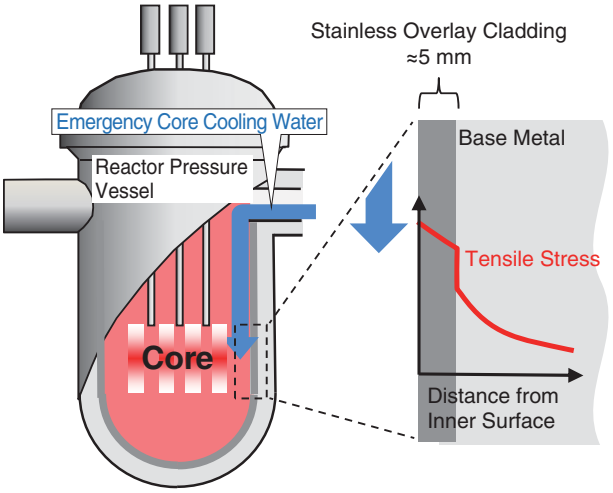

Fig.2-5 RPV and PTS event
When the emergency core cooling water is injected into RPV under high temperature and pressure condition, tensile stress occurs at the inner surface of RPV because of the thermal stress. This stress is superimposed on the stress created by the internal pressure.

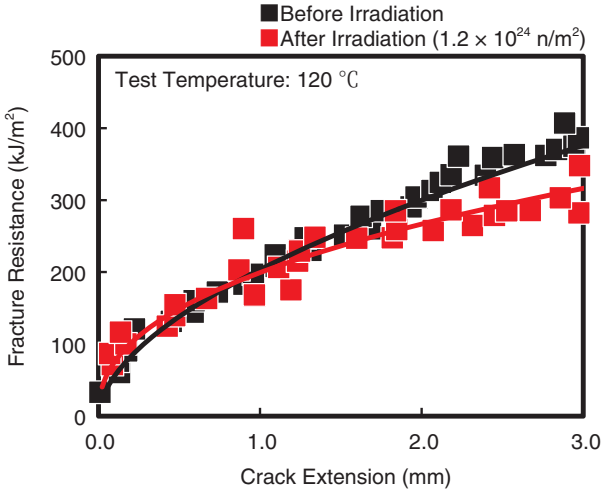

Fig.2-6 Fracture resistance curves of stainless overlay cladding
The fracture resistance of cladding materials increases as the crack extension proceeds. The fracture resistance curves indicate no obvious degradation of the cladding materials after neutron irradiation.

The reactor pressure vessel (RPV) is the most important component for safe operation of a nuclear power plant. Pressurized thermal shock (PTS) is one of the most severe events that may lead to the failure of the pressurized water reactor (PWR). PTS is a transient event caused by rapid cooling of the inner surface of the RPV, which is consequently due to the injection of emergency core-cooling water. PTS causes high tensile stress on the inner surface of the RPV (Fig.2-5). Assessing the structural integrity of the RPV during a PTS event postulates the formation of an axial semi-elliptical crack on the inner surface of the RPV base metal or weld metal. To prevent the corrosive effects of the reactor coolant, the inner surface of a RPV is overlaid with cladding made of 5-mm-thick austenitic stainless steel. A PTS event may lead to higher tensile stress in the cladding region. Understanding the properties of fractures in cladding materials that have been irradiated by neutrons is necessary to improve the assessment of the structural integrity of a RPV.

We tested the elastic-plastic fracture toughness of cladding materials subjected to a neutron fluence of 1.2×10^{24} n/m^2. Typical fracture resistance curves for cladding materials before and after irradiation are shown in Fig.2-6. The test temperature of 120 °C is the temperature range in which tensile stress increases during a PTS event. As shown in the figure, the fracture resistance of cladding materials increases as the crack extension proceeds. No obvious degradation appears in the fracture resistance curves of the cladding materials after neutron irradiation. These properties are similar to what is found at other temperatures, and no brittle fracture appears in the low-temperature region. These results suggest that the fracture properties of the cladding region change little over the long-term operation of a RPV.

This study provides data on the materials' properties that will improve the assessment of structural integrity and contribute to the preparation by academic societies of the requisite standards.

Reference

Tobita, T. et al., Effect of Neutron Irradiation on the Mechanical Properties of Weld Overlay Cladding for Reactor Pressure Vessel, Journal of Nuclear Materials, vol.452, issues 1–3, 2014, p.61–68.

2–3 Structural Integrity Assessment of Nuclear Components Operated over a Long Period
— Probabilistic Fracture Mechanics Analysis for Ni-Based Alloy Welds —

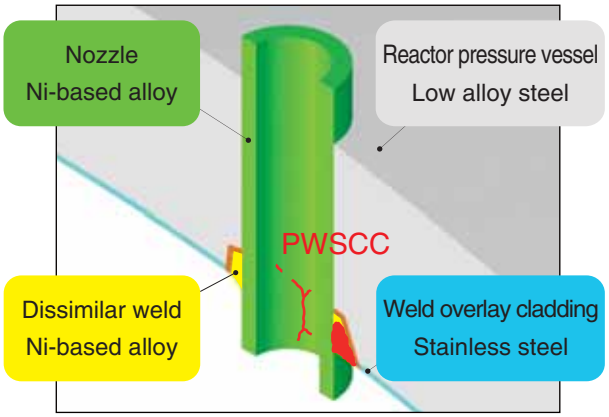

Fig.2-7 Schematic of PWSCC at a vessel head penetration
PWSCC occurs at dissimilar welds at the penetration nozzles of reactor vessel heads of pressurized water reactors due to material (Ni-based alloy), environmental (water condition), and stress (weld residual stress, etc.) factors.

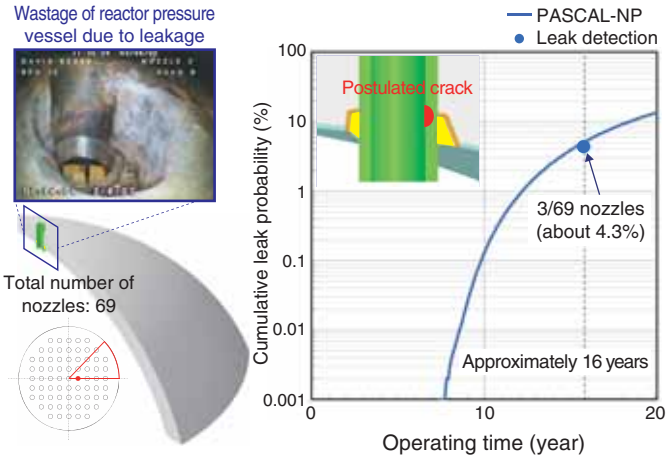

Fig.2-8 Case study for leakage due to PWSCC at the Davis-Besse nuclear power plant
A case study was performed using the PASCAL-NP code to describe vessel head penetrations caused by PWSCC at the Davis-Besse nuclear power plant (United States). The study considers the scatter in time for crack initiation, the crack growth rate, the residual stress distribution, etc. Analytical results for cumulative leak probability are consistent with the leak detection data.

During long-term operation, primary water stress corrosion cracking (PWSCC) was detected at dissimilar metal welds of Ni-based alloys at vessel head penetration of the pressurized water reactors (PWRs) (Fig.2-7).

Some features of PWSCC differ from those of SCC reported at piping joints of primary loop recirculation system in boiling water reactors (BWRs), e.g., PWSCC initiates and grows in Ni-based alloys at geometrically complicated welds.

Some factors related to PWSCC, such as crack initiation time, crack growth rate, and residual stress distribution, have large scatter.

To account for this scatter, we developed a probabilistic fracture mechanics (PFM) analysis code PASCAL-NP to assess the structural integrity of dissimilar metal welds subjected to PWSCC.

PASCAL-NP contains functions that describe crack initiation and crack growth and evaluate failures for various patterns of crack locations and orientations at geometrically complicated dissimilar metal welds, including NiSCC in a BWR. Using a Monte Carlo approach and considering the scatter described above, this code evaluates the probabilities of failure for events such as leakage and break of components.

Fig.2-8 shows the results of a case study on leakage near the vessel head penetrations at the Davis-Besse nuclear power plant, which suffered from PWSCC. The analytical cumulative leak probability exceeds 5% after 16 years. These PFM analysis results are consistent with the leak detection data, which provides about 4.3% probability (i.e., 3 of 69 leaks were detected).

PFM is expected to be a rational and useful method to estimate failure probabilities due to unexperienced events, to assess risks considering aging degradation of nuclear components, and to develop a plan of risk-informed in-service inspection. To advance the assessment of structural integrity, we continuously improve PASCAL-NP by incorporating the latest knowledge.

Reference

Udagawa, M. et al., User's Manuals of Probabilistic Fracture Mechanics Analysis Code for Ni-Based Alloy Welds, PASCAL-NP, JAEA-Data/Code 2013-013, 2013, 145p. (in Japanese).

2–4 Investigating Gas Inflow Influences in Accidents
— Concentration Analysis with Gas Measurement Device —

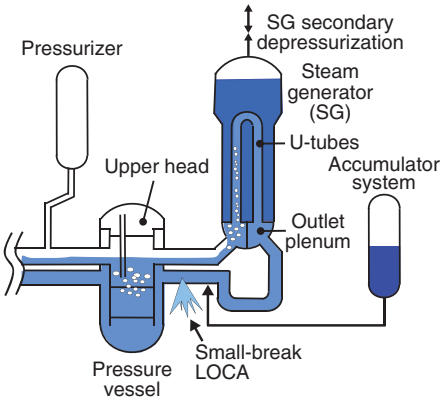

Fig.2-9 PWR small-break LOCA and accident-management measure
SG secondary depressurization is an effective accident-management measure for core cooling because steam condenses in the U-tubes during the PWR small-break LOCA.

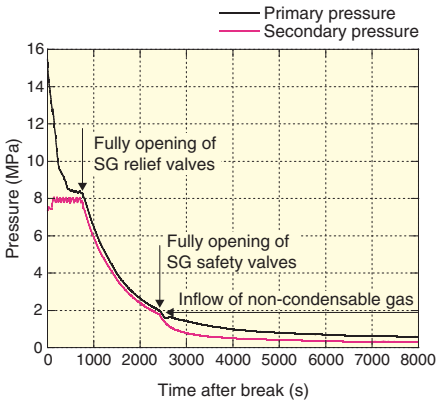

Fig.2-10 Primary and secondary pressures under non-condensable gas inflow
The decreasing rate of the primary pressure became smaller than that of the secondary pressure after non-condensable gas inflow during the SG secondary depressurization period, suggesting a delay in the coolant injection into the core.

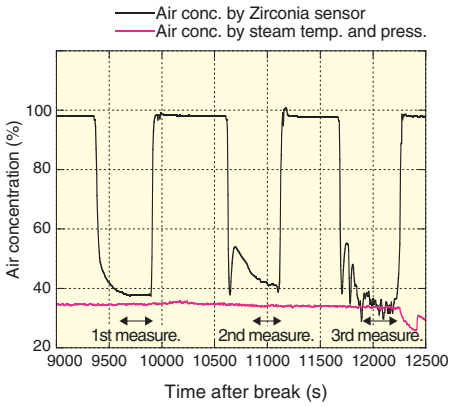

Fig.2-11 Air concentration at SG outlet plenum
Non-condensable gas from ACC tanks accumulated in SG outlet plenum through air concentration, as confirmed by a Zirconia sensor and the estimated value based on steam temperature and pressure at SG outlet plenum.

Previous research at the large scale test facility (LSTF) simulated mainly small-break loss-of-coolant accidents (LOCAs) in PWR to clarify specific thermal-hydraulic phenomena and to confirm the effectiveness of accident management (AM) measure.

When the high-pressure injection system of an emergency core cooling system (ECCS) completely fails during a PWR small-break LOCA, core damage would occur due to the loss of the primary coolant and the delay of water injection into the core by the actuation of an ECCS, such as the accumulator (ACC) system. Steam generator (SG) secondary depressurization is an effective AM measure for core cooling because of the steam condensation in the SG U-tubes (Fig.2-9). When the isolation of ACC system is failed, ingress of non-condensable gas used for the pressurization of ACC tanks to the primary system may cause degradation in the primary depressurization after the completion of the ACC coolant injection. It is thus necessary to clarify how gas inflow influences the small-break LOCA progression with the SG secondary depressurization.

A Zirconia sensor has been employed for measuring oxygen concentration in engineering applications, such as exhaust gas for chimney. A gas-measurement device to directly measure oxygen concentration in steam-gas mixtures was developed using a Zirconia sensor under high-pressure condition (<2 MPa), and a pressure control valve for the Zirconia sensor was installed up-stream of the sensor. The gas concentration could thus be measured at the SG outlet plenum and the upper head of the vessel, where non-condensable gas may have passed through.

We conducted a simulation test on a PWR horizontal leg small-break LOCA for the OECD/NEA ROSA Project at the LSTF. SG secondary depressurization as an AM action was initiated by fully opening the SG relief valves 10 min after the safety injection signal, considering a grace period to start an operator action. We further assumed that enhanced SG depressurization was conducted by fully opening the SG safety valves when the primary pressure decreased to 2 MPa. The primary pressure decreased following the secondary pressure after the start of the SG secondary depressurization, while the decreasing rate of the primary pressure became smaller than that of the secondary pressure after the non-condensable gas inflow (Fig.2-10). The gas concentration was analyzed through the measurements at the SG outlet plenum (Fig.2-11) and the upper head of the vessel. The results of the analysis confirmed that non-condensable gas from the ACC tanks accumulates in the U-tubes and in the outlet plenum of the SG.

Detailed experimental data obtained from the LSTF simulations were useful for the validation and verification of thermal-hydraulic best-estimate computer codes of the ROSA Project organizations, such as nuclear regulatory agencies.

Reference

Takeda, T. et al., Measurement of Non-Condensable Gas in a PWR Small-Break LOCA Simulation Test with LSTF for OECD/NEA ROSA Project and RELAP5 Post-Test Analysis, Experimental Thermal and Fluid Science, vol.51, 2013, p.112–121.

2–5 Dissolution of Compacted Clays in High-Level Radioactive Waste Repositories
— Alkaline Dissolution Inhibited by Accessory Minerals in Bentonite —

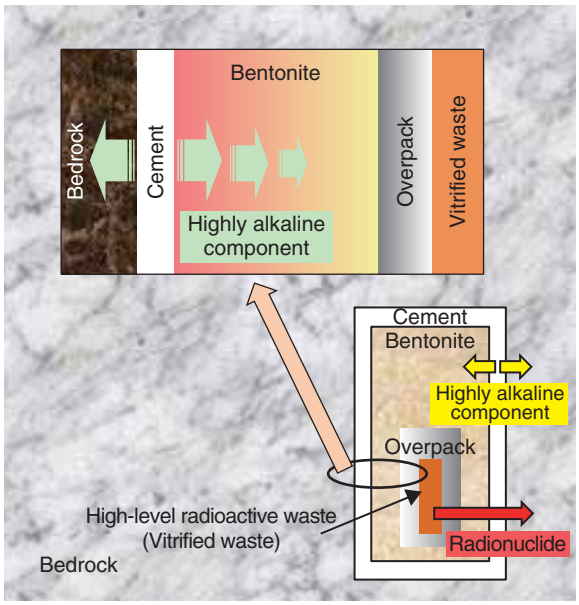

Fig.2-12 Conceptual view of disposal system for HLW
Vitrified HLW is encapsulated in an iron container (overpack), surrounded by an engineered buffer material (bentonite), and placed in stable bedrock. Cement used for mechanical support of shafts and drifts increases the alkalinity of surrounding water, and over a long period, it likely deteriorates the properties of the bentonite buffer.

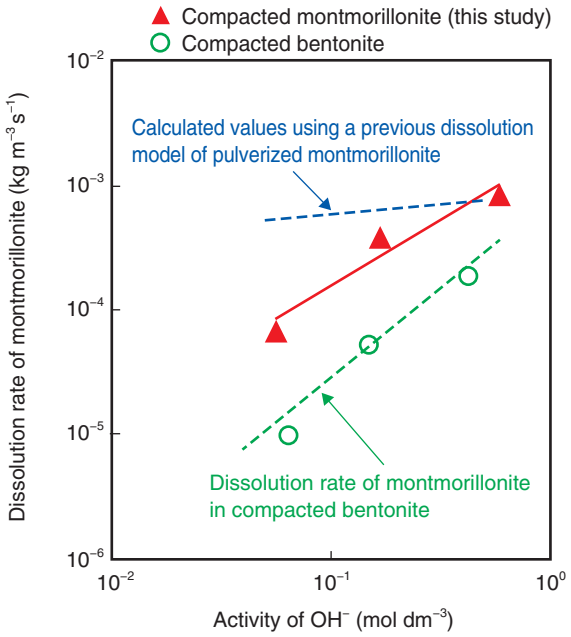

Fig.2-13 Dissolution rate of montmorillonite in highly alkaline solutions
The dissolution rate of montmorillonite was higher in compacted montmorillonite than in compacted bentonite. Dissolution of montmorillonite was inhibited in the compacted bentonite. The difference is due to decreased activity of OH^- stemming from the dissolution of accessory minerals.

In geological disposal of high-level radioactive waste (HLW), vitrified waste containing long-lived radionuclides is encapsulated in an iron container called an overpack, surrounded by an engineered bentonite buffer material (compacted bentonite), and placed in a repository in stable bedrock, as shown in Fig.2-12. The high sorptivity and low permeability of bentonite retards outward radionuclide movement. Because the radionuclide-confining property of the bentonite depends on the montmorillonite content, the dissolution of montmorillonite induced by the highly alkaline component supplied from the cementitious materials in the system must be revealed to evaluate the long-term barrier function of this system.

Previous studies on the dissolution rates of clays in alkaline solutions used pure pulverized montmorillonite; hence, the rates were obtained for a much lower solid/solution ratio than that warranted by the disposal conditions. Whether the rates may be applied to predict the dissolution of compacted bentonite under current disposal conditions remains a question. Therefore, by experiment, we determined the dissolution rate of montmorillonite in compacted bentonite. The dissolution rate thus obtained for compacted bentonite was lower and depended more strongly on the activity of hydroxide ions (OH^-) than the rates obtained in previous studies. However, the mechanism behind such differences has not yet been clarified.

The present study experimentally investigated the dissolution rate of pure compacted montmorillonite at 130 °C. The dissolution rate of montmorillonite is found to be higher and depends slightly less on the activity of OH^- in pure compacted montmorillonite than on its activity in compacted bentonite, as shown in Fig.2-13. These results suggest that the dissolution of montmorillonite in compacted bentonite is inhibited by decreasing the activity of OH^- by dissolving accessory minerals, such as silica, in the bentonite. The logarithmic plot of the dissolution rate shows that the effect of the inhibition would thus be enhanced at lower activity of OH^-.

The present study was sponsored by the Secretariat of the Nuclear Regulation Authority (NRA) (formerly the Nuclear and Industrial Safety Agency (NISA), Ministry of Economy, Trade and Industry (METI), Japan).

Reference

Sawaguchi, T. et al., Alkaline Dissolution Behavior of Montmorillonite under Compacted Condition, Genshiryoku Bakkuendo Kenkyu (Journal of Nuclear Fuel Cycle and Environment), vol.20, no.2, 2013, p.71-78 (in Japanese).

2–6 Acquisition of Evaluation Data for Severe Accident in Reprocessing Plant
— Acquisition and Evaluation of Airborne-Release Data from Boiling Accident —

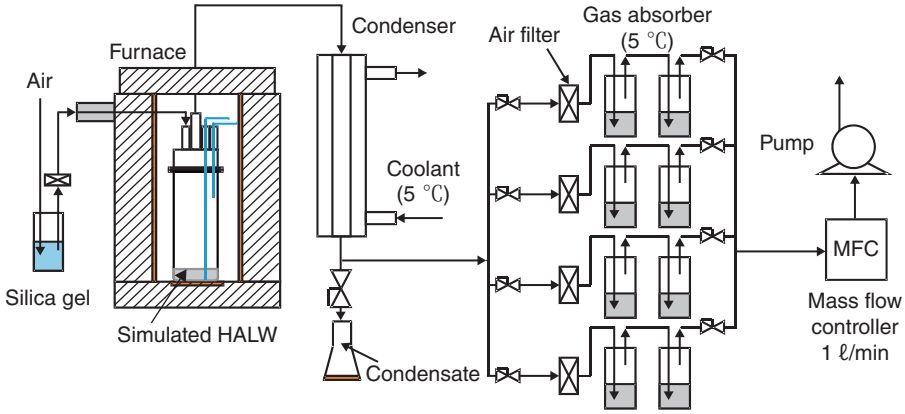

Fig.2-14 Apparatus to obtain release ratio of each element
Simulated HALW was heated to 300 °C, and condensates were collected at regular time intervals. The release ratios of elements were obtained by analyzing the respective condensates.

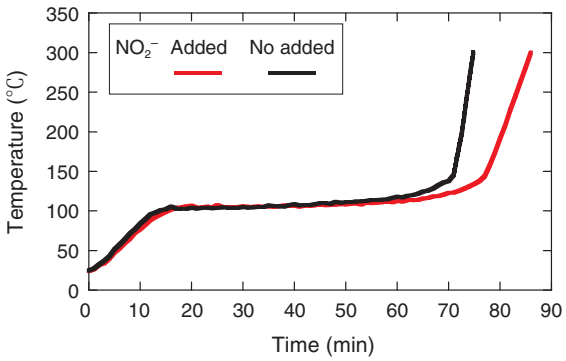

Fig.2-15 Time dependence of sample temperature
Simulated HALW continued boiling for about 70 min and dried out after boiling.

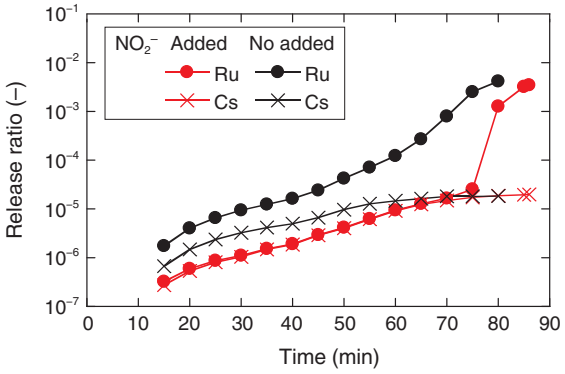

Fig.2-16 Time dependence of release ratios
The nitrite ion (NO_2^-) is thought to prevent nitric acid from oxidizing nitrosyl Ru early in the boiling step.

When the high active liquid waste (HALW) is no longer cooled, it may boil and dry out, and radioactive materials, which are dissolved in HALW, may be released in the air. Therefore, understanding the release and transport of these materials is necessary to evaluate safety issues in the case of an accident. This study simulates the release ratio of each element by virtually heating HALW, which was prepared using a stable isotope selected with reference to the composition of HALW. Fig.2-14 shows the apparatus used to obtain the release ratio. In the simulation, HALW was heated to 300 °C with the vapor flow rate being set equal to that estimated for an accident. Figs.2-15 and 2-16 show the time dependence of the temperature and the release ratio, respectively. The release ratio of ruthenium (Ru) rapidly increases beginning at the latter part of boiling step and continuing to the drying step. At 300 °C, it increases to about 10^{-2}. The release ratio of Ru is three orders of magnitude greater than that of nonvolatile elements, such as cesium (Cs). The release ratio of Ru appears to be greater than that of Cs because nitric acid is concentrated in the dried out HALW and concentrated nitric acid oxidizes nitrosyl Ru to create a volatile Ru species. However, in the boiling step, both Ru and Cs are considered to be present in the mist, which is generated by a bubble breaking in the boiling HALW. These elements are then released in the air. Fig.2-16 shows that the release ratio of Ru is greater than that of Cs at the boiling step without adding nitrite ions (NO_2^-) as the radiolysis product of nitric acid in HALW. Upon adding NO_2^-, the release ratio of Ru becomes the same as that of Cs. Consequently, NO_2^- is thought to prevent nitric acid from oxidizing nitrosyl Ru to create a volatile Ru species in HALW early in the boiling step.

The release data of each element were obtained in this simulation. In the next step of the simulation, we will obtain transportation data for each element released in the air and develop a model to analyze the release and transport due to a boiling accident.

The present study was accomplished in collaboration with Japan Nuclear Fuel Limited (JNFL) and the Japan Nuclear Energy Safety Organization (JNES).

Reference

Amano, Y. et al., Study on Release and Transport of Aerial Radioactive Materials in Reprocessing Plant, Proceedings of International Nuclear Fuel Cycle Conference (GLOBAL 2013), Salt Lake City, Utah, USA, 2013, paper 7568, p.1411–1417., in CD-ROM.

Advanced Science Pioneers the Future

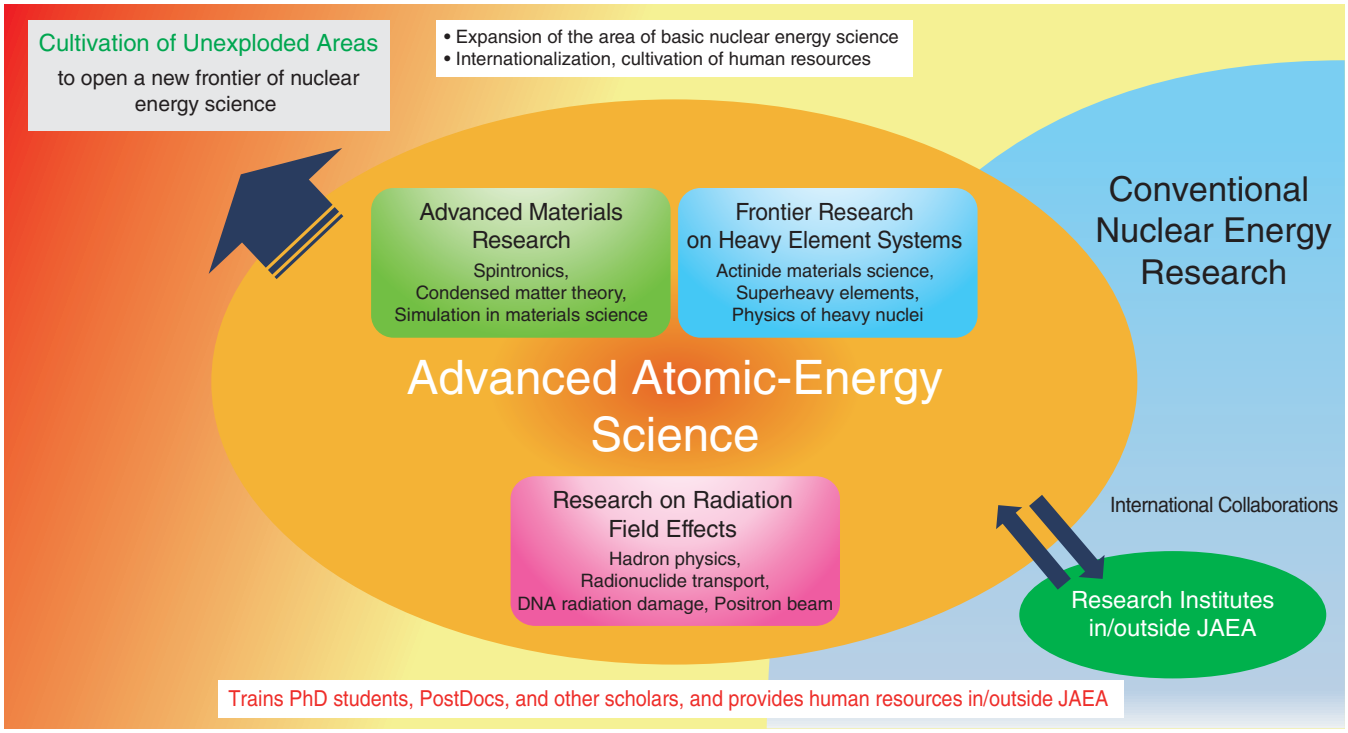

Fig.3-1 Advanced research to open a new frontier of nuclear science
Nuclear research trains PhD students, postdocs and other scholars, and provides human resources both in and outside JAEA.

Basic science supports the greater part of atomic energy-related science and technology. In the development of atomic energy research, it is particularly crucial to respond to the new phase of atomic energy that we will be entering in the next few decades, as well as constantly seeking solutions to today's energy problems.

As for the Advanced Science Research Center (ASRC), our role is to explore the unlimited possibility of atomic energy from the perspective of basic science. In this process, we aim to open up new research fields and strive to further develop science and technology. Beginning in FY 2010, we have conducted our mid-term plan, focusing on three main areas: advanced materials research, frontier research on heavy element systems, and research on radiation field effects (Fig.3-1).

Advanced materials research has been conducted with the aim of creating spintronic materials and advancing the theory of solid state physics. In the research of heavy element systems, we have performed diverse studies on actinide compounds and development of new materials, as well as studying the nuclear science of superheavy elements. Our research on radiation field effects has included hadron physics, the study of radiation effects on bio-molecules, and the technical development and application of spin polarized positron beams. Through interactions between the three areas and collaboration with other divisions, we have been working on cultivating new fields of atomic energy science (Fig.3-1).

We have made a number of highlighted achievements during FY 2013. Through advanced materials science, a new principle of the generation of a magnetic flow with copper and aluminum was proposed (Topic 3-1). A method of determining the spin status of a conduction electron in graphene was revealed (Topic 3-2). Substantial results have been obtained by frontier research on heavy element systems; the study of the nematicity and superconductivity of a uranium (U) compound (Topic 3-3), and the elucidation of the dielectric degradation of a ceramic condenser due to hydrogen impurities in ferroelectric materials (Topic 3-4) are marked examples. Prominent results toward an explanation of the ecological effects of radiation were also acquired through research on radiation field effects. The discovery of the fact that DNA damage has an effect on normal chromosomes (Topic 3-5), and the development of an effective method for analyzing the behavior of U elements in various environments (Topic 3-6) were cases in point. In hadron physics research at the Japan Proton Accelerator Research Complex (J-PARC), challenging experiments to extend the limit of the neutron-number fraction were conducted. The experiments included a search for neutron-rich Λ hyper nuclei, which have a higher fraction of neutrons than usual (Topic 3-7).

In an effort to respond to the accident at the Tokyo Electric Power Company, Incorporated Fukushima Daiichi Nuclear Power Station, we have successfully visualized the movements of radiocesium deposited into trees and foliage (Chapter 1, Topic 1-8). As a part of the research into the environmental fate of radioactive materials, we have demonstrated a basic study of bio-decontamination methods using fungi.

3–1 Flow of Spins Resulting from Acoustic Wave

— Towards Rare-Metal-Free Magnetic Devices —

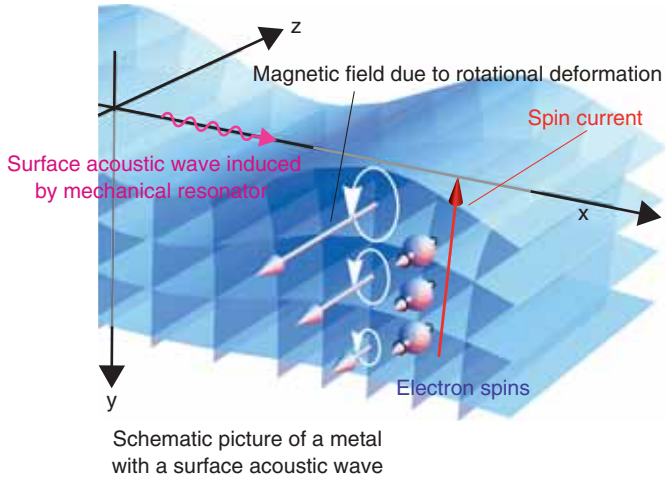

Fig.3-2 Spin-current generation by acoustic wave
We have proposed a new method for spin-current generation using the deformational motion of metal induced by acoustic waves.

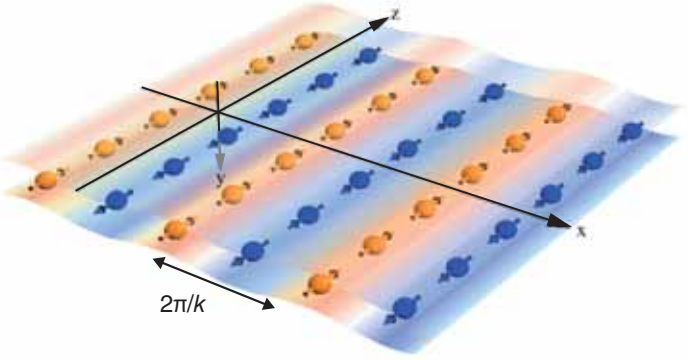

Fig.3-3 Magnetic pattern induced on the surface
Spin current due to the acoustic wave induces a magnetic stripe pattern on the metal surface, whose spatial period is the same as the wavelength of the acoustic wave ($2\pi/k$, where k is the wave number of the acoustic wave).

Electrons have two fundamental properties, electricity and magnetism. In particular, the origin of magnetism is known as "spin," which is related to the spinning motion of electrons. Recent progress of nanotechnology enables us to control the "spin current," a flow of spins. Researchers have been studying the relation between spin current and magnetism, and developing next-generation electronic devices using spin current.

Conventionally, the generation of spin current has required magnets or rare metals since such materials have special qualities that align electron spins. In other words, common metals, such as aluminum (Al) or copper (Cu), cannot be utilized for spin-current generation because they have weak spin-control properties.

We have found that the deformation of crystals can align spins and have proposed a new method for spin-current generation using the deformation of common materials, such as Al or Cu.

We formulated a theory of spin current in metals deformed by acoustic wave injection. When acoustic waves are injected into metals using piezoelectric devices, which convert electric signals into acoustic waves, the so-called surface acoustic waves (SAWs) are created (Fig.3-2). SAWs propagate along the x-axis and the excited local rotational deformation of the metal. The rotational deformation induces magnetic fields whose intensity increases toward the metal surface. In general, spin has the following properties:

(1) Spin aligns parallel to the magnetic field

(2) Spin moves to where a stronger magnetic field is applied

Thus, the magnetic field induced by the SAW aligns the third component of spins to the z-axis and flows the spins along the y-axis. As a result, a stripe pattern of spins appears on the metal surface, as shown in Fig.3-3.

We have also found that sufficient spin current can be created for magnetic devices if a SAW with several GHz range is injected into Al or Cu. This means that our method does not require magnets or rare metals for spin-current generation. Hence, our findings are expected to offer more options for spin-current generation than ever before and a new route to develop rare-metal-free magnetic devices.

Reference

Matsuo, M., Ieda, J. et al., Mechanical Generation of Spin Current by Spin–Rotation Coupling, Physical Review B, vol.87, issue 18, 2013, p.180402–1–180402–4.

3–2 Elucidation of the Spin State of Conduction Electrons in Graphene

— Significant Progress for Spintronic Applications of Two Dimensional Materials —

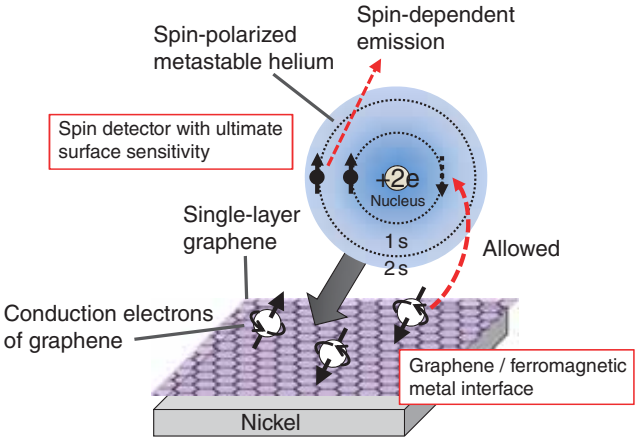

Fig.3-4 Schematic of the experimental method
When a low velocity spin-polarized metastable helium beam is incident on the sample surface, the helium atoms rebound above the surface without penetrating into the interior. During the collision, a surface electron of graphene moves toward the helium atom, and the helium atom ejects a substitutional electron. Since the transfer from the sample surface to the helium atom is allowed only for electrons with a specific spin direction, the ejected electron carries the spin information of the graphene surface electrons.

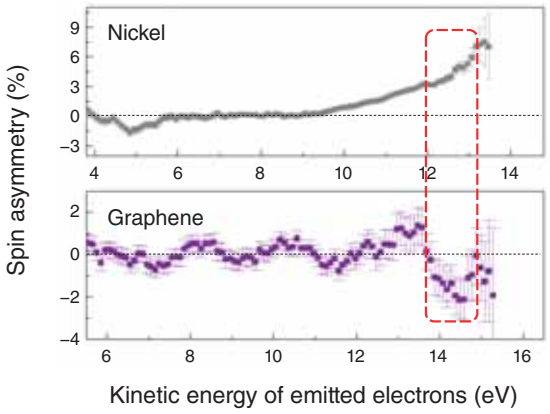

Fig.3-5 Spin asymmetries of graphene and nickel
The horizontal axes indicate the electron energy in graphene and nickel, respectively. The energies surrounded by a broken-line square correspond to the energies of the conduction electrons. The spin asymmetry (vertical axis) reflects electronic spin state. If there is no spin polarization, the asymmetry becomes 0%. At the graphene-nickel junction, the induction of spin polarization in graphene is observed. The spin polarization of graphene is found to be in the opposite direction to that of nickel.

Since the discovery of a convenient fabrication method using micromechanical exfoliation from bulk graphite (2010 Nobel Prize in physics), graphene has attracted world-wide attention as an innovative nanoelectronic material. In the spintronics field, graphene is also expected to be an ideal spin-transport material. Techniques for the manipulation of electron spins in graphene are indispensable for realizing the applications of graphene to spintronic devices; in particular, the technique of spin injection from a magnetic electrode is a key issue. For the purposes of spintronic application, it is necessary to understand the spin state of graphene in contact with magnetic metal. However, it has been difficult to use conventional techniques to analyze the electronic spin states of graphene, since the weak signals from graphene of a single atomic layer are easily buried in the strong signals from the magnetic metal substrate.

In this study, selective detection of the electron spins in graphene at a junction of graphene and magnetic metal was successfully demonstrated by employing a spin-polarized metastable helium beam with an extremely high surface sensitivity (Fig.3-4). The graphene-magnetic metal junction was prepared by chemically synthesizing graphene on a nickel thin film. Fig.3-5 shows the spin state of the graphene electrons obtained by the irradiation of the spin-polarized metastable helium beam. The conduction electrons of graphene contacted with nickel were found to be spin-polarized in the opposite direction from the conduction electrons of nickel. The opposite spin polarization directions of graphene and nickel could explain why the spin injection efficiency is very low in graphene spin devices with graphene-magnetic metal contacts.

The present study provides direct information on how the conduction electrons of graphene were affected by the contact with magnetic metals. Our research achievement is also expected to greatly contribute to the design of spin-related functions based on various two-dimensional materials that are attractive for future spintronic application.

The present study was accomplished in collaboration with National Institute for Materials Science (NIMS) and the University of Science and Technology of China.

Reference

Entani, S. et al., Spin Polarization of Single-Layer Graphene Epitaxially Grown on Ni(111) Thin Film, Carbon, vol.61, 2013, p.134–139.

3–3 A Precursor to Exotic Superconductivity

— Nematicity and Superconductivity in URu_2Si_2 —

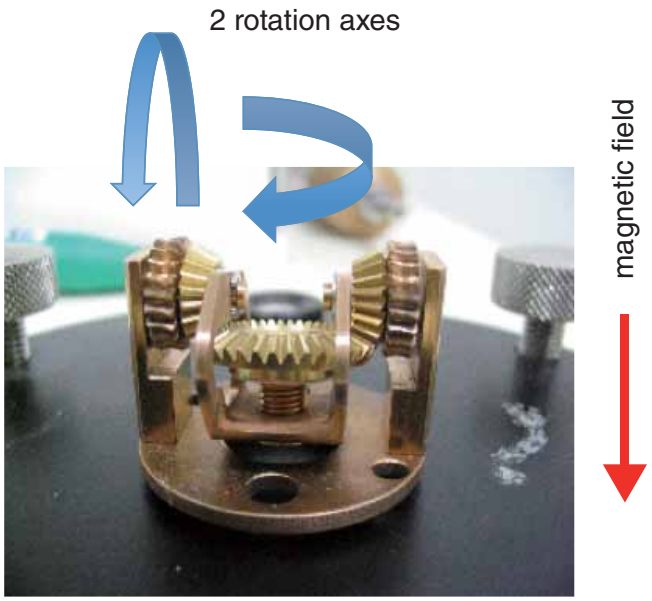

Fig.3-6 Two-axis rotating stage
The sample can be rotated precisely along two perpendicular axes in an applied field *H*.

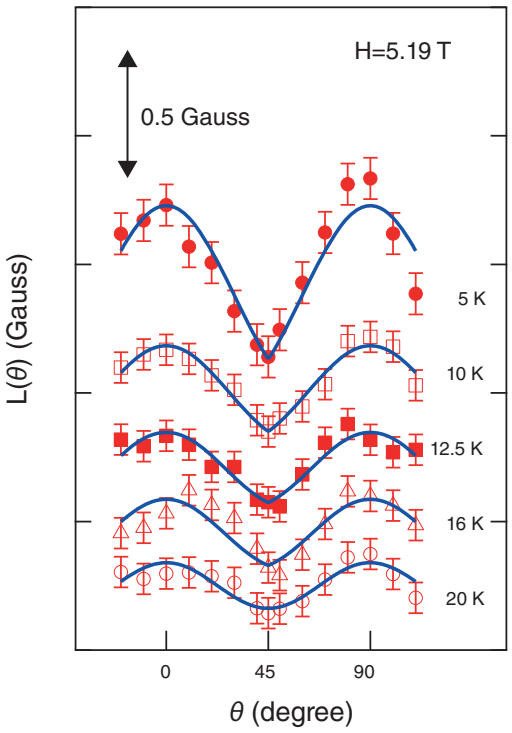

Fig.3-7 Field-angle (θ) dependence of Si-NMR line width, L(θ)
Below 17.5 K, the amplitude of the θ-dependence increases. The pointed minimum at 45° indicates 2-fold anisotropy.

In the superconducting state, two electrons can form a superconducting pair. To form such pairs, an attractive interaction between the electrons is necessary. In conventional superconductors, the origin of the attractive interaction is a lattice vibration. In contrast, a magnetic fluctuation is considered to be the origin in actinide superconducting compounds. Since a high superconducting transition temperature T_c can be expected for magnetic fluctuation-induced superconductivity, it is important to clarify its mechanism.

In URu_2Si_2, a so-called "hidden order state" appears below 17.5 K (−256 °C). As the superconducting state appears at lower a temperature of 2 K (−271 °C), magnetic fluctuation in the hidden order precursor state is believed to induce the superconductivity. However, the hidden order has not been identified in 25 years, which is one of the important issues facing condensed matter physics.

URu_2Si_2 has 4-fold symmetry in the paramagnetic state above 17.5 K. Recently, however, it has been revealed that the electronic state shows a symmetry breaking from a 4-fold state to a 2-fold state in the hidden ordering regime. In this study, the magnitude of the 2-fold anisotropy was determined precisely using nuclear magnetic resonance (NMR). At first, a two-axis rotating stage was developed to rotate a sample precisely (Fig.3-6). Using this stage, the field angle (θ) dependence of the Si-NMR line width was precisely determined (here θ is defined against the [110] crystal direction in the basal plane). Based on this, the magnitude of the 2-fold anisotropy was found to be smaller than the previously reported value (Fig.3-7).

A future superconductor with a higher T_c is considered to be realizable in a magnetic fluctuation-mediated superconducting system, since the T_c of phonon mediated superconductors has already reached its peak. If a new room-temperature superconductor were to be found, it would be quite useful for improving energy efficiency in electronic devices.

We are going to further investigate actinide compounds to clarify the mechanism behind superconductivity in detail.

Reference

Kambe, S. et al., NMR Study of In-Plane Twofold Ordering in URu_2Si_2, Physical Review Letters, vol.110, issue 24, 2013, p.246406-1-246406-5.

3–4 Hydrogen-Induced Insulation Degradation of Ceramic Capacitors
— Microscopic Evidence Provided by Muons —

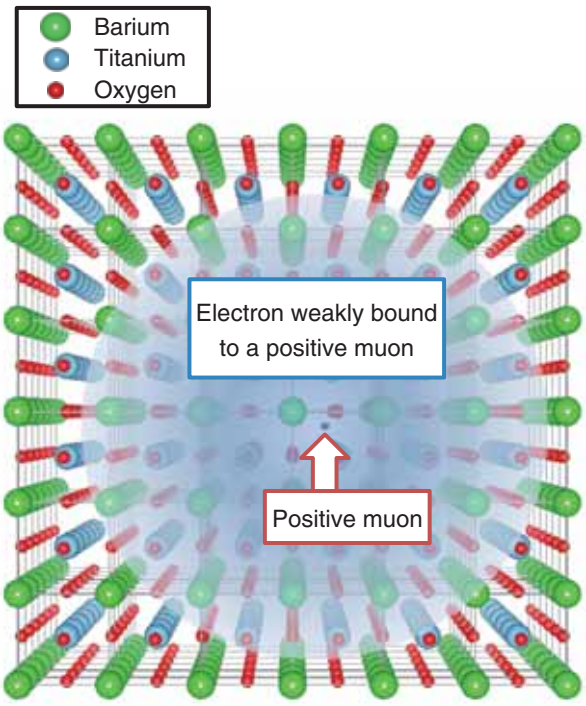

Fig.3-8 A schematic of the muon-electron bound state in $BaTiO_3$
The widely spread electron orbital suggests that the electron is very weakly bound to the positive muon in $BaTiO_3$.

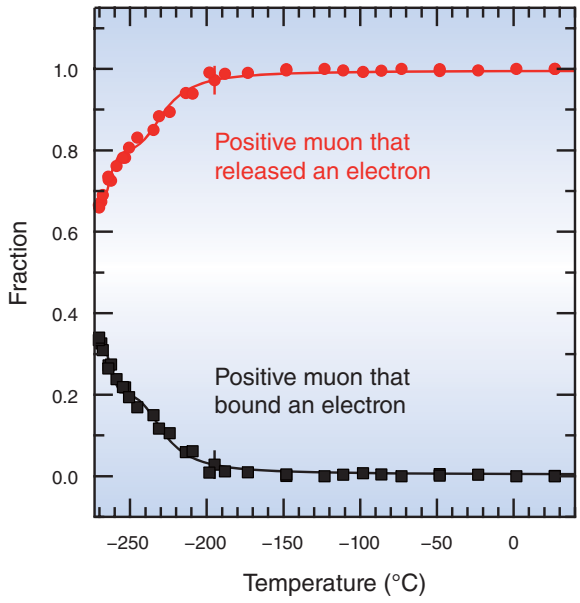

Fig.3-9 Electron release from the hydrogen-like muon-electron bound state in $BaTiO_3$
The black squares and red circles represent the fractions of positive muons with and without a bound electron, respectively. The solid curves are the best fits to an ionization model.

Multilayer ceramic capacitors (MLCCs) are fundamental components of electronic circuits and are indispensable for state-of-the-art electronic devices. Since the performance of MLCCs heavily depends on that of dielectric materials, controlling the quality of dielectric materials is vitally important. As the internal electrodes of typical MLCCs contain an easily-oxidizable element, the annealing process to unify the dielectrics and electrodes is performed in a reducing atmosphere containing hydrogen (H). On the other hand, this process can cause insulation degradation, depending on the annealing conditions. Intensive studies are under way to identify the origin of this degradation.

In this work, we focused on the risk of H incorporation into dielectrics in the annealing process, and studied the behavior of H in a typical dielectric material, barium titanate ($BaTiO_3$). The electronic structure of H impurities in $BaTiO_3$ is not obvious, since H can assume various charge states in materials. To tackle this issue, we used positive muons in place of H. It is well established that the electronic structure of a muon-electron bound state is identical to that of H except for small isotope corrections. Thus, we can imitate H impurities in $BaTiO_3$ with positive muons and selectively probe their influences. Another advantage of using a muon is its high sensitivity; one can obtain microscopic information corresponding to H impurities in the dilute limit, which is difficult to access by other experimental techniques.

A positive muon beam was irradiated to a $BaTiO_3$ single crystal at the J-PARC muon facility, and the local electronic structure around the implanted muons was investigated by means of the muon spin rotation technique. We observed a signal from muons that weakly bound an electron below −190 °C, which suggested that the electron orbital was widely spread, as shown in Fig.3-8. The weakly bound electrons were gradually released with increasing temperature, as shown in Fig.3-9. The released electrons could move freely around the crystal and led to electric conductivity, thus decreasing the insulating performance of $BaTiO_3$. Hydrogen impurities in $BaTiO_3$ are also thought to release electrons according to a similar mechanism, resulting in insulation degradation at device operating temperatures.

Reference

Ito, T. U. et al., Shallow Donor Level Associated with Hydrogen Impurities in Undoped $BaTiO_3$, Applied Physics Letters, vol.103, issue 4, 2013, p.042905-1-042905-4.

3–5 A Study to Reveal the Mechanism of Radiobiological Effects

— DNA Damage Induces Aberrations in Normal Chromosomes in a Living Cell —

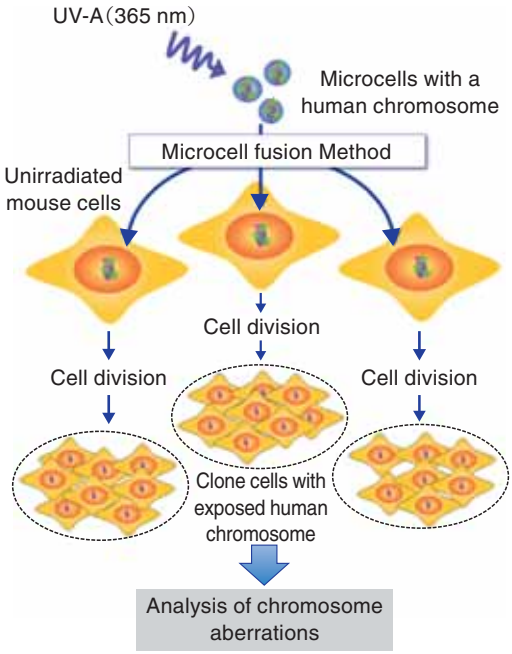

Fig.3-10 Transfer of damaged DNA by a microcell fusion method
Microcells containing a human chromosome were exposed to UV-A, and then transferred to unirradiated mouse cells. The cells were cultured, and many clones with a stable cell division function were selected. The resulting chromosome aberrations were microscopically observed in the cells and analyzed.

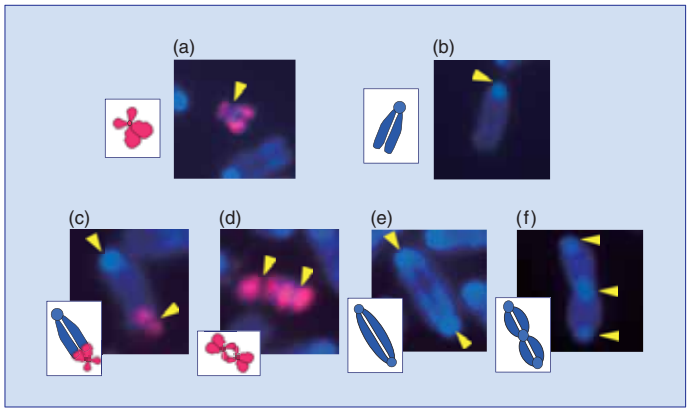

Fig.3-11 Typical chromosome aberrations microscopically observed
Human and mouse chromosomes are indicated in red and blue, respectively. Yellow arrows show pieces of apparatus, the so-call "centromere," used to pull the chromosomes into both daughter cells during cell division. Normal human (a) and mouse (b) chromosomes are shown in the upper panels. The abnormal chromosomes comprise a mouse chromosome and a human chromosome (c), two human chromosomes (d), and two (e) and three (f) mouse chromosomes, which are shown in the lower panels.

As one of the genetic effects through multiple repetitions of cell division, chromosome aberrations are occasionally induced in the progeny cells after ionizing irradiation. This is known to be "genetic instability," which is strongly involved in the induction of late radiation effects, such as carcinogenesis. The detailed mechanism behind it, however, has not yet been fully understood.

In this study, we focused on DNA damage as a trigger of the instability, particularly DNA base damage, which might persist even after repeated cell divisions. The bases normally work as elementary units of genetic code in DNA, and their alteration is thought to raise mutation frequencies. In addition to DNA damage, irradiation could also induce damage to cytoplasmic organelles. To exclude the cytoplasmic effects, we applied a microcell fusion method to observe genetic instabilities induced only by DNA base damage.

Sub-cellular small structures called microcells, including one human chromosome, were irradiated and then transferred into unirradiated normal mouse cells (Fig.3-10). The human chromosome is considerably different from those of the mouse cell, such that the exposed human chromosome was easily distinguished from unirradiated mouse chromosomes by means of microscopic observations. It was confirmed beforehand that normal chromosome transfer did not induce any genetic instabilities. Ultraviolet light (wavelength: 365 nm), known as UV-A, was used as the source of the irradiation, because it has been known to preferentially induce the same sort of DNA base lesions that are induced by ionizing radiation. After the chromosome transfer, the cells were cultured for 20 days or a month to obtain various clonal cell lines that stably undergo cell division.

The analysis of the chromosomes in the clones revealed that certain types of aberrations, such as fusions between normal mouse chromosomes, were frequently induced, in addition to fusions between the human chromosomes, or between human and mouse chromosomes (Fig.3-11). Furthermore, it was observed that the number of chromosomes in the clone cells abnormally increased from the normal number of 43 to twice that number or more.

These evidences indicate that a novel mechanism of signal transfer from damaged to normal chromosomes could result in the genetic instability in the unirradiated cells. Detailed investigation is expected to reveal the induction process of radiation carcinogenesis in the low dose region in the near future.

The present study was partly supported by the Ministry of Education, Culture, Sports, Science and Technology of Japan (MEXT) KAKENHI Grant-in-Aid for Young Scientists (B) (No.20710045).

Reference

Urushibara, A., Yokoya, A. et al., Induction of Genetic Instability by Transfer of a UV-A-Irradiated Chromosome, Mutation Research, vol.766, 2014, p.29–34.

3–6 Discovery of Uranium Migration in Groundwater with Silica Colloid

— Devisal of an Effective Method for Elucidating the Chemical Forms of Trace Actinides in Environmental Water —

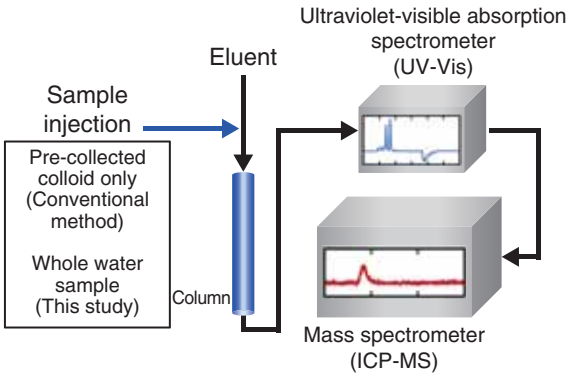

Fig.3-12 SEC-UV-Vis-ICP-MS analysis
Sample components are separated by their size as they pass through a column of eluent. The eluent was introduced on-line to an ultraviolet-visible (UV-Vis) spectrometer and then to an inductively coupled plasma mass spectrometer (ICP-MS) to analyze its components. The conventional method analyzes colloids only, using a single column. This study used two columns with opposite charges to analyze both the colloid and the ions by directly injecting environmental water into the columns. The results obtained by the two columns were compared.

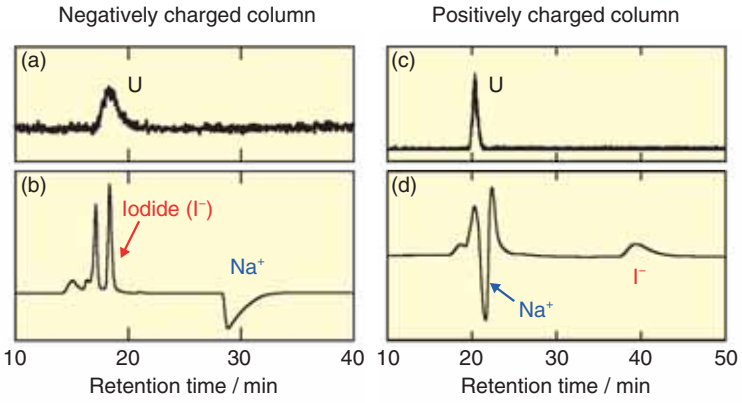

Fig.3-13 SEC-UV-Vis-ICP-MS analysis of Horonobe groundwater
(b), (d) Ultraviolet absorption. (a), (c) ^{238}U. The sizes of components can be estimated based on the retention times of colloids with known sizes. Larger colloids are eluted faster. For a colloid, the sizes estimated by two columns with opposite column charges are similar. For an ion, very different sizes are estimated, because the retention times differ greatly between the two columns, due to the interaction between the ion and the charge of the column (b, d).

It is thought that actinides do not migrate in environmental water (EW) in ionic form, but rather, migrate together with colloids by being adsorbed onto them. However, this theory has not yet been experimentally confirmed because there have not been any methods for effectively investigating trace actinides in EW and thereby determining what colloids transport them and whether actinide ions can migrate by themselves.

The SEC-UV-Vis-ICP-MS method has been used to analyze colloids in EW. This method separates colloids by their sizes and detects trace elements in them (Fig.3-12). In the conventional method, relatively large colloids in EW are collected in advance, and are then injected into a separation column for analysis. This method has the disadvantage of being incapable of analyzing ions and small colloids. To solve these problems, we took note of the charge of the separation columns. By injecting EW as it is into a separation column, actinides in all states are detected. Since colloids and ions are separated by sizes and charges, respectively, it is predicted that colloids and ions can be distinguished by comparing the two results obtained by columns with opposite charges.

We analyzed trace uranium (U) in the groundwater collected at Horonobe, Hokkaido (Fig.3-13). A single peak of U was detected by each column. The sizes of the uranium-bearing substances, estimated from the times when the peaks appeared, were very similar to each other. This result shows that U was present as a colloid.

Trace U does not form an intrinsic (true) colloid. All the silica contained abundantly in the groundwater was eluted with U. This result revealed that U was present as a pseudocolloid, which comprised U adsorbed onto silica colloid. To our knowledge, we are the first to have discovered this type of pseudocolloid of U. The results also revealed that this groundwater did not contain U ions, because no other U peaks were detected.

This study devised a powerful analytical method for elucidating the forms of trace actinides in EW. This method is broadly applicable to various water samples, including experimental samples, and future application in various research fields is expected.

Reference

Kozai, N. et al., Characterization of Saline Groundwater at Horonobe, Hokkaido, Japan by SEC-UV-ICP-MS: Speciation of Uranium and Iodine, Water Research, vol.47, issue 4, 2013, p.1570–1584.

3–7 Search for $^{6}_{\Lambda}$H Hypernuclei

— Can We Make Neutron-Rich Hypernuclei? —

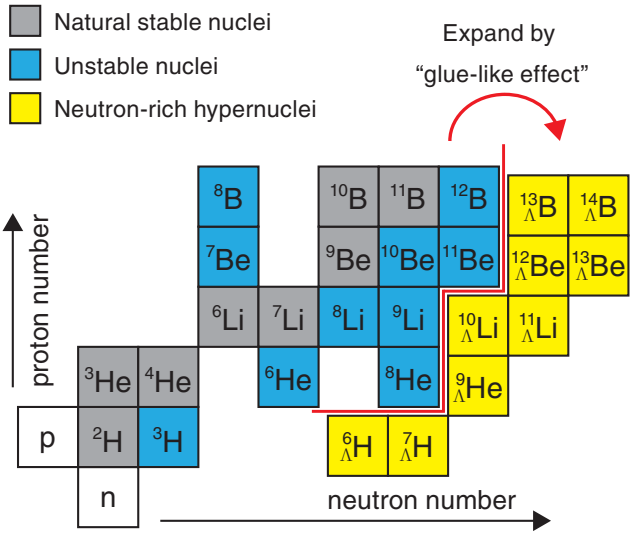

Fig.3-14 Nuclear chart of ordinary nuclei and hypernuclei
The horizontal axis shows the number of neutrons, and the vertical axis shows the number of protons. The grey boxes correspond to existing natural nuclei. The blue boxes correspond to unstable nuclei measured by experiments. The production of hypernuclei, indicated by yellow boxes, is possible using glue-like effects at J-PARC.

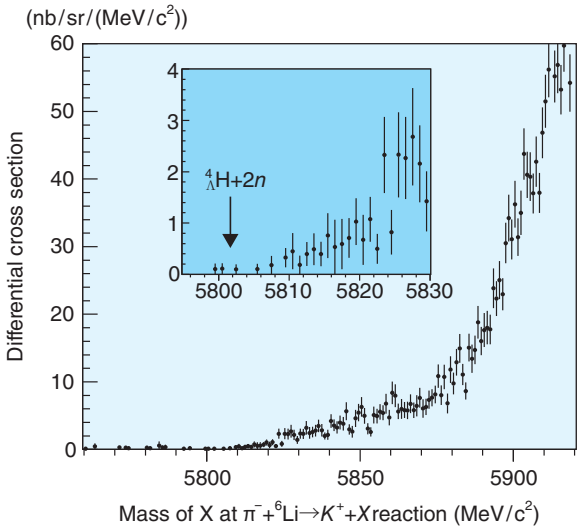

Fig.3-15 Mass of X in the reaction: π^- + ^{6}Li ⟶ K^+ + X
A magnified view of the Λ bound region is shown in the inset. The arrow labeled $^{4}_{\Lambda}$H + 2n shows the particle decay threshold (5801.7 MeV/c^2).

Ordinary nuclei comprise nucleons, i.e., protons and neutrons. On the other hand, Λ hypernuclei comprise one Λ particle together with nucleons. The Λ particle, which is of the species "hyperon," has a new degree of freedom: *strangeness*. This introduces an additional attractive force between the Λ particle and the nucleons, and causes a shrinkage of the nuclei. We call this a "glue-like effect." Using this, the nuclear chart expands in the strangeness sector. Fig.3-14 shows the nuclear chart of ordinary and hypernuclei. The region of hypernuclei (represented by yellow boxes) can be expanded into the neutron-rich region.

Thus, we attempted to produce a $^{6}_{\Lambda}$H hypernucleus, which comprises one proton, four neutrons, and one Λ. The core nucleus ^{5}H is unbound. Success in making $^{6}_{\Lambda}$H by adding a Λ could allow the production of very neutron-rich nuclei, with neutron-proton ratios as large as four.

The FINUDA (FIsica NUcleare a DAfne) group has reported three candidate events for $^{6}_{\Lambda}$H. However, the error in the mass was as large as about 1 MeV/c^2. We should confirm the mass with a larger amount of data.

This study was conducted with the K1.8 beam line of J-PARC's Hadron Experimental Facility. $^{6}_{\Lambda}$H is produced via the reaction π^-+^{6}Li→K^++X(X=$^{6}_{\Lambda}$H), which changes two protons to one neutron and one Λ particle. Fig.3-15 shows the mass spectrum of X. The arrow in the inset indicates the sum of $^{6}_{\Lambda}$H and two neutrons, and thus, the maximum-mass threshold of $^{6}_{\Lambda}$H. Unfortunately, no significant peak structure was observed around this arrow. An upper limit of the cross section was estimated to be 1.2 nb/sr. From this result, we determined that the production cross section of $^{6}_{\Lambda}$H must be much lower if it exists and indicated that there is room for the discussion of the theoretical model of the production mechanism.

Reference

Sugimura, H. et al., Search for $^{6}_{\Lambda}$H Hypernucleus by the ^{6}Li(π^-, K^+) Reaction at p_{π^-} = 1.2 GeV/c, Physics Letters B, vol.729, 2014, p.39–44.

Promoting Basic R&D on Nuclear Energy and Creation of Innovative Technology to Meet Social Needs

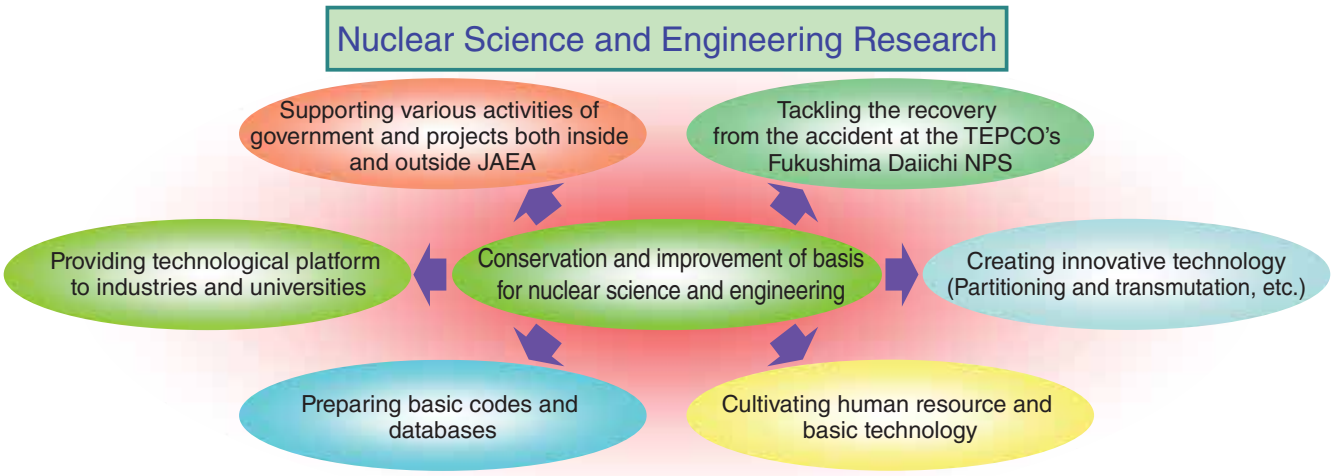

Fig.4-1 Roles of nuclear science and engineering research
We serve various roles to conserve and improve the foundation of nuclear science and engineering.

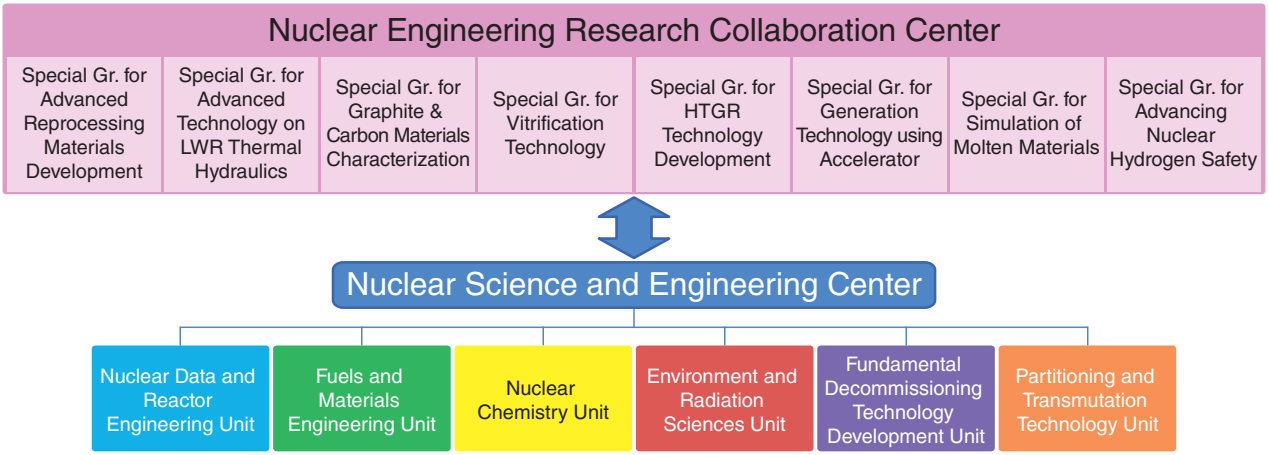

Fig.4-2 Nuclear Engineering Research Collaboration Center
To create innovative and practical products, joint research with industry and academia is being promoted.

Nuclear science and engineering research aims to promote activities, as shown in Fig.4-1, including recovering from the accident at the Tokyo Electric Power Company, Incorporated Fukushima Daiichi Nuclear Power Station (1F) and developing transmutation technologies to reduce the amount of long-lived radioactive waste. In the field of nuclear data and reactor engineering, we are working on the Japanese Evaluated Nuclear Data Library (JENDL), measuring nuclear data, and developing methods to design nuclear reactors using advanced theoretical, experimental, and simulation approaches (Topics 4-1, 4-2, and 4-3). In the fuels and materials engineering field, we are promoting research on nuclear fuels and materials used in reactors and on fuel-cycle facilities (Topics 4-4 and 4-5). In the nuclear chemistry field, we are promoting the analysis of basic data for reprocessing and detecting extremely small amounts of nuclear materials (Topics 4-6, 4-7, and 4-8). In the environmental and radiation science field, we are promoting studies on radionuclides in the environment and the development of a database for radiation protection (Topics 4-9 and 4-10). Joint research with industry and academia is also being promoted via the Nuclear Engineering Research Collaboration Center (Fig.4-2).

Developing the fundamental technology to decommission 1F involves enhancing our capabilities to characterize fuel debris, to analyze the durability of materials, to develop criticality management strategies, and to estimate radioisotope production (Chapter 1, Topics 1-1, 1-9, 1-10, 1-14, 1-16, and 1-19).

Using accelerator-driven subcritical systems (ADS), we are studying technologies to partition minor actinide (MA) nuclides (e.g., neptunium and americium) and fission products from spent nuclear fuel, and to perform MA transmutation.

Basic technology development is conducted at the JAEA research facilities. These technologies target radiation measurement (Topics 4-11 and 4-12) methods to assess durability of capsule materials in the reactor exposed to long-term irradiation (Topic 4-13) and safety management systems for the radiation-controlled area (Topic 4-14).

4–1 Improving the Prediction Accuracy of the Decay Heat from Nuclear Force
— Clarify Effect of Tensor Force on β Decay —

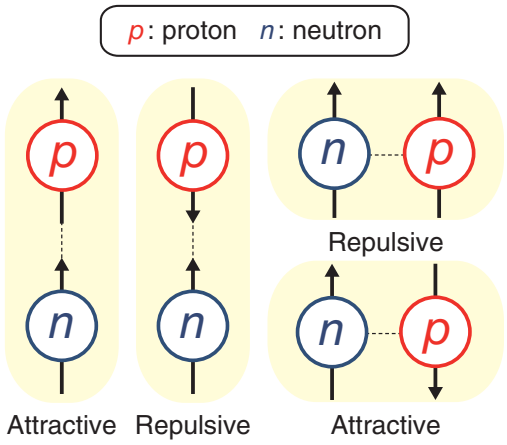

Fig.4-3 Interaction due to tensor force between proton and neutron
The tensor force is either attractive or repulsive depending on the direction of the "spin" (spin axis is represented by arrows in the figure) and the relative positions of the proton and neutron. The attractive tensor force plays an important role in β decay.

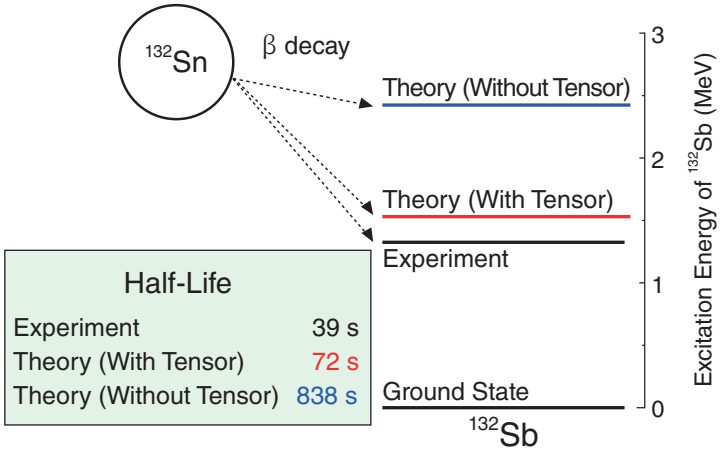

Fig.4-4 Half-life of ^{132}Sn and excitation energy of daughter nucleus ^{132}Sb with and without tensor force
The horizontal lines in the figure indicate the excitation energy of ^{132}Sb. By considering the tensor force, the half-life of ^{132}Sn and the excitation energy of ^{132}Sb obtained by theory approach the experimental results.

Fission products (FPs) generated in nuclear power plants and fragments produced by nuclear disintegration reactions in accelerators contain unstable nuclei. Unstable nuclei typically change into more stable nuclei by β decay. β decay involves emission of an electron (positron), an antineutrino (neutrino), and a photon, and delivers energy to the environment. The energy released in β decay of a single nucleus is very small. However, spent nuclear fuel contains an enormous quantity of FPs, which produces a large amount of heat (decay heat). The decay heat is one of the problems that complicate the reprocessing of spent nuclear fuel and the disposal of radioactive waste. In addition, decay heat is the main reason that lots of heat is generated in the damaged nuclear reactors of the TEPCO's Fukushima Daiichi NPS. However, some aspects of β decay remain unexplained by current theoretical models. In particular, theoretical models cannot reproduce energy by β decay or the half-life of nuclei with magic numbers. This fact reduces the accuracy predicting decay heat.

To solve this problem, we focus on the tensor force, which is not accounted for in the conventional models. The tensor force is one of the fundamental nuclear forces that govern the interaction between protons and neutrons, the constituents of the nucleus. Fig.4-3 shows the characteristic feature of the tensor force. The tensor force is either attractive or repulsive depending on the "spin" of the particles involved. Spin is analogous to the rotation of the particle and the relative position of proton and neutron. We developed a new theoretical model that includes the tensor force and numerically analyzed it to study how the tensor force affects β decay. We found that the attractive tensor force plays an important role in β decay. As shown in Fig.4-4, the half-life of the magic-number nucleus, tin-132 (^{132}Sn), approaches the experimental result and the excitation energy of its daughter nucleus, antimony-132 (^{132}Sb), is accurately reproduced.

This result contributes to improving the accuracy of predicting decay heat and should be useful in various fields of research, such as cosmic nucleosynthesis and fundamental research in nuclear physics.

Reference

Minato, F. et al., Impact of Tensor Force on β Decay of Magic and Semimagic Nuclei, Physical Review Letters, vol.110, issue 12, 2013, p.122501–1–122501–5.

4-2 Understanding the Behavior of Molten Material in Severe Accidents
— Developing Numerical Simulation Method of Melt Relocation —

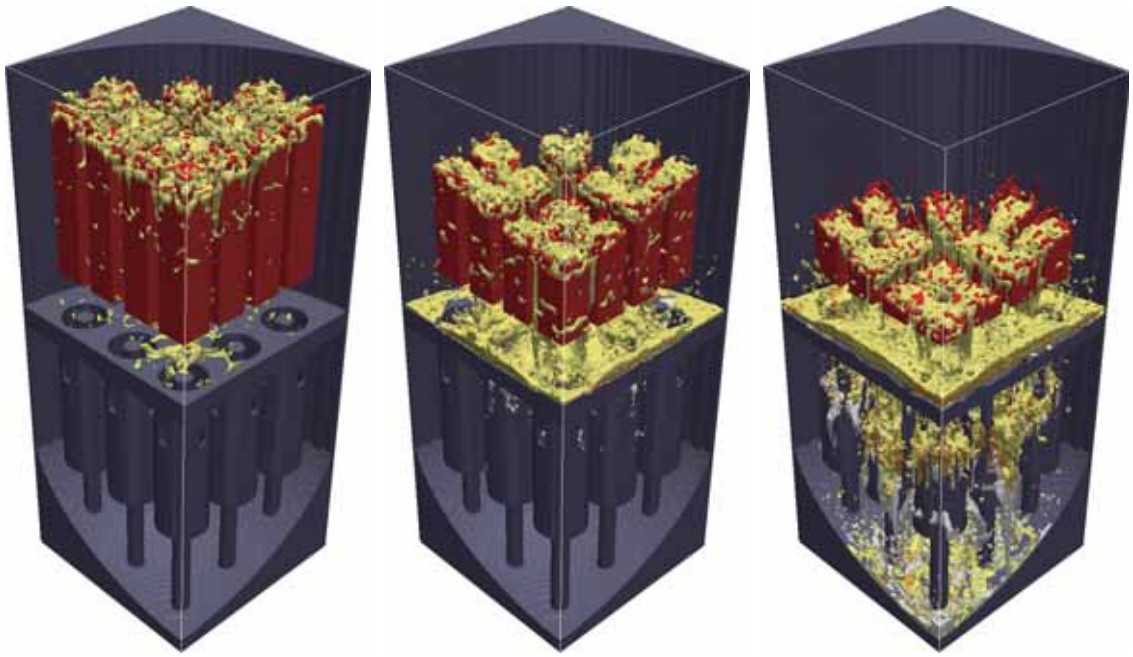

(a) The early stage of the core melting (b) Melt relocates to the core plate (c) Melt intrudes into and accumulates at the lower plenum

Fig.4-5 Transition of molten-material relocation
(a) Fuels were melted by heating from above, and then the melted fuel relocated downward. (b) Molten fuels accumulate on the core plate and some flows into the control-rod guide tubes (CRGTs). (c) Molten fuel enters the lower plenum through the CRGTs and accumulates in the lower region.

In the accident at the TEPCO's Fukushima Daiichi NPS (1F), the meltdown is believed to have occurred in the reactor pressure vessel (RPV), following which the molten fuel reached the lower head. Although understanding in detail how molten fuels distribute in the RPV is very important, the distribution is quite difficult to measure because of the high radiation. In this case, a numerical simulation is useful. Although some severe accident (SA) codes have been used to numerically simulate SAs, detailed simulations of melt relocation remain very limited. In addition, because the boiling water reactor (BWR) accident at 1F is without precedent in the world; most simulations to date deal with pressurized water reactors (PWRs). Therefore, we are developing a new simulation code to elucidate the details of melt relocation in SAs. Because at least two components are involved inside the RPV, uranium fuel (heating element) and the remaining structure (nonheating element), we improved the code so that it can distinguish between these two. We also designed a numerical method that can efficiently calculate the changing shape of the molten materials, which enables the code to treat thermal hydraulics, including complicated interactions between molten fuels and the other structures shown in Fig.4-5. Thus, by providing a detailed treatment of molten materials and a simulation of the relocation of the multicomponent melt, we implemented a unified simulation of the system, including the heating material (uranium fuel) and the nonheating materials (Zry, SUS, B_4C, etc.). Therefore, the results from this code are expected to provide information that will complement the results obtained from existing SA codes.

In the future, we will implement some physical models and also validate the code to ensure an accurate understanding of how melt behaves inside a RPV.

Reference

Yamashita, S. et al., Development of Numerical Simulation Method for Relocation Behavior of Molten Materials in Nuclear Reactors: Analysis of Relocation Behavior for Molten Materials with a Simulated Decay Heat Model, Proceedings of the 22nd International Conference on Nuclear Engineering (ICONE 22), Prague, Czech Republic, 2014, ICONE22-30972, 9p., in CD-ROM.

4–3 Improving Uranium Accountancy

— Demonstration of a Novel Nondestructive Assay for Nuclear Waste Drums at Ningyo-toge —

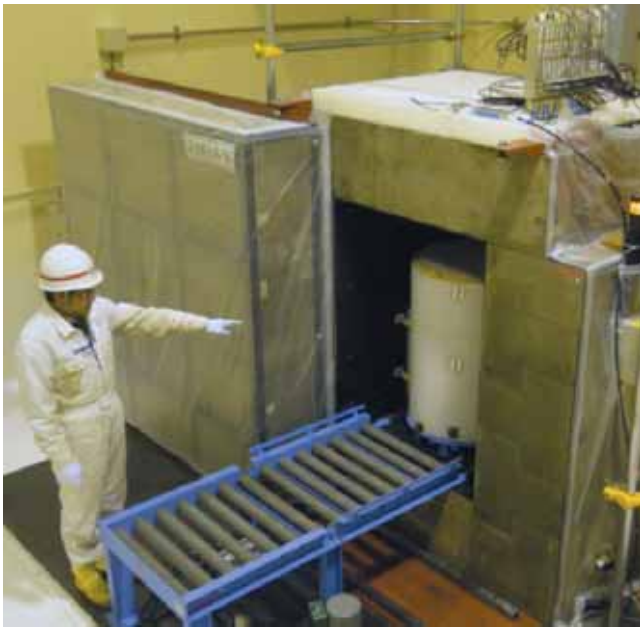

Fig.4-6 Photograph of NDA device (JAWAS-N) built at Ningyo-toge
This NDA device was constructed using 0.5-m-thick concrete blocks, wherein a neutron generator, ^{3}He detector bank, and turntable were installed (Fig.4-7). On the outside, the device is 2 m long, 2 m wide, and 2.2 m high. On the inside it is 1 m long, 1 m wide, and 1.2 m high.

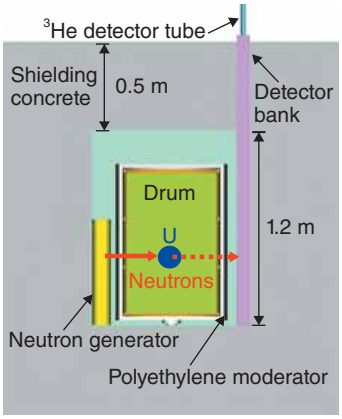

Fig.4-7 Schematic inner view of JAWAS-N
The FNDI method directly irradiates fast neutron to a drum and detects only the fast neutrons resulting from the nuclear-fission between the moderated neutrons and ^{235}U.

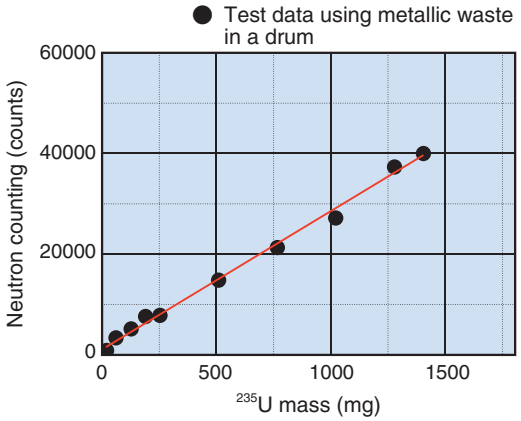

Fig.4-8 Linear relationship between ^{235}U mass and the neutron counting measured in JAWAS-N
The mass of ^{235}U contained in a waste drum is specified by neutron counting, whose results are independent of spatial (nonuniform) distribution of ^{235}U.

When nuclear-facility operators place U-contaminated dismantling wastes in waste drums for strict storage, they are legally required to implement nuclear material accountancy. Therefore, the Ningyo-toge Environmental Engineering Center (NEEC) of Japan Atomic Energy Agency (JAEA) uses the passive γ-ray measurement method to determine the amount of uranium (U) contained in the drums.

However, with this method, the results of the measurements are strongly perturbed when the matrix and U are nonuniformly distributed in the drum. Occasionally, the measurement error is large and becomes a matter of great concern for U accountancy.

To overcome this difficulty, the Nuclear Science and Engineering Center (NSEC) of JAEA developed a nondestructive assay (NDA) for ^{235}U called the fast-neutron direct-interrogation (FNDI) method. To promote the practical application of this method, an NDA device (JAWAS-N) that uses the FNDI method was newly constructed at the NEEC (Fig.4-6).

In this method, fast neutrons (14.4 MeV) from a neutron generator irradiate a waste drum, and the fast neutrons that result from nuclear fission between the moderated neutrons and ^{235}U in the drum are detected (Fig.4-7). Since fast neutrons are not strongly affected by the nonuniform distribution of matrix and U, the ^{235}U mass can be determined by counting the neutrons that correspond to ^{235}U.

To date, fundamental research has shown that the result of neutron counting increases in proportion with the ^{235}U mass in the drum, as shown in Fig.4-8; hence, the ^{235}U mass could be obtained with small error regardless of the chemical composition and location of nuclear materials in the drum.

Since the FNDI method can precisely determine the total mass of ^{235}U, the other isotopes can be identified if the enrichment of U is known. Combining this method with the conventional methods enables the proper determination of the mass of U (^{238}U+^{235}U). Therefore, more R&D is planned to further improve this method.

Reference

Japan Atomic Energy Agency, Measurement Method for Mass of Fissile Materials, and the Measurement Deivce, Patent Application Publication, pub.no.JP2014-174123, 2014-09-22, (in Japanese).

4–4 Improving the Evaluation Accuracy of the Long-Term Integrity of Nuclear Reactors
— Developing a Model of the Microstructural Evolution under Neutron Irradiation —

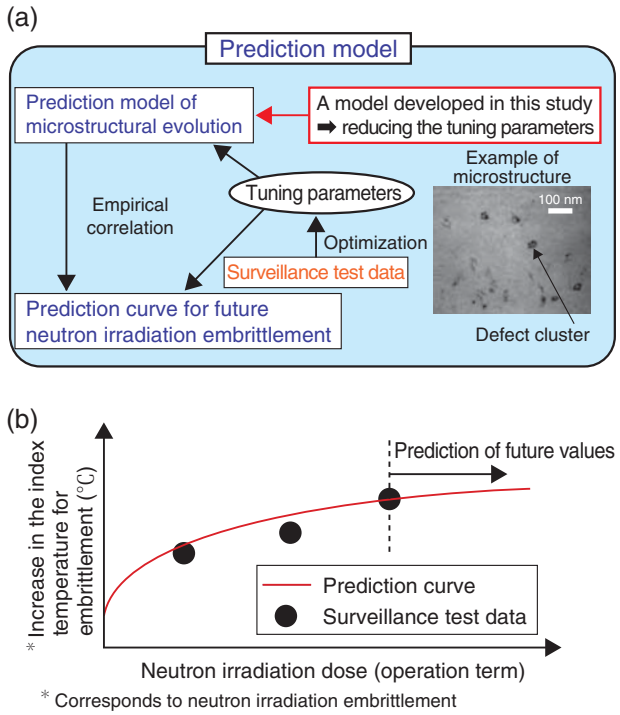

Fig.4-9 Schematic of the model used to predict embrittlement due to neutron irradiation
(a) Flow chart showing steps involved in creating curve to predict irradiation embrittlement, and (b) schematic of the prediction curve. We reduced the tuning parameters by developing a model to predict the microstructural evolution.

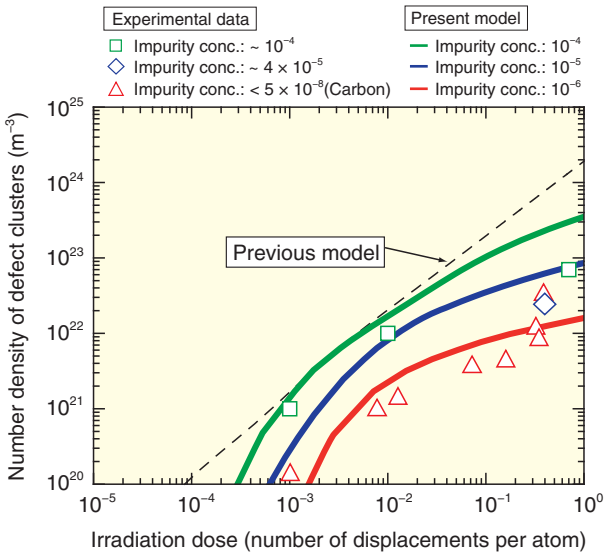

Fig.4-10 Density of defect clusters as a function of neutron-irradiation dose
Compared with the prediction of a previous model (dashed line), which did not include impurity effects, the present model (solid lines) with impurity effects better reproduces the experimentally observed defect density as a function of neutron-irradiation dose.

Metallic materials subjected to long-term neutron irradiation due to fission in nuclear reactors suffer microstructural modifications, which result in neutron-irradiation embrittlement of these materials. To understand and predict the rate at which irradiation embrittlement proceeds is thus a vital issue for ensuring the long-term integrity of nuclear reactors.

Fig.4-9 shows a schematic of the current model used to predict neutron-irradiation embrittlement. The prediction curve is estimated by solving empirical equations that correlate the calculated microstructural change to the increase in irradiation embrittlement. By optimizing the parameters involved in reproducing data on irradiation embrittlement obtained from surveillance pieces, the future integrity of nuclear reactors can be predicted. However, these parameters must sometimes be significantly modified, especially as the operating life of nuclear reactors increases; hence, improving the accuracy of the model used to make these predictions is a crucial issue.

To address this issue, we modeled how the migration of defect clusters (produced by irradiation) is affected by impurity atoms as fundamental physical processes that were not considered in previous models. With this approach, we aim to develop a versatile model capable of treating various metallic materials and irradiation conditions in a unified fashion. Based on the latest results of research on how impurities affect the formation and the growth of defect clusters (which is one of the primary causes of irradiation embrittlement), we developed a model to predict the microstructural evolution of materials and demonstrated its validity. Fig.4-10 shows how defect-cluster density depends on the neutron-irradiation dose in pure iron, which is the basic material of nuclear reactors. This model reduces the range over which parameters must be tuned and significantly improves the consistency between model and experimental data (e.g., it reproduces the saturation in defect density upon increasing neutron-irradiation dose and the defect density as a function of impurity concentration).

This result shows the importance of incorporating more fundamental physical processes into prediction models. By further developing the present model, we expect to improve the accuracy with which the increase in neutron-irradiation embrittlement is predicted, thus better securing long-term operation of nuclear reactors.

Reference

Abe, Y. et al., Effect of Carbon Impurity Content on Microstructural Evolution in Neutron-Irradiated Alpha Iron: Cluster Dynamics Modeling, Materials Research Society Symposium Proceedings, vol.1535, 2013, 7p.

4–5 Developing a Database of Fundamental Properties for Partitioning and Transmutation

— Evaluating Thermodynamic Data on Intermetallic Compounds with Electrochemical Techniques —

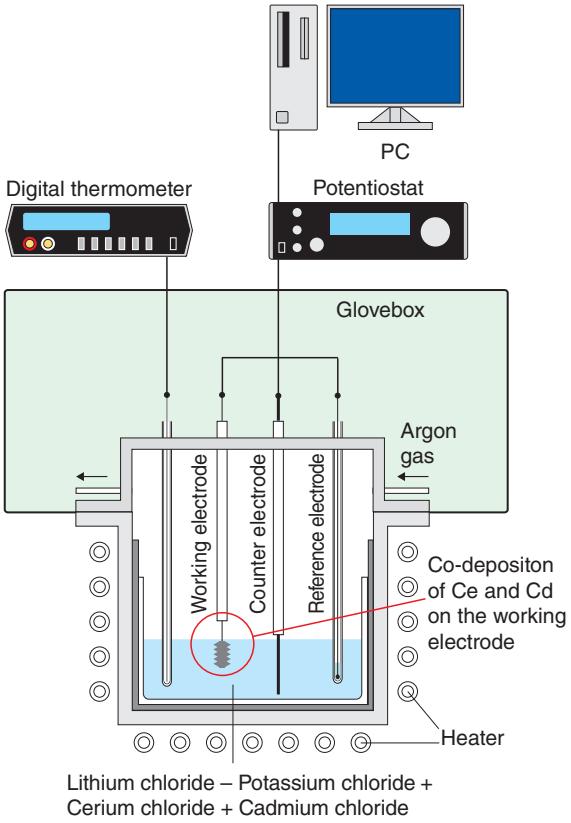

Fig.4-11 Concept of the electrochemical method applied in the present study
The Gibbs free energy of formation of Ce-Cd intermetallic compounds is evaluated based on the plateau potentials of intermetallic compounds formed by co-deposition of Ce and Cd on the working electrode in molten salts of lithium chloride and potassium chloride.

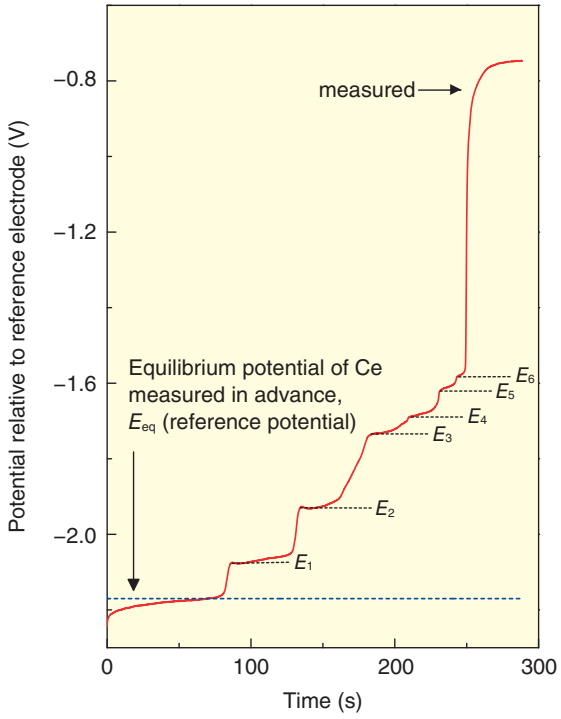

Fig.4-12 Chronopotentiogram of equilibrium potential of Ce-Cd intermetallic compounds relative to reference electrode (673 K)
The red solid line indicates the variation in potential. Blue dashed lines indicate the equilibrium potential for Ce and the six plateau potentials for Ce-Cd intermetallic compounds (E_1–E_6).

Partitioning and transmutation is a promising concept for advanced nuclear fuel cycles. In this approach, minor actinides (MAs) are recycled and transmuted to reduce the environmental impact of nuclear waste. Since MAs are highly radioactive and give off significant decay heat, a pyrochemical method is a proper candidate for reprocessing. In the pyrochemical reprocessing method proposed by JAEA, MAs are selectively collected in a liquid cadmium (Cd) cathode in the molten salt bath, following which they are recovered as alloys by Cd distillation and separation. Developing such a pyrochemical reprocessing requires a database of various fundamental properties. Cd distillation and separation requires thermodynamic data on various Cd intermetallic compounds because the decomposition of the intermetallic compounds may be dominant in the last stage of Cd distillation.

Fig.4-11 presents the electrochemical method used in the present study, in which the three-electrode technique was adopted for electrochemical measurements, from which the Gibbs free energy of formation of various intermetallic compounds was determined.

Cerium-Cadmium (Ce-Cd) intermetallic compounds form by co-deposition of Ce and Cd metals on the working electrode. The Gibbs free energy of formation of Ce-Cd intermetallic compounds was determined from the difference between two potentials: the redox reaction potential for Ce^{3+}/Ce and the plateau potential for the Ce-Cd intermetallic compound (E_1–E_6) in the molten salt (Fig.4-12).

These results represent the first determination of the Gibbs free energy of formation of these six Ce-Cd intermetallic compounds.

Based on the similarity between lanthanide (Ln) and actinide (An), we plan to use An with this electrochemical method and evaluate the Gibbs free energy of formation of An-Cd intermetallic compounds.

Reference

Shibata, H. et al., Evaluation of Gibbs Free Energies of Formation of Ce–Cd Intermetallic Compounds using Electrochemical Techniques, Journal of Physics and Chemistry of Solids, vol.75, issue 8, 2014, p.972–976.

4–6 Extraction of Strontium Using a Macrocyclic Compound

— Extraction Enhanced by Applying Ionic Liquid Solvents —

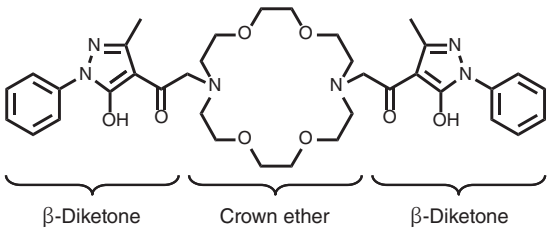

Fig.4-13 Chemical structure of the macrocyclic compound

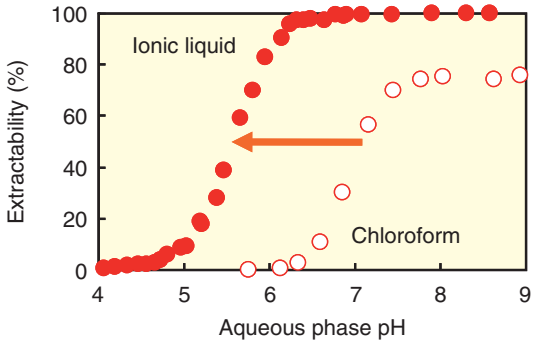

Fig.4-14 Extraction of strontium in the ionic liquid and chloroform
Strontium can be extracted in a lower-pH region when using an ionic liquid, resulting in significant improvement in the extraction.

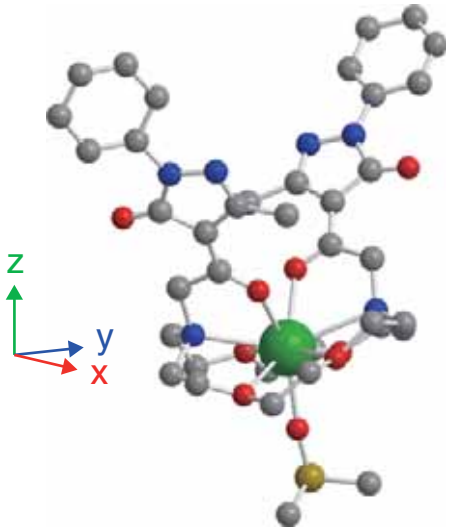

Fig.4-15 Crystal structure of the strontium complex extracted into chloroform
Strontium ( ) is coordinated by six oxygen ( ) and two nitrogen ( ) atoms from the macrocyclic compound and one oxygen ( ) atom from the solvent. and are carbon and sulfur atoms, respectively.

Strontium-90 (^{90}Sr), which is a fission product, is a β-ray emitting nuclide with a half-life of 28.8 years. In the human body, it accumulates in the bones. Thus, an efficient technique is required to remove ^{90}Sr from contaminated soil and seawater.

One effective technique to separate and remove metal ions including radionuclides is solvent extraction, which is a technique for extracting a target substance from an aqueous solution into an organic solvent (containing extractants) immiscible with water. This technique is widely used in industry to separate and recover rare metals.

As an extractant for strontium, we synthesized a macrocyclic compound (Fig.4-13) bearing two β-diketone moieties and used it to investigate solvent extraction with an ionic liquid. Ionic liquids have received significant attention recently as a replacement for organic solvents in the extracting medium. Ionic liquids are room-temperature molten salts composed only of ions and are expected to serve as functional solvents with unprecedented advantages due to their properties, which differ from those of conventional solvents.

To evaluate the advantages of using an ionic liquid as an extracting solvent to extract strontium ions, we compared the characteristics of the ionic liquid for extraction with those of chloroform, which is known as a general extracting solvent (organic solvent). We thus clarified that the extraction of strontium using the ionic liquid was remarkably enhanced compared with that using chloroform (Fig.4-14). A subsequent study comparing the extraction into the ionic liquid with that into chloroform shows that the 1:1 complex of strontium forms with the macrocyclic compound and is extracted in both systems. Analysis of the crystal structure of the complex extracted into chloroform reveals that strontium is encapsulated in the cavity of the ring and is coordinated by the two β-diketone moieties (Fig.4-15).

Furthermore, to understand why extraction into the ionic liquid is enhanced compared with chloroform, the structures of the complexes extracted into both solvents were analyzed by X-ray absorption spectroscopy. The strontium–oxygen distance in the complex in the ionic liquid is 2.51 Å, which is less than the distance found for the complex in chloroform (2.55 Å). Therefore, we conclude that strontium is more strongly held in the ionic liquid and the shorter strontium–oxygen distance leads to the enhanced extraction.

The present study was accomplished in collaboration with Kanazawa University.

Reference

Okamura, H. et al., Specific Cooperative Effect of a Macrocyclic Receptor for Metal Ion Transfer into an Ionic Liquid, Analytical Chemistry, vol.84, issue 21, 2012, p.9332–9339.

4–7 Controlling Valences by Electrocatalysis of Pt Particles

— Rapid and Selective Valence-Control Method for Actinide —

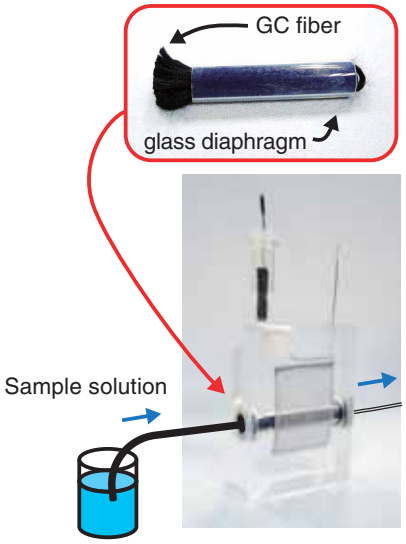

Fig.4-16 Flow electrolysis with column electrode
The column electrode is a working electrode of GC fiber packed tightly in a porous-glass-tube diaphragm. Electrolysis while letting the sample solution flow through the GC fibers enables a rapid and effective valence control of ions.

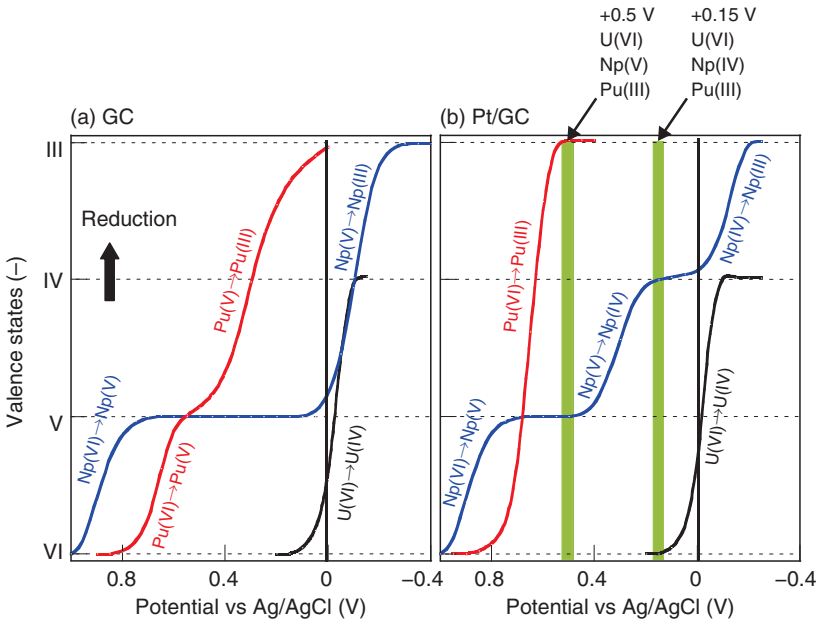

Fig.4-17 Valence changes of U, Np, and Pu ions by flow electrolysis
Valence changes of U, Np, and Pu as a function of potential applied by electrolysis with (a) GC fiber column electrode and (b) platinized GC (Pt/GC) fiber column electrode. For the Pt/GC electrode, Np can be controlled to be tetravalent. Hence, different oxidation states can be prepared for the U, Np, and Pu ions.

Actinides (An) such as uranium (U), neptunium (Np), and plutonium (Pu), in aqueous solutions exist as ionic species ranging from trivalent to hexavalent configuration. The chemical properties of these solutions depend on the valence of the ions; hence, a proper understanding of how to precisely adjust the valence of An ions in solution is required for efficient chemical separation and precise analysis.

We are developing a flow electrolysis method that uses as working electrode the column packed with glassy carbon (GC) fiber (Fig.4-16). Flow electrolysis is conducted by passing the solution through the column electrode, which can rapidly reach exhaustive electrolysis. The redox of An ions between tetravalent (An^{4+}) and pentavalent (AnO_2^+) accompanies the transformation of ions. Consequently, the reaction is slow, and large overpotentials are necessary. We find that the overpotential decreases as a result of electrocatalysis when platinum (Pt) is used as the working electrode material. Reaction rates at normal Pt surfaces are very small, however, and a long time period is needed to reach exhaustive electrolysis.

To address this problem, we tried to develop a rapid electrolysis wherein the column electrode exploited electrocatalytic effect. A column electrode with the platinized GC (Pt/GC) fiber serving as electrode was prepared by electrodeposition of platinum black onto GC fiber from a chloroplatinic acid solution.

The relationships between the applied potential and the valence of U, Np, and Pu upon electrolytic reduction with GC and Pt/GC electrodes are shown in Fig.4-17. At the conventional GC electrode (a), Np(V) is immediately reduced to Np(III), whereas Pu(V) is slowly reduced to Pu(III) because of the large overpotential for Np(V) and Pu(V) reduction. These results indicate that the selective control of valence is difficult. However, at the Pt/GC electrode (b), Np(IV) can be precisely prepared. Thus, U, Np, and Pu ions can be prepared in various oxidation states (e.g., U(VI), Np(IV), and Pu(III) when +0.15 V is applied).

The results of this study may be applied to obtain precise coulometric speciation of individual valence ions by measuring electric charge during electrolysis. They may also be applied to controlling the valence for the separation of An ions.

The present study was partly supported by the Ministry of Education, Culture, Sports, Science and Technology of Japan (MEXT) KAKENHI Grant-in-Aid for Scientific Research (C) (No.22560832).

Reference

Kitatsuji, Y. et al., Flow Electrolysis of U, Np and Pu Ions Utilizing Electrocatalysis at a Column Electrode with Platinized Glassy Carbon Fiber Working Electrode, Electrochimica Acta, vol.74, 2012, p.215–221.

4–8 Selective Detection of Higher Enriched Uranium Particles

— Secondary Ion Mass Spectrometry Combined with Solid-State Nuclear-Track Detection —

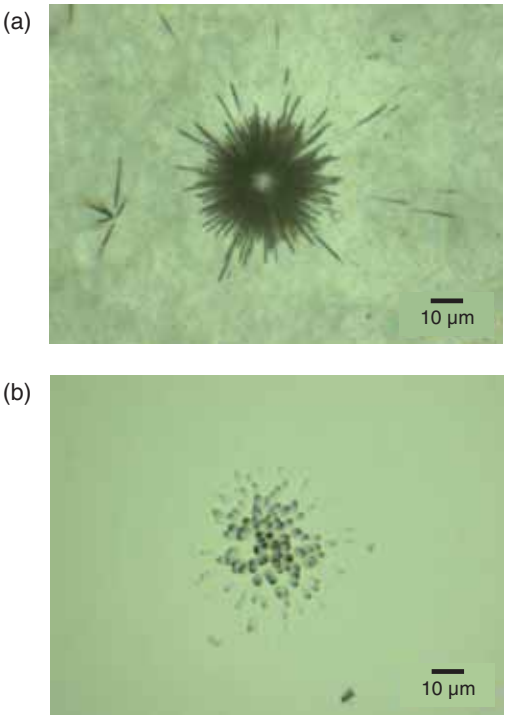

Fig.4-18 Images of (a) fission tracks and (b) alpha tracks from U particles
Fission or alpha tracks were created in a nuclear-track detector by U particles and were observed with an optical microscope.

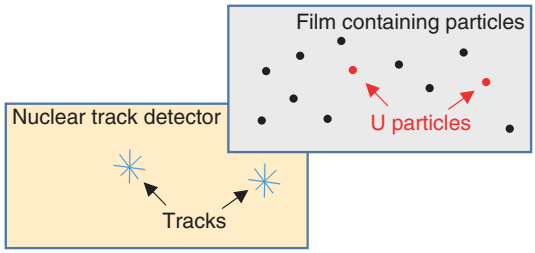

Fig.4-19 Identification of U particles
A film containing particles was fabricated and placed in contact with a nuclear-track detector. U particles were identified by observing the tracks.

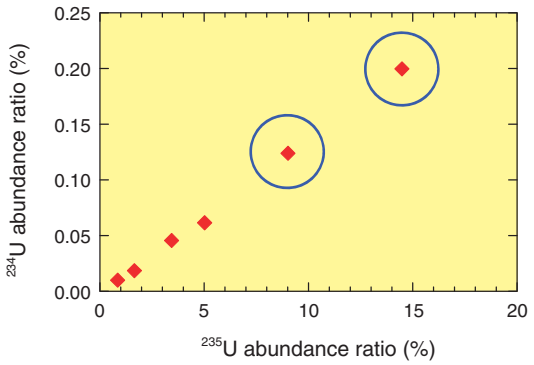

Fig.4-20 U isotope abundances in individual particles taken at a nuclear facility and measured with SIMS
Two particles with ^{235}U abundances over 9% were detected. Such particles were detected only when using nuclear-track detection.

Undeclared nuclear activities related to nuclear-weapon production should be monitored to ensure peaceful use of atomic energy. We routinely analyze environmental samples taken at nuclear facilities by inspectors of International Atomic Energy Agency (IAEA). Based on the isotope ratio results, IAEA verifies nuclear materials used and nuclear activities in the facilities.

Secondary ion mass spectrometry (SIMS) is a technique used to analyze isotope ratios. Here, individual particles are irradiated with focused ion beams and sputtered ions of each isotope are detected. To measure individual particles with SIMS, the locations of such particles in the sample should be exactly identified before analysis. In this study, we developed a technique to identify uranium (U) particles by detecting nuclear-tracks. The procedure is as follows. A film containing particles is fabricated and placed in contact with a nuclear-track detector. The sample is then irradiated with thermal neutrons in a nuclear reactor. When U in a particle absorbs neutrons, the U undergoes fission, which creates tracks in the detector. Since the tracks can be observed with an optical microscope (Fig.4-18(a)), U particles can be identified by observing the tracks (Fig.4-19). As another method, alpha tracks created by the alpha decay of U can be used to identify U particles (Fig.4-18(b)). In this case, no neutron source is necessary.

Since the number of tracks relates to the ^{235}U isotope abundance in the particle, we can identify more-enriched U particles by selecting the particles with a larger number of tracks. The identification of U particles abundant in ^{235}U is especially important to detect nuclear activities related to nuclear-weapon production. Fig.4-20 shows a SIMS result for a sample taken from a nuclear facility. Here, we identified particles with a larger number of tracks and analyzed the U isotope abundances with SIMS. Consequently, two particles with higher ^{235}U abundances can be detected, which is impossible to do by SIMS without prior nuclear-track detection.

The present study was sponsored by the Secretariat of the Nuclear Regulation Authority (NRA).

Reference

Esaka, F. et al., Secondary Ion Mass Spectrometry Combined with Alpha Track Detection for Isotope Abundance Ratio Analysis of Individual Uranium-Bearing Particles, Talanta, vol.120, 2014, p.349–354.

4–9 Mechanism of Greenhouse Gas Emission from Rice Paddy

— Simulation of Atmospheric Ammonia Exchange Using the Land Surface Model for Transport of Radioactive Materials —

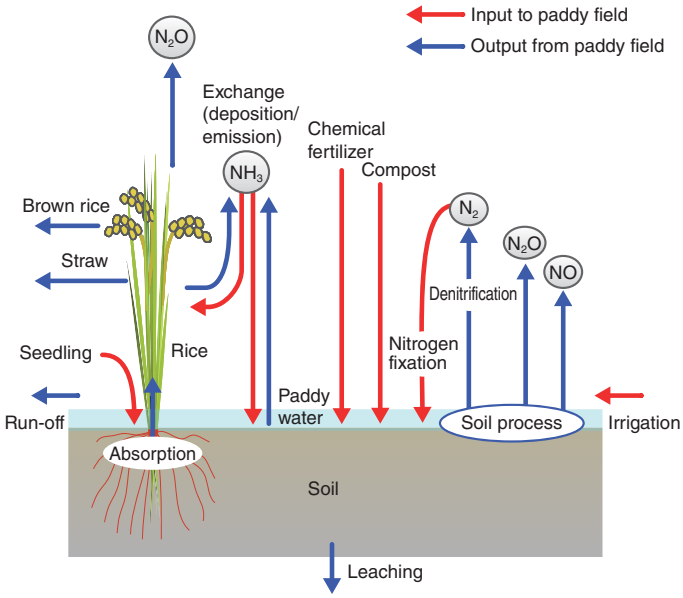

Fig.4-21 Nitrogen cycling at rice paddy
Greenhouse gases, such as nitrous oxide, relate to various processes. Bidirectional NH_3 exchange (deposition and emission) between the atmosphere and the rice paddy is hard to accurately be quantified.

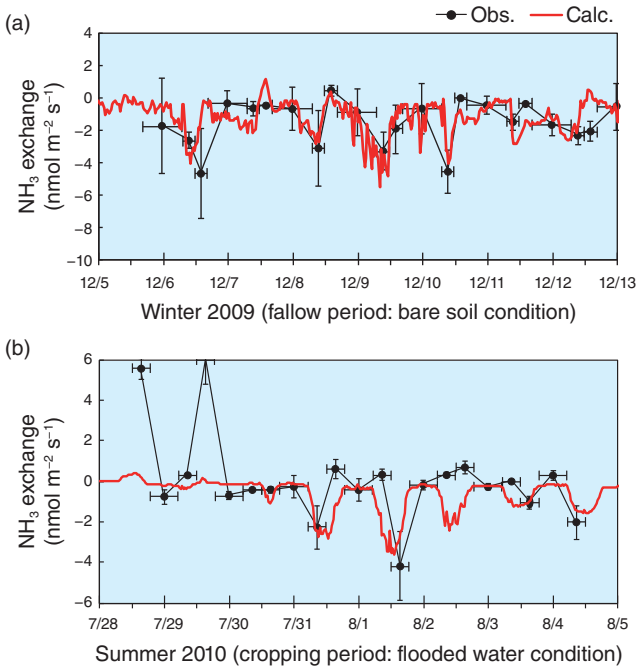

Fig.4-22 SOLVEG simulation of NH_3 exchange over rice paddy (a) during fallow period and (b) cropping period
Upon incorporating NH_3 exchange process into SOLVEG, the model reproduced the dynamics observed in NH_3 exchange (positive: emission, negative: deposition) between the atmosphere and the rice paddy.

To develop the model for various environmental material-transport studies, we applied the SOLVEG (Multi-layer Atmosphere-SOiL-VEGetation Model) to those studies, which is the land surface model for prediction of radioactive materials transfer between atmosphere and land surface. In the present study and in cooperation with National Institute for Agro-Environmental Sciences, Japan, we newly modeled ammonia (NH_3) exchange process above rice paddy fields.

Rice paddies are not only the major arable ecosystems providing the staple food in Asia, but also substantial sources of greenhouse gases such as nitrous oxide (N_2O). The emission of greenhouse depends on complicated processes of nitrogen cycling between the atmosphere, rice paddies and soil (Fig.4-21). NH_3 in the atmosphere above paddy fields is absorbed by the stomata of rice foliage and/or is dissolved by paddy water (NH_3 deposition). However, NH_3 is often emitted from the paddy when nitrogen fertilizer is provided (NH_3 emission). The accurate estimate of this bidirectional NH_3 exchange (the difference between NH_3 emission and deposition) is not straightforward and remains a key issue in the prediction of the greenhouse gas emission from rice paddies.

Hence, we developed new modules for SOLVEG to predict the paddy water temperature and the NH_3 concentrations in the foliage and at the surface of paddy water or soil. The modified SOLVEG model reproduced the observed NH_3 exchange rate at the Mase rice paddy site in Ibaraki, Japan (Fig.4-22). We also investigated how amount of NH_3 is exchanged during rice growth. The result revealed that the recapture by the foliage of NH_3 from the surface of the paddy water (NH_3 recapture) tends to increase with rice growth. Once maturity is reached, most volatilized NH_3 is recaptured in rice canopies and no longer transfers to the atmosphere. By allowing the reduction of the vaporization loss of NH_3 to the atmosphere, this result is useful for managing supplemental fertilization of rice paddies.

The present study was partly supported by Japan Society for the Promotion of Science (JSPS) KAKENHI Grant-in-Aid for Scientific Research (A) (No.22248026).

Reference

Katata, G. et al., Coupling Atmospheric Ammonia Exchange Process over a Rice Paddy Field with a Multi-Layer Atmosphere-Soil-Vegetation Model, Agricultural and Forest Meteorology, vol.180, 2013, p.1–21.

4–10 Influence of Physical Characteristics on Internal Dosimetry

— Use of Human Models to Compare Caucasians with Japanese —

Table 4-1 Averages of Japanese and reference values of Caucasians for physiques and organ masses in adult male
Body size for Japanese is usually smaller than that for Caucasian. However, the relative mass of each organ for a Japanese with respect to that for a Caucasian differs.

Physique	Average of Japanese adult male		ICRP reference value of Caucasian adult male
Height (cm)	170	<	176
Weight (kg)	64		73
Organ mass (kg)	**Average of Japanese adult male**		**ICRP reference value of Caucasian adult male**
Liver	1.600	<	1.800
Colon	0.330	<	0.370
Adipose tissues	13.900	<	18.200
Lungs	1.200	=	1.200
Thyroid	0.019	≒	0.020
Brain	1.470	>	1.450
Kidneys	0.320	>	0.310

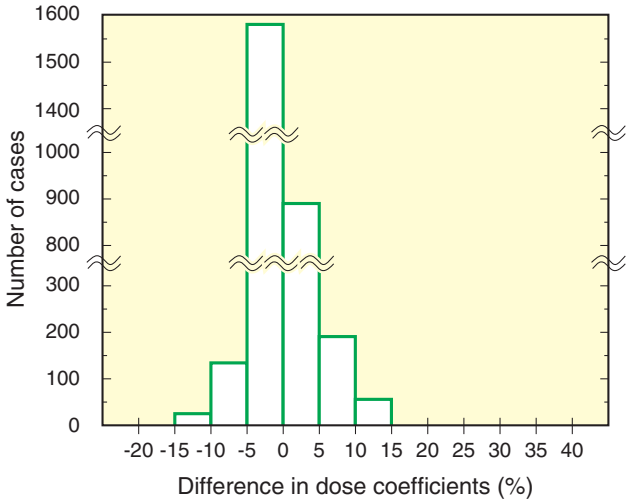

Fig.4-23 Histogram showing difference in dose coefficients between JM-103 and ICRP models
The percent difference was calculated as follows:
(Dose of JM-103 / Dose of ICRP model – 1) × 100

Assessing the internal dose due to the intake of radioisotopes (RIs) requires the knowledge of the ratio of energy deposited in the target organ to energy emitted by radiation from the source regions. These ratios are called the specific absorbed fractions (SAFs) and are calculated with human models that reproduce the shapes of organs, tissues, and body. For dose assessments, the International Commission on Radiological Protection (ICRP) has defined reference human models (ICRP models) that have the heights, weights, and organ masses appropriate for Caucasians. In the future, SAF data and effective doses per unit intake of RI (i.e., dose coefficients) will be published based on the calculations using the ICRP models.

The typical Japanese body size, however, is generally smaller than that of a Caucasian, and organ masses for Japanese also differ from those of Caucasians, as shown in Table 4-1. We analyzed discrepancies in SAFs and dose coefficients between Japanese and Caucasian due to differences in body size and organ mass (these are the physical characteristics), because dose coefficients given by the ICRP are used to establish radiation-protection standards in Japan.

We developed a human model named JM-103, whose physical characteristics are those of an average Japanese adult male. In this study, calculations of SAFs using JM-103 were performed for photons and electrons at 15 energies from 10 keV to 5 MeV, and for various combinations of 41 source regions and 33 target organs. Comparing the results of this calculation with SAFs based on the ICRP model reveals differences between the SAFs derived from organ masses and the weights of the two models. Next, we calculated the dose coefficients (D_e) using the SAFs of JM-103 and the ICRP model for 2894 cases, considering intake pathways and the chemical forms of 923 RIs.

Fig.4-23 shows the distribution of the difference in D_e between the JM-103 and ICRP models. The maximum D_e was about 40%, which was due to the differences in the SAFs between the models. However, the results show that, in 97% of all cases calculated, the D_e ranged from −10% to 10%. Thus, only in a limited number of cases the D_e were significantly affected by differences between the representative physical characteristics of Japanese and Caucasians. Thus, we conclude that the dose coefficients used by ICRP are applicable to the Japanese population for radiation protection.

Reference

Manabe, K. et al., Comparison of Internal Doses Calculated using the Specific Absorbed Fractions of the Average Adult Japanese Male Phantom with Those of the Reference Computational Phantom–Adult Male of ICRP Publication 110, Physics in Medicine and Biology, vol.59, no.5, 2014, p.1255–1270.

4–11 Ensuring the Reliability of Measurements of Exposure of Workers and Public to High-Energy γ-rays — Establishment of the High Energy γ-ray Calibration Field —

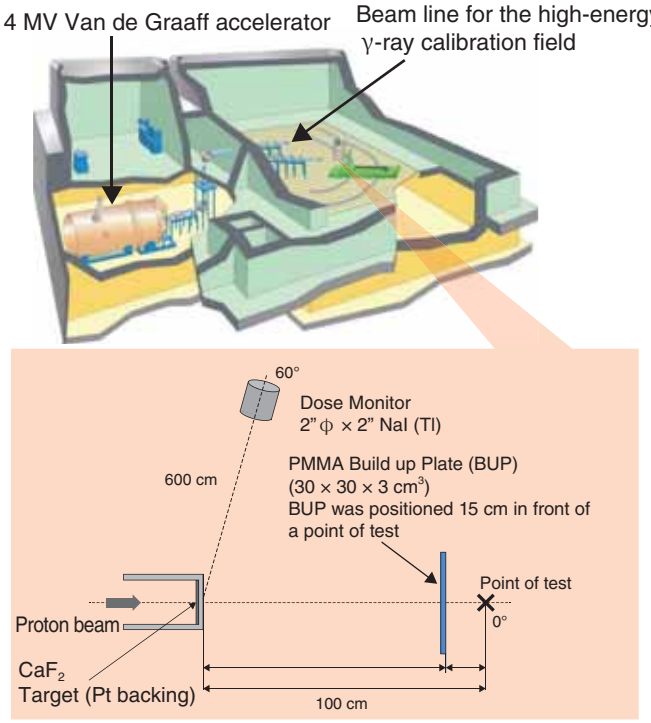

Fig.4-24 Schematic of the high-energy γ-ray calibration field (at Facility of Radiation Standards)

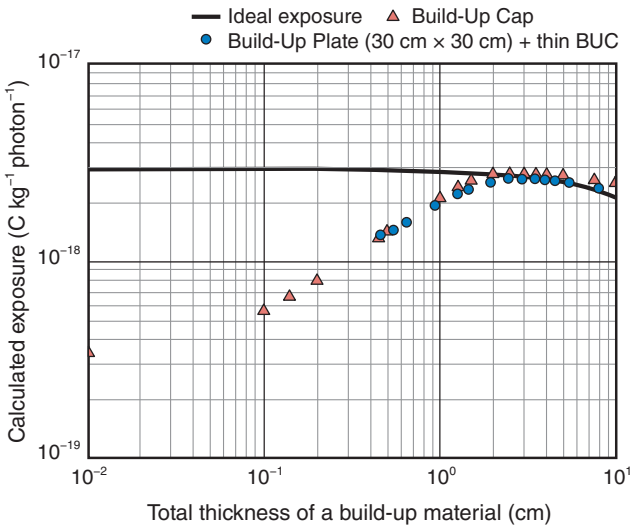

Fig.4-25 Exposures calculated at test point as a function of thickness and shape of build-up materials
Ideal exposures were calculated based on the γ-ray fluence at 100 cm and the mass-energy absorption coefficient for dry air, which reflects the attenuation of γ-ray fluence with increasing thicknesses of build-up materials. The ideal exposure represents the exposure predicted when electrons due to γ-rays fully contribute to charges collected at a point of test as well.

The 6-7 MeV high energy γ-ray calibration field was established at the Facility of Radiation Standards and serves to ensure the reliability of readings for dosimeters used in high-energy γ-ray fields.

The reliability of dosimeter readings is ensured by the so-called "calibration," which donates the periodic checks of whether dosimeter readings are correct. Well-defined radiation fields, called "calibration fields," are required for proper calibration. The FRS has established various types of radiation calibration fields, including X-ray, γ-ray, β-ray and neutrons, which it offers to companies and institutes working in the field of radiation protection.

For exposure to γ-rays, fixed γ-ray calibration fields are only available up to 2 MeV, and dosimeters have been calibrated in these fields. In contrast, the emission of 6 MeV γ-rays resulting from the $^{16}O(n, p)^{16}N$ reaction in the coolant water is widely recognized as a substantial source of radiation exposure, which is particularly relevant for BWRs. Furthermore, for therapeutic and industrial purposes, γ-rays with energies greater than several tenths of MeVs are produced by electron accelerators and high-energy X-ray generators. The calibration field for 6-7 MeV γ-rays should tell us how widely available dosimeters respond to γ-rays with these energies or higher. However, no high-energy γ-ray calibration field is available in Japan for radiation protection. We thus developed a 6-7 MeV γ-ray field produced by the nuclear reaction $^{19}F(p, \alpha\gamma)^{16}O$ using the 4 MV Van de Graaff accelerator at the FRS (Fig.4-24) for calibration purposes.

Because of the high energy of incident γ-rays, introducing an ionization chamber (IC) with a thicker build-up cap is required to precisely determine air kerma rates at a point of test (100 cm). This means that measurement conditions significantly differ from those of routine calibrations. We investigated the method of using a conventional IC coupled with the same build-up plate (BUP) introduced for routine calibrations. Throughout a series of Monte Carlo calculations, as shown in Fig.4-25, we assessed the measurement arrangement for the conventional IC and for the BUP, and found the optimal arrangement to be a BUP made of polymethylmethacrylate with the dimension of 30×30×3 cm^3 and positioned 15 cm in front of a point of test. The method would allow us to properly calibrate the dosimeters that are most widely available.

In addition, introducing a cylindrical 2"ϕ × 2" NaI(Tl) scintillation detector as monitor allows us to quite precisely determine reference air kerma rates at a point of test when irradiating with γ-rays for regular calibrations.

Reference

Kowatari, M. et al., Measurement of Air Kerma Rates for 6- to 7-MeV High-Energy γ-ray Field by Ionisation Chamber and Build-Up Plate, Radiation Protection Dosimetry, vol.162, no.4, 2014, p.446-458.

4–12 Measuring Radiation Intensity in Nuclear Reactors

— Developing γ-ray Detectors for Remote Inspection in Primary Containment Vessel —

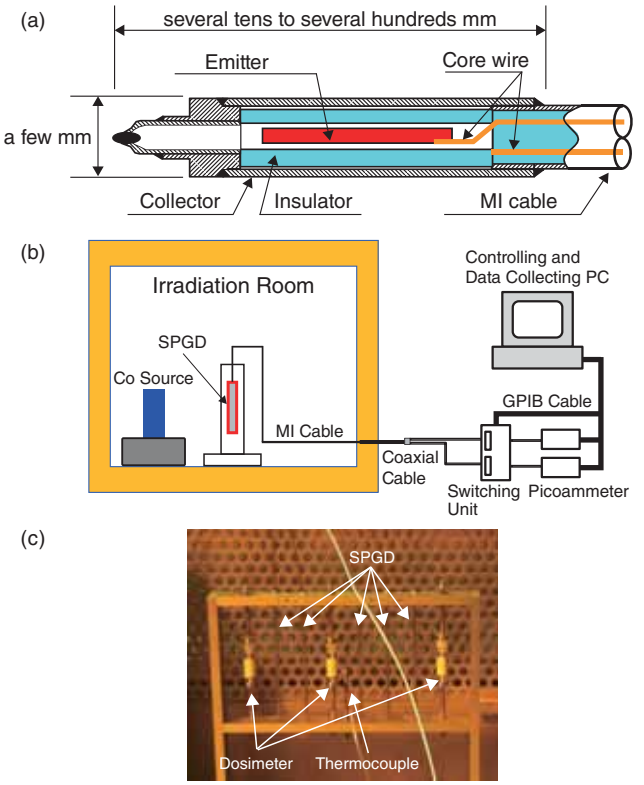

Fig.4-26 Schematic of SPGD and irradiation experiment
(a) SPGD is a γ-ray detector with a diameter of only a few millimeters and comprises an emitter, collector, and insulator. (b) Output currents from SPGDs when irradiated under same conditions that were measured by a switching unit and picoammeter. (c) Irradiation conditions were precisely determined by thermocouple and dosimeters positioned near the SPGDs.

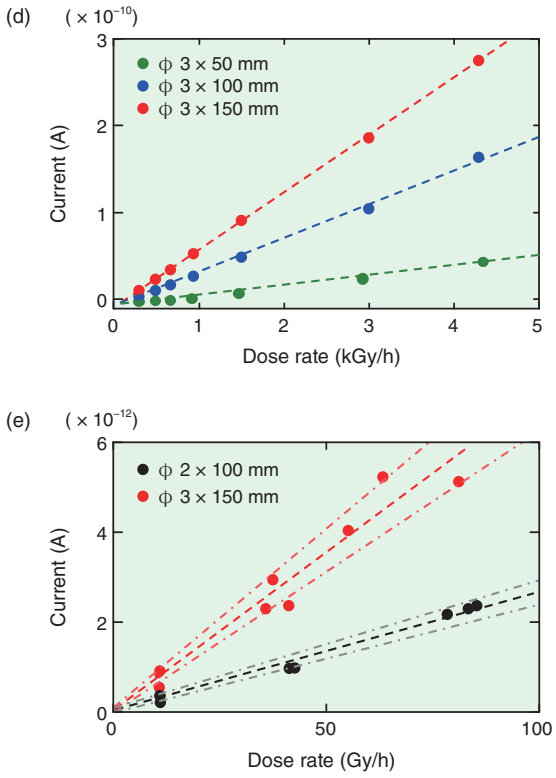

Fig.4-27 Output currents of SPGDs with γ-ray-dose rate
(d) Output currents of SPGDs used in this study were proportional to the dose rates up to and over 4000 Gy/h. (e) Lower-detection limit was about 10 Gy/h.

The fuel debris must be removed to decommission the TEPCO's Fukushima Daiichi NPS (1F). However, the high-radiation environment precludes a visual confirmation of the primary containment vessel (PCV) at 1F.

Therefore, we are developing a method to measure radiation that uses a self-powered gamma detector (SPGD) as a means to obtain the distribution of the debris in PCVs. The SPGD does not require a complex structure and an external electric power source because the output current is obtained from electrons generated by γ-rays impinging on the emitter. This means that the SPGD can be only a few millimeters in diameter and can therefore access intricate piping systems (Fig.4-26).

To determine the applicability of the SPGD be to 1F, we fabricated thin SPGDs with lead (Pb) emitters of various lengths and diameters, and investigated their γ-ray detection limits. The relationship between the γ-ray intensity and the output current was obtained in irradiation rooms where the of γ-ray intensity distribution was known. The results indicate that the length of emitter influences the output current more than the diameter.

Until now, the dose rate in the PCV was considered to be up to tens of gray per hour, with the higher-intensity radiation doubtless occurring closer to the core. In a high-dose-rate environment, the output current was linear in dose rate to over 4000 Gy/h (Fig.4-27(d)). In a low-dose-rate environment, above 10 Gy/h, the average discrepancy with respect to the approximate curve (dashed lines) was estimated to be ~14%, as indicated by dash-dotted lines (Fig.4-27(e)). Thus, the SPGDs used in this study can measure the γ-ray-dose rate with fair accuracy. These results show that the measuring range of the SPGDs corresponds to the intensity of radiation in the PCV of 1F and that the SPGDs may serve as a detector in such an environment.

By leveraging the results of the present study, we plan to further improve the structure of the SPGDs to increase their sensitivity and their ability to interrogate intricate pipe systems.

Reference

Takeuchi, T. et al., Development of a Self-Powered γ Detector, Journal of Nuclear Science and Technology, vol.51, issues 7–8, 2014, p.939–943.

4–13 Technical Development for In-Pile Irradiation-Assisted Stress Corrosion Cracking Test Capsules — Research on Safety Evaluation of Light Water Reactors —

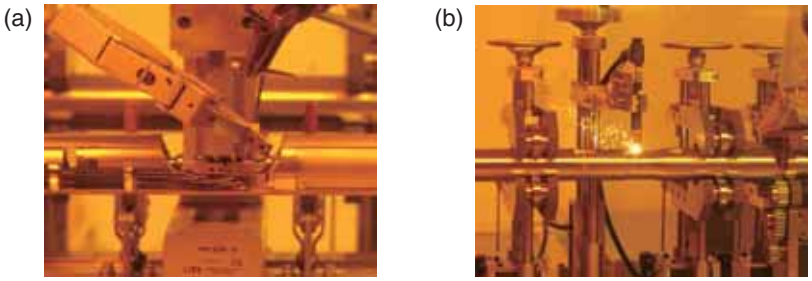

Fig.4-28 Assembling works in hot cell
(a) Pre-irradiated specimens are installed in an in-pile test capsule and (b) welding is conducted in a hot cell by the remote-welding apparatus.

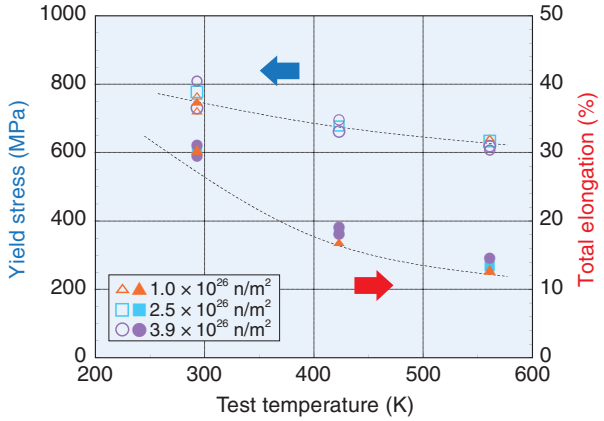

Fig.4-29 Result of tensile test in air
Irradiated specimens are sufficiently ductile at the estimated temperature of the outer tube of the pre-irradiation capsule.

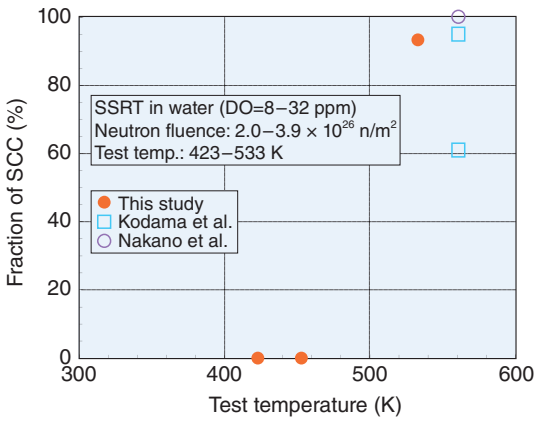

Fig.4-30 SCC fracture rate measured by SSRT
The SCC fracture is not observed in irradiated specimens at the estimated temperature of the outer-tube of the pre-irradiation capsule.

Irradiation-assisted stress corrosion cracking (IASCC) is recognized as one of the key safety issues for managing the core components of light water reactors (LWRs). We plan to do *in situ* crack-propagation experiments to simulate IASCC in the Japan materials testing reactor (JMTR).

To perform these experiments, specimens must be irradiated up to the threshold of IASCC. Next, the specimens are to be relocated to in-pile test capsules and the capsules are to be assembled. Two technical hurdles remain to be solved: one is the development of welding and assembling techniques appropriate for capsules in a hot cell, and the other is the development of methods to evaluate the integrity of pre-irradiation capsules that will be irradiated in the JMTR.

We therefore developed a remote-welding apparatus that can rotate a capsule to perform circumferential welding. We tested the resulting welds many times by varying the parameters of rotation speed and welding current. However, obtaining a suitable weld in a single welding pass proved impossible. Thus, we used two-pass circumferential welding. This method efficiently preheats the first weld, which is then completely by the second weld, making it possible to weld and assemble capsules in the hot cell. Fig.4-28 shows photographs of welding and assembling.

We also evaluated the integrity of the structural material of the capsules. When specimens are irradiated, the structural materials of the pre-irradiation capsule also receive irradiation up to the threshold fluence of IASCC. Thus, we must evaluate the integrity of the heavily irradiated structural materials of the capsules.

Specimens were fabricated from stainless steel irradiated in the JMTR for over 20 years (neutron irradiation at 1.0–3.9 × 10^{26} n/m^2). Tensile tests in air and slow-strain-rate testing (SSRT) in water were performed.

Fig.4-29 shows the result of the tensile tests, and Fig.4-30 shows the SCC fracture rate determined after SSRT.

Under irradiation, the temperature of the outer tube of the capsule is estimated to be 423 K. These results show that the structural material of the capsule is sufficiently ductile and will not undergo SCC fracturing at the operating temperature.

By overcoming these two hurdles, we can perform the in-pile IASCC tests required to investigate life-time management, which is important for evaluating the safety of LWRs.

Reference

Shibata, A. et al., Development of Remote Welding Techniques for In-Pile IASCC Capsules and Evaluation of Material Integrity on Capsules for Long Irradiation Period, Journal of Nuclear Materials, vol.422, issues 1-3, 2012, p.14-19.

4–14 Developing a Real-Time Management System for Workers in Radiation-Controlled Areas
— Worker-Safety Management in Radiation Controlled Areas —

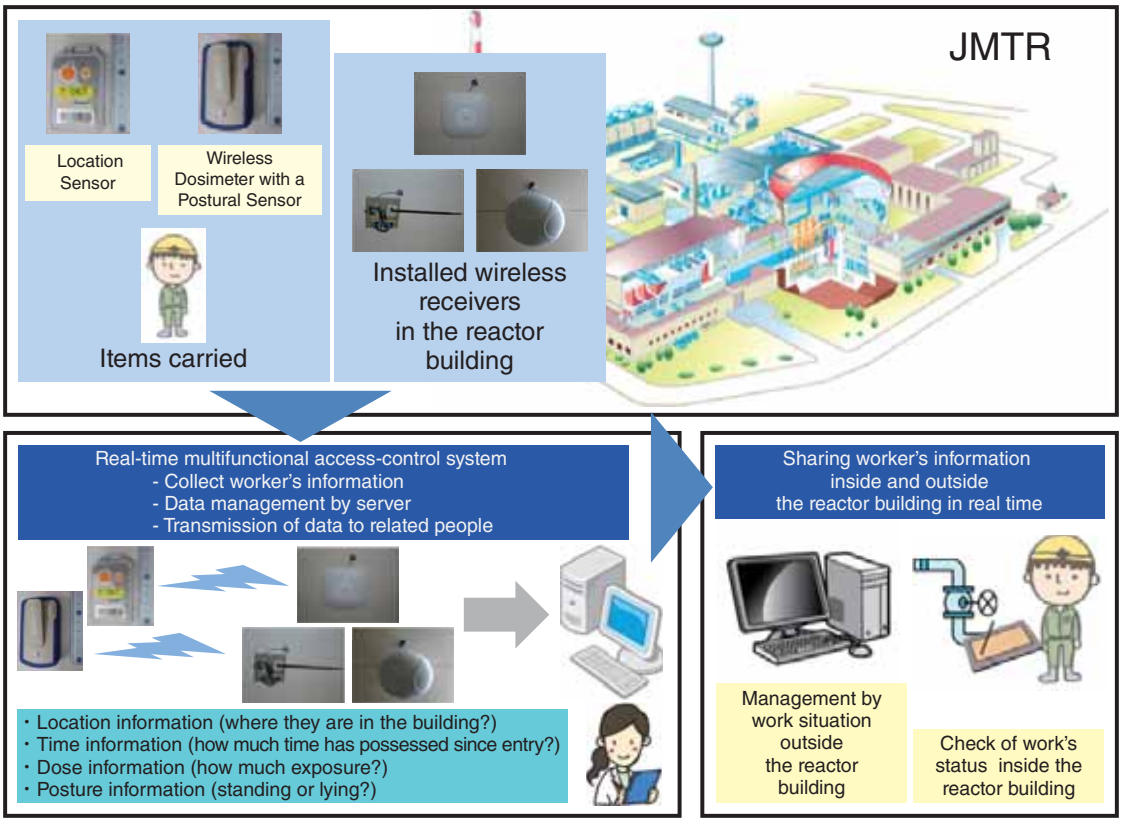

Fig.4-31 Schematic of a real-time multifunctional access-control system
Developed using the patent of Hitachi Aloka Medical, Ltd. and the joint patent of JAEA. Access control and individual dose are managed in real time.

In a radiation-controlled area, such as a reactor building, the safety management of access control and dose for workers, including prevention of radiation hazards, is required. Advances in management techniques are always required, as is the use of the latest technology.

In the Japan Materials Testing Reactor (JMTR), no system, such as an administrator, that was able to manage the access control and individual dose for workers in the reactor building in real time, existed. Therefore, the administrator had the difficult job of managing, and this management system was difficult for the workers in the reactor to understand. Furthermore, information sharing was sometimes insufficient on both sides.

To confront this situation, the JAEA and Hitachi Aloka Medical, Ltd. developed a "real-time multifunctional access-control system" (Fig.4-31), which comprises items that workers carried (location sensors and wireless dosimeters with posture sensors), wireless receivers, and data acquisition servers. Each worker's location, time of entering, dose, and posture can be displayed on a PC or tablet in real time. Information may now be shared between the administrator and workers, between workers, and with people inside and outside the reactor building. The status of workers (where they are in the building, how much time has elapsed since their entry, their exposure, and whether they are standing or lying) is monitored by the PC. The management is improved due to the visibility offered by a graphical display of the worker's dose and location on a map. Furthermore, safety management is facilitated by an alarm that is triggered as a function of dose, posture, and entering time. In particular, combining the wireless dosimeter and posture sensor is useful for safety management because the posture information can quickly save a worker who has an accident, even when he/she is working alone.

Safety management of workers in a radiation area has been improved by the installation of this system, and by the information sharing it promotes between administrators and workers, and with people inside and outside the reactor building. In addition, since this system is wireless and based on notebook PCs, it can contribute to the management of workers' conditions in outdoor decontamination projects, such as the decontamination of the Fukushima area, which does not have sufficient radiation control.

Reference

Hiyama, K. et al., Development of Safety Management System for Works in Radiation Controlled Area (Joint Research), JAEA-Technology 2013-045, 2014, 32p. (in Japanese).

Quantum Beam Science and Technology Researches and Research Sites

— R&D Using Quantum Beam Facilities and Fundamental Technologies —

"Quantum beam" is a generic term for neutron beams, ion beams, electron beams, high-intensity lasers, and synchrotron X-rays, which are generated from accelerators, high-intensity laser facilities, and research reactors. Recently, "quantum beam technology" has been extensively developed, with the most advanced manufacturing and observations being conducted using highly controlled quantum beams.

There are several large quantum beam facilities such as J-PARC, TIARA, J-KAREN, SPring-8 beamlines, and JRR-3 in JAEA. We have generated numerous results from these facilities. In this chapter, we introduce representative research results on "quantum beam" science and technology.

Development of Beam Technologies for Quantum Beam Facilities

Technological Development at J-PARC

J-PARC comprises a series of three proton accelerators —Linac, 3 GeV synchrotron (RCS), and 50 GeV synchrotron— and three experimental facilities. The facilities include the Materials and Life Science Experimental Facility (MLF), which provides neutron and/or muon beams for a wide range of studies, the Hadron Experimental Facility for nuclear and particle physics experiments using particles such as K-mesons, and the Neutrino Experimental Facility for the T2K experiment of particle physics using neutrinos. All these experimental facilities are open to users from across the globe.

In the fiscal year (FY) 2013, there were significant advances at Linac and RCS toward the upgrade of the beam power to 1 MW. Annular-ring coupled structure (ACS) cavities (Fig.5-1), developed in J-PARC, were installed to upgrade the acceleration energy from 181 MeV to 400 MeV at the downstream of Linac. The newly installed ACS section is shown to have the following features. The accelerating beams are very efficient and suppress the transverse accelerating field caused by the axial symmetry of an ACS. At the RCS, by virtue of the newly developed beam tuning techniques, the beam losses can be reduced to an acceptable level not only at the injection point but also in the acceleration section.

Consequently, we successfully delivered a 532 kW beam to the neutron source of MLF, the highest power thus far reported. A test operation with a 1 MW beam was scheduled for October 2014.

Users at MLF conducted experiments at 18 neutron and 2 muon beamlines with a proton beam power of 300 kW over 4 run cycles. The number of submitted proposals was 533, approximately the number submitted in FY 2012. This chapter presents the outcomes from MLF (Topics 5-13, 5-14) and RCS (Topics 5-15, 5-16).

Fig.5-1 Annular-ring coupled structure (ACS) cavities installed at the downstream of Linac

Technological Development at TIARA

The Takasaki Ion Accelerators for Advanced Radiation Application (TIARA) consists of four ion accelerators. Together with an electron accelerator and gamma-ray irradiation facilities, the TIARA accelerators are available to researchers in JAEA and other organizations for R&D activities on new functional and environmentally friendly materials, biotechnology, the radiation effects of materials, and quantum beam analysis. Practical technological developments currently in progress involve microbeam formation, single ion hits, techniques for large-area uniform irradiation, efficient beam transmission and acceleration (Topic 5-17) at the cyclotron, three-dimensional in-air PIXE analysis, and a three-dimensional microfabrication technique at the electrostatic accelerators.

In FY 2013, a technique for controlling the irradiation field shape of the large-area uniform irradiation of a several-hundred-MeV heavy ion beam was developed using a multi-pole magnetic field. The beam intensity distribution is made uniform by a pair of octupole magnets, and the shape of the uniform irradiation field is controlled by quadrupole magnets (Fig.5-2). According to both beam optical calculations and experimental results, the two quadrupole magnets closest to the irradiation chamber are most effective for shape control. A quantitative method for estimating the shape and uniformity of the field was also established using a radiochromic film. Irradiation fields of various sizes and aspect ratios, such as rectangles and ribbons, were formed using these techniques.

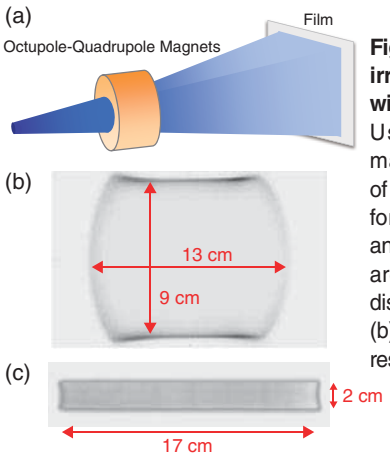

Fig.5-2 Large-area uniform irradiation field measured with a radiochromic film
Using (a) the multi-pole magnet system, Ar beams of 520 MeV and 385 MeV are formed into (b) a rectangle and (c) a ribbon. The shaded areas show beam intensity distribution. The uniformity of (b) and (c) is ±7% and 10%, respectively.

Kansai Photon Science Institute

In the Kizu District, we eagerly engage in R&D activities concerning lasers. For instance, we develop high quality lasers and study the use of electron beams, ion beams, and X-rays generated by high-intensity short-pulse lasers. Currently, we are improving the quality of our high-intensity short-pulse lasers (Fig.5-3). Since FY 2013, we have been installing high repetition rate pump lasers and renewing the pulse compression gratings to achieve a more frequent and higher power beam supply.

In the Harima District, we have been developing and improving a state-of-the-art analysis technique for expressing the functional and reaction mechanisms of materials. For this purpose, we employ four JAEA synchrotron radiation beamlines at SPring-8. These beamlines are also applied to nanotechnology, energy, and environmental studies; for example, a decontamination technique for revitalization at Fukushima.

Furthermore, external researchers are now being supported under the Nanotechnology Platform Project entrusted to us by MEXT. This project was granted a supplementary budget for FY 2012, which was invested in new equipment for nitride semiconductor film formation, and renewing the kappa-type X-ray diffractometer of two JAEA beamlines in FY 2013.

Fig.5-3 JAEA Kansai Advanced Relativistic ENgineering (J-KAREN) laser system

Advanced R&D on Quantum Beam Science and Technology

JAEA's large quantum beam facilities have been employed in diverse science and technology fields, mainly for sustainable living and green innovations (Fig.5-4).

By controlling the beam parameters, quantum beams can be used to probe atomic- or molecular-level information. Quantum beams can further investigate materials at nanometer scales (i.e., at the atomic or molecular level), because they interact with the material's constituent atoms to change their configuration, composition, and electronic state. In medical applications, these beams are used for radiotherapy, which focuses a beam onto cancer cells (Fig.5-5).

We have been developing new beam sources and enhancing the beam intensities. These improvements will assist the clarification of unknown phenomena and extend the applicability of quantum beams. Additionally, quantum beam "probes" have yielded good results in materials science, environment and energy, medicine, and biotechnology, which are related to life sustainability and green innovations.

In this chapter, we introduce our recent research (Topics 5-1, 5-2, 5-3, 5-4, 5-5, 5-6, 5-7, 5-8, 5-9, 5-10, 5-11, and 5-12) on advanced beam technology and the application of quantum beams to the above mentioned fields.

We are also contributing to the recovery from the accident at the Tokyo Electric Power Company, Incorporated Fukushima Daiichi Nuclear Power Station. For example, we have been developing improved decontamination materials (Chapter 1, Topic 1-12).

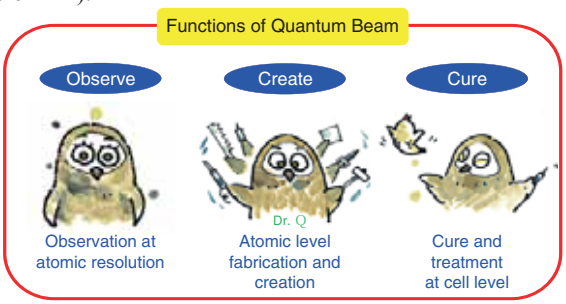

Fig.5-5 Characteristics of quantum beams

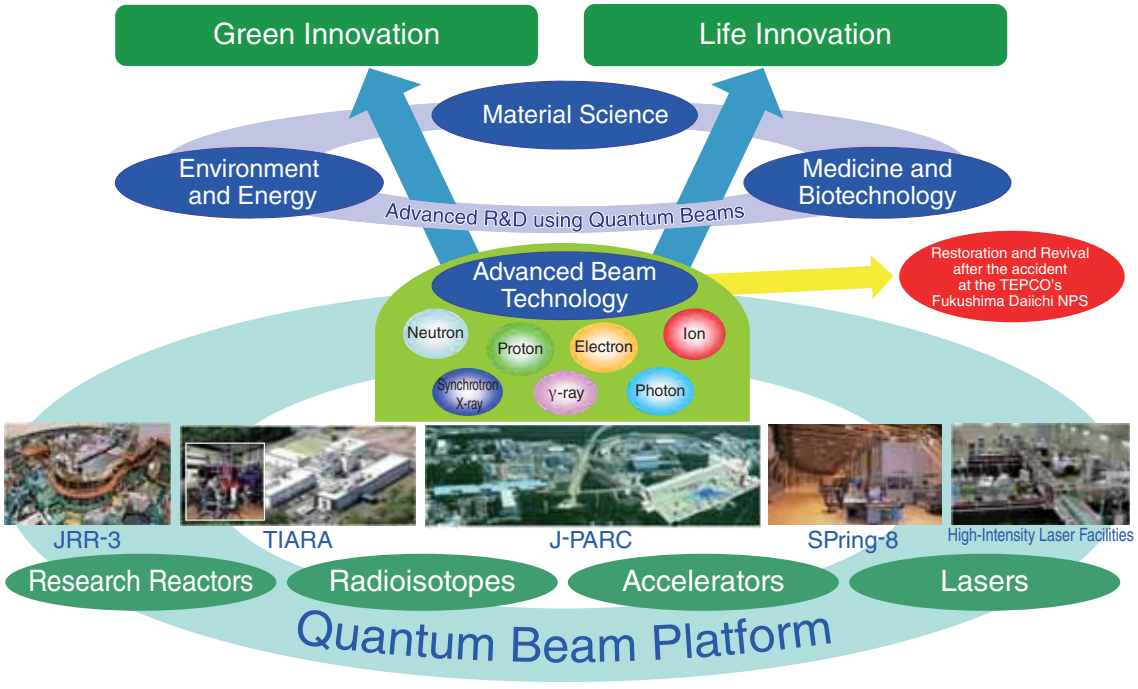

Fig.5-4 Quantum beam facilities and research system for quantum beam science and technology in JAEA

5–1 Biocompatible Plastic Fabrication by Ion Beam

— Development of Micro/nanofabrication and Surface Modification Technique Using Focused Ion Beam for Medical Applications —

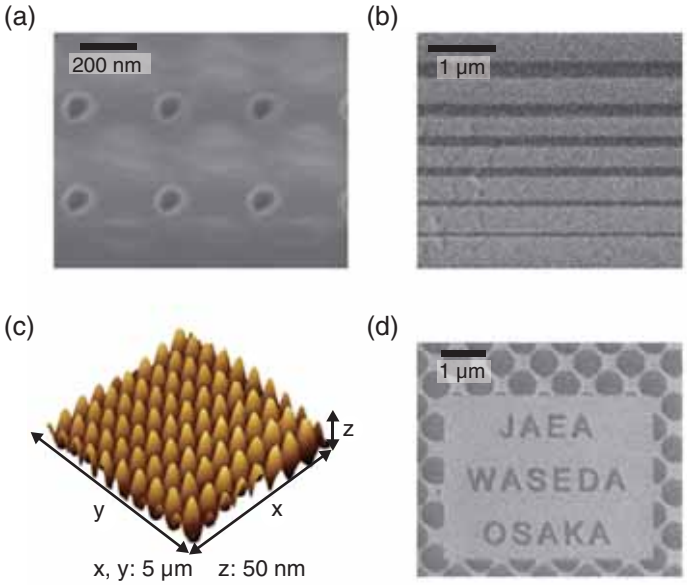

Fig.5-6 Microfabricated poly (L-lactic acid) using focused ion beam
Poly (L-lactic acid) was precisely fabricated by a 30 kV Ga focused ion beam; (a) 80-nm-diameter holes, (b) 60-240-nm-wide grooves, (c) micro concave-convex structure, (d) 100-nm-wide alphabets.

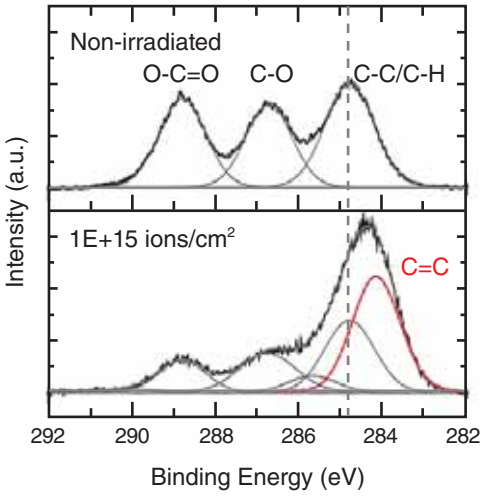

Fig.5-7 Chemical bonds on the fabricated bottom of poly (L-lactic acid) measured by X-ray photoelectron spectroscopy
Under irradiation by a focused ion beam, the peaks attributed to the C-O bond and to the C-C and C-H bonds at 284.8 eV decreased, while that attributed to the C=C bond at 284.1 eV increased.

Micro/nanofabrication techniques for fabricating biocompatible materials are essential for the development of devices used in advanced medical treatment and biological research. Biocompatible materials have low heat and chemical stabilities; therefore, they cannot be precisely fabricated by any standard method. Here we developed a new technique for the micro/nanofabrication of biocompatible plastic, which exhibits locally high cell adhesion, using a focused ion beam (FIB).

As the target material, we selected poly (L-lactic acid) (PLLA), a highly biocompatible and biodegradable polymer. PLLA is typically used in medical applications such as implants and sutures that are degraded and absorbed by the body after healing. The irradiation effect on the surface modification of PLLA was investigated using 30 kV Ga FIB. The heat induced by FIB irradiation enhanced the diffusion and desorption of the decomposed PLLA fragments. On the other hand, fabrication accuracy was reduced by the thermal deformation of the heat-unstable PLLA. To increase fabrication precision, we reduced the thermal deformation by optimizing the sample preparation and irradiation conditions, such as the dose, dose rate, PLLA thickness, and beam diameter. Micrographs of successfully fabricated microstructures, such as fine holes, grooves, and alphabets, are presented in Fig.5-6.

Fig.5-7 shows the X-ray photoelectron spectra of the C1s in PLLA before and after irradiation. It appears that the PLLA surface was directly carbonized and became C=C-bond rich. Because decomposed fragments such as H_2, CO_2, and CH_4 were physically sputtered and desorbed to/from the PLLA surface, the surface gradually became similar to a diamond-like carbon (DLC). The number of C=C bonds is known to strongly affect cellular adhesion to DLC surfaces. Thus, the surface modification technique can be used to control cellular adhesion onto PLLA.

This micro/nanofabrication technique was achieved by merging fine processing and material modification techniques. It is potentially applicable to the manufacture of biocompatible devices, such as micromachines and lab-on-a-chip, used in tissue engineering and bio-research to enhance the longevity and well-being of society.

The present study was accomplished in collaboration with Osaka University and Waseda University.

Reference

Oyama, T. G., Nagasawa, N. et al., Micro/Nanofabrication of Poly(L-lactic acid) using Focused Ion Beam Direct Etching, Applied Physics Letters, vol.103, issue 16, 2013, p.163105-1-163105-4.

5–2 Application of Composite-Type Optical Fiber Technique for Medical Instrument Development — Industrialization of Composite-Type Optical Fiber Technique and Startup of JAEA-Supported Venture Business —

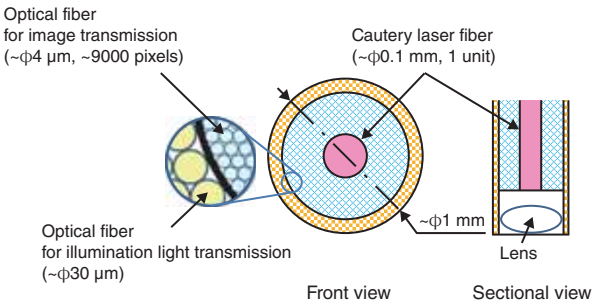

Fig.5-8 Schematic of the composite-type optical fiberscope system
This configuration enables the fabrication of a composite-type optical fiberscope suited to each medical field.

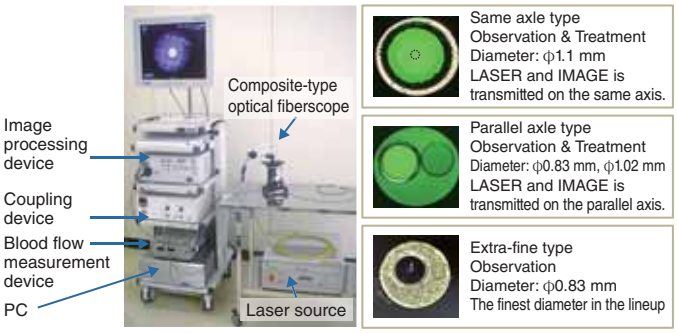

Fig.5-9 Minimally invasive laser treatment system and the tips of various fiberscopes
This system enables various tests and laser surgeries.

The PDT device for a peripheral lung-cancer treatment (unapproved medical device)

Fig.5-10 Example of industrial development of the device
This basic system was developed by the JAEA-authorized venture business for the treatment of peripheral lung cancer. Four medical institutions are promoting a clinical study of the new treatment.

Minimally invasive treatments have been promoted by recent advances in medical engineering. Such treatments may reduce the burden of care and abridge hospitalization time, enhancing patients' quality of life. The composite-type optical fiber can transmit an image and a laser beam in parallel. With this technology, a specific tool has been developed that allows remote manipulation of the thermo-nuclear experimental reactor and the large-sized nuclear installation at JAEA. Because the developed technique is applicable to various regions in the body, it may greatly benefit the burgeoning minimally invasive surgery market. We are applying this technique to the development of various medical instruments.

Fig.5-8 shows the configuration of the composite-type optical fiberscope (same axle type). The center core and surrounding optical fibers transmit the laser beam and the image, respectively. The left panel of Fig.5-9 is a photograph of the minimally invasive laser treatment system. The right panels show the tip of the fiberscope adapted to various tests and treatments. Currently, we are trialing this system on lung cancer therapy.

Although central lung cancer can be treated by photodynamic therapy (PDT) at the transbronchial site, PDT is unsuitable for early peripheral lung cancer because existing endoscopes cannot reach the peripheral lung field. On the other hand, a composite-type optical fiberscope with an outside diameter of 1 mm can be inserted into the peripheral lung field, allowing detailed observation and precise irradiation of peripheral lung cancer. The developed fiberscope is also expected to provide a new PDT laser surgery device. Toward these goals, we have patented the composite-type optical fiberscope, and accumulated knowledge of the instrumental assembly. Furthermore, we have networked with related organizations and several medical scientific societies. The composite-type optical fiber technique has been evaluated as compatible with medical needs and eminently suited to a new business enterprise.

Therefore, it was adopted in the FY 2012 "Program for Creating STart-ups from Advanced Research and Technology" (START Program), which competes for government grants from Ministry of Education, Culture, Sports, Science and Technology (MEXT).

These efforts resulted in the successful launch of the new venture business "OK Fiber Technology Co., Ltd." of JAEA in September, 2013. The business aims to distribute the device based on the composite-type optical fiber technique across the globe. In this venture, the PDT device for peripheral lung cancer treatment is being continuously developed (Fig.5-10).

The present study was partly supported by the Program for Creating STart-ups from Advanced Research and Technology (START Program) "The industry and medical tool development project based on the composite-type optical fiber" of the Ministry of Education, Culture, Sports, Science and Technology of Japan (MEXT).

Reference

Oka, K. et al., Medical Application of Composite-Type Optical Fiberscope, Oyo Butsuri, vol.80, no.12, 2011, p.1069-1072 (in Japanese).

5–3 Doping Effect of Ferroelectrics

— Improvement of Ferromagnetic Mechanism of Bismuth Ferrite —

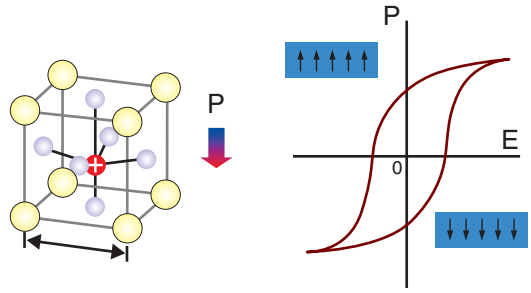

Fig.5-11 Hysteresis loop of ferroelectric material
An electric field applied to a ferroelectric material redistributes the electric charge in the material. This phenomenon is called polarization. The direction of polarization in a crystal is visualized by the D-E hysteresis loop.

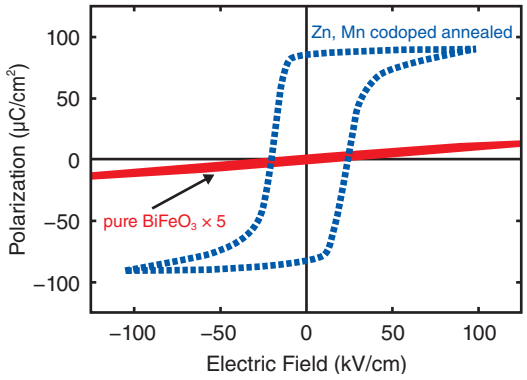

Fig.5-12 D-E hysteresis loop of bismuth ferrite
Although bismuth ferrite is slightly affected by an external electric field, its ferroelectric properties are dramatically improved by doping with small amounts of Zn and Mn, and a hysteresis loop develops.

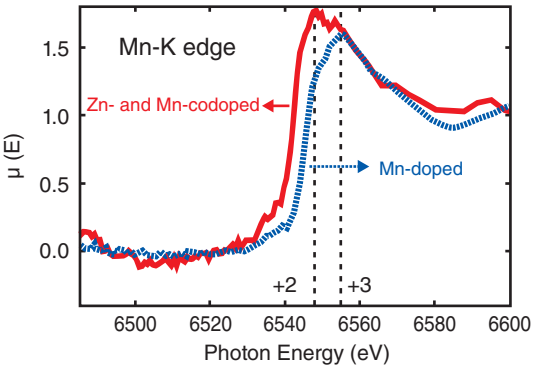

Fig.5-13 XAFS spectra of doped Mn
The valence of Mn differs between samples doped with both Zn and Mn, and those doped with Mn only.

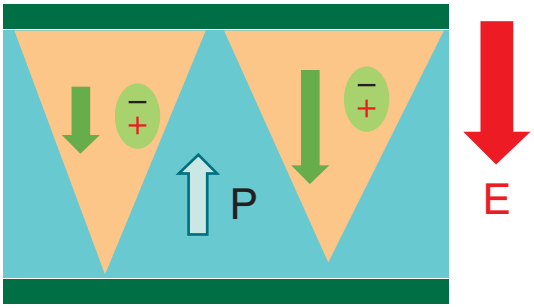

Fig.5-14 Defect-induced polarization reversal
Since the valence and local structure of the host phase differs from that of the dopants, the doped Zn and Mn generate defect-induced polarization, which nucleates domain reversal. Consequently, the ferroelectricity of bismuth ferrite improves and the hysteresis loop opens.

When a ferroelectric thin film is implanted with a small number of ions from the ion beam irradiation equipment, its ferroelectric property is often improved. However, as few ions can become embedded in a thin film, a detailed structural analysis is precluded, and the mechanism by which the ions improve the ferromagnetic properties cannot be clarified. However, ion implantation into bulk medium induces the same effect, allowing investigation of the doping effect.

Although bismuth ferrite ($BiFeO_3$) exhibits small polarization, its ferroelectric property is dramatically improved by codoping with small quantities of zinc (Zn) and manganese (Mn). Figs.5-11 and 5-12 illustrate the polarization principle and the D-E hysteresis loop of $BiFeO_3$, respectively. The coercive electric field of $BiFeO_3$ is very large and spontaneous polarization is rare. However, spontaneous polarization is incited by codoping with Zn and Mn.

Here we investigated ferromagnetic improvement in $BiFeO_3$ codoped with small quantities of Mn and Zn codoping. As the valence of Zn is stable, the investigation relies on the fluctuating valence of Mn. Moreover, local structure analysis is more suitable than conventional crystal structure analysis because the surrounding doped ions break the translational symmetry of the $BiFeO_3$ structure. The X-ray absorption fine structure (XAFS) was then measured using beamline BL14B1 in SPring-8, which is dedicated to JAEA.

Fig.5-13 shows the results of the XAFS measurements. The Mn valence state in codoped $BiFeO_3$ (+2) differs from that in Mn-doped $BiFeO_3$. Because hetero-valence ion doping alters the structure of the bismuth sites, it induces polarization defects. These defects initiate domain reversal in the presence of an electric field. The polarization reversal induced by the defect, which improves the ferroelectric property of the codoped $BiFeO_3$, is shown in Fig.5-14.

The present study was partly sponsored by the Ministry of Education, Culture, Sports, Science and Technology of Japan (MEXT) KAKENHI Grant-in-Aid for Scientific Research (C) (No.21560877).

Reference

Yoneda, Y. et al., Electronic and Local Structures of Mn–Doped $BiFeO_3$ Crystals, Physical Review B, vol.86, no.18, 2012, p.184112–1–184112–11.

5–4 Distinction between Polarizations Induced by Magnetic Cycloids and Exchange Striction
— Importance of Magnetic Cycloids for Multiferroic Materials —

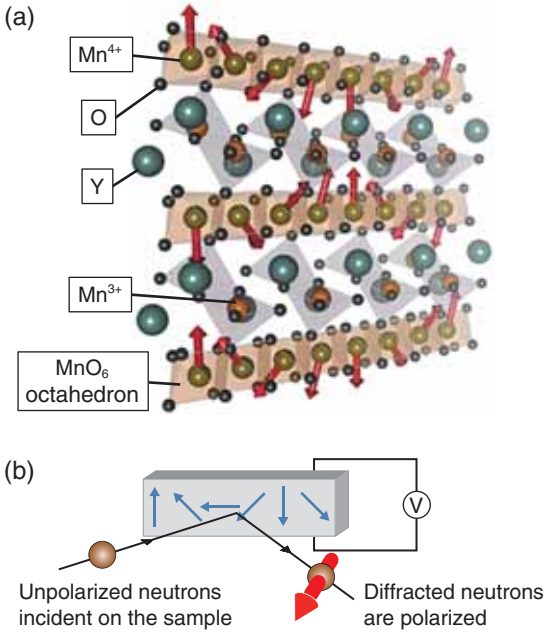

Fig.5-15 Cycloidal structure of YMn_2O_5 and experimental set-up
(a) Mn^{4+} spins (➡) form a cycloidal structure.
(b) The cycloidal structure (⟶) aligns the diffracted neutron spins.

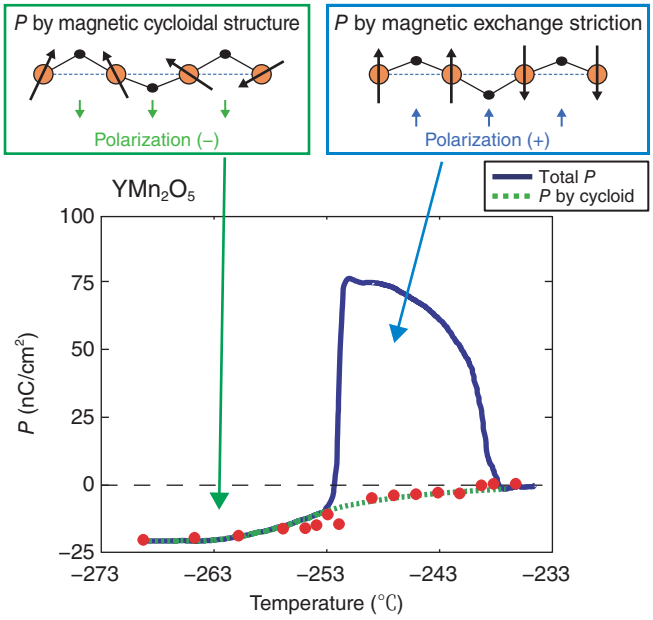

Fig.5-16 Polarization (*P*) in YMn_2O_5
At temperatures between –238 °C and –253 °C, magnetic exchange striction induces positive *P*, whereas, at temperatures below –253 °C, cycloidal structures induce negative *P*. Data points indicate *P* induced by cycloidal structures estimated from polarized neutron diffraction.

We successfully distinguished the electric polarization induced by magnetic chiral structures and magnetic exchange striction in multiferroic compounds by simultaneously measuring the spontaneous polarization and polarized neutron diffraction.

The magnetoelectric (ME) effects of multiferroic compounds arise from coupling between magnetism and ferroelectricity. This characteristic of multiferroic compounds is expected to be exploited in future devices. Below 240 °C, RMn_2O_5 compounds (where *R* denotes the rare-earth element Bi or Y) establish ferroelectricity and magnetic order as their Mn^{4+} spins spontaneously form cycloidal arrangements (Fig.5-15(a)). Below −250 °C, this system displays a rich variety of ME effects depending on the *R* atoms. The origin of the ME effect in this compound has been explained by two models, one driven by the cycloidal structure and the other by magnetic exchange striction. However, the correct model has yet to be clarified.

We found that both models can be distinguished by the character of polarized neutrons which can detect cycloidal structures. To this end, we performed polarized neutron diffraction measurements on a single YMn_2O_5 crystal. The electric polarization was controlled by electric fields provided by electrodes attached to the crystal surface. Fig.5-15(b) shows a schematic of the experiment. By simultaneously measuring the chirality of the cycloidal structure and the electric polarization in the presence of an electric field at different temperatures, we found that exchange striction occurs below −238 °C (as evidenced by the positive polarization in Fig.5-16), whereas a magnetic cycloidal structure develops below −253 °C (giving rise to negative polarization). Given the rich ME effects below −253 °C, we infer that polarization induced by cycloidal structures is an important property of multiferroic materials, and can be exploited in future applications.

The present study was accomplished in collaboration with Tohoku University and is summarized in the Reference.

Reference

Wakimoto, S. et al., Role of Magnetic Chirality in Polarization Flip upon a Commensurate–Incommensurate Magnetic Phase Transition in YMn_2O_5, Physical Review B, vol.88, issue 14, 2013, p.140403-1-140403-5.

5–5 Development of an Aluminum-Based Hydrogen Storage Alloy

— To Realize Light-Weight Hydrogen Storage Alloys —

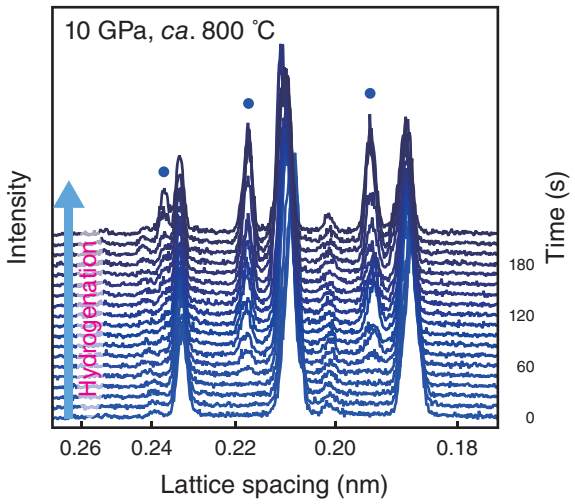

Fig.5-17 *In situ* synchrotron radiation X-ray diffraction profiles of hydrogenated Al_2Cu
Closed circles (●) indicate the Bragg peaks from Al_2CuH. The hydrogenation reaction began 60 s after incubation of the sample at *ca*. 800 °C.

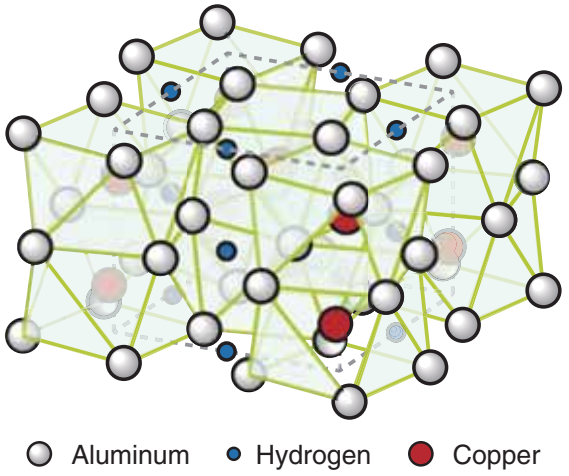

Fig.5-18 Crystal structure of Al_2CuH
The interstitial nature of the synthesized aluminum-based hydride, Al_2CuH, was confirmed both experimentally and by theoretical calculations.

Developing safe and efficient hydrogen storage is among the primary technological challenges to realizing a hydrogen-based economy. Lightweight hydrogen storage materials are required for automotive applications. Aluminum is a suitable material because it is lightweight, harmless, and abundant in nature. However, although complex aluminum hydrides have been extensively investigated, they have not been considered for hydrogen storage applications. Apart from complex aluminum hydrides, few aluminum-based interstitial hydrides have been synthesized to date, although interstitial hydride —referred to as a "hydrogen-storage alloy"—exhibits excellent hydrogen reversibility.

We synthesized an aluminum-based interstitial hydride by hydrogenating a powdered aluminum–copper alloy (Al_2Cu) at high pressure and temperature. Under these conditions, hydrogen becomes extremely reactive. High-pressure and high-temperature conditions were generated by a cubic-type multi-anvil apparatus. The hydrogenation conditions were explored by an *in situ* synchrotron radiation X-ray diffraction measurement system installed on the BL14B1 at SPring-8.

Fig.5-17 shows the X-ray diffraction profiles of Al_2Cu hydrogenated at 10 GPa. After 60 s incubation at *ca*. 800 °C, new Bragg peaks (●) began to appear in the profile. The appearance of the peaks indicated that Al_2Cu was hydrogenated to Al_2CuH. The formed hydride was recovered at ambient conditions, and its crystal structure was characterized by a powder X-ray diffractometer. The obtained crystal structure of Al_2CuH (Fig.5-18) is consistent with the formation of an aluminum-based interstitial hydride. This structure is further supported by first-principles calculations.

We conclude that an aluminum-based interstitial hydride, Al_2CuH, was successfully synthesized. The experimental and theoretical results of this study will assist the exploration of other aluminum-based interstitial hydrides, and the development of practical lightweight hydrogen storage materials.

The present study was partly sponsored by New Energy and Industrial Technology Development Organization (NEDO), and by Japan Society for the Promotion of Science (JSPS) KAKENHI Grant-in-Aid for Scientific Research (Nos. 25220911, 25420725).

Reference

Saitoh, H. et al., Synthesis and Formation Process of Al_2CuH_x: A New Class of Interstitial Aluminum–Based Alloy Hydride, APL Materials, vol.1, no.3, 2013, p.032113–1–032113–7.

5–6 Synchrotron Radiation Mössbauer Absorption Spectroscopy Improved by Electron Detection

— Highly Efficient Mössbauer Spectroscopy of Many Periodic Table Elements Is Now Achievable —

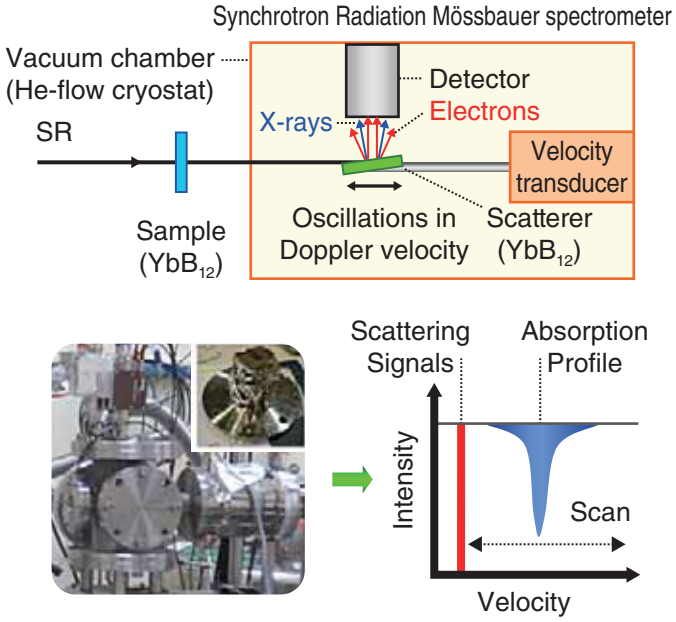

Fig.5-19 Schematic of the SRMS spectrometer (upper panel), an outside view of the APD detector placed in a vacuum chamber (lower left panel), and scheme of the energy scan process for obtaining the Mössbauer spectrum (lower right panel)

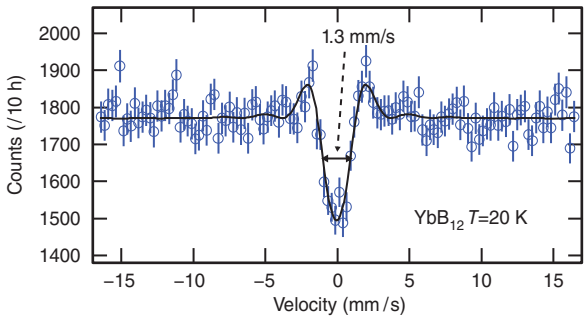

Fig.5-20 ^{174}Yb Mössbauer spectrum
The transmitter is YbB_{12} at 20 K, and the scatterer is YbB_{12} at 26 K.

H																	He
Li	Be	Unsuitable										B	C	N	O	F	Ne
Na	Mg	Mössbauer-active probe										Al	Si	P	S	Cl	Ar
K	Ca	Sc	Ti	V	Cr	Mn	Fe	Co	Ni	Cu	Zn	Ga	Ge	As	Se	Br	Kr
Rb	Sr	Y	Zr	Nb	Mo	Tc	Ru	Rh	Pd	Ag	Cd	In	Sn	Sb	Te	I	Xe
Cs	Ba	*	Hf	Ta	W	Re	Os	Ir	Pt	Au	Hg	Tl	Pb	Bi	Po	At	Rn
Fr	Ra	**	104~														
*Lanthanide		La	Ca	Pr	Nd	Pm	Sm	Eu	Gd	Tb	Dy	Ho	Er	Tm	Yb	Lu	
**Actinide		Ac	Th	Pa	U	Np	Pu	Am	Cm	Bk	Cf	Es	Fm	Md	No	Lr	

Fig.5-21 Elements highlighted in light blue are suitable for Mössbauer spectroscopy

Synchrotron radiation Mössbauer spectroscopy (SRMS) is a powerful tool used in diverse research areas. SRMS provides information on magnetism, valences, crystal fields, and electron densities by exploiting the hyperfine interactions between the nucleus and its surrounding electrons. So far, the spectrum has been measured by detecting the fluorescent X-rays and γ-rays released after nuclear resonant absorption while largely disregarding the concurrent internal conversion electrons (ICEs). To effectively utilize the ICEs, we developed an advanced SRMS spectrometer that detects the ICEs along with the X-rays and γ-rays. The device is constructed from a windowless avalanche photodiode detector and a vacuum chamber with a helium (He) gas-flow cryostat (Fig.5-19). In this system, the synchrotron radiation (SR) X-rays transmitted through the target sample (transmitter) are resonantly scattered by the reference sample (scatterer). The resulting spectrum is acquired by counting the delayed scattering signals from the resonantly excited nuclei in the scatterer, and plotting them as a function of the Doppler velocity.

As a feasibility study, we measured the Mössbauer spectrum of the 76.5 keV excited state of ^{174}Yb, which exhibits a short lifetime (τ = 2.58 ns). The experiment was conducted at the undulator beamlines BL11XU and BL09XU of SPring-8. YbB_{12} powder samples were used as both transmitter and scatterer. The counting rate (measurement efficiency) of the constructed device was up to 500% higher than that of the previous detection system, and the spectrum was obtained within 10 h. A clear absorption profile is shown in Fig.5-20. The line width is approximately 1.3 mm/s, sufficient to determine the ^{174}Yb-hyperfine parameters.

In summary, a novel system for acquiring SRMS was successfully developed at SPring-8. The improved measurement efficiency enabled the first observation of the ^{174}Yb SR-Mössbauer spectrum at 76.5 keV. Clearly, the developed device will enable SRMS studies of many other Mössbauer-active nuclides (Fig.5-21). Moreover, a high-brilliance SR source offers new research possibilities in transmission and scattering Mössbauer experiments. We believe that SR-based Mössbauer spectroscopy has entered a new stage in both fundamental and practical studies.

The present study was partly supported by Japan Society for the Promotion of Science (JSPS) KAKENHI Grant-in-Aid for Scientific Research (S) (No.24221005) and a Grant-in-Aid for Research Activity Start-up (No.24810014).

Reference

Masuda, R., Mitsui, T. et al., Synchrotron Radiation–Based Mössbauer Spectra of ^{174}Yb Measured with Internal Conversion Electrons, Applied Physics Letters, vol.104, no.8, 2014, p.082411–1–082411–5.

5–7 Toward the Development of Protein Absorbents for Rare and Harmful Metals

— Structural Characteristics of Halophilic Proteins Clarified by a Quantum Beam —

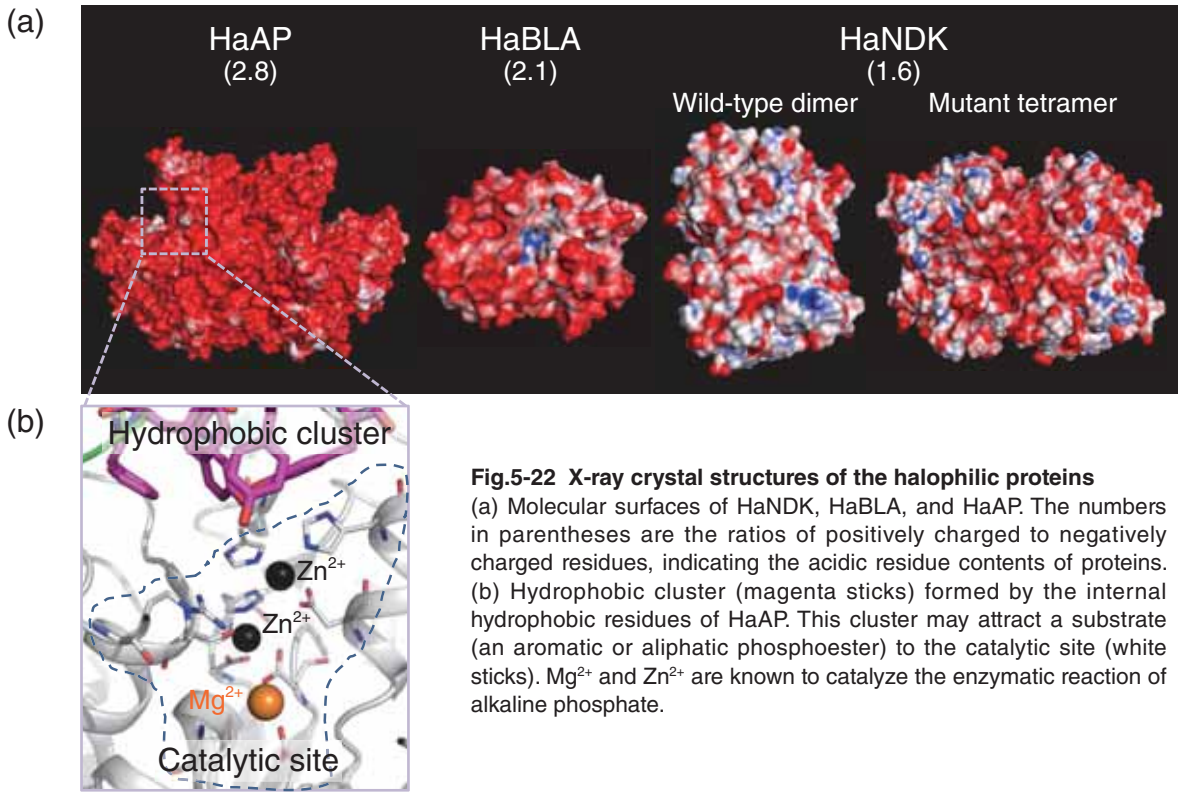

Fig.5-22 X-ray crystal structures of the halophilic proteins
(a) Molecular surfaces of HaNDK, HaBLA, and HaAP. The numbers in parentheses are the ratios of positively charged to negatively charged residues, indicating the acidic residue contents of proteins. (b) Hydrophobic cluster (magenta sticks) formed by the internal hydrophobic residues of HaAP. This cluster may attract a substrate (an aromatic or aliphatic phosphoester) to the catalytic site (white sticks). Mg^{2+} and Zn^{2+} are known to catalyze the enzymatic reaction of alkaline phosphate.

Halophilic bacteria living in salt-rich environments such as salt lakes, halite, and salted foods produce special proteins called "halophilic proteins." The surfaces of these proteins exhibit abundant quantities of acidic amino acids; consequently, they become negatively charged. We have exploited this property to develop protein absorbents of rare and harmful metals. As the molecular design of such absorbents requires knowledge of the protein's tertiary structure, we conducted X-ray crystallographic analysis of several halophilic proteins; namely, nucleoside diphosphate kinase (HaNDK), β-lactamase (HaBLA), and alkaline phosphatase (HaAP) (Fig.5-22(a)). Here we describe the structural study of HaAP, which possesses the highest number of acidic residues among the three candidate proteins.

A detailed structure of HaAP (Fig.5-22(a)) was acquired using the X-ray beams at SPring-8 and the Photon Factory. The negative charge density at the molecular surface of HaAP (0.0028 e/A^2) is strikingly higher than those of alkaline phosphatases from other halophiles and a non-halophilic *Escherichia coli* strain (0.0004–0.0019 e/A^2), whose X-ray structures are known. This property suggests that HaAP can interact with various metal ions, including rare and harmful metal ions.

Next, we clarified the relationship between the structure and enzymatic function of HaAP. Halophilic proteins usually lose their enzymatic activity at low salt concentrations, as their tertiary structures are destabilized by electrostatic repulsion between the side chains of the acidic residues. However, HaAP is exceptional because it maintains enzyme activity over a wide salt concentration range (1–4 mol/ℓ NaCl). Our structural study revealed more internal hydrophobic residues in HaAP than in alkaline phosphatases from other halophiles and non-halophilic *E. coli* (24–27). These abundant internal hydrophobic residues may help to stabilize the HaAP, thereby preserving its enzymatic activity at low salt concentrations (Fig.5-22(b)). Therefore, protein absorbents modeled on the HaAP structure might be functional in a wide range of saline environments, from freshwater regions to salt lakes.

Moreover, using the designed protein absorbents, rare and harmful metals can be collected by unique methods. For example, if the protein absorbents are expressed in specific parts of plants, such as their seeds, we can envision an efficient, cost-economical means of sequestering rare and harmful metals from different environments.

The present study was accomplished in collaboration with Kagoshima University.

Reference

Arai, S. et al., Structural Characteristics of Alkaline Phosphatase from the Moderately Halophilic Bacterium *Halomonas* sp. 593, Acta Crystallographica Section D, vol.70, no.3, 2014, p.811–820.

5–8 Observation of Living Cells under a Soft X-ray Microscope

— Laser Plasma Soft X-ray Microscope with a Combination of Intense Laser Plasma Soft X-ray Source and Contact Microscopy —

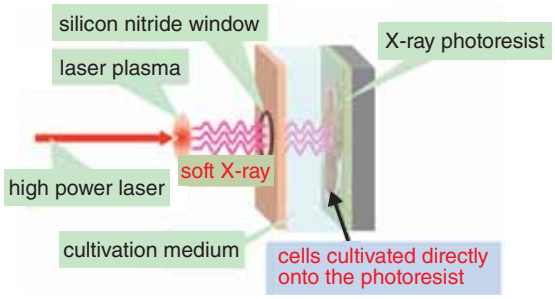

Fig.5-23 Conceptual design of the laser plasma soft X-ray microscope
Soft X-rays generated from the laser plasma were irradiated onto cells directly cultivated on an X-ray photoresist, and the soft X-ray images of the cells were recorded on the photoresist.

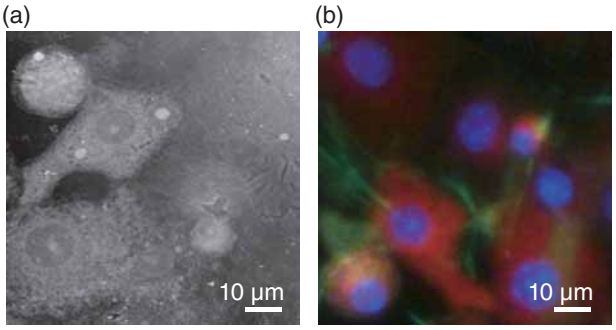

Fig.5-24 (a) Soft X-ray image and (b) fluorescent image of living cells
The red, blue, and green regions in the fluorescent image are the mitochondria, nuclei, and cytoskeleton, respectively.

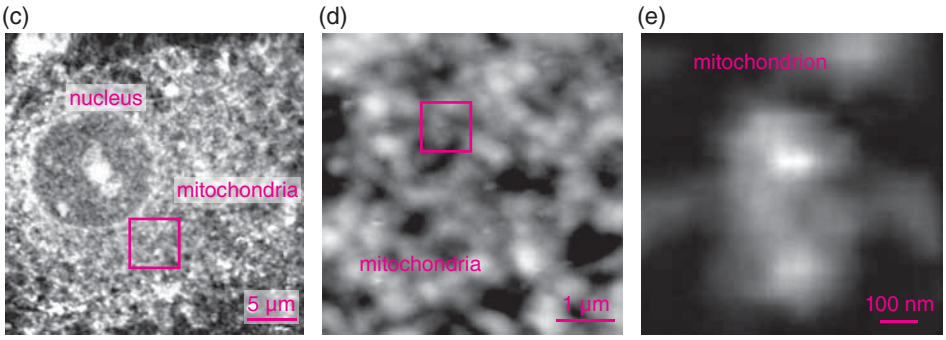

Fig.5-25 Soft X-ray images of the inner structures of living cells at different scales
Nuclei and mitochondria are clearly recognized.

We have developed a laser plasma soft X-ray microscope that combines a laser plasma soft X-ray source with contact X-ray microscopy. The laser plasma soft X-ray source offers high brightness and short pulse duration, whereas contact X-ray microscopy allows observation of cells cultivated *in situ*.

By combining these two techniques, we can observe living cells at a high spatial resolution. Intense soft X-rays were generated by irradiating a thin-foiled gold target with an intense laser beam. Fig.5-23 shows the conceptual design of the laser plasma soft X-ray microscope. Soft X-rays generated from the laser plasma were irradiated onto cells directly cultivated on an X-ray photoresist, and the soft X-ray images of the cells were recorded on the photoresist. The cells were then labeled with several fluorescent dyes and observed under a fluorescence microscope. The resulting fluorescent images were directly compared with the soft X-ray images.

Fig.5-24 shows the soft X-ray image (a) and the fluorescent image (b) of the living cells. The red, blue, and green regions in the fluorescent image are the mitochondria, nuclei, and cytoskeleton, respectively. Comparing the fluorescent images, we find that all organelles are clearly identified in the soft X-ray image.

Soft X-ray images of the inner structures of living cells are presented in Fig.5-25. Panel (c) clearly shows the mitochondria surrounding the nucleus. The mesh-like structures of the mitochondria are visible in panel (d), while panel (e) reveals a single mitochondrion, the first image of this organelle in living cells. The laser plasma soft X-ray microscope is expected to contribute further to life science studies.

The present study was partly supported by Japan Society for the Promotion of Science (JSPS) KAKENHI Grant-in-Aid for Scientific Research (C) (No.25390134).

Reference

Kado, M. et al., In Situ Observation of Cellular Organelles with a Contact X-ray Microscope, Journal of Physics: Conference Series, vol.463, 2013, p.012056-1-012056-4.

5-9 Inhibition of Cadmium Movement in Crops by a Peptide

— Visualization of Elements in Roots Using a Positron-Emitting Tracer Imaging System —

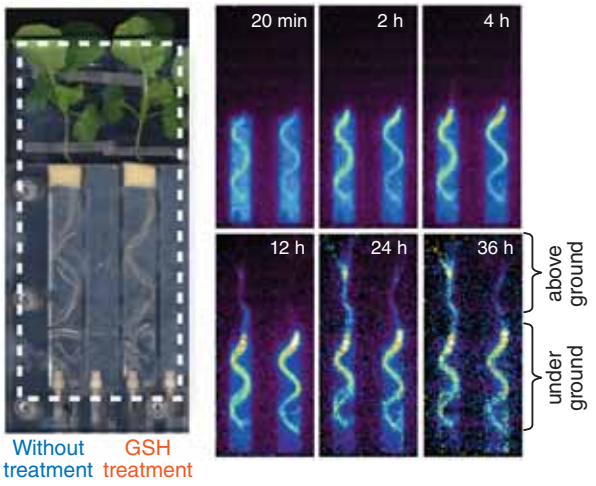

Fig.5-26 Root-zone imaging of Cd in oilseed rape plants
The plants were inserted into an acrylic vessel (left) and radioactive Cd was fed to the root. Subsequently, we could view the uptake of Cd from the hydroponic solution by the root and the movement to the aboveground part of the plant (right). The bright regions in the right panel show the Cd distribution.

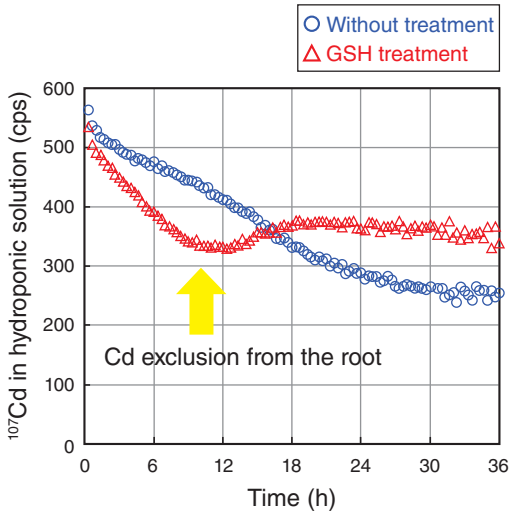

Fig.5-27 Time course of ^{107}Cd radioactivity in solution
In the untreated plants, Cd was continuously taken up and the ^{107}Cd content in solution correspondingly decreased. On the other hand, in the plant treated with GSH, the ^{107}Cd content in solution increased 12 h after ^{107}Cd feeding. This result indicates that Cd was excluded into solution from the root.

Reducing cadmium (Cd) accumulation in crops is a globally important food safety requirement. To reach this goal, studies have proposed numerous approaches such as cleansing of Cd-contaminated soil by crops that readily accumulate the metal, and exploring the crop cultivation conditions that minimize Cd uptake. In promoting these studies, it is very important to observe directly the process of Cd uptake from the roots. We have been developing a non-invasive imaging method called the positron-emitting tracer imaging system (PETIS) that can visualize the movement of various radioactive elements in intact plants. However, PETIS observations have been limited to the aboveground parts of the plant, because it was considered that, if the roots were immersed in a hydroponic solution containing a radiotracer, the visualization of the element of interest through the roots would be hindered by the intense radiation.

In this study, we developed a specialized vessel that minimizes the volume of the hydroponic solution in the field of view. The aim was to improve the counting efficiency of radiation signals from the roots. Within the vessel, the movement of the elements of interest into and through the roots can be directly observed. Using this newly developed "root-zone imaging," we observed the movement of a radioisotope of Cd (^{107}Cd) in oilseed rape plants. The movement of the radioisotope from the roots to the aboveground parts was suppressed by feeding a tripeptide, glutathione (GSH), to the roots (Fig.5-26). Moreover, a detailed analysis of the dynamic image revealed that Cd was partially excluded from the root to the solution after feeding with GSH (Fig.5-27). From these results, we deduced that GSH activates the exclusion of Cd from the roots, suppressing its movement to the aboveground parts.

This study suggests that the application of GSH is very promising in the development of a technique for reducing Cd in crops. Furthermore, as the root-zone imaging is applicable to other elements, it will facilitate the understanding of general mechanisms by which plants take up various nutrients and environmental pollutants.

The present study was partly supported by Japan Society for the Promotion of Science (JSPS) KAKENHI Grant-in-Aid for Scientific Research (B) (Nos.17380194, 19380185, 23380155, 23380194).

Reference

Nakamura, S., Suzui, N. et al., Application of Glutathione to Roots Selectively Inhibits Cadmium Transport from Roots to Shoots in Oilseed Rape, Journal of Experimental Botany, vol.64, issue 4, 2013, p.1073–1081.

5–10 Challenge for Nanoscale Analysis by X-ray Spectroscopy in Combination with Electron Microscopy

— Development of a Multilayer Grating Spectrometer for Use with Electron Microscopes —

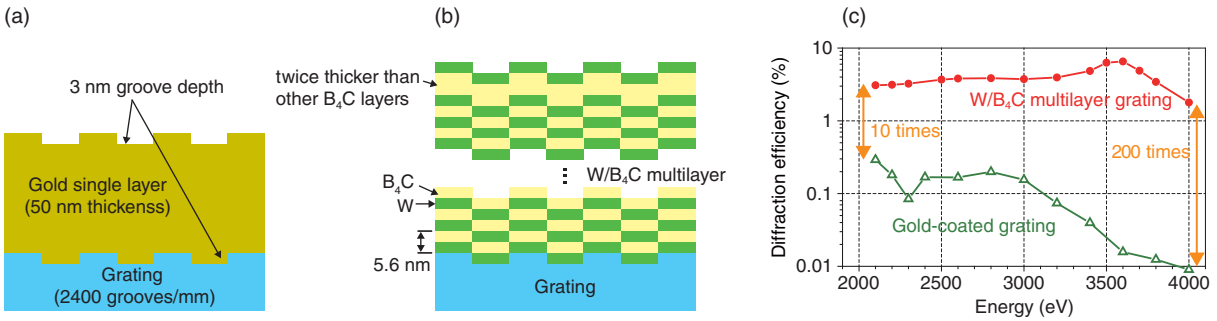

Fig.5-28 Schematics of (a) a gold-coated grating and (b) an aperiodic W/B_4C multilayer grating. (c) The measured diffraction efficiencies of both gratings are plotted as functions of photon energy at a constant angle of incidence
The W/B_4C multilayer grating shows uniformly high diffraction efficiency across the measured energy range.

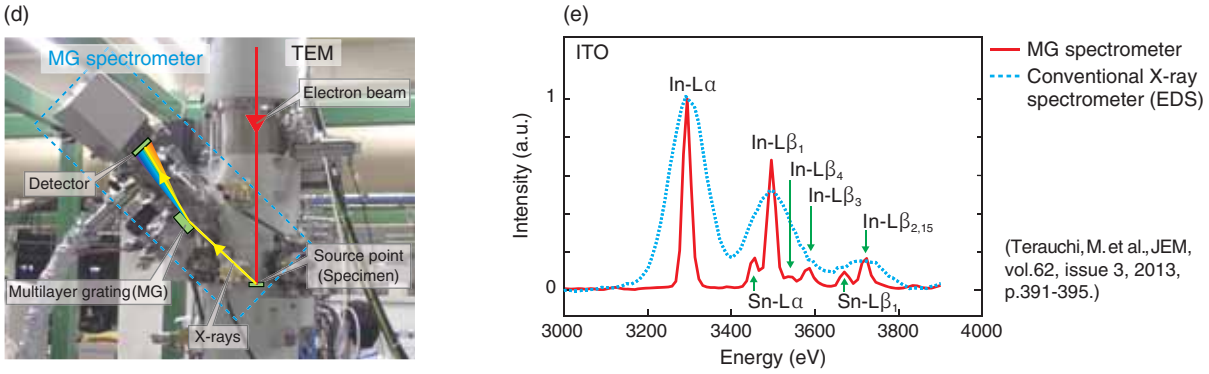

Fig.5-29 MG spectrometer installed in (d) a TEM and (e) emission spectra from ITO
The MG spectrometer better resolves the fine structure of the spectra, such as the Sn-Lα and In-Lβ_1 peaks, than conventional EDS.

Electron microscopes (EMs) are useful tools for the structural analysis of materials at nanometer scales. X-rays are generated when a material is irradiated by an electron beam. If the X-ray intensity distribution is plotted as a function of the photon energy by using an X-ray spectrometer with a diffraction grating featuring many narrow grooves on its surface, we can analyze the valence electronic structure underlying the material properties. As conventional soft X-ray gratings are coated with a thin gold film, their use becomes impractical at energies around the gold absorption edges (approximately 2.2 keV). To overcome this problem, we designed an aperiodic W/B_4C multilayer structure and applied it to a wideband multilayer grating covering 2.0–4.0 keV at a constant angle of incidence.

Fig.5-28 presents schematics of an Au-coated grating (AG) (a) and the designed aperiodic W/B_4C multilayer grating (MG) (b). The measured diffraction efficiency curves of both gratings are plotted in panel (c). The diffraction efficiencies of the MG at 2.1 keV and 4.0 keV are 10 and 200 times higher than those of the AG, respectively. The MG also shows uniformly high efficiency over the entire energy range. This result is attributable to the reflective characteristic of the B_4C layer just below the topmost W layer, whose thickness is twice that of the other layers in the structure, as shown in Fig.5-28(b).

Fig.5-29 is a photograph of the MG spectrometer installed in a transmission EM. Also shown are the emission spectra from indium-tin-oxide measured by the MG spectrometer and a conventional energy-dispersive spectrometer (EDS). The L emission spectra of Sn and In (e.g., Sn-Lα and In-Lβ_1) are more clearly resolved by the high-resolution MG spectrometer than by EDS.

By combining X-ray spectroscopy with EM, we have established a unique technique for extracting morphological and electronic structure information. This technique is expected to assist the development of electronic devices and functional materials.

The present study was partly supported by the project of Collaborative Development of Innovative SEEDs from the Japan Science and Technology Agency (JST).

Reference

Imazono, T., Development of a Soft X-ray Flat-Field Spectrograph in the 50-4000 eV Range and Its Application to Electron Microscopes, Oyo Butsuri, vol.83, no.4, 2014, p.288-292 (in Japanese).

5–11 Discovery of X-ray Coherent Mirage

— Indication of the Potential of New X-ray Optics Using Plasma —

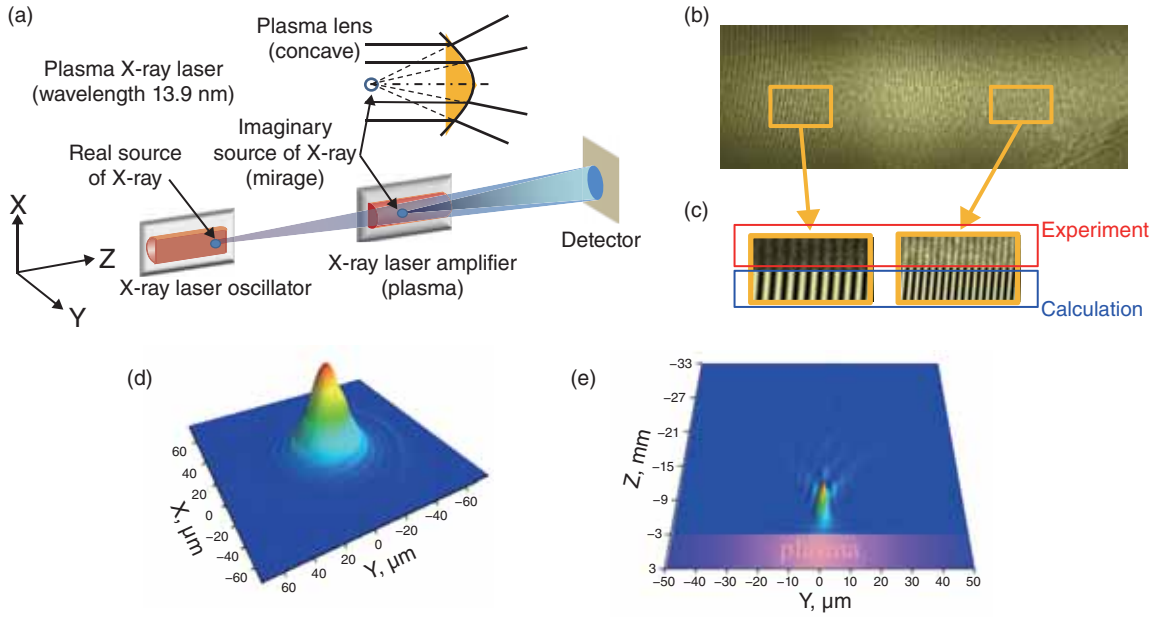

Fig.5-30
(a) Schematic of the formation of an X-ray mirage. The plasma acts like a convex lens, refracting a portion of the X-ray laser beam. An imaginary source, displaced from the position of the original source, is formed.
(b) Interference fringes of the X-ray laser obtained at the detector position.
(c) Comparison of the experimental fringes with the calculated result.
(d), (e) We reproduced the imaginary source by theoretical modeling based on the experimental result.
(d) Spatial profile of the imaginary source in the X–Y plane.
(e) Spatial profile in the Y–Z plane.

Mirages are well-known phenomena aroused in the Earth's atmosphere. They result from the uncontrolled deflection of light rays from rectilinear propagation in inhomogeneous media. Mirages in the X-ray range have been considered extremely difficult to form because the refractive indices of conventional materials to X-rays are close to unity, which essentially excludes refraction.

JAEA has developed plasma X-ray lasers with excellent narrow beam divergence. We injected these X-ray laser beams into a plasma that amplifies X-rays of the same wavelength (Fig.5-30(a)), and obtained a coaxial interference pattern (Fig.5-30(b)). Coaxial interference patterns are generated if two coherent X-ray sources are positioned on the same straight line from the observation point. To explain the observed phenomena, we considered that the plasma behaves as an inhomogeneous atmosphere, i.e., a portion of the X-ray laser beam is refracted and expanded by a concave lens effect in the plasma, forming an imaginary source that appears to exist at the lens focal point. Indeed, if the imaginary source is assumed to lie inside the plasma, the calculated and experimental fringe patterns are completely consistent (Fig.5-30(c)). Considering its similarity to ordinary mirage formation, we conclude that we have generated the first example of an X-ray mirage.

To visualize the imaginary source (the X-ray mirage) on the basis of the experimental result, we have developed a theoretical calculation code, accounting for X-ray refraction and amplification in the plasma. The simulated spatial profiles of the imaginary source are presented in Figs.5-30(d) and (e). The formation of an X-ray mirage was found to strongly depend on the amplification effects of the plasma.

The X-ray mirage discovered in the present study may be adopted in novel plasma-based X-ray optics and methods for diagnosing plasmas, providing useful information of the density profiles, amplification effects, and other properties of plasmas.

The present study was partly supported by Japan Society for the Promotion of Science (JSPS) KAKENHI Grant-in-Aid for Scientific Research (B) (No.25289244).

Reference

Magnitskiy, S., Pikuz, T. et al., Observation and Theory of X–ray Mirages, Nature Communications, vol.4, 2013, p.1936–1–1936–7.

5–12 Transparency of Sodium in the Ultra-Violet Spectral Range
— Imaging by Light Illumination through an 8-mm-Thick Sodium Sample —

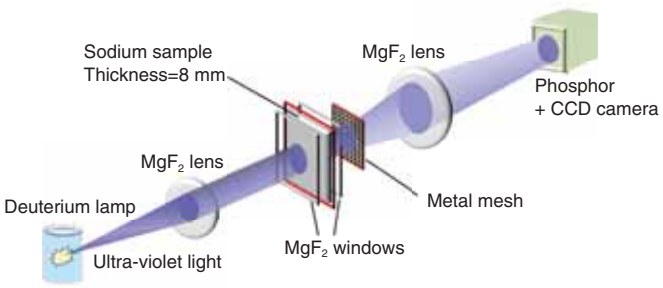

Fig.5-31 Set-up of the imaging experiment
The ultra violet light illuminates the sodium sample through optical elements to form an image on the camera.

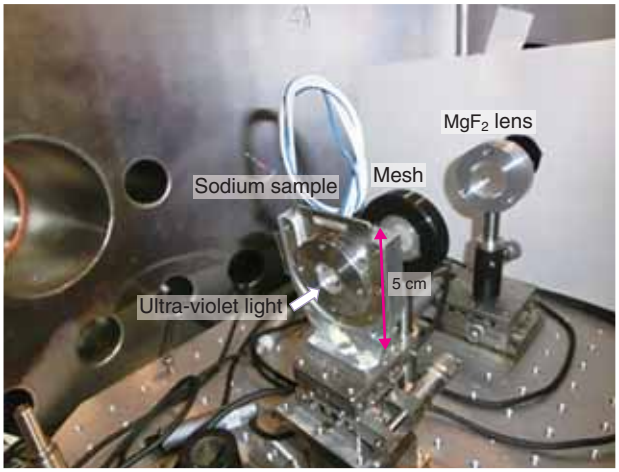

Fig.5-32 Photograph of an 8-mm-thick sodium sample and the imaging system
At the center of the photo, the fresh sodium sample is visible with metallic reflection.

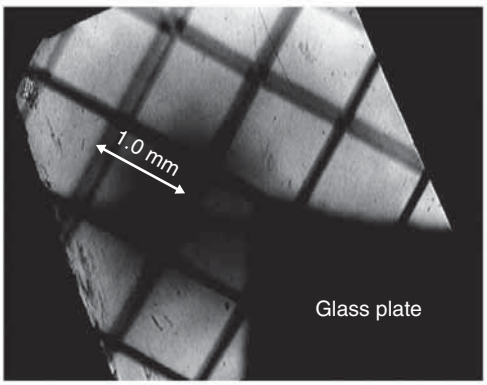

Fig.5-33 Image of a metal mesh composed of 100-μm-thick wires spaced by 1 mm, illuminated by ultra-violet light that shone through an 8-mm-thick sodium sample
The blackened area corresponds to the area covered by a 1-mm-thick glass plate, which is opaque to this range of wavelengths.

The surface of fresh sodium reflects visible light. As is well known, surface electrons oscillate when exposed to incident light and emit light at the same wavelength. At shorter wavelengths of incident light, the electrons cannot follow the electric field of the light, and the light penetrates the sodium interior. However, the light is significantly dumped by phenomena such as electron-phonon scattering. To date, transparent sodium has not been experimentally investigated.

On the other hand, the optical properties of alkali metals (including sodium) have been intensively studied since the pioneering work of Wood in the1930s. In the1960s, the Oak Ridge National Laboratory team obtained a plasma wavelength of 218 nm. At wavelengths below 218 nm, sodium is partially transparent down to some threshold; namely, the core electron excitation wavelength (40.5 nm). The Oak Ridge team tried to measure the transmittance of a sub-μm-thick solid sodium layer coated onto a quartz and lithium fluoride (LiF) substrate. However, the thickness restricts the dynamic range of the transmittance. Therefore, we require a considerably thicker sodium region to clarify the transmittance.

In this study, we fabricate relatively thick sodium samples (>1 mm) in the spectral range beyond 115 nm, which corresponds to the shortest transmission wavelength of magnesium fluoride (MgF_2) windows, and evaluate their transmittance. First, we determined the spectral transmittance between 115 nm and ~200 nm. At ~120 nm, the transmittance of 3-mm-thick solid sodium samples admitting the MgF_2 windows was several tens of percent. Furthermore, the transmittance weakly depended on temperature up to 150 °C (note that the melting point of solid sodium is 97 °C).

To confirm the transmittance, we also performed a simple imaging experiment with an 8-mm-thick sodium sample. Figs.5-31 and 5-32 show a schematic of the experiment and a photograph of the setup, respectively. We recorded a clear image of a metal mesh with 1 mm separation onto a two-dimensional charge coupled device detector (Fig.5-33). This result encourages us to design an optical imaging device for viewing objects inside or through solid or liquid sodium media, and to determine the physical origin of high transmittance, which has not previously been demonstrated.

Reference

Daido, H. et al., Demonstration of Partially Transparent Thick Metallic Sodium in the Vacuum Ultraviolet Spectral Range, Optics Express, vol.21, issue 23, 2013, p.28182–28188.

5–13 Innovative Technique for Elucidating Diffusion through Materials

— Development of an Advanced Analysis Method for Quasielastic Neutron Scattering —

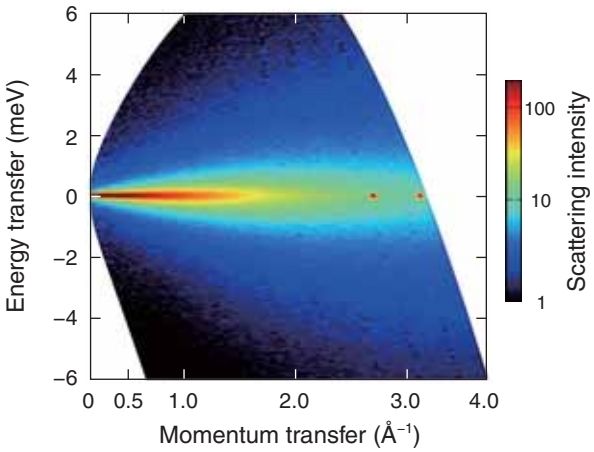

Fig.5-34 Quasielastic neutron scattering of water
Quasielastic scattering spectra obtained by a neutron scattering experiment. The signal is spread like a mound around the elastic scattering of zero energy transfer. Because more than one diffusion mode exists, the routes, speeds, and types of the modes are difficult to identify because their signals overlap. The red dot indicates the signal generated by the sample cell.

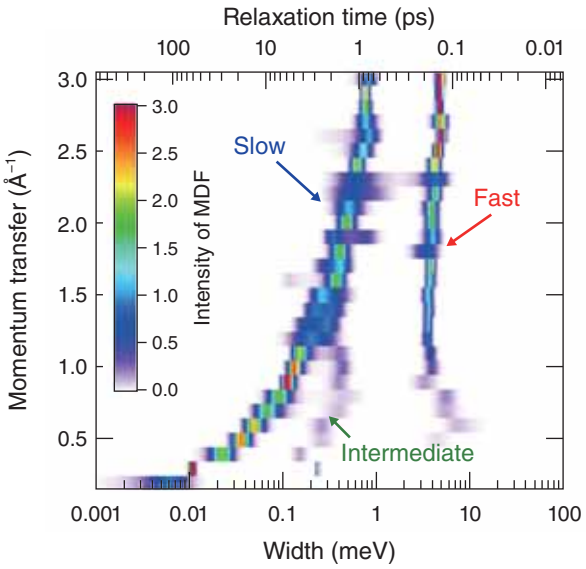

Fig.5-35 Calculated mode distribution function of water
Using the newly developed analysis, we computed the mode distribution function (MDF) of water. Each diffusion mode is independently represented. Consequently, we can directly evaluate the number of modes, and their types and speeds.

Diffusion is an important process in materials and living tissue. For instance, it is involved in the functional expression of proteins, and plays a role in the capabilities of ion and proton conductors, which are now being investigated as battery materials. Therefore, by elucidating diffusion mechanisms, we can control the functional expressions and capabilities of materials. Quasielastic neutron scattering (QENS) is among the few powerful techniques that can investigate the relationships between time and space in the diffusion motions of atoms and molecules. Therefore, QENS allows an in-depth study of diffusion. However, the correctness of diffusion models is difficult to demonstrate by conventional QENS analysis, as the model must be assumed prior to analysis, and therefore cannot naturally emerge from the results.

We have developed a versatile analysis method that requires no model assumptions. By this method, we can understand the model from the obtained results. We represent all diffusion processes of a material as a set of "simple diffusions." In a "simple diffusion," on average, the particles gradually spread out with a constant relaxation time. In this scenario, the diffusion process can be converted into the intensity distribution of the relaxation time. We call this distribution the mode distribution function (MDF). The MDF directly provides the number of diffusion motions, and their types and speeds. The conversion to MDF adopts the maximum entropy method based on information theory.

We applied this new method to a diffusion study of water. QENS experiments were performed on AMATERAS at J-PARC. AMATERAS can measure over a wide area at high resolution and is ideally suited for this method. A QENS spectrum of liquid water is shown in Fig.5-34. The characteristics of the diffusion are not directly interpretable from this figure. However, the MDF obtained from the QENS spectrum (Fig.5-35) clearly shows three types of motions. In particular, an unsuspected intermediate motion is discovered. Therefore, the MDF reveals the detailed characters of diffusion motions. This result is important for understanding the overall picture of diffusion in water.

We hope that such diffusion studies will advance a wide range of research fields and uncover new knowledge that will benefit science and technology.

Reference

Kikuchi, T. et al., Mode-Distribution Analysis of Quasielastic Neutron Scattering and Application to Liquid Water, Physical Review E, vol.87, no.6, 2013, p.062314-1-062314-8.

5–14 Achievement of High-Quality Pulsed Cold Neutron Beam

— Performance Evaluation of the J-PARC Cryogenic Hydrogen System —

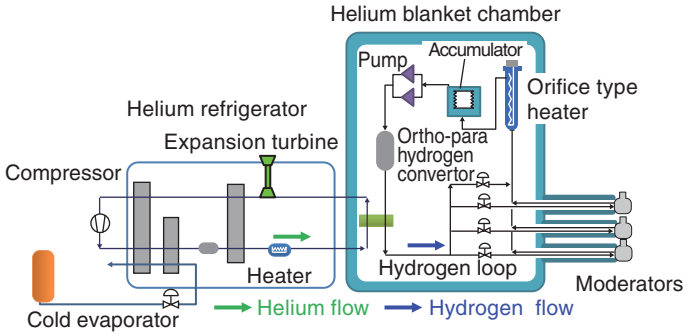

Fig.5-36 Cryogenic hydrogen system for the J-PARC spallation neutron source
Supercritical hydrogen at 20 K and 1.5 MPa is supplied to the moderators, which convert the generated fast neutrons to cold neutrons.

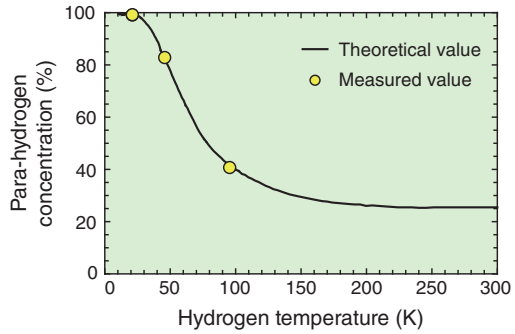

Fig.5-37 Measured para-hydrogen concentration during a cool-down process
The measured para-hydrogen concentration, which agrees with the theoretical values, exceeds 99% at 20 K.

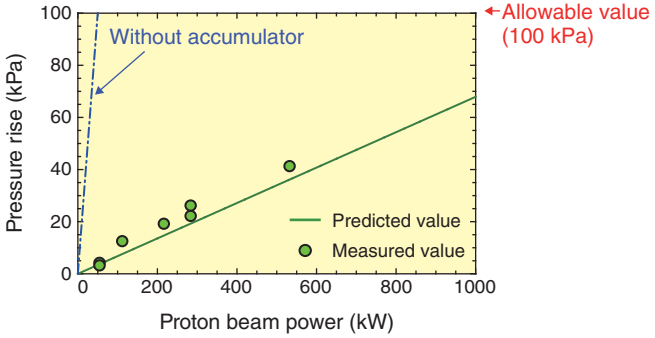

Fig.5-38 Effect of proton beam power on pressure rise in the hydrogen loop
At each power of the proton beam, the developed system reduces the pressure rise to below the maximum allowed value.

At J-PARC, 3 GeV protons with a power of 1 MW are injected onto a mercury target at a repetition rate of 25 Hz, producing fast neutrons via the spallation reaction. The high-energy neutrons are slowed to thermal and/or cold neutrons in hydrogen moderators, which receive supercritical hydrogen at 1.5 MPa and below 20 K. We aimed to maintain the para-hydrogen concentration in the hydrogen moderator above 99%. Cold neutrons are effectively slowed by the excitation of para-hydrogen to ortho-hydrogen. Moreover, the neutron scattering cross section of para-hydrogen is lower than that of ortho-hydrogen by two orders of magnitude. Therefore, we obtained a pulsed cold neutron profile with a narrow full-width-half-maximum (approximately 100 μs) and a short tail. These pulsed neutrons are suitable for crystal and magnetic structural analyses.

The presence of ortho-hydrogen and large changes in hydrogen density degrade the pulse shape. Therefore, we developed a cryogenic hydrogen system in which supercritical para-hydrogen circulates at the largest flow rate thus far achieved (9.5 m^3/h). This large flow rate reduces the fluctuations in the moderator temperature to below 3 K (Fig.5-36).

We installed an ortho-para hydrogen convertor with a catalyst of hydrous ferric oxide. Furthermore, we developed a hydrogen gas sampling system, which safely fills a glass cell with hydrogen gas obtained from a high-pressure, low-temperature environment. The para-hydrogen concentration was measured during the cool-down process by a laser Raman spectrometric method. The measured and theoretical para-hydrogen concentrations closely match and satisfy the requirements at 20 K (Fig.5-37).

One major challenge is to mitigate the pressure fluctuations below 0.1 MPa. These fluctuations, caused by large stepwise heat loads when the beam is on, are problematic because supercritical hydrogen behaves as an incompressible fluid and lacks a vapor-liquid interface. To overcome this problem, we developed a novel equipment with a bellows structure, called an “accumulator.” Pressure fluctuations are mitigated by spontaneous expansion or contraction of the bellows, which enclose helium gas (boiling point = 4.2 K). At beam powers below 532 kW, the measured pressure rises agree with the predicted values. We expect that the pressure rise can be maintained below the upper allowable limit at a beam power of 1 MW (Fig.5-38).

This technology will enable the steady production of high-quality cold neutron beams at the rated 1 MW operation. Potentially, it will advance neutron beam research, thereby contributing to science, technological developments, and industrial promotion.

Reference

Tatsumoto, H. et al., Operational Characteristics of the J-PARC Cryogenic Hydrogen System for a Spallation Neutron Source, AIP Conference Proceedings 1573, 2014, p.66–73.

5–15 Dose Rate after Beam Operation of J-PARC 3 GeV Synchrotron

— Investigation and Measurement of Dose Rate Distribution of Radioactive Nuclides Produced in the Accelerator for Higher Output Power —

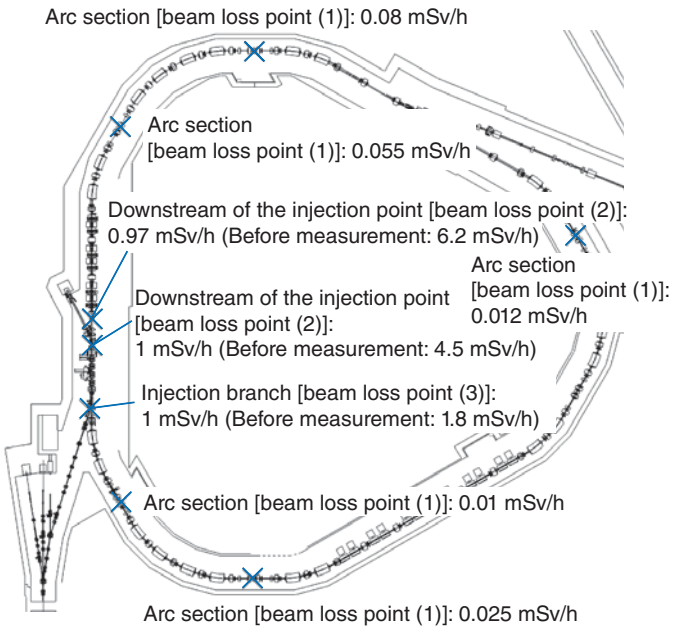

Fig.5-39 Residual dose distribution of J-PARC 3 GeV synchrotron
This figure shows the dose rates at the surfaces of the magnets and vacuum chambers after accelerator operation. These data were acquired after continuous operation at 200 kW for one month, and 300 kW for 3 days. Data were acquired on July 2012 except at point (3), which was measured on March 2014 after reducing the beam loss at that point.

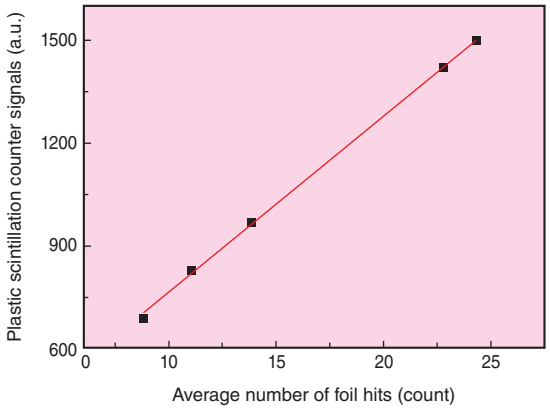

Fig.5-40 Beam loss as a function of average number of foil hits
This graph shows the output signals of the plastic scintillation counter as a function of the average number of times that the circulating beam hits the carbon foil. The plastic scintillation counter was positioned downstream from the carbon foil. The average number of foil hits was controlled by varying the injection orbit or the carbon foil position. The radiation generated by interaction between the carbon foil and the circulating beam increased with the average number of foil hits, thereby increasing the signal intensity.

The 3 GeV rapid cycling synchrotron (RCS) at J-PARC has been operational since 2007. The RCS ring generates a high-power proton beam (1 MW) at a repetition rate of 25 Hz, which is supplied to the main ring and the neutron production target. In the RCS, negative hydrogen ions are accelerated to 400 MeV by a linac and passed through a thin carbon foil, which converts them into protons by removing the two electrons. The protons are then injected into the synchrotron and accelerated to 3 GeV in 20 ms.

In a high-intensity accelerator such as J-PARC, minimizing the beam loss is vital to retaining the activation of the accelerator components within an allowable level. Based on experience with the RCS and other accelerators, provided that the dose rate immediately after beam stop is below 1 mSv/h at the accelerator component surfaces, the exposure dose during maintenance work can be suppressed to less than several hundred μSv. Therefore, to ensure that the dose rate remains below 1 mSv/h, we must understand the distribution of the dose rate generated by the beam loss. To this end, we measured the dose rate on the equipment surfaces during each maintenance period, and elucidated the dose rate conditions produced by the various operation modes. Additionally, we considered the cause of the activation and appropriate countermeasures.

Fig.5-39 shows the measured dose rate around the RCS. Most of the radioactivity generated by the accelerator components is concentrated at the injection section (the area of the straight line on the left side of Fig.5-40). Away from the injection section, the dose rate remains below 0.1 mSv/h [beam loss point (1)]. In the injection section, peaks of local activation appear downstream of the injection point [beam loss point (2)] and at the branch between the injection and the circulating beam [see beam loss point (3), Fig.5-39]. The results indicate that the activation at point 2 is sourced from interaction between the beam and the thin carbon film (see beam-study results in Fig.5-40), while the beam loss at point 3 is caused by increased pressure of the injection beam transport line. After decreasing the beam loss by inserting another source, we increased the beam power while retaining the dose rate below 1 mSv/h at both loss points.

In summary, we increased the beam power by reducing the beam loss.

Reference

Yamamoto, K. et al., Beam Power and Residual Dose History of J-PARC RCS, Progress in Nuclear Science and Technology, vol.4, 2014, p.238-242.

5–16 Magnetic Shielding via Vacuum Chambers for Beam Orbit Stabilization

— Development of Vacuum Chambers of Magnetic Materials at J-PARC —

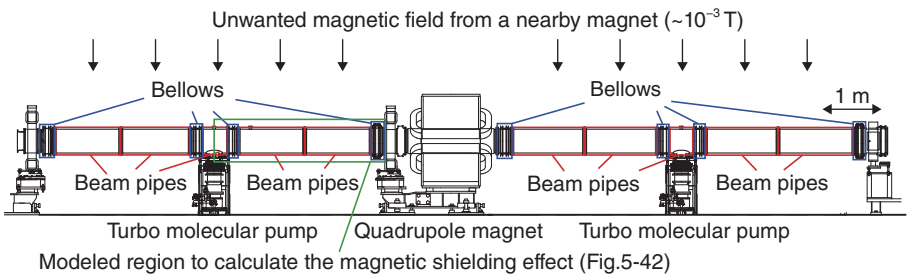

Fig.5-41 Location of the vacuum chambers of magnetic materials in the 3 GeV synchrotron at J-PARC
At the extraction section in the synchrotron, stray magnetic fields from a nearby magnet leak into the synchrotron beam line, distorting the beam orbit. The vacuum chambers of magnetic materials were developed to shield the beam from these unwanted magnetic fields.

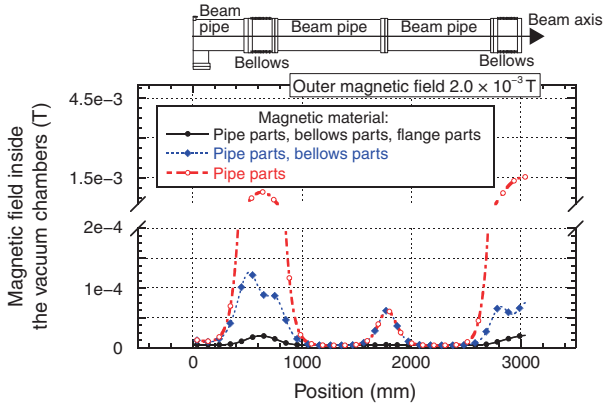

Fig.5-42 Calculated magnetic field inside the vacuum chambers, assuming that each component of the vacuum chambers is constructed from magnetic materials
The area surrounded by the green rectangle in Fig.5-41 was modeled in the calculation. The most effective magnetic shielding was achieved when all components were constructed from magnetic materials.

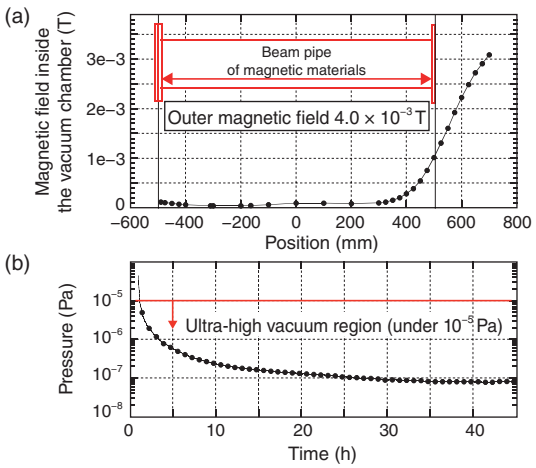

Fig.5-43 Measured magnetic shielding performance and vacuum performance of the vacuum chamber
(a) The vacuum chamber of magnetic materials effectively shielded the external magnetic field.
(b) The vacuum chamber achieved ultra-high vacuum conditions.

A main source of beam loss in synchrotrons is beam orbit distortion, caused by the entry of unwanted stray magnetic fields from the magnets at a nearby beam line. In the J-PARC 3 GeV synchrotron, a magnet along the beam extraction line injected a ~10^{-3} T stray magnetic field into the vacuum chambers, distorting the beam orbit by approximately 10 mm from the chamber center. Stray magnetic fields are most effectively shielded by completely surrounding the beam region with magnetic material. Therefore, we decided to manufacture the vacuum chambers of magnetic materials. The developed vacuum chambers demonstrate superior magnetic shielding and vacuum performances.

Fig.5-41 shows the layout of the extraction section of the synchrotron, where the vacuum chambers of magnetic materials are installed. According to the beam orbit calculation, the external magnetic field should be suppressed to less than one-tenth in this beam region. Fig.5-42 shows the calculated magnetic field, assuming that each component of the vacuum chambers is constructed from magnetic materials. To ensure effective shielding, all the components, including the bellows, flange, and pipe parts, should be made from magnetic materials. To this end, permalloy and ferritic stainless steel were selected for the thin (pipes and bellows) and thick (flanges) parts, respectively.

Machining generates internal stress, which generally reduces the magnetic permeability of a material. However, magnetic permeability can be recovered by annealing. On the other hand, to reduce outgassing, vacuum materials are baked at high temperature under high-vacuum conditions. To achieve magnetic annealing while reducing the outgassing, we heat-treated the vacuum chambers under high vacuum. Fig.5-43 shows the magnetic shielding and vacuum performances. The external magnetic field was suppressed to less than one-tenth inside the chamber, and the magnetic materials ensured ultra-high vacuum. By constructing the vacuum chambers of magnetic materials, we can realize superior magnetic shielding and vacuum performances and a stable beam orbit within the synchrotron.

Reference

Kamiya, J. et al., Vacuum Chamber Made of Soft Magnetic Material with High Permeability, Vacuum, vol.98, 2013, p.12–17.

5–17 Observation of the Beam Injected into the Acceleration Region of the Cyclotron
— Development of an Emittance and Acceptance Measurement System —

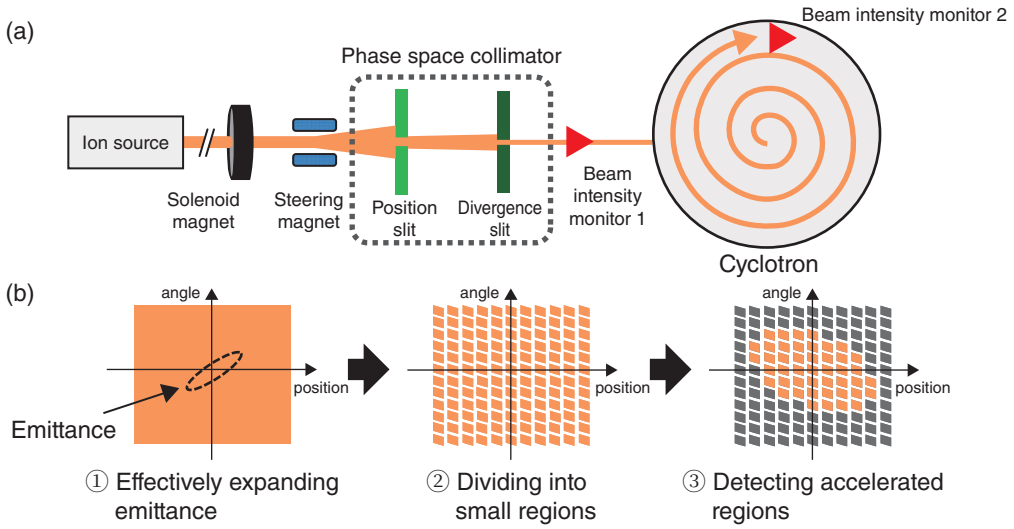

Fig.5-44 (a) Emittance and acceptance measurement system and (b) acceptance measurement procedure
The system is composed of electromagnets that effectively expand beam emittance, a phase space collimator that limits the position and angle range of the beam, and two beam intensity monitors.

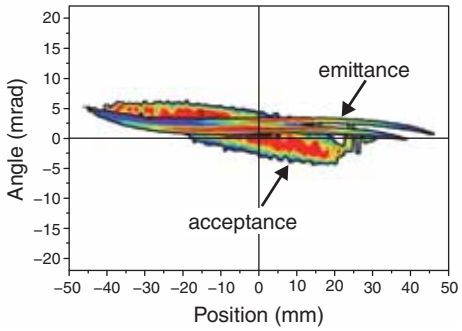

Fig.5-45 Results of emittance and acceptance measurements
(modified from Kashiwagi, H. et al., Rev. Sci. Instrum., vol.85, no.2, 2014, p.02A735-1-02A735-5.)
The relationship between the acceleration region and injected beam region is visualized by displaying the measured emittance and acceptance in one graph.

The TIARA cyclotron facility produces various types of ion beams for different researches (such as bioscience and material sciences) by changing the ion species in each experiment. Beam injection tuning that maximizes the ratio of the accelerated beam current to the beam current injected into the cyclotron is required to ensure sufficient current for each experiment. The tuning corresponds to the overlapping of emittance (a region occupied by the injected beam) and acceptance (an acceleration region) in phase space. Because any emittance regions outside the acceptance are not accelerated, the emittance must be matched to the acceptance. Although various methods are available for measuring the emittance, no method has been developed for measuring the acceptance of a cyclotron. To fill this gap, we devised a method for measuring the acceptance, and developed a transverse emittance and acceptance measurement system for visualizing the emittance–acceptance relationship.

Figs.5-44(a) and (b) are schematics of the measurement system and procedure, respectively. The acceptance is determined by the following three steps: (1) The beam emittance from the ion source is effectively expanded by solenoid magnets and a steering magnet to ensure sufficient measurement range (Fig.5-44(b)①). (2) The expanded emittance is divided into many small regions by two slits called phase space collimator (Fig.5-44(b)②), and the beamlets with the regions are sequentially injected into the cyclotron. (3) The acceptance is obtained by aggregating the accelerated beamlets detected by beam intensity monitor 2 (Fig.5-44(b)③). The emittance is obtained by measuring the beam intensity of each region divided by the phase space collimator using beam intensity monitor 1.

Fig.5-45 shows the measured emittance and acceptance on a single plot. We succeeded to visualize the relationship between the injected beam emittance and the acceptance of the cyclotron using the system.

On the basis of the results of the emittance and acceptance measurements, we will develop a beam injection tuning system that overlaps the emittance and acceptance to maximize the ratio of the accelerated beam.

Reference

Kashiwagi, H. et al., A Transverse Emittance and Acceptance Measurement System in a Low-Energy Beam Transport Line, Review of Scientific Instruments, vol.85, no.2, 2014, p.02A735-1-02A735-5.

Research and Development of High Temperature Gas-Cooled Reactor, Hydrogen Production, and Heat Application Technologies

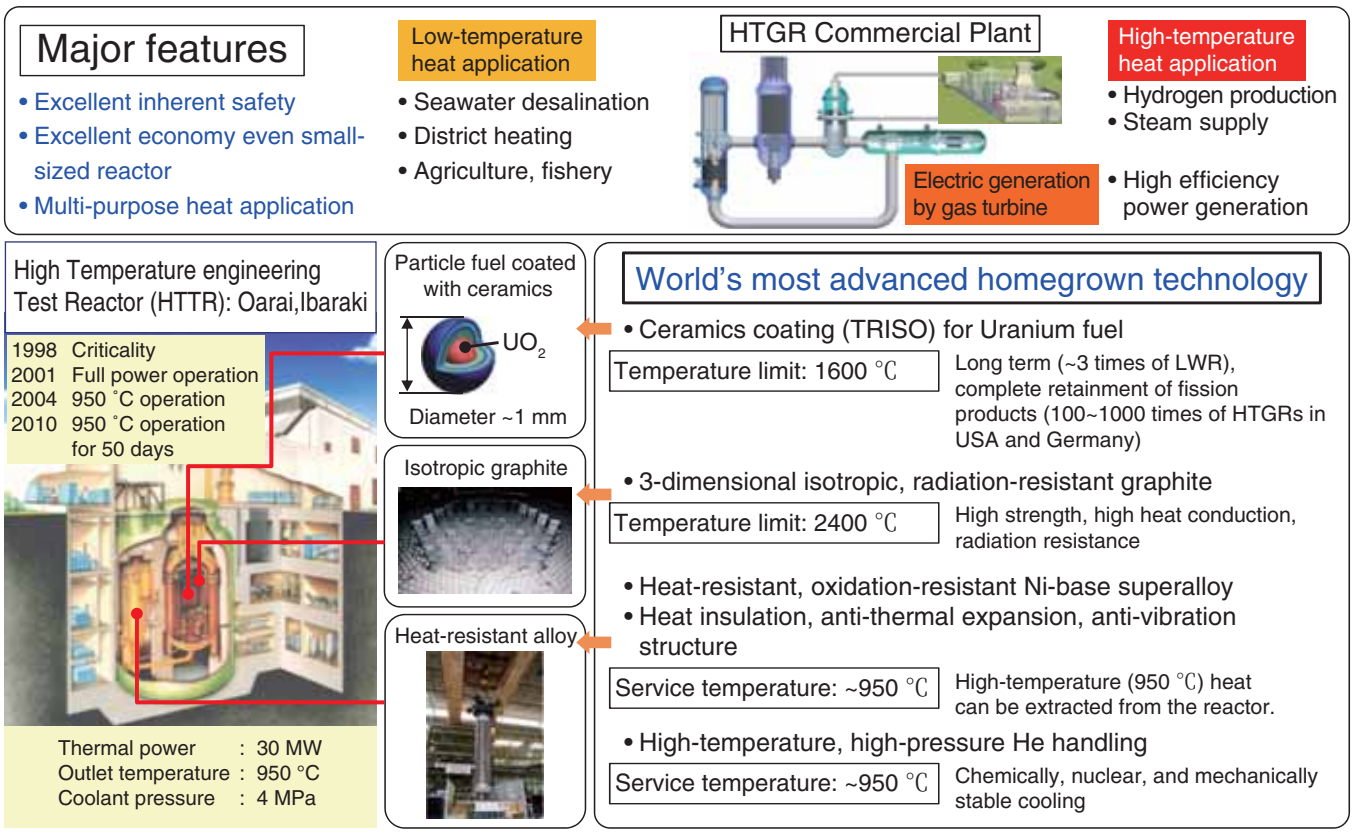

Fig.6-1 Outline of HTGR; Features, Heat utilization, Major specifications, and HTTR technologies
HTGRs are helium gas-cooled, graphite-moderated thermal neutron reactors capable of meeting various heat application requirements, such as hydrogen production and power generation. In particular, they are strongly expected to regain the public's trust in nuclear power because of their inherent safety.

To reduce greenhouse gas emissions and remedy the fragility of Japan's energy supply-demand structure arising from excessive dependence on fossil fuel resources from abroad, nuclear energy should be used not only for power generation but also various heat applications. The Strategic Energy Plan, Large-boned Policy, and Japan Revitalization Strategy, decided by the cabinet in 2014, indicated the promotion of research and development of a high temperature gas-cooled reactor (HTGR) as a national policy because of the reactor's excellent inherent safety and ability to meet energy demands from various industries.

An HTGR can supply temperatures of 950 °C using inert helium (He) gas as a coolant. Three other cutting-edge Japanese technologies that make it feasible to obtain such high temperatures in an HTGR have been developed by JAEA. The first is a technology for fabricating ceramic-coated fuel particles with a diameter of approximately 1 mm. Ceramics remain stable even at 2500 °C and provide superior heat-resistant coating layers for containing radioactive fission products within fuel particles. The second is a technology for fabricating isotropic and radiation-resistant graphite blocks. The third is a technology for manufacturing heat- and oxidation-resistant super-alloys with careful composition of alloy contents. With these major technologies as well as further knowledge of high temperature structural design and the like, we generated a temperature of 950 °C in the high temperature engineering test reactor (HTTR) for the first time in the world in 2004, and maintained this temperature over 50 days of operation in 2010 (Fig.6-1).

It is feasible to prevent explosive gas generation by physical phenomena, as well as accidental overheating and oxidation of the fuel coating layers, without any engineered safety features. The inherent safety features assure no harmful release of radionuclides to general public and environment in any accident.

The heat from HTGR is useful for not only power generation but also hydrogen production for fuel cell cars and direct reduction iron-making, and for supplying steam to industries. Waste heat can be utilized for desalination, among other applications. Research and development of the thermochemical IS process for producing hydrogen by splitting water molecules has been conducted. A continuous hydrogen production test is underway to establish the applicability of this technology to industrial plants, with the test facility consisting of components made of existing steel and ceramic materials.

For practical applications of HTGR, we intend to perform integration tests of HTTR and heat application systems for power generation and hydrogen production, and research such Topics as advanced safety (Topics 6-1, 6-2, 6-3, 6-4).

6–1 Demonstration Plan for the World's First Nuclear Heat Application with the High Temperature Engineering Test Reactor

— Toward the Industrial Use of Nuclear Heat —

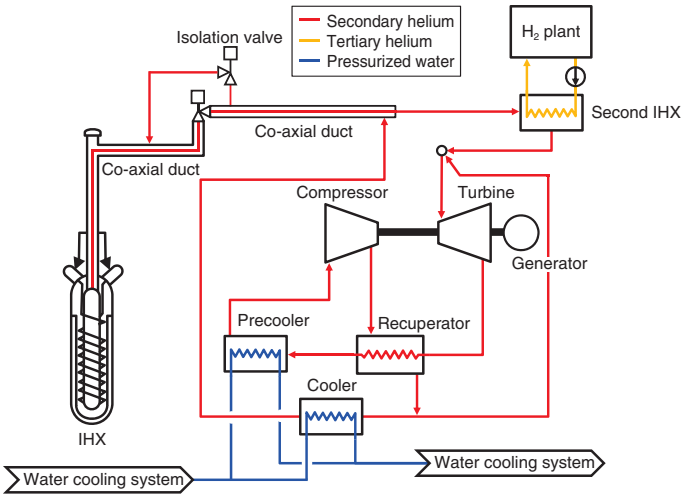

Fig.6-2 Flow diagram of the candidate heat application system coupled to the HTTR
The nuclear heat transferred to the secondary helium (He) system at the intermediate heat exchanger (IHX) is used by the He gas turbine system and the H_2 plant for power generation and hydrogen production.

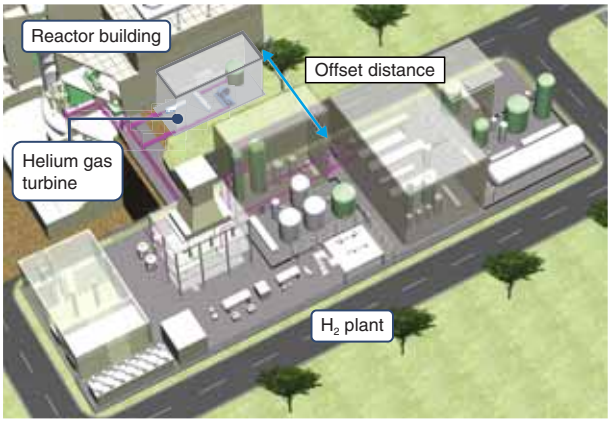

Fig.6-3 Candidate heat application system layout coupled to the HTTR
An appropriate offset distance is set between the reactor building and H_2 plant to ensure the integrity of the reactor building (including safety-related systems, structures, and components) and the habitability of the reactor control room against leakages of combustible and hazardous chemicals.

For the utilization of nuclear heat in industrial applications such as hydrogen production and high-efficiency power generation, the following technical issues should be resolved. First, a formulation of the safety requirements and a validation of the design considerations for coupling a hydrogen production plant (H_2 plant) to a nuclear facility must be completed. Second, the overall performance of the He gas turbine must be confirmed. The present study identifies the tests that must be conducted using the HTTR. Additionally, plant concepts are proposed for the heat application system to be coupled to the HTTR.

We aim to formulate safety requirements through a licensing review of the Nuclear Regulation Authority for coupling an H_2 plant to the HTTR. The design considerations will also be validated by a test simulating H_2 plant accident. Furthermore, continuous operation at the rated power, in addition to start-up and shut-down test operations of the He gas turbine, will be performed to demonstrate safe and reliable operation at steady and transient conditions assumed in the actual environment for the performance confirmation of the He gas turbine.

System configurations are investigated to minimize the amount of modification to the existing HTTR facility, as well as to simulate the configuration of a commercial system. A cascade configuration with a second intermediate heat exchanger (IHX), which transfers heat to the H_2 plant, and a He gas turbine, which consists of a turbine, compressor, generator, precooler, and recuperator, is selected as one of the candidates (Fig.6-2). Additionally, the plant layout is preliminarily determined with sufficient offset distance to ensure the integrity of the reactor building (including safety-related systems, structures, and components) and habitability of the reactor control room against leakages of combustible and hazardous chemicals (Fig.6-3).

Further study will be conducted for system design, component design, and layout design to finalize the plant concept. Furthermore, a safety evaluation will be performed to expedite the first-of-a-kind demonstration of nuclear heat application with the HTTR.

Reference

Sato, H. et al., HTTR Demonstration Test Plan for Industrial Utilization of Nuclear Heat, JAEA-Technology 2014-031, 2014, 30p. (in Japanese).

6–2 Compatibility between Effective Plutonium Incineration and Nuclear Proliferation Resistance

— Conceptual Study of a Plutonium Burner High Temperature Gas-Cooled Reactor System —

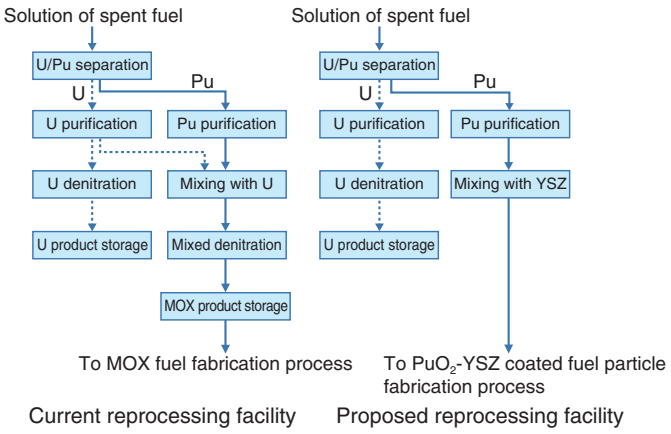

Fig.6-4 Pu flow in the reprocessing facilities
Connecting the Pu nitrate solution line directly to the fuel fabrication process allows the elimination of the mixed denitration process and MOX product storage.

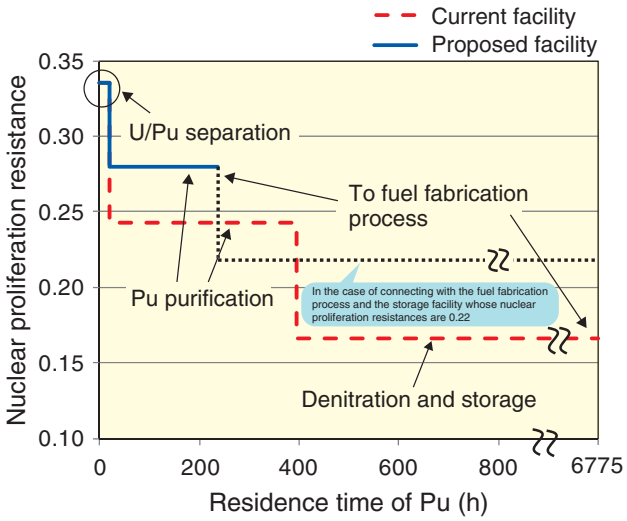

Fig.6-5 Nuclear proliferation resistance based on the AFCI method
The nuclear proliferation resistance of the proposed reprocessing facility is superior to that of the current system because it has an AFCI nuclear proliferation resistance value of 0.28 and a shorter residence time of Pu from the separation process.

We have been conducting a conceptual study on using a plutonium (Pu) burner HTGR system to achieve effective incineration of ^{239}Pu, which is significant for nuclear non-proliferation in the long term.

In Japan's reprocessing facility, Pu recovered from light water reactor spent fuel is mixed with uranium (U), as shown in Fig.6-4, to prevent an increase in nuclear proliferation risk by avoiding the existence of pure Pu. The Pu/U mixed solution line is connected to the denitration process, and then Pu/U mixed dioxide fuel (MOX fuel) is fabricated.

When used in a reactor, the MOX fuel generates additional Pu through a neutron capture reaction with ^{238}U. In other words, more efficient incineration of Pu would require Pu fuel without U. One challenge to fabricating Pu fuel without U is how to do it without reducing nuclear proliferation resistance in the reprocessing facility. In the proposed reprocessing facility shown in Fig.6-4, Pu is mixed with yttria-stabilized zirconia (YSZ) instead of U. YSZ is essentially chemically inactive, and the Pu/YSZ mixed solution line is connected to the fabrication process for PuO_2-YSZ coated fuel particles. The nuclear proliferation resistances of the proposed and current reprocessing facilities are evaluated quantitatively using the US Advanced Fuel Cycle Initiative (AFCI) method. The results in Fig.6-5 show that the proposed reprocessing facility is superior to the current system in terms of nuclear proliferation resistance. Additionally, the fabrication of PuO_2-YSZ coated fuel particles is possible without major research or development, because a similar technology has already been developed and used for the fabrication of UO_2 coated fuel particles for the HTTR.

PuO_2-YSZ coated fuel particles are composed of 0.5-mm-diameter PuO_2-YSZ kernels and four coating layers made of pyrolytic carbon and SiC. Owing to the use of YSZ as fuel matrix, it is very difficult to recover Pu from a PuO_2-YSZ coated fuel particle. As a result, the PuO_2-YSZ coated fuel particle is considered to have excellent nuclear proliferation resistance in many aspects including fuel fabrication, reactor operation, and disposal of the spent fuel. Additionally, the PuO_2-YSZ coated fuel particle is excellent for safe geological disposal because the leach rate of the fission product in YSZ is two orders of magnitude smaller than that in glass.

A preliminary analysis has been performed for a Pu burner HTGR rated at 600 MWt to investigate the incineration rate of ^{239}Pu. The result shows that 95% of ^{239}Pu is incinerated by optimizing a fuel shuffling scheme. In future work, we will prepare the nuclear design of a Pu burner HTGR and a fuel design that would allow a very high burnup of around 500 GWd/t.

Reference

Fukaya, Y., Goto, M. et al., Proposal of a Plutonium Burner System Based on HTGR with High Proliferation Resistance, Journal of Nuclear Science and Technology, vol.51, issue 6, 2014, p.818–831.

6–3 Economic Evaluation of a High Temperature Gas-Cooled Reactor Iodine-Sulfur Process Hydrogen Production System

— Investigation of Hydrogen Production Cost and Competitiveness —

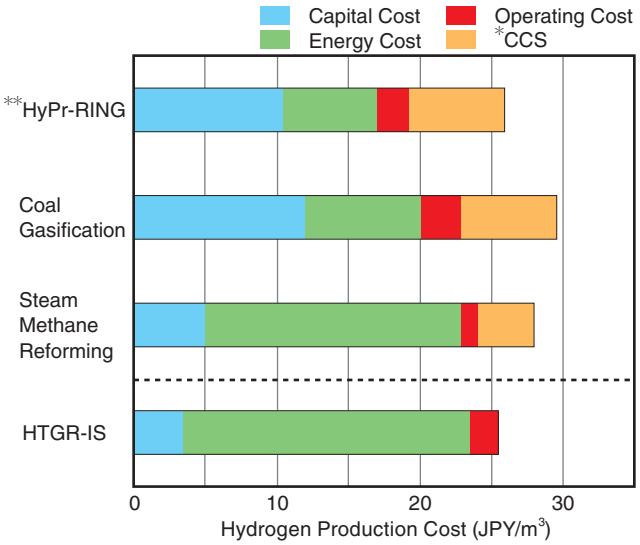

* CCS: Carbon dioxide Capture and Storage
** HyPr-RING: A hydrogen production process wherein CaO is fed to a coal gasifier to absorb CO_2 as $CaCO_3$

Fig.6-6 Hydrogen production costs under processes using fossil fuels and HTGR-IS
The competitiveness of a future HTGR-IS hydrogen production system with existing hydrogen production processes is shown. The competitiveness of HTGR-IS is partly due to there being no need for CCS.

Table 6-1 Competitiveness of the HTGR-IS hydrogen production cost in the industry
HTGR-IS hydrogen production cost satisfies the requirement for hydrogen reduction steelmaking and fuel cell vehicles (FCV) in the case when the hydrogen production thermal efficiency is over 40% and HTGR availability is over 80%. A goal of our R&D is to reduce the cost.

HTGR-IS Hydrogen Production Cost (JPY/Nm^3)	Hydrogen Production Thermal Efficiency (%)	HTGR Availability (%)	Economical Competitive Hydrogen Production Cost for Hydrogen Reduction Steelmaking (JPY/Nm^3)	Economical Competitive Hydrogen Production Cost for FCV (JPY/Nm^3)
45.2	30	70	33	39-48
41.4	30	80		
31.4	40	80		
25.4	50	80		

Stable, large-scale hydrogen production technologies are needed for the expected low-carbon society. The thermochemical iodine-sulfur (IS) process is one promising technology that harnesses heat energy from HTGRs.

Aiming at the formulation of a safety standard for connecting the HTTR to a hydrogen production facility, and at the establishment of a design applicable to the standard, we are verifying the integrity of process components and a facility made of industrial materials as a technological base for a connection test. Although an economic evaluation of HTGR-IS hydrogen production by a practical plant is necessary, accurate cost estimation using an optimized large-scale commercial plant is difficult at present.

An economic evaluation of hydrogen production by a future commercial HTGR-IS system was performed on the basis of economic evaluation data from an existing commercial plant using fossil fuel as a raw material. The following operational data were assumed: hydrogen production thermal efficiency of 50%, HTGR availability of 80%, and renewal of hydrogen production facilities every 10 years. The construction cost of a hydrogen production facility was set at two times that of a naphtha reforming plant of similar scale, assuming component rationalization and material cost reduction by technological development. Heat and electricity prices were set at 0.7 JPY/MJ and 5.8 JPY/kWh. The hydrogen production cost was estimated at 25.4 JPY/Nm^3. Capital and energy costs account for 13% and 78% of the total hydrogen production cost, respectively. Decreasing the HTGR construction cost and increasing HTGR availability are important for cost reduction. In Fig.6-6, this estimation is compared with evaluations of existing hydrogen production processes based on fossil fuels. The proposed HTGR-IS hydrogen production system is competitive with the existing systems, without any carbon dioxide capture and storage (CCS) being required. Considering the competitiveness of HTGR-IS hydrogen production costs in the industry, as in Table 6-1, the process satisfies the cost requirements for hydrogen reduction steelmaking and fuel cell vehicles in the case when the hydrogen production thermal efficiency is over 40% and the HTGR availability is over 80%. We will continue research and development of HTGR-IS hydrogen production, setting low cost as a goal.

Reference

Iwatsuki, J. et al., Economic Evaluation of HTGR IS Process Hydrogen Production System, JAEA-Review 2014-037, 2014, 14p. (in Japanese).

6–4 Toward a Demonstration that Reactor Safety Can Be Secured Using Only Natural Phenomena — To Establish a Test Procedure to be Employed Soon after Restart —

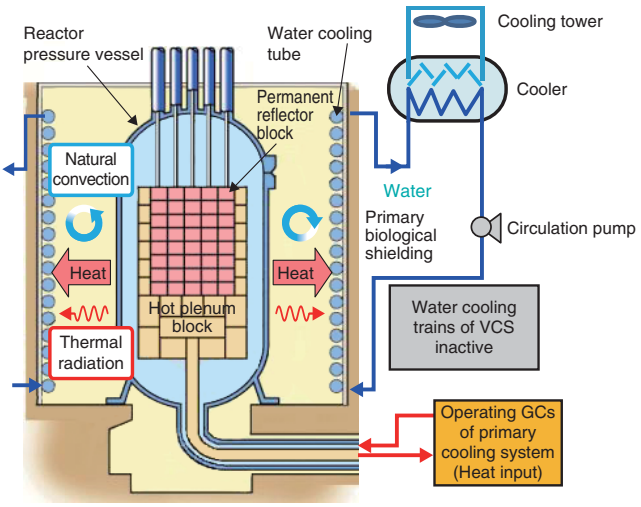

Fig.6-7 Vessel cooling system (VCS)
The VCS, which is set around the reactor pressure vessel on the surface of the primary biological shielding made of concrete, passively removes the retained residual and decay heat from the reactor core via the reactor pressure vessel by natural convection and thermal radiation.

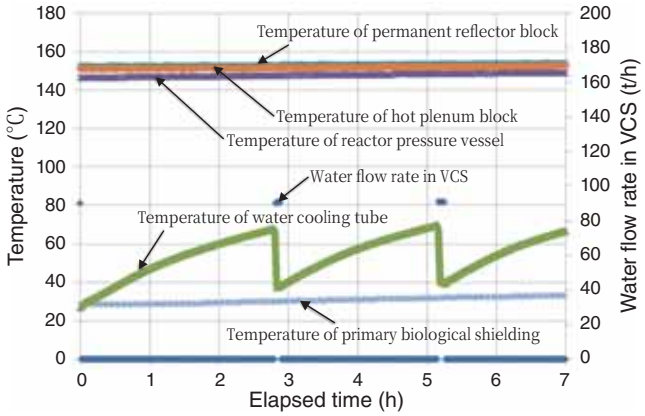

Fig.6-8 Effectiveness of the method for restricting local temperature rise of the water cooling tube
The water circulation pump was restarted twice for several minutes after 3 and 5 h following the start of the test. The temperature changes in the permanent reflector block, hot plenum block, reactor pressure vessel, and primary biological shielding were negligibly small, in contrast to that in the water cooling tube.

One of the safety demonstration tests for the HTTR is the loss of forced core cooling test, in which the forced cooling of the reactor core is lost without inserting control rods into the core and cooling by the vessel cooling system (VCS), as shown in Fig.6-7. It will be demonstrated that the HTGR is inherently safe because of natural phenomena within the actual reactor, even if those functions are not available to shut it down or cool it. This makes it possible to design a reactor that is free of severe accidents.

On the other hand, the local temperature of the uncovered cooling tube by the thermal reflector exceeds the limit from viewpoint for long-term use during the test, although the reactor remains safe. This temperature rise can be restricted by restarting the circulation pump for a sufficiently short period of time. However, it is difficult to predict numerically whether restarting the circulation pump would influence the temperatures of reactor internal structures such as a permanent reflector block, because the configuration of the water cooling tubes is complicated.

The reactor cannot be restarted unless the conformity to the new regulation standards is checked. Thus, in order to establish a safe and promising test procedure, a test was conducted using non-nuclear heat input from gas circulators while stopping water flow in the VCS. Multiple thermocouples were set to measure the temperatures of water cooling tubes to specify the position at which the temperature locally increased.

The test results showed the locally increased temperature position, although the temperature was sufficiently lower than the maximum allowable working temperature. On comparing the measured and numerical results, it was found that the local temperature rise of the cooling tube was restricted by starting up the circulation pump for a sufficiently short time (5 min) against the duration period of the test (7 h). On the other hand, the measured temperatures of the permanent reflector blocks, hot plenum blocks, reactor pressure vessel, and primary biological shielding (which were focused on as aspects of safety), were not influenced by the short-term pump restart, as shown in Fig.6-8.

Furthermore, from the results of the flow rate measurement of natural circulation of water by a high-accuracy electromagnetic flow meter, it was found that the natural circulation flow did not have any cooling effect on the temperature of the water cooling tube, because the flow rate increased and then decreased soon after the VCS was stopped.

Through this investigation, a procedure for the loss of forced core cooling test was established, which may be used soon after the restart of HTTR. The safety demonstration test, which shows that the inherent safety of the HTGR can be maintained by natural phenomena, has attracted attention from around the world, and has been conducted as an international joint research project.

Reference

Takada, S. et al., Proposal of Safety Demonstration Test Plan of HTTR by Cold Test of Loss of Forced Cooling with Vessel Cooling System Inactive, JAEA-Technology 2014-001, 2014, 34p. (in Japanese).

R&D of Fast Reactor Cycle Technology

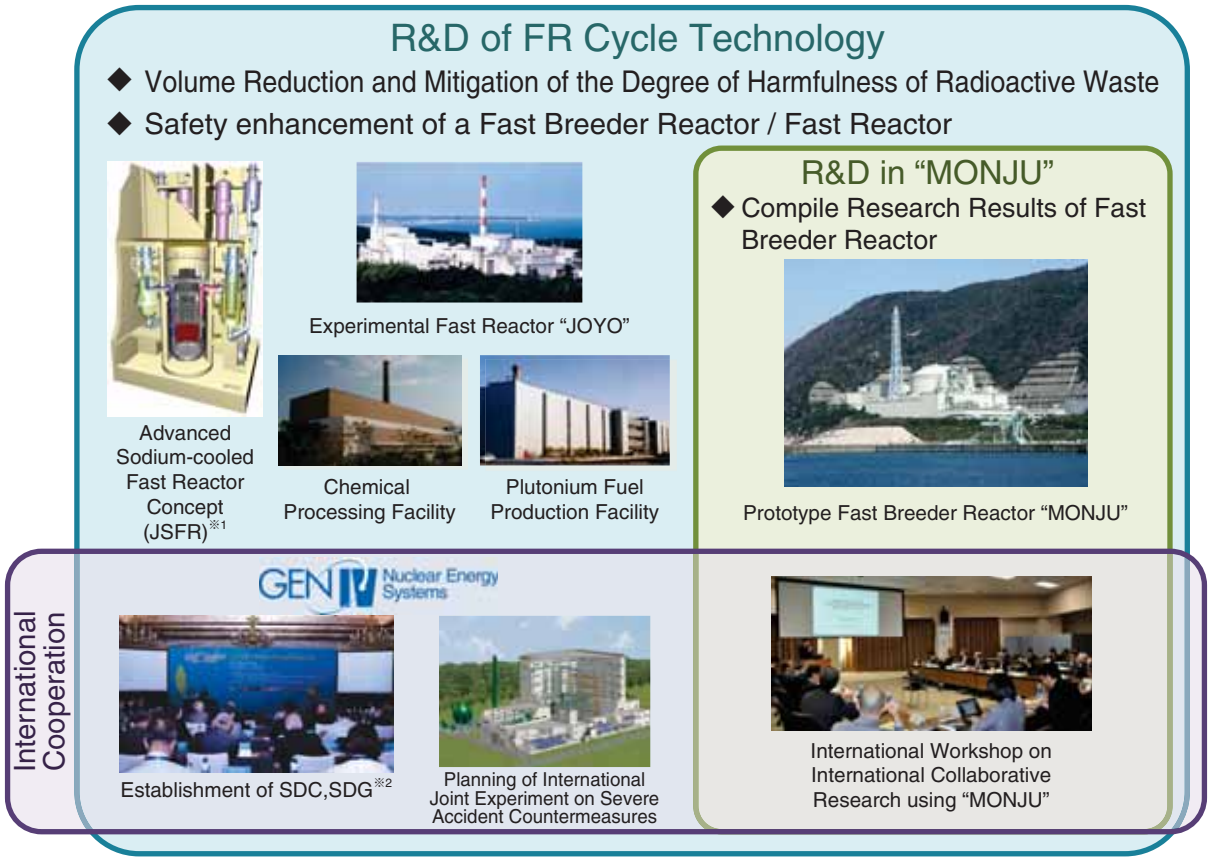

※1 JSFR: Japan sodium-cooled Fast Reactor
※2 SDC: Safety Design Criteria, SDG: Safety Design Guidelines

Fig.7-1 Overview of the research and development of fast reactor cycle technology
In line with Japan's new national energy policies, we are planning to promote research and development on "volume reduction and mitigation of the degree of harmfulness of radioactive waste" and "safety enhancement of a fast breeder reactor/fast reactor," utilizing international cooperation from FY 2014 onwards.

Prior to FY 2011, research and development activities had been conducted toward the commercialization of fast reactor (FR) cycle technology with the cooperation of electric utilities; the main concept was a combination of a sodium-cooled FR, advanced aqueous reprocessing, and simplified pelletizing fuel fabrication. After the accident at the Tokyo Electric Power Company, Incorporated Fukushima Daiichi Nuclear Power Station, we had focused our activities on efforts required to retain the technical capacity and to enhance safety of FR. Then, in April 2014, the Cabinet of Japan decided to approve the new Strategic Energy Plan as the basis for the orientation of Japan's new energy policies. In accordance with this plan, we have implemented R&D activities on "volume reduction and mitigation of the degree of harmfulness of radioactive waste" and "safety enhancement of a fast breeder reactor (FBR)/FR," utilizing international cooperation from FY 2014 onwards. On the safety enhancement issue, "Safety Design Criteria (SDC)" that we proposed were approved at the Generation-IV International Forum (GIF) in May 2013. "Safety Design Guidelines (SDG)," which are guidance documents for SDC, are currently being developed (Fig.7-1). This chapter describes the subsequent enhancement of safety and reliability, considering the features of a sodium-cooled FR and basic research on fuel cycle technology.

Experimental data showed a possibility of retaining degraded core material in a reactor vessel during a core destructive accident in a FBR/FR (Topic 7-1).

The reactor building of the Japan sodium-cooled FR (JSFR) is designed to have high resistance against extreme wind, snowfall, and fire, as well as earthquakes and tsunamis (Topic 7-2).

Regarding the sodium/water chemical reaction, which is an important issue for ensuring the safety and protection of the steam generator (SG), an analysis system has been developed for evaluating heat transfer tube failure propagation by reacting jet (Topic 7-3).

For the inspection of SG tubes, a technique for a large-scale simulation of a magnetic field around the structure has been developed (Topic 7-4).

A promising candidate material for long-life fuel cladding tubes has been developed through efforts at improving chemical compositions and fabrication methods (Topic 7-5).

With respect to the FBR fuel cycle, the fundamental data have been acquired to establish future reprocessing during a period of co-existence of light water reactors and FBR/FR (Topic 7-6).

7–1 Investigation of Molten Core Material Behavior

— An Experimental Study on the Containment of Core Disruptive Accidents —

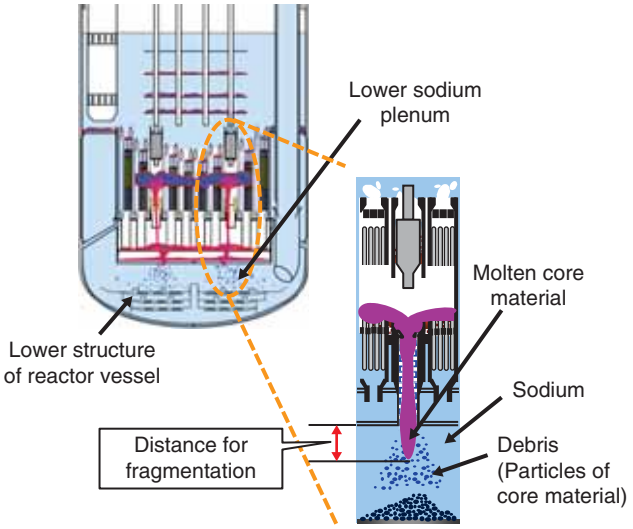

Fig.7-2 In-vessel retention (IVR) of molten core material
Although a column of molten core material may impose a large thermal load on the lower structure and thus degrade the integrity of a reactor vessel, if the column is fragmented into smaller particles, it will be easier to achieve IVR by the efficient quenching of the molten core material.

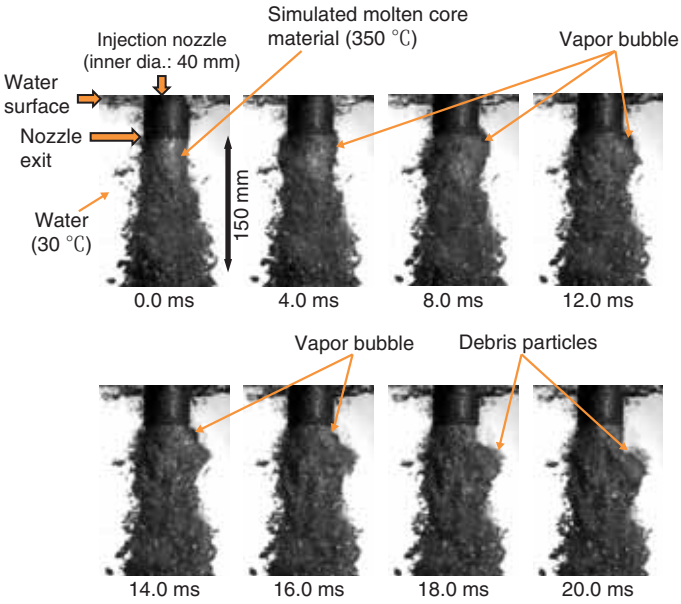

Fig.7-3 Images of fragmentation behavior
We conducted a fundamental experiment under visual observation using a high density melt and water to simulate molten core material and sodium, respectively. Our observations clarified the fragmentation behavior induced by local coolant-boiling and vapor expansion.

To contain the impact of core disruptive accidents (CDAs) of sodium-cooled fast reactors in the reactor vessels, it is important to retain molten core material within the vessel during CDAs. This concept is called in-vessel retention (IVR).

Molten core material discharged into the lower sodium plenum through control rod guide tubes has the potential to impose a significant thermal load on the lower structures of the reactor vessels, and thus may cause reactor vessel failure, compromising IVR. However, as shown in Fig.7-2, if the molten core material is fragmented into smaller particles well before it reaches the lower structures, the thermal load should be significantly reduced by enhanced quenching of this material. Hence, the development of a method for evaluating the distance for fragmentation is crucial for achieving IVR.

In this study, to obtain experimental data on the distance for fragmentation, we conducted a fundamental experiment that simulated the discharge behavior of molten core material under a sodium-cooled condition using simulants which enabled visual observation, as well as the establishment of a wide range experimental condition (e.g., discharge diameters). In the sodium-cooled condition, it is believed that a heat transfer mode with a liquid-liquid direct contact should be maintained, since even though sodium boiling would occur, the formation of a stable vapor film should be hindered at the contact interface between the molten core material and sodium. Fig.7-3 shows the fragmentation behavior of the simulated molten core material in such a heat transfer mode, which was established by a combination of the simulated molten core material and water. The experimental results revealed that fragmentation in the sodium-cooled condition was induced by thermal factors, including local coolant boiling and vapor expansion, in contrast to light water reactor conditions where the fragmentation would be induced by hydrodynamic instabilities. Moreover, the experimental results showed that thermal interactions facilitated the fragmentation and reduced the distance for fragmentation down to approximately 10 percent of the value predicted using the existing representative correlation.

The present study, which contributes to the development of a method for evaluating the distance for fragmentation, suggests that the high coolability of sodium is effective for IVR. This study was sponsored by the Ministry of Education, Culture, Sports, Science and Technology of Japan (MEXT).

Reference

Matsuba, K. et al., Fundamental Experiment on the Distance for Fragmentation of Molten Core Material during Core Disruptive Accidents in Sodium-Cooled Fast Reactors, International Electronic Journal of Nuclear Safety and Simulation, vol.4, no.4, 2013, p.272–277.

7–2 Aiming for Robustness for the Reactor Building to Withstand Severe Natural Disasters — Evaluation of External Hazards to the Reactor Building —

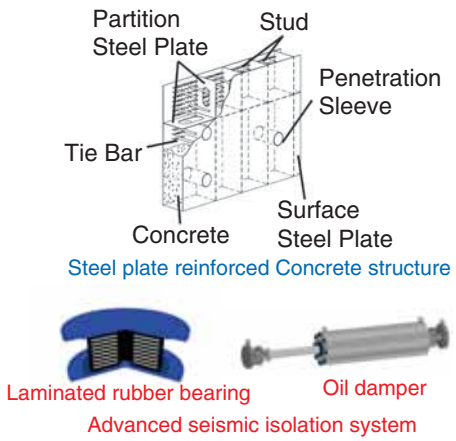

Fig.7-4 Steel plate reinforced concrete (SC) structures and the advanced seismic isolation system
SC structure comprising a pair of steel plates with a concrete filling in between, and an advanced seismic isolation system with laminated rubber bearings and dampers have been investigated.

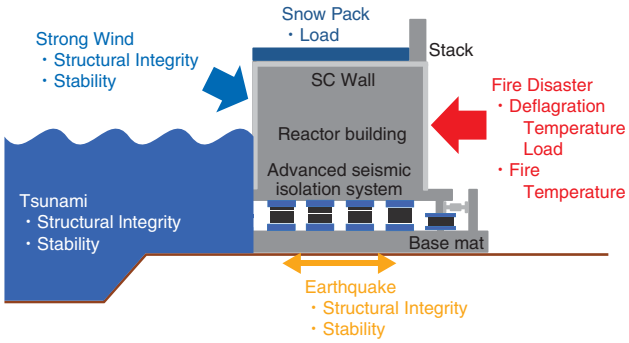

Fig.7-5 Evaluated external hazards
The evaluated external hazards were earthquake, tsunami, snowpack, strong wind, and fire disaster.

Table 7-1 Results of structural integrity evaluation of a reactor building and seismic isolation system against an earthquake
The results of the earthquake evaluation show that the structural integrity and stability of the reactor building and the advanced seismic isolation system were maintained, and the margin (evaluated value/requirement) was greater than two.

	Evaluated items		Margin
Reactor building	Structural integrity	Bending Moment (NS / EW)	2.8 / 2.9
		Shear force (NS / EW)	2.2 / 3.6
	Stability	Overturning	7.7
		Sliding	6.5
		Vertical bearing capacity	7.8
Seismic isolation system	Laminated rubber bearing	Shear strain	2.1
		Tensile strain	9.7
		Compressed strain	2.4
	Oil damper	Displacement	2.3

Table 7-2 Results of structural integrity evaluation of a reactor building and seismic isolation system against a tsunami
The results of the tsunami evaluation show that the structural integrity and stability of the reactor building and advanced seismic isolation system were maintained if an appropriate wall thickness was set.

	Evaluated items			Margin
SC structure	Member	Wall Member (wall thickness 1250 mm)	Bending Moment	1.2
			Shear force	1.3
		Building	Bending Moment (NS / EW)	471 / 286
			Shear force (NS / EW)	32 / 16
	Stability	Overturning		20
		Sliding		22
		Vertical bearing capacity		11
Seismic isolation system	Laminated rubber bearing	Shear strain		3.2
		Tensile strain		402
		Compressed strain		– (Not occur)
	Oil damper	Displacement		1.8

A steel plate reinforced concrete (SC) structure has been considered for the building wherein the sodium-cooled fast reactor (SFR) is housed. The SC structure comprises a pair of steel plates with a concrete filling in between, held together by studs, etc. In addition, an advanced seismic isolation system with laminated rubber bearings and oil dampers has been investigated for adoption against earthquakes (Fig.7-4).

In response to the Great East Japan Earthquake and the accident at the TEPCO's Fukushima Daiichi NPS in March 2011, the structural integrity and stability of reactor buildings against external hazards have been re-evaluated. Fig.7-5 shows the evaluations for earthquake, tsunami, snowpack, strong wind, and fire. These external hazards are threats to the structural integrity and stability of the reactor building; hence, to protect the safety of a reactor building, it must be constructed in such a way as to withstand them. In fact, it is necessary to ensure that loads due to earthquakes and tsunamis do not damage an outer wall nor affect the reactor building inside.

The results of the evaluation against earthquake and tsunami are shown in Tables 7-1 and 7-2, respectively. They show that the structural integrity of a reactor building can presumably be maintained with appropriate wall thickness, and that seismic or tsunami loads do not lead to the reactor building being damaged. Evaluation results were also obtained showing that structural integrity could be maintained against other evaluated events, such as snowpack, strong wind, and fire.

This study includes some of the results of the "technical development program on a commercialized FBR plant" entrusted to Japan Atomic Energy Agency (JAEA) by the Ministry of Economy, Trade and Industry of Japan (METI).

Reference

Yamamoto, T. et al., Evaluation of External Hazard on JSFR Reactor Building, Proceedings of 2013 International Congress on Advances in Nuclear Power Plants (ICAPP 2013), Jeju Island, Korea, 2013, paper FD211, 9p., in USB Flash Drive.

7–3 Numerical Simulation for Safety Evaluation of the Steam Generators in Fast Reactors
— A Multiphysics Evaluation System for Tube Failure Accidents —

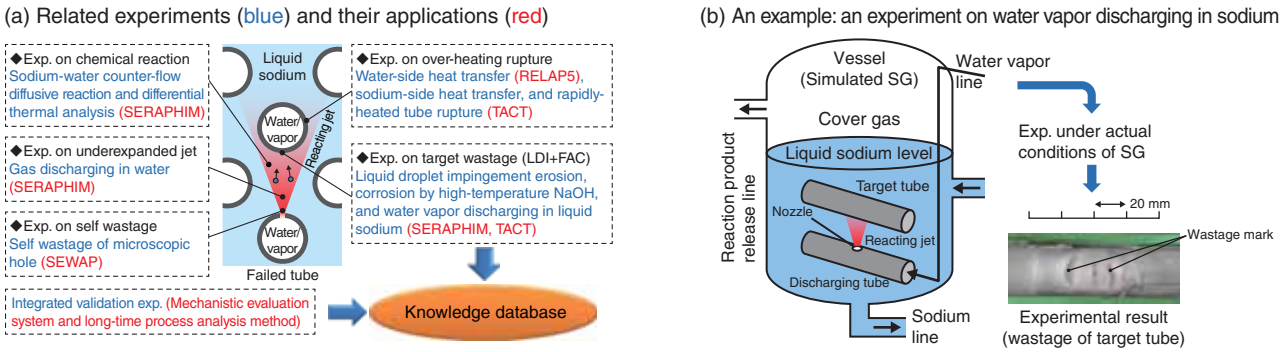

Fig.7-6 Phenomena appearing under tube failure accidents in a steam generator and their related experiments
Some experiments related to tube failure accidents were performed to develop and validate the numerical methods.

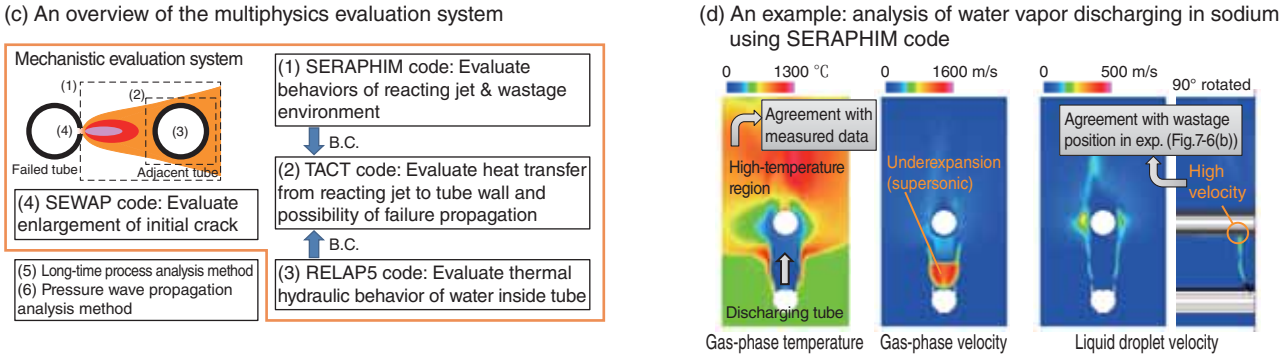

Fig.7-7 A multiphysics evaluation system and an example of numerical simulation
To evaluate tube failure accidents, a multiphysics evaluation system comprising mechanistic numerical methods was developed. The applicability of the numerical methods was confirmed through the analyses of the related experiments.

When pressurized water or vapor leaks from a failed heat transfer tube in a steam generator (SG) of sodium-cooled fast reactors, a high-velocity, high-temperature jet reacts chemically with the surrounding sodium and causes wastage and degradation of the mechanical strength on the adjacent tubes (Fig.7-6). Significant progress of such material damage may lead to failure propagation. Prevention of failure propagation is a major concern in designing the SG. In this study, a multiphysics evaluation system comprising mechanistic numerical methods was newly developed to evaluate the possibility of the occurrence of the failure propagation. The developed system is applicable to a wider variety of operating conditions and design options of the SG than the conventional evaluation method based on exhaustive demonstration experiments.

The systematic experiments shown in Fig.7-6 were conducted for the elucidation of phenomena and the acquisition of data to validate the numerical methods. In these experiments, we succeeded in identifying a dominant process in the sodium-water chemical reaction, measuring the sodium-side and water-side heat transfer behaviors, measuring the rupture behaviors of the rapidly-heated tube, deriving a correlation between the wastage rate and some parameters relevant to liquid droplet impingement erosion and flow accelerated corrosion, and so forth. As an example, Fig.7-6 shows the experiment on water vapor discharging in liquid sodium to obtain data for target wastage under actual plant conditions. A knowledge database including the quantitative uncertainty of the experimental data was constructed. As shown in Fig.7-7, the mechanistic numerical methods were developed for the three regions: (1) the reacting jet, (2) the heat transfer tube, and (3) the inside of the tube. About region (1), a SERAPHIM code with an incorporated wastage environment evaluation model was developed. The applicability of the SERAPHIM code was confirmed through the analysis of the abovementioned water vapor discharging in liquid sodium (Fig.7-7). A TACT code involving the numerical models for heat transfer from the reacting jet to the tube wall and failure judgment (region (2)), and a RELAP5 code involving the water-side heat transfer correlation applicable to the rapid heating condition (region (3)) were also constructed. Our evaluation system can make a large contribution toward designing the SG with an appropriate safety margin.

The present study was partly supported by the Ministry of Education, Culture, Sports, Science and Technology of Japan (MEXT).

Reference

Uchibori, A. et al., Development of Numerical Evaluation Methods for Multi-Physics Phenomena under Tube Failure Accident in Steam Generator of Sodium-Cooled Fast Reactor, Nippon Kikai Gakkai Ronbunshu, B Hen, vol.79, no.808, 2013, p.2635-2639 (in Japanese).

7–4 Challenges Facing the Improvement of Inspection Technology for Steam Generator Tubes
— Large Scale 3D Simulations of ISI of FBR "Monju" SG Tubes Using ECT —

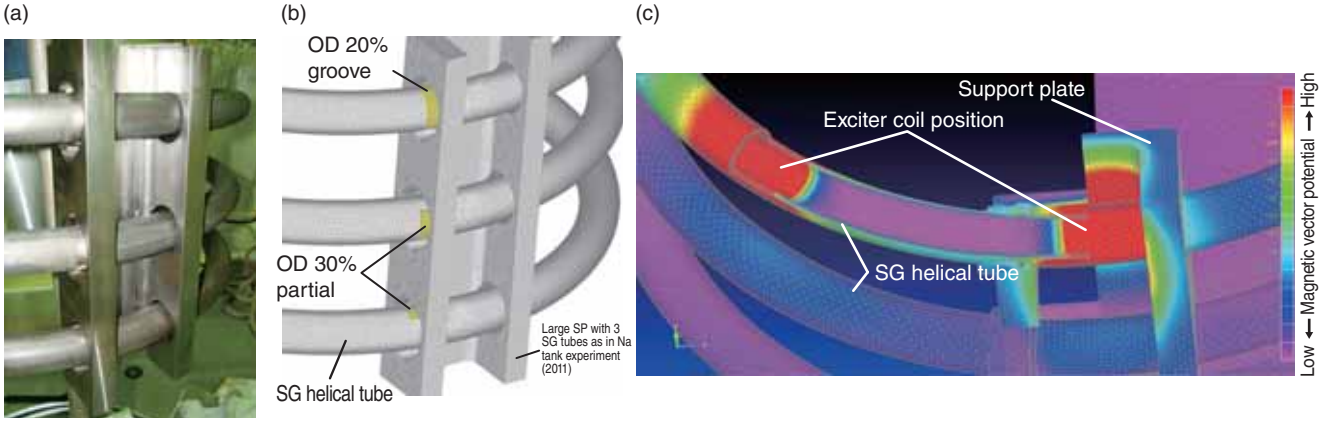

Fig.7-8 (a) View of the mock-up test model; (b) FEM model; (c) Magnetic vector eddy current field distribution
(a) A large support plate (SP) model with three SG helical tubes. (b) FEM model using 2nd order tetrahedrons. (c) The magnetic vector eddy current field distribution obtained by scanning the upper SG helical tube with ECT sensors.

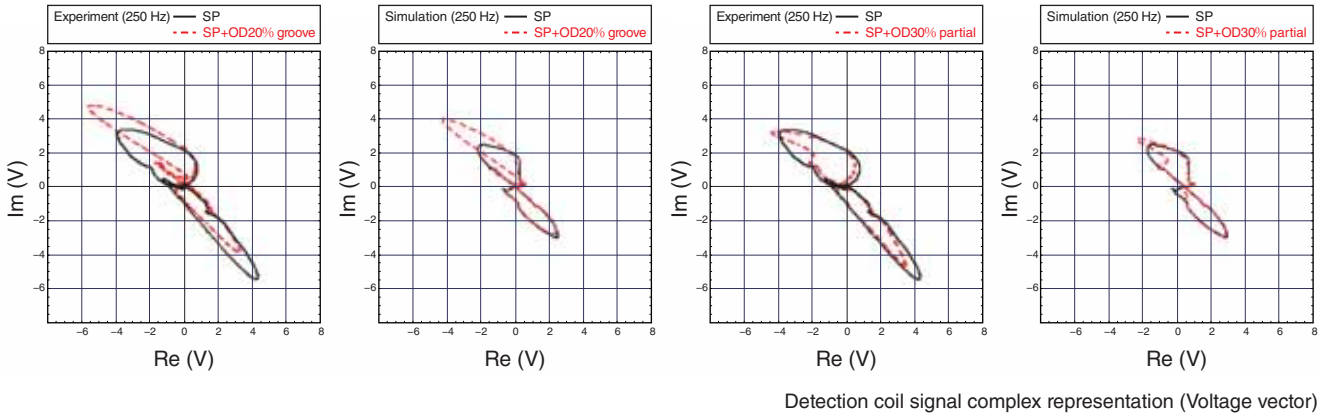

Fig.7-9 Comparison between ECT measurements and FEM simulations of SP and defects
The OD20% groove is a fully circumferential defect and the OD30% partial groove is a quarter-circumferential defect. The excitation frequency in both experiment and simulation is 250 Hz.

The eddy current technique (ECT) is a well-established method for detecting defects in metallic structures, which is easier and more repeatable than alternatives; it works by monitoring changes in a coil's impedance. When applying ECT to the assessment of the soundness of the SG tubes of "Monju" FBR, the complexity of the large metallic support plate (SP) structure surrounding the long SG helical tubes adds additional electromagnetic interference or noise in the primary electromagnetic field created by the ECT coils. To improve the inspection technology for FBR SG tubes, precise evaluation of these effects requires reliable and verified numerical electromagnetic tools operating in conditions as close as possible to those in "Monju."

A three dimensional (3D) electromagnetic code, using finite element method (FEM), researched and developed in-house at JAEA, analyzed the electromagnetic field of an ECT system composed of excitation-detection coils. The code was validated by comparing numerical simulations with experimental measurements using three SG helical tubes with a large SP mock-up (Fig.7-8(a)). Large scale numerical simulations of FEM models with up to 5 million second-order tetrahedrons (Fig.7-8(b)) were run on JAEA supercomputers with 1024 parallel CPU cores, distributed in a mixed Open MP-MPI environment (Fig.7-8(c)). Variation in the defect signals due to helical structures and defect proximity to the SP was compared against measurements for outer tube defect (OD) grooves spanned full circumferential with depth 20%tw (from tube wall thickness), and around defects that spanned only a quarter part of the circumference and had a depth of 30%tw. A full comparison with the experimental results for defect and SP signals validated the FEM computation of ECT signals for SG helical tubes (Fig.7-9).

Large scale numerical simulations using reliably tested and verified FEM codes are aimed at providing improved understanding of the ECT signal/noise ratio, where electromagnetic interference appears due to the close proximity of multiple tubes or intricate 3D structure geometries to facilitate further development of inspection technology for "Monju" SG tubes.

Reference

Mihalache, O. et al., Large Scale 3D FEM Electromagnetic Simulations and Validations for FBR Steam Generator Tubes, Studies in Applied Electromagnetics and Mechanics, vol.38, 2014, p.94–102.

7–5 Development of Long Life Fuel Cladding Tube for the Fast Reactor

— 11Cr-ODS Steel with Sufficient Strength, Toughness, and Corrosion Resistance —

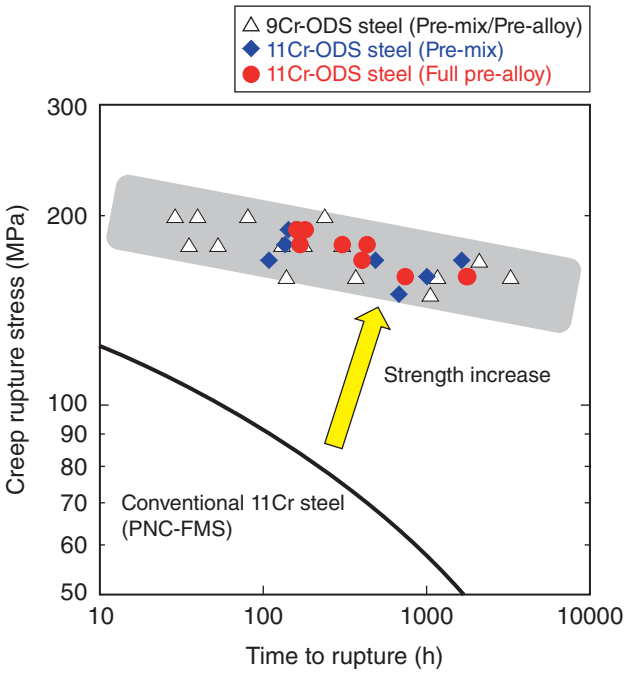

Fig.7-10 Creep strength of 9 and 11Cr-ODS steels at 700 °C
The 9 and 11Cr-ODS steels exhibit the same level of creep strength, showing that the effect of Cr increase on creep strength is small. The suspected reason is that 11Cr-ODS steel is sufficiently strengthened by the application of oxide dispersion.

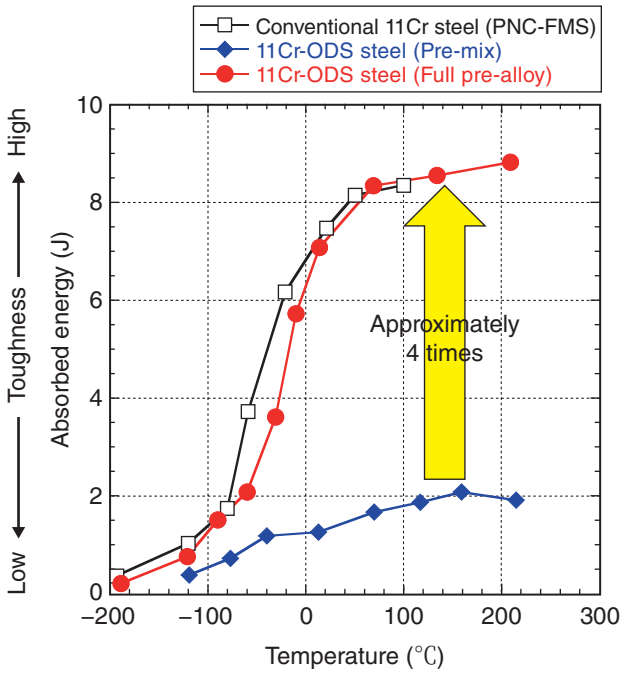

Fig.7-11 Toughness of full pre-alloy and premix ODS steels
We have succeeded in producing 11Cr-ODS steel with good toughness. The toughness is equal to that of conventional 11Cr steel (PNC-FMS) with good toughness, which is not strengthened by oxide dispersion.

To make the advanced fast reactor (FR) safe and economical, it is necessary to develop fuel cladding tube with superior strength and dimensional stability, since the cladding tube will be used under severe conditions (e.g., high temperature and high-dose neutron irradiation). Hence, we have researched and developed oxide dispersion-strengthened (ODS) steel cladding tubes. 9Cr-ODS steel cladding tubes have been produced as a primary candidate, and engineering requirements for mass scale production of these tubes have been studied.

If the dissolution of cladding tubes in nitric acid increased during the spent fuel reprocessing process, the amount of high-level radioactive waste (vitrified waste) and the cost of the fuel-cycle system would both increase. Therefore, we have also developed ODS steels containing over 9wt% Cr to improve corrosion resistance in nitric acid.

High-Cr ODS steel should be granted properties equivalent to those of 9Cr-ODS steel to be satisfactory for use as a fuel cladding tube. Therefore, the matrix must be tempered martensite, as it is for 9Cr-ODS steel. We selected 11Cr for the high-Cr martensitic ODS steel, and modified the other element concentrations based on our research into the structure control (i.e., crystal structure and grain size) and strengthening mechanism. The high-temperature and long-term strength of the optimized 11Cr-ODS steels were evaluated by creep tests at 700 °C which is assumed to be the highest temperature that the cladding will attain during normal operation of an advanced FR. The creep strength of 11Cr-ODS steels was much better than that of conventional 11Cr heat-resistant steel (PNC-FMS), and nearly equal to that of the 9Cr-ODS steels, as shown in Fig.7-10.

In general, high strength steels tend to have low toughness, i.e., they are weak against cracks and impacts. In addition, ODS steel is subject to the influence of defects, such as inclusions (i.e., coarse oxide and nitride), that degrade its toughness. We applied a full pre-alloy metallurgy method to the production of 11Cr-ODS steels, instead of a simple pre-mix metallurgy method. The pre-alloy method can greatly decrease inclusions, leading to fracture. The toughness of the full pre-alloy ODS steel is much greater than that of pre-mix ODS steel, as shown in Fig.7-11.

We have confirmed the potential of 11Cr-ODS steel with good corrosion resistance for use as the material for the long life fuel cladding tube. In the next step, we will proceed to conduct several kinds of tests on the cladding tubes composed of full pre-alloy 11Cr-ODS steels.

Reference

Tanno, T. et al., Evaluation of Mechanical Properties and Nano–Meso Structures of 9–11%Cr ODS Steels, Journal of Nuclear Materials, vol.440, issues 1–3, 2013, p.568–574.

7–6 Toward a New Reprocessing Process for the Transitional Period to the Fast Reactor Cycle

— The Development of a Uranium and Plutonium Co-recovery Process (Co-processing Process) —

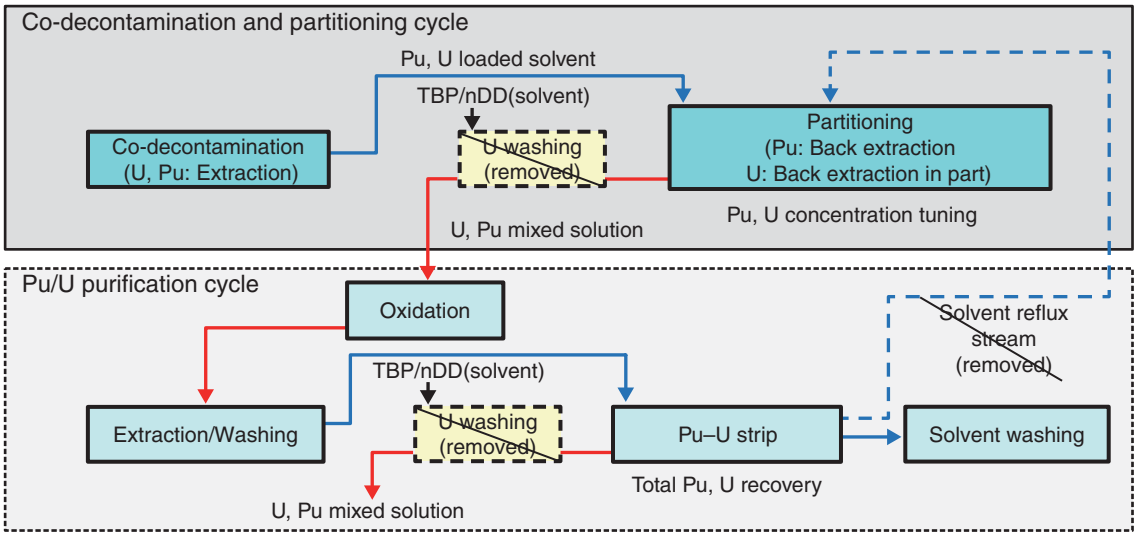

Fig.7-12 Schematic of the co-recovery process
The elimination of the U washing stages and the solvent reflux stream, which are both part of the conventional PUREX process, prevents Pu isolation in the process and improves its proliferation resistance.

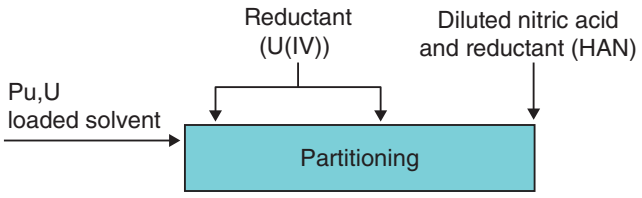

Fig.7-13 Reduction of Pu in the partitioning stage
Pu is stripped into an aqueous phase in this stage by reducing it to trivalency using U(IV) and HAN as reductants.

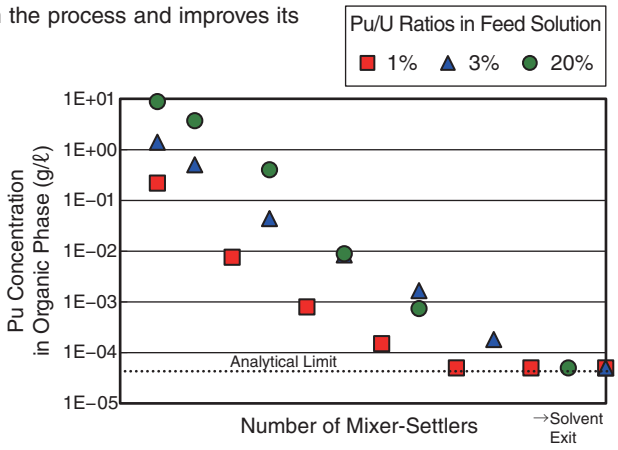

Fig.7-14 Pu concentration profiles in the partitioning stage
Pu is completely stripped in this stage because Pu concentrations in solvent effluents are less than the analytical limit.

The transition from the current light-water reactor (LWR) cycle to the FR cycle will span several decades. In this period, LWRs and FRs will coexist, and not only UO_2 fuel but also mixed oxide (MOX) fuels will be discharged from these reactors. For the purpose of reprocessing these spent fuels with varying plutonium contents, a U-Pu co-recovery process (co-processing process) is currently being developed. In contrast to the conventional reprocessing process (PUREX), which recovers Pu separately from U, the co-processing process will recover the two elements together to prevent the isolation of Pu to improve the proliferation resistance (Fig.7-12).

Mixer-settler tests of the co-processing process have been conducted using U/Pu nitric acid solutions at the Operational Testing Laboratory (OTL) of the Tokai Reprocessing Plant (TRP). To assure complete stripping of Pu in a mixture with U in the partitioning stage, the appropriate usage of reductants (U(IV) and HAN)—which reduce Pu to a non-extractable trivalent state—has been evaluated in the tests (Fig.7-13).

The adopted Pu/U ratios of the feed solutions used in the tests were 1%, 3%, and 20%, considering the composition of the future spent fuels from a LWR, a LWR-MOX hybrid, and a FR-MOX reactor. In the tests, complete stripping of Pu in a mixture with U has been observed at all Pu/U ratios (Fig.7-14), and the U/Pu ratios in the recovered U/Pu mixed solutions could be controlled within the 0.5–2.0 U/Pu ratio range, which was suitable for the fabrication of FR-MOX fuel.

Further tests are to be conducted to improve the process, and will use centrifugal contactors.

The present study was sponsored by the Agency for Natural Resources and Energy, Ministry of Economy, Trade and Industry, of Japan (METI), in the FY 2010 and 2011.

Reference

Yamamoto, K., Ohbu, T. et al., Development of U and Pu Co-Recovery Process (Co-Processing) for Future Reprocessing, Proceedings of International Nuclear Fuel Cycle Conference (GLOBAL 2013), Salt Lake City, USA, 2013, paper 7797, 4p., in CD-ROM.

Progress in Decommissioning of Nuclear Facilities and Treatment and Disposal of Radioactive Waste

Safe and efficient decommissioning of our nuclear facilities and treatment and disposal of radioactive wastes are important issues to consider in our research and development activities. We are currently setting up systems to decommission nuclear facilities and manage radioactive waste and are also developing the related technologies (Fig.8-1).

Furthermore, we will be responsible for disposing radioactive waste generated not only from our research facilities but also from universities, industrial facilities, and other sites.

R&D for the decommissioning of nuclear facilities

We have developed an engineering system for decommissioning and a verification or evaluation system for clearance. It is important to assess the applicability of these systems to the decommissioning of several nuclear facilities of JAEA. We already confirmed that the system is applicable to a research reactor. This time, we applied the system to decommissioning of the Uranium Refining and Conversion Plant, which is one of the nuclear fuel cycle facilities, and showed that the system is applicable to it. (Topic 8-1).

R&D for waste treatment and disposal

There are various chemical forms of sludge-like uranium-bearing waste, and its uranium concentration is very high.

We must select which uranium separation process to apply to various uranium-bearing wastes. Therefore, we have been developing a process for selective separation of uranium by using mineral acid. As part of this study, we confirmed that the process that uses hydrochloric acid is applicable to the CaF_2 sludge and spent filter aid (Topic 8-2).

R&D to characterize radioactive waste

For the safe disposal of radioactive waste packages, their radioactive content must be evaluated. Therefore, we developed related techniques to enable reasonable and effective analysis of the radioactive waste. However, because some radionuclides contained in the radioactive waste are hard to analyze, we developed a new method to analyze ^{242m}Am (Topic 8-3).

Moreover, to deal with the accident at the Tokyo Electric Power Company, Incorporated (TEPCO) Fukushima Daiichi Nuclear Power Station (NPS), we are developing a new analytical method to measure the concentration of radionuclides in the wastewater. Our systematic method to analyze radioactive waste is also being applied to determine the concentration of radionuclides in or on the rubble and trees (Chapter 1, Topics 1-20, 1-21).

Disposal of low-level radioactive waste

Trench-type disposal is a method for disposing low-level radioactive waste in a facility without engineered barrier located at a few meters below the surface. To improve the safety of the trench facility, it is important to reduce the rate at which rainfall infiltrates into the waste layer (due to the low permeability of cover soil). Therefore, we evaluated the rate of water infiltration when a geomembrane and a low-permeability soil layer are installed in the upper cover soil, considering the permeability of these layers. We found out that using a low-permeability soil layer and a geomembrane is effective to reduce water infiltration rate into the waste layer of the trench facility (Topic 8-4).

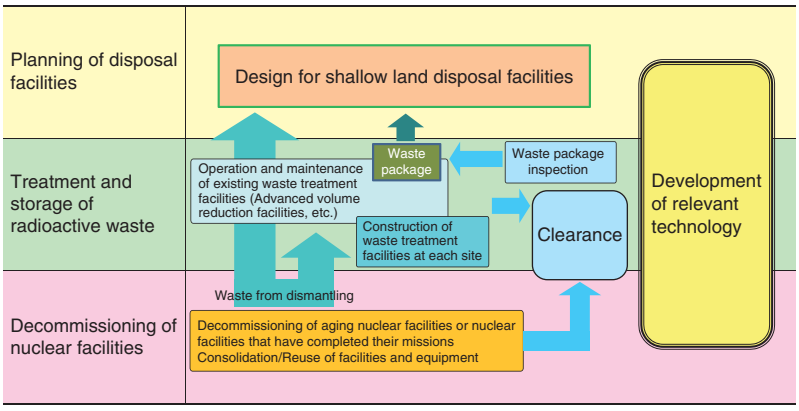

Fig.8-1 Outline of measures for decommissioning of nuclear facilities and treatment and disposal of radioactive waste
We are setting up systems to decommission nuclear facilities and manage radioactive waste. In addition, we are developing related technologies (e.g., decommissioning, treatment, and disposal) and constructing radioactive waste treatment and disposal facilities.

R&D to Improve Technology and Reliability of Geological Disposal in Japan

Geological disposal is one option for long-term isolation from human environments of high-level radioactive waste (HLW) produced during nuclear power generation. This is a critical issue that the present generation must sensibly deal and that remains crucial despite any revision of the national nuclear energy policy. In Japan, spent fuel from power reactors is reprocessed to extract reusable uranium and plutonium for power generation. The liquids separated from the spent fuel during chemical reprocessing are solidified into a stable glass form. In the Japanese disposal concept, vitrified wastes are encapsulated in a thick steel overpack surrounded by highly compacted bentonite and then placed in a stable geological environment at more than 300 m below the surface (Fig.8-2). Implementing geological disposal of

HLW is a long-term project that will last over 100 years. The project begins with site selection and continues to repository construction and operation, which will be followed by backfill for repository closure. It is thus of great importance to proceed efficiently with the project, as a national responsibility, by continuously improving its sound technical basis and applying these attitudes to implementation, regulatory activities, and, most importantly, to enhance public confidence. To this end, we made and will continue to make steady progress in research and development (R&D) in various fields, such as in geoscience, repository engineering, and safety assessment, to improve the technologies used for and reliable geological disposal in Japan.

At present, our R&D focuses specifically on projects at two underground research laboratories (URLs)—one at Mizunami, which researches crystalline rocks, and the other at Horonobe, which researches sedimentary formations (Fig.8-3)—with the main aim being to develop a sound technical basis for formulating and implementing safety regulations. At the end of 2013, some research galleries were made available for use at a depth of 500 m at Mizunami and at 350 m at Horonobe. Multidisciplinary investigations are ongoing, because the reliability of various investigative techniques should be tested and verified before the site characterization program begins (Topics 8-5, 8-6, and 8-7). In addition, studies on tectonics, volcanic and faulting activities, and so on are in progress to evaluate the long-term stability of geological environments in Japan (Topics 8-8 and 8-9). In parallel with such geoscience efforts, we are conducting an extensive study to assess the performance of the disposal system, of engineered barrier systems, and of the long-term chemistry and migration of radionuclides at Tokai to expand our knowledge base for geological disposal (Topics 8-10, 8-11, and 8-12). These studies exploit data and information about geological environments that were obtained through geoscience research at both URLs. The prototype knowledge management system that was developed in 2010 is being improved to systematically provide and transfer multiple associated R&D results to both implementer and regulator and to ensure their safety.

Our efforts also focus on promoting public understanding by disseminating relevant information and by opening our R&D facilities to the public.

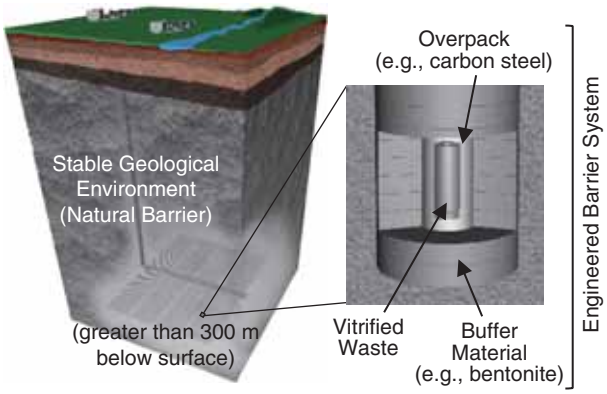

Fig.8-2 Schematic view of basic concept for the geological disposal of high-level radioactive waste (HLW) in Japan

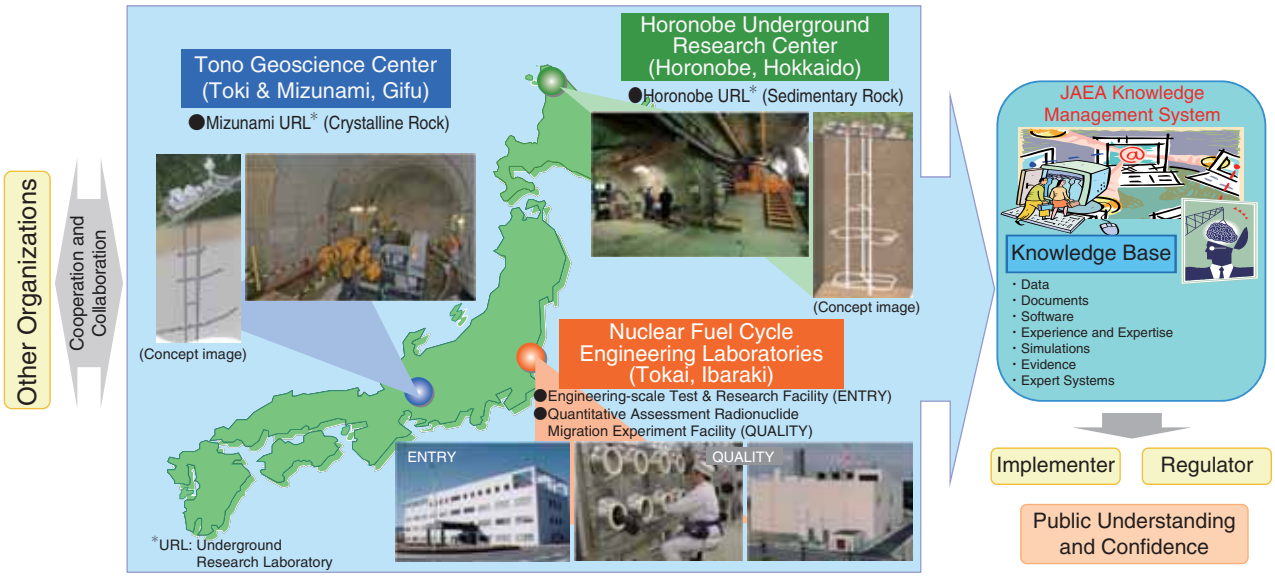

Fig.8-3 System for implementing JAEA R&D activities

Implementing Safety Measures at Tokai Reprocessing Plant and Enhancing Reprocessing Technologies

After the Great East Japan Earthquake and the accident at the TEPCO's Fukushima Daiichi NPS, various emergency safety measures were implemented at the Tokai Reprocessing Plant (TRP). To reduce the probability of hazards at the TRP, efforts focused on solidifying and stabilizing as soon as possible the highly active liquid waste (HALW) at the Tokai Vitrification Facility (TVF) and the plutonium solution at the Plutonium Conversion Development Facility (PCDF). Vitrifying the all stored HALW is estimated to require two decades. Thus, an advanced glass melter is under development to make steady progress on the solidification and stabilization of the HALW.

For low-level radioactive effluents, a cement-based solidification method accompanying a nitrate-ion decomposition process has been developed to reduce the environmental impact.

The following studies on advanced reprocessing technologies are ongoing:

- Separating Ruthenium from HALW (Topic 8-13).
- Developing Uranium and Plutonium co-recovery process.

8–1 Toward an Optimized Decommissioning Plan

— Development of Formula to Evaluate Manpower Requirements for Dismantling Nuclear Facility —

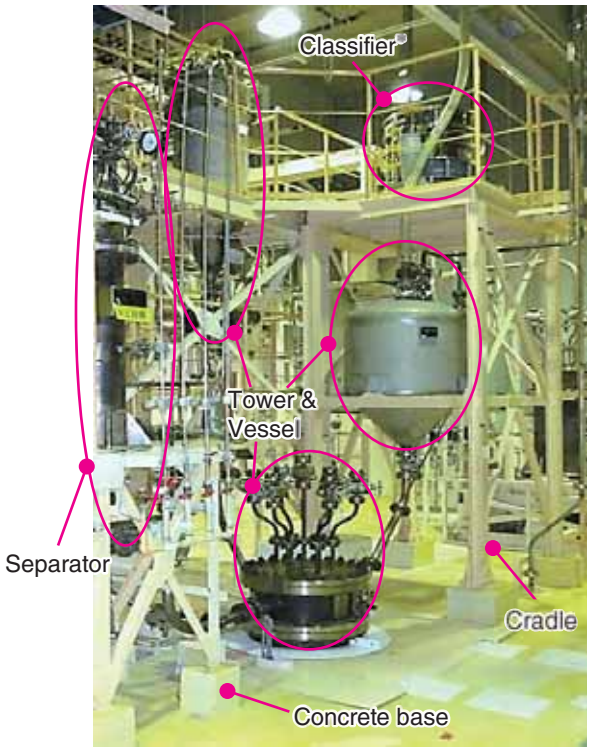

* Here, "Classifier" is categorized as "Crusher."

Fig.8-4 Typical DP equipment and its state before dismantling
All DP equipment was contaminated with U compounds and installed in "Cradle" or on "Concrete base."

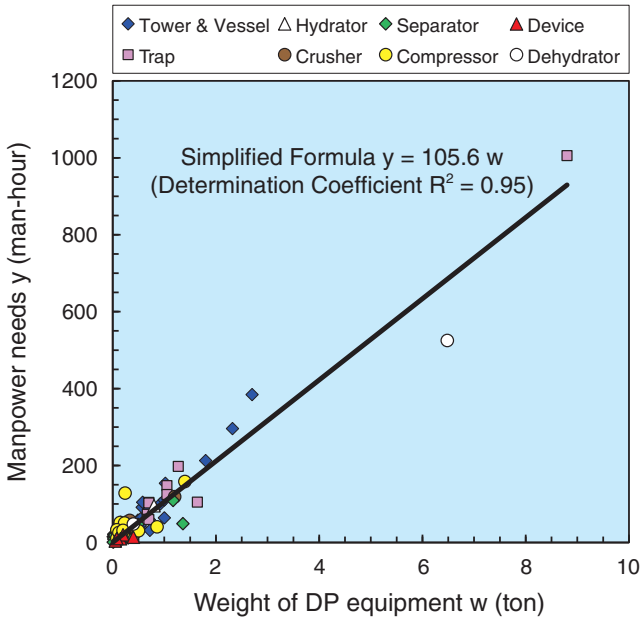

Fig.8-5 Correlation between the weight of DP equipment and manpower requirements for dismantling DP equipment
Almost all types of DP equipment were dismantled by the similar procedure. Because of this, the manpower requirements for dismantling these types of DP equipment could be estimated by one simplified formula with high accuracy, although the number of data or their range for each type of DP equipment was limited.

Nuclear facilities are dismantled when their mission is complete. To implement effective dismantling, we are setting up a system to estimate a priori project management data such as cost, manpower requirements, exposure dose, and waste generation. This system uses formulas established by analyzing data collected during previous dismantling projects.

The formulas to determine the manpower requirements for dismantling the equipment, for example, were represented by linear approximations with the equipment weight according to the equipment type. We have already confirmed that these formulas are applicable to a research reactor, but not to other types of nuclear facilities. Therefore, we verified the formulas for use with one of the uranium (U) handling facility: the U Refining and Conversion Plant (URCP).

At the URCP, many types of equipment were dismantled, such as "Tower & Vessel," "Trap," "Crusher," "Separator," and "Compressor." The correlation between equipment weight and manpower required for dismantling were analyzed, revealing that the formulas for the type of equipment could be also applied to the URCP. However, few actual data were collected for some types of equipment that making formulas for these was impossible. Moreover, some formulas had low accuracy because every equipment was very light and the distribution of data was localized.

Therefore, we considered grouping the actual data together for equipment that had similar installation and dismantling procedures. In this case, we determined that most types of dry conversion process-related equipment (DP equipment) used to run U powder inside were supported by "Cradle" and "Concrete base" (Fig.8-4) and were dismantled by a similar procedure. Because of this, a simplified formula was fit to these types of DP equipment (Fig.8-5). The simplified formula depends on the total weight of the DP equipment and accurately provides the manpower requirements for dismantling all DP equipment.

We are currently developing an appropriate formula as per the type of nuclear facility, and improve the system to the useful one to optimize the decommissioning plan.

Reference

Izumo, S. et al., Development of Evaluation Models of Manpower Needs for Dismantling the Dry Conversion Process-Related Equipment in Uranium Refining and Conversion Plant (URCP), Proceedings of the ASME 2013 15th International Conference on Environmental Remediation and Radioactive Waste Management (ICEM 2013), Brussels, Belgium, 2013, ICEM2013-96097, 9p., in CD-ROM.

8–2 Efficient Separation of Uranium from Sludge-Like Uranium-Bearing Waste

— Developing Process to Selectively Separate Uranium by Using Hydrochloric Acid —

Fig.8-6 Drums for storing sludge-like uranium-bearing waste

Fig.8-7 Sludge-like uranium and the spent adsorbent

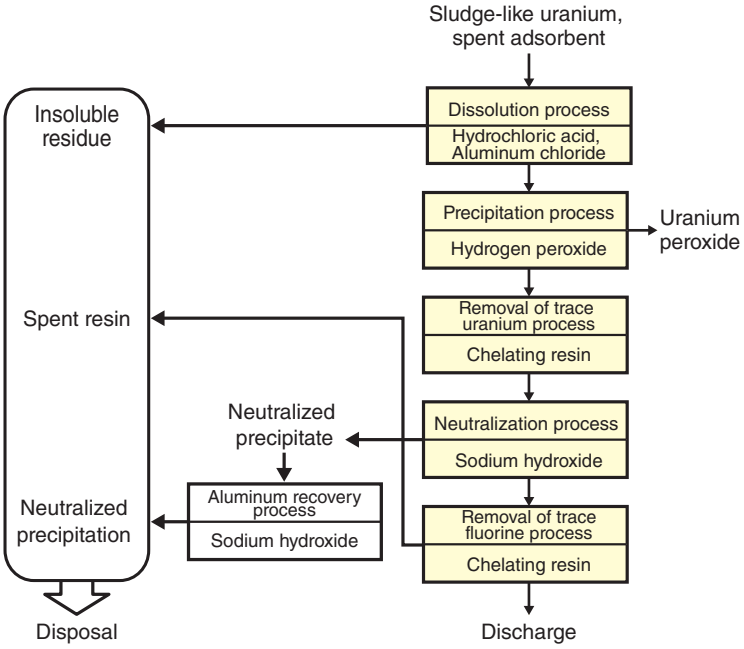

Fig.8-8 Process using hydrochloric acid to separate uranium from sludge-like uranium-bearing waste

Technologies for producing uranium (U) hexafluoride were developed from 1964 to 2001 at the Ningyo-toge Environmental Engineering Center. Consequently, approximately 1500 t of uranium-bearing waste was generated and safely stored in drums (Fig.8-6).

Some waste is in a pellet form, and other wastes have a high fraction of insoluble component, U, or hazardous elements (Fig.8-7). To remove U and hazardous elements from various uranium-bearing wastes, we proposed the hydrochloric acid (HCl) process (Fig.8-8). U is dissolved in HCl (dissolution process) and separated as a precipitate (precipitation process) by using hydrogen peroxide. Trace U and hazardous materials remaining in the solution are removed by using a chelating resin that absorbs the ions that need to be removed. Aluminum chloride is added in the solution during the dissolution stages to decrease the concentration of impurities mixed in with the separated U. The aluminum is then selectively recovered and reused. The insoluble residue, the spent resin, and the neutralized precipitate should be disposed of as a radioactive waste. As part of the present study, we investigated whether the process can be used for CaF_2 sludge and the spent filter aid. Approximately 90% of the U was separated at the precipitation stage. Furthermore, highly concentrated U (60–70wt%), which might be useful as a resource, was separated. The study confirmed that the concentration of U in solution dropped below the discharge standard concentration and that, by removing trace U, the concentration of U in the neutralized precipitate became sufficiently low.

The investigation results confirm that the majority of the U in CaF_2 and the spent filter aid is separated and that U concentration becomes sufficiently low to be disposed of. We will investigate whether the process can be used for other sludge and spent adsorbents.

Reference

Ohashi, Y. et al., Technique for Recovering Uranium from Sludge-Like Uranium-Bearing Wastes using Hydrochloric Acid, Journal of Nuclear Science and Technology, vol.51, issue 2, 2014, p.251–265.

8–3 Developing Rapid Method to Analyze Radioactive Waste

— Developing Method to Analyze ^{242m}Am in Low-Level Radioactive Waste —

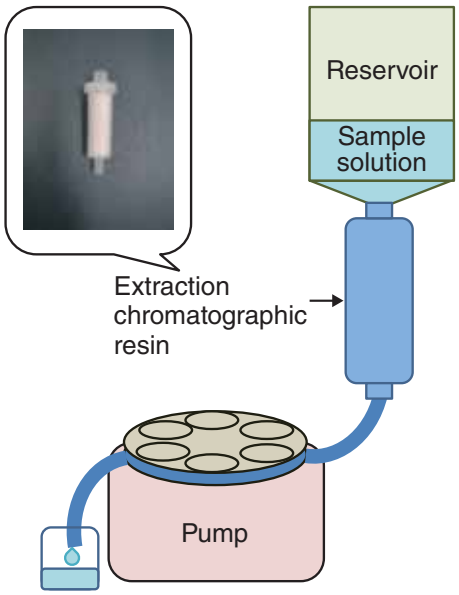

Fig.8-9 System of extraction chromatography
A cartridge-type of extraction chromatographic resin was used. Solution in a reservoir is pumped from downstream into the cartridge.

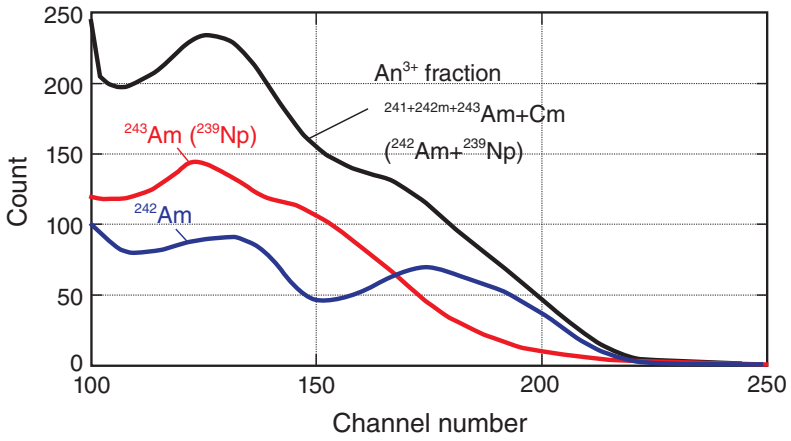

Fig.8-10 β-ray spectrum of ^{242}Am and so on
An^{3+} fraction contains $^{241+242m+243}$Am and Cm, and β-ray spectrum of ^{242}Am and ^{239}Np, which are progeny nuclides of ^{242m}Am and ^{243}Am, respectively is obtained. ^{243}Am source was prepared to estimate β-ray spectrum derived from ^{239}Np, which was subtracted from the spectrum of the An^{3+} fraction to obtain the β-ray spectrum of ^{242}Am.

The radioactive inventory of low-level radioactive waste (LLW) must be evaluated to dispose of LLW. However, some nuclides that are important for safety are difficult to analyze, such as americium-242m (^{242m}Am). Thermal ionization mass spectrometry (TIMS) is a conventional method to determine the content of ^{242m}Am. ^{242m}Am can also be analyzed by α-ray of curium-242 (^{242}Cm), which is the progeny nuclide of ^{242m}Am (^{242}Cm method). Although the TIMS measuring time is short, more sample is required than for ^{242}Cm method. However, less sample is available for the ^{242}Cm method, it takes several months to determine the ^{242m}Am content. In addition, both methods require separation of Am from Cm.

In the present study, we developed a new method to determine the ^{242m}Am content that involves measuring β-ray emission from ^{242}Am, which is the progeny nuclide of ^{242m}Am. To measure β-rays from ^{242}Am, Am must be separated from β-ray emitting nuclides in LLW. Therefore, we used a separation method based on extraction chromatography (Fig.8-9). First, trivalent actinides (An^{3+}) and lanthanides (Ln^{3+}) were separated from the major elements in LLW by using transuranic resin (Eichrom Technologies), which has selectivity for transuranic elements. Next, An^{3+} was separated from Ln^{3+}, which has similar chemical properties and contains some β-ray emitting nuclides, by using a tetravalent actinide resin (Eichrom Technologies). This An^{3+} fraction contains Cm, but the influence of Cm on the β-ray measurement can be subtracted because there is no β-ray emitting Cm in LLW. Conversely, β-rays from neptunium-239 (^{239}Np), which is a progeny nuclide of ^{243}Am, have to be detected and considered. Therefore, a ^{243}Am source was prepared to measure β-ray spectra of ^{239}Np, which were subtracted from those of An^{3+} to obtain the radioactivity of ^{242}Am (Fig.8-10). As a verification, the value obtained was compared with that determined by the ^{242}Cm method.

The separation step in the new method to determine the radioactivity of ^{242}Am is simpler than that for the TIMS and ^{242}Cm methods. Less sample is required by this new method than by the TIMS method and is comparable to that required by the ^{242}Cm method. The measuring time for this new method is considerably shorter than that for the ^{242}Cm method.

Reference

Shimada, A. et al., A New Method to Analyze ^{242m}Am in Low-Level Radioactive Waste Based on Extraction Chromatography and β-ray Spectrometry, Analytical Chemistry, vol.85, no.16, 2013, p.7726–7731.

8–4 Study to Improve the Safety of Trench Facility

— Suppression of Infiltrated Water to Reduce Radioactive Substances from the Facility —

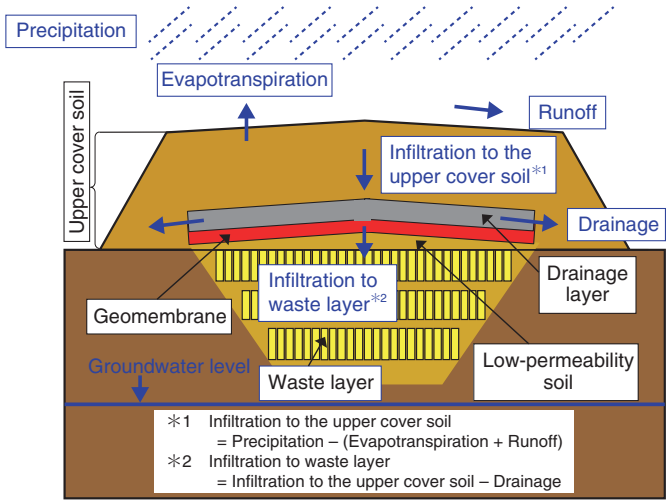

Fig.8-11 Model of water flow through upper cover soil at the facility
Upper cover soil conditions:
Model 1:
Geomembrane over 25-cm-thick low-permeability soil layer
Model 2:
50-cm-thick low-permeability soil layers with no geomembrane

Table 8-1 Resulting runoff, evapotranspiration, and water infiltration into upper cover soil
44% of the rainfall infiltrates into upper cover soil.

(unit: mm/year)

Precipitation	Runoff	Evapotranspiration	Infiltration in the upper cover soil
1264	85	627	552

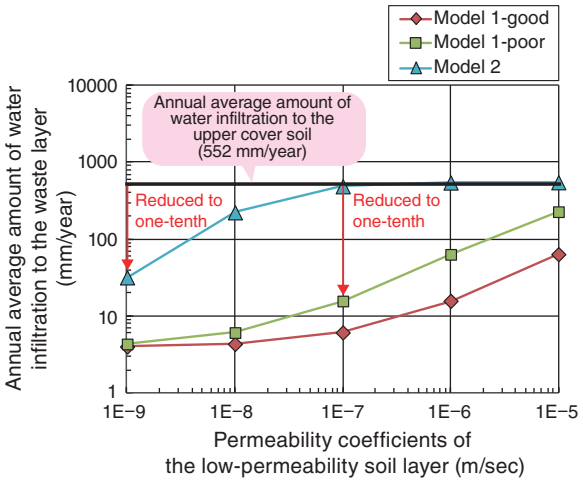

Fig.8-12 Result of water infiltration in the waste layer
The water infiltration in the waste layer is adequately reduced when the permeability of low-permeability soil layer is low.

We are considering to dispose of very low-level radioactive waste in the trench facility. The waste layer is placed above the groundwater level; therefore, to evaluate the safety of the facility, we must determine if the upper cover soil prevents rainfall from infiltrating into the waste layer.

As shown in Fig.8-11, two models were evaluated, i.e., Model 1, in which drainage, geomembrane, and a low-permeability soil layer were installed in the upper cover soil, and Model 2, in which a low-permeability soil layer thicker than that of Model 1 was installed, but without a geomembrane. Specifically, after obtaining the rainfall infiltration in the upper cover soil based on the weather conditions of Japan, we determined for both the models the extent to which water infiltrates in the waste layer as a function of the permeability coefficients of the low-permeability soil layer.

A set of pseudo weather data was used in this determination. Using a Fourier series and a gamma distribution, the pseudo weather data were created from real weather data (i.e., precipitation, temperature, and solar radiation) observed daily at a single measurement point in the Kanto area, Japan, which has an annual rainfall of approximately 1200 mm. For the geomembrane, we used the following parameters: a permeability coefficient of 1×10^{-11} m/sec (standard value), a constant deflection (poor) or slight deflection (good), and the number of flaws per hectare. The permeability coefficients of the low-permeability soil layer were set within the range between that of sandy soil and clay. Based on these conditions, we calculated the water infiltration in the upper cover soil and the waste layer of the facility.

The results indicate an annual average water infiltration in the upper cover soil of approximately 550 mm for an average annual rainfall of approximately 1200 mm (Table 8-1). Fig.8-12 shows that the annual average water infiltration in the waste layer was reduced to less than one-tenth of the water infiltration in the upper cover soil when the low-permeability soil layer has a permeability coefficient below 1×10^{-7} m/sec in Model 1 and below 1×10^{-9} m/sec in Model 2. In addition, we confirmed that drainage increases as the permeability coefficient of the low-permeability soil layer decreases.

The study concludes that using a low-permeability soil layer is effective for suppressing water infiltration in the waste layer of the trench facility. Moreover, placing a geomembrane suppresses water infiltration.

Reference

Kurosawa, R., Sakai, A. et al., Evaluation of Infiltration Water through the Upper Cover Soil in Trench Type Disposal Facility for Low Level Radioactive Wastes Generated from Research, Industrial and Medical Facilities, JAEA-Technology 2014-013, 2014, 89p. (in Japanese).

8–5 Visualization of Geosynthesis Procedure

— Geosynthesis Data Flow Diagram (Construction Phase) —

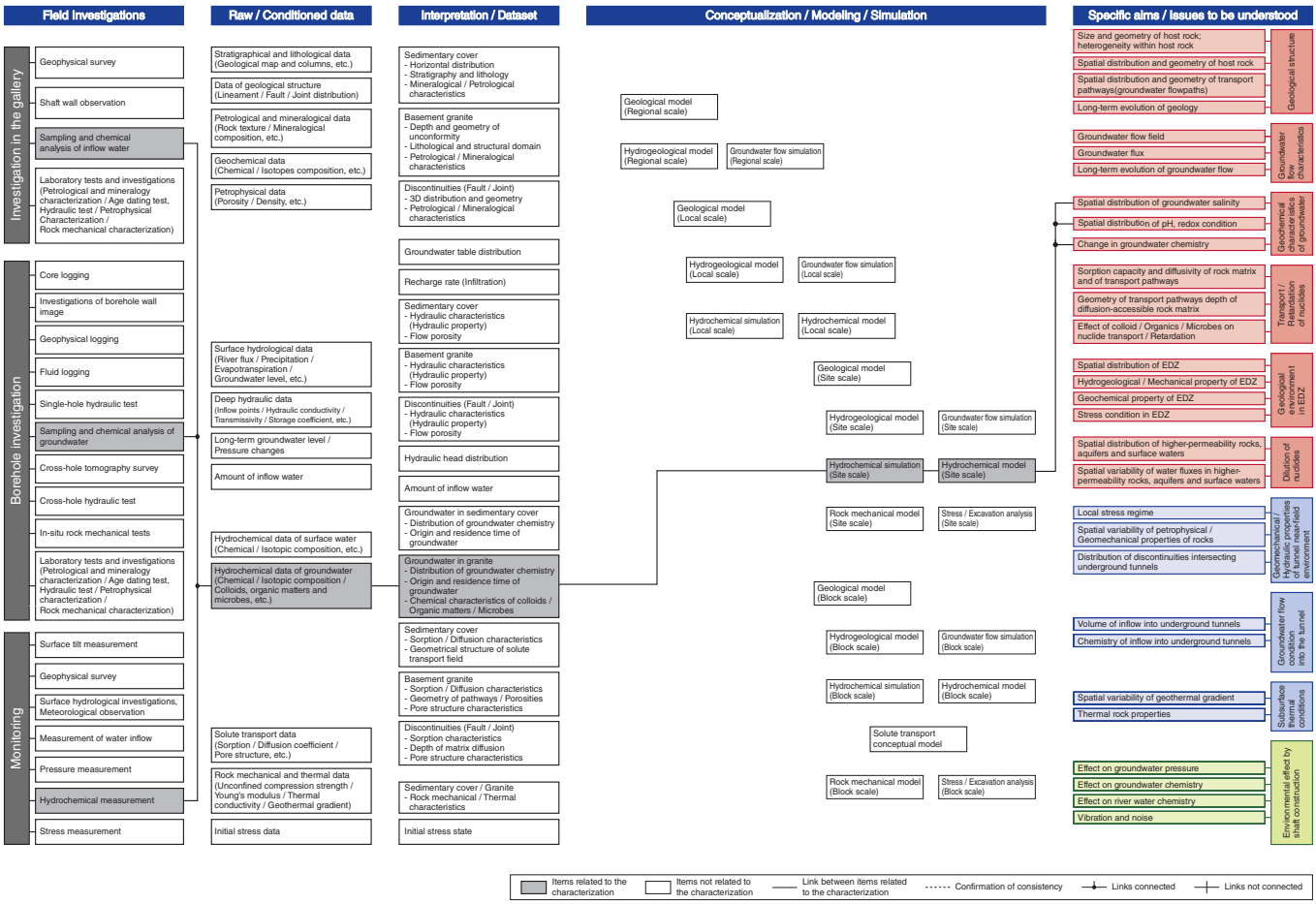

Fig.8-13 Example of geosynthesis data flow diagram (groundwater geochemistry: site scale)

We are pursuing a geoscience research and development project called the Mizunami Underground Research Laboratory (MIU) project. The project studies a crystalline rock environment to construct a scientific and technological basis for the geological disposal of high-level radioactive waste.

The MIU project is planned in three overlapping phases, i.e., the surface-based investigation phase (phase I), the construction phase (phase II), and the operation phase (phase III). Currently, the project is in phases II and III.

In phase II, the adequacy of models of the geological environment established in phase I is evaluated by using data accumulated during phase II. Based on the results of this evaluation, we determine whether various elemental technologies adopted to characterize the geological environment in phase I are applicable and feasible. These technologies include the planning, investigation, and modeling methods. Furthermore, a series of procedures are organized to evaluate design, construction, and safety, and a geosynthesis data flow diagram is established (Fig.8-13). This data flow diagram integrates the data flow from investigation to modeling and analysis. It combines in a rational way the items of the investigation that make the results reflect the safety assessment and design.

In this sense, the geosynthesis data flow diagram provides a rational framework, from “investigation” to “modeling” and “analysis,” for achieving individual goals and tasks. The experience and knowledge obtained by performing the investigation, modeling, and evaluation should be compiled by using the geosynthesis data flow diagram.

This approach should prove useful for both implementing and regulating high-level radioactive waste disposal.

Reference

Hama, K. et al., Mizunami Underground Research Laboratory Project-Preparation of Geosynthesis Data Flow Diagram (Construction Phase), JAEA-Data/Code 2013-010, 2013, 58p. (in Japanese).

8–6 Research in Onshore Mud Volcanism

— Origin of Muddy Sand from Kamihoronobe Mud Volcano —

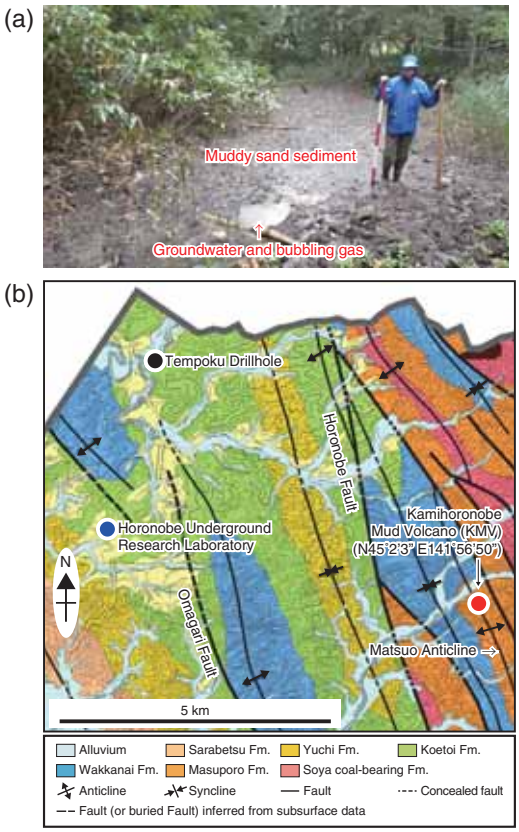

Fig.8-14 (a) Photograph of vent from which muddy sand and gas was sampled. (b) Geological map of the area of KMV
(modified from Miyakawa, K. et al., G³, vol.14, no.12, 2013, p.4980-4988.)

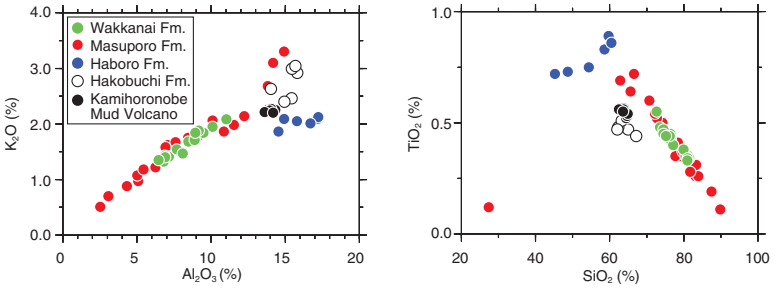

Fig.8-15 Bivariate plots of K_2O–Al_2O_3 and SiO_2–TiO_2 relationships for muddy sand and core samples from the area of Fig.8-14
(modified from Miyakawa, K. et al., G³, vol.14, no.12, 2013, p.4980-4988.)

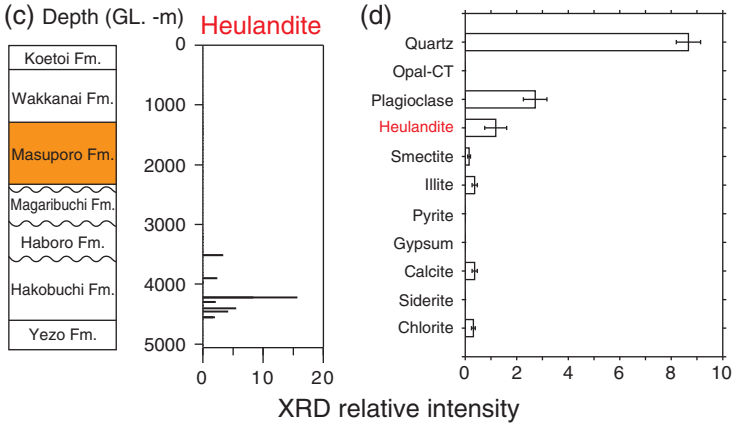

Fig.8-16 Abundances of minerals as a function of depth: (c) heulandite from a report on Tempoku Drilling (JNOC, 1995) and (d) data from the present study
(modified from Miyakawa, K. et al., G³, vol.14, no.12, 2013, p.4980-4988.)
XRD relative intensity, which is defined as the XRD intensity from a mineral in the sample divided by the intensity of a quartz standard and multiplied by 100.

Recently, applied earth science research into onshore mud volcanism has focused the safety of underground facilities, disaster mitigation, and the greenhouse effect on the climate. A topographical heightening created by a mud irruption along with high-pressurized groundwater and/or gas is called a mud volcano (MV), and the genetic process of creating a MV is called mud volcanism or the MV phenomenon.

Our R&D program must assess the geosphere stability to isolate radioactive waste over the long term. The goals of this R&D activity may be summarized in the following sequential steps: (1) determine the relationship between anomalously high formation pressure and mud volcanism, (2) narrow the range of geological settings where MV can occur in the future, and (3) clarify the impact of MV to the waste disposal system. Because only two onshore MVs are known in Japan (i.e., the Niikappu MV in Hokkaido and the Matsudai MV in Niigata), information from the case studies of other onshore MVs is needed to completely characterize onshore MVs. In this study, we investigated the origin of muddy sand sediments from the Kamihoronobe MV (KMV) located in Hokkaido (Fig.8-14).

Fig.8-15 compares the SiO_2, TiO_2, K_2O, and Al_2O_3 contents of KMV samples with those of core samples from each formation in this area, as described in the Tempoku Drilling (TD) (JNOC, 1995; Fig.8-14(b)). Fig.8-15 suggests that the chemical compositions of the KMV samples indicate a mix of materials from the Masuporo, Haboro, and Hakobuchi formations. By analyzing with X-ray diffraction (XRD), we compared the mineral composition of muddy sand samples with that of core samples (see published TD report) (Fig.8-16). Fig.8-16(c) shows that stratigraphically, heulandite, which is a type of clay mineral, is detected only in the Hakobuchi Formation, and Fig.8-16(d) shows that heulandite occurs in the muddy sand sediments. Considering that the Masuporo Formation is the youngest sedimentary formation below the KMV, the depth of the Hakobuchi Formation was estimated from the thickness of the formation to be 2200–2400 m (Fig.8-16(c)). Based on this evidence, we concluded that muddy sand from the KMV migrated from depths of over 2200–2400 m and was incorporated in the rock fragments from overlying formations.

Although we concluded that the materials came from great depths, we still need to study how MVs are generated and their lifetime or cycle time.

Reference

Miyakawa, K., Tokiwa, T. et al., The Origin of Muddy Sand Sediments Associated with Mud Volcanism in the Horonobe Area of Northern Hokkaido, Japan, Geochemistry Geophysics Geosystems, vol.14, no.12, 2013, p.4980–4988.

8–7 Investigation of Damage to Rock Mass in Gallery Excavation

— Based on Seismic Velocity and Fracture Distribution around Gallery Wall —

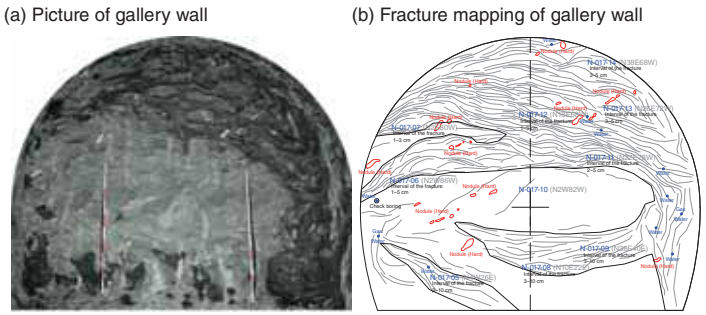

Fig.8-17 Example of fractures induced by gallery excavation
Gray lines in (b) indicate fractures induced by gallery excavation.

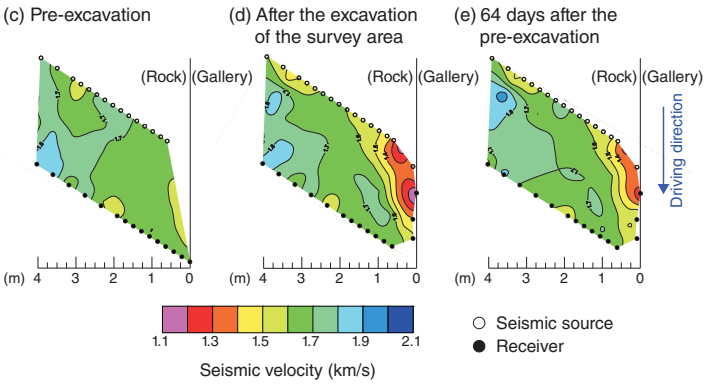

Fig.8-18 Results of seismic tomography survey
Velocity contour map of rock mass around gallery wall.

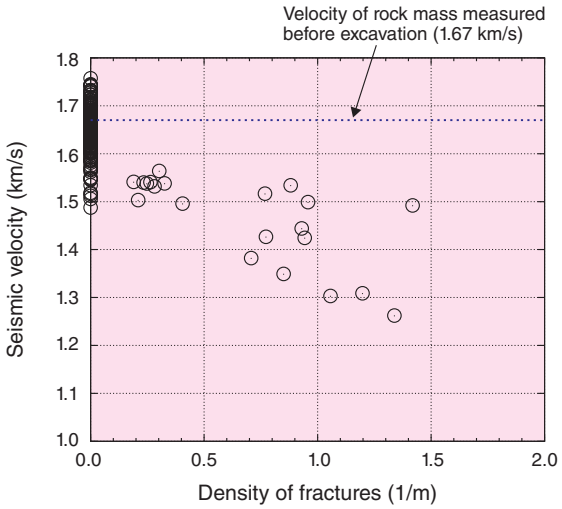

Fig.8-19 Relationship between seismic velocity and density of fracture
The circles in the graph represent the relationship between seismic velocity of each ray path and fracture density calculated based on the number of fractures intersected by each ray path.

In the construction of a deep underground gallery, fractures are induced around the gallery wall because of stress redistribution in response to excavation, as shown in Fig.8-17. In addition, because of these fractures, the hydraulic conductivity of the rock mass increases. Such a zone is called an excavation damaged zone (EDZ). To dispose of high-level radioactive waste, evaluation of an EDZ is important for safety assessment.

The Horonobe Underground Research Laboratory is conducting a seismic tomography survey at the depth of each gallery (140 m, 250 m, and 350 m) to investigate the extent of an EDZ. Fig.8-18 shows how seismic velocity changes in response to excavation. These results were obtained from a seismic tomography survey performed in the 250 m gallery. From the results shown in Fig.8-18(c), the seismic velocity of the pre-excavation rock mass ranges from 1.6 to 1.8 km/s. From the results shown in Figs.8-18(d) and (e), the layer in which the seismic velocity decreased remarkably (<1.4 km/s) extended approximately 1.0 m in the gallery wall. To investigate the mechanism producing the variations in seismic velocity, we obtained the number of fractures intersected by the ray path of a seismic wave based on the result of the fracture mapping of the gallery wall. Next, the fracture density for each ray path was calculated by dividing the number of fractures by the length of each ray path. Fig.8-19 shows the relationship between seismic velocity and fracture density. The figure shows that seismic velocity decreases almost linearly as fracture density increases. Thus, we expect that fracture density around the gallery wall could be estimated from the seismic velocity around the gallery wall. Furthermore, hydraulic tests reveal that enhanced hydraulic conductivity extends approximately 1.2 m into the gallery wall. Consequently, the EDZ in the 250 m gallery is estimated to extend approximately 1.2 m in the gallery wall. In the near future, we will construct a conceptual model of an EDZ based on the results of in situ tests and observations made in the 350 m gallery and in vertical shafts.

Reference

Aoyagi, K. et al., Quantitative Assessment of an Excavation Damaged Zone from Variations in Seismic Velocity and Fracture Distribution around a Gallery in the Horonobe Underground Research Laboratory, Rock Engineering and Rock Mechanics; Structures in and on Rock Masses, p.487–492.

8–8 Detection of Unrecognized Volcanic Activity by Sand Grain

— Developing Method based on Mineral and Chemical Analysis of Sand Grain in Sedimentary Rock —

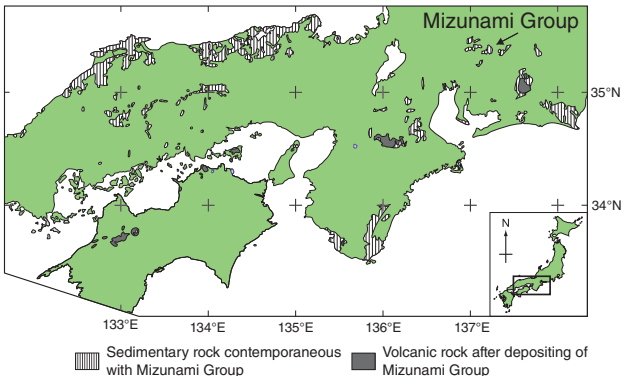

Fig.8-20 Distribution of sedimentary rock contemporaneous with Mizunami Group and volcanic rock after depositing Mizunami Group in Southwest Japan
Mizunami Group was deposited contemporaneously with the opening of the Japan Sea. Contemporaneous sedimentary rock, distributed around the Seto Inland Sea and from the San'in district to the Chubu District, does not contain volcanic rock. Large-scale volcanic activity is not inferred in the area.

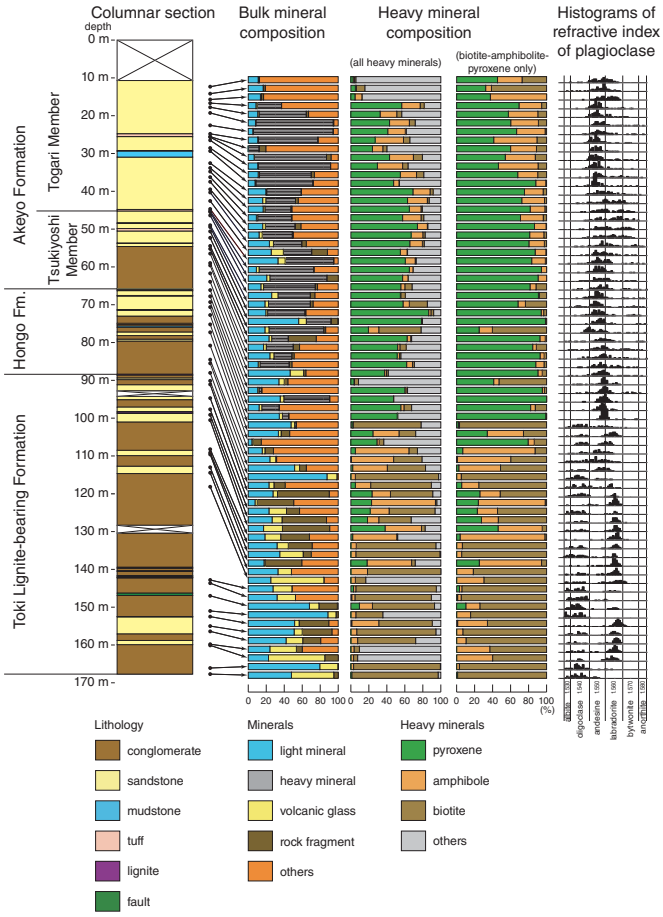

Fig.8-21 Columnar sections of the studied drill core of the Mizunami Group with bulk and heavy mineral compositions and refractive indices of plagioclase
Subspecies of plagioclase can be identified based on refractive index. Large amounts of volcanic glass are contained in the upper part of the group, and zeolite, which is an alteration product of volcanic glass, is contained in the lower part. Thus, the Mizunami Group contains large amounts of volcanic glass.

The Mizunami Group was deposited around the Mizunami Underground Research Laboratory between 20 and 15 million years ago. The group was deposited contemporaneously with the back-arc spreading event that formed the present-day Japan Sea and that involved extensive volcanic activity along the coast of the Japan Sea. However, in Southwest Japan, no volcanic activity seemed to have occurred during the deposition of the Mizunami Group (Fig.8-20).

When we studied the depositional age of the Mizunami Group, we found volcanic ash dispersed in the group. Such information, however, was obtained within a limited horizon, so we collected sandstone samples over a wider stratigraphic horizon and examined them to see if they contained volcanic ash.

In general, volcanic ash is composed of minerals and volcanic glass, but in older strata, volcanic ash is diagenetically altered to diagenetic minerals such as zeolite. We tried to find minerals that originated from volcanic ash. The Mizunami Group normally consists of sand and clay derived from basement granite and older sedimentary rock, so we tried to identify heavy minerals and plagioclase derived from other rock types.

The investigation revealed that sandstone contains volcanic glass and/or alteration products and that the sandstone mineralogically divides into three types: (1) characterized by the presence of biotite and variations in plagioclase from albite to oligoclase, (2) characterized by the dominance of amphibole and labradorite, and (3) characterized by the dominance of pyroxene and andesine (Fig.8-21). Because basement granite contains biotite and albite, type 1 sandstone derived from granite and types 2 and 3 derived from volcanic ash. Volcanic activity, which supplied volcanic ash to the Mizunami area, is divided into two phases based on variations in mineralogical and chemical compositions. These mineralogical and geochemical compositions suggest that the volcanic activity evolved over time.

The volcanic ash does not derive from volcanic activity along the coast of the Japan Sea. This study indicates that unrecognized volcanic activity occurred in and around the Mizunami area, even though the origin of the ash is unclear. This study reveals that unknown volcanic activity contemporaneous with Japan Sea formation occurred from central to western part of the Japanese Island.

Reference

Sasao, E., Petrographic Study of the Miocene Mizunami Group, Central Japan; Detection of Unrecognized Volcanic Activity in the Setouchi Province, Island Arc, vol.22, issue 2, 2013, p.170-184.

8–9 Large Inland Earthquake Triggered by Latent Magmatism

— Helium Isotopes as a Tool for Detecting Concealed Active Faults —

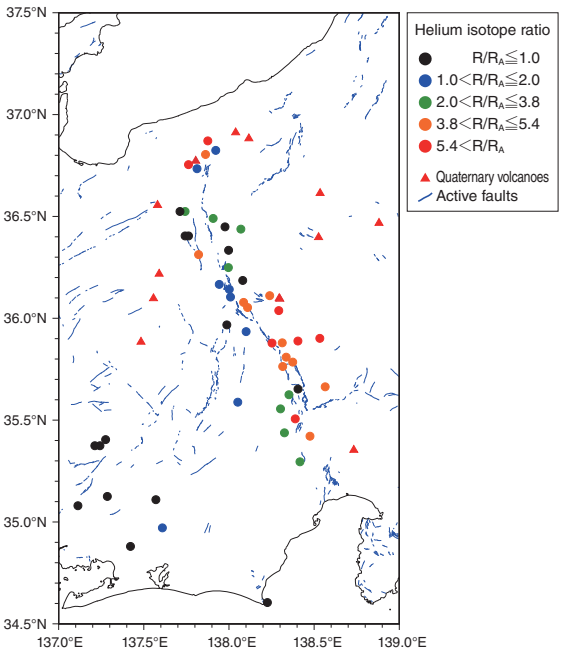

Fig.8-22 Geographical distribution of helium isotope ratios around the Itoigawa-Shizuoka tectonic line
The helium isotope ratios (R = $^3He/^4He$) from hot spring and drinking wells along the Itoigawa-Shizuoka tectonic line are larger than the atmospheric value (R_A).

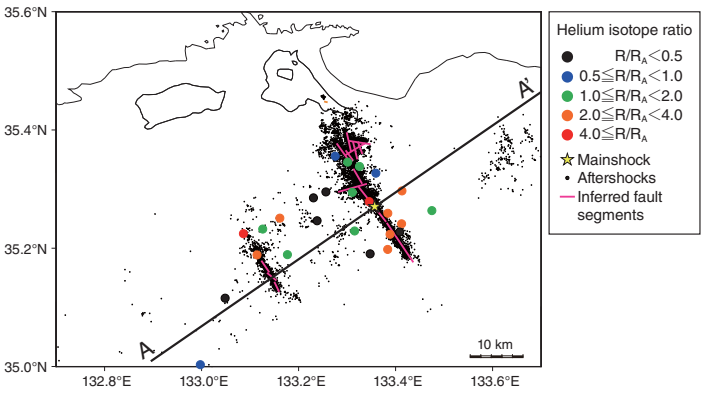

Fig.8-23 Geographical distribution of helium isotope ratios in aftershock area of 2000 western Tottori earthquake
The helium isotope ratios in the aftershock area decrease with distance from the inferred faults.

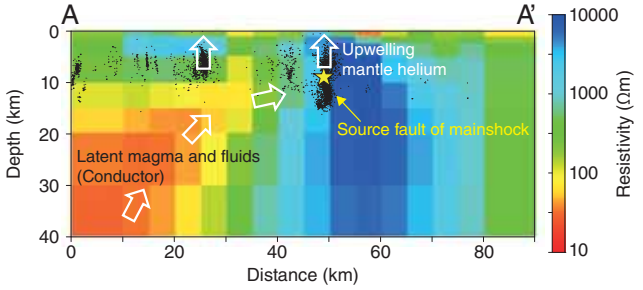

Fig.8-24 Electrical resistivity beneath aftershock area of 2000 western Tottori earthquake
A prominent conductor is visible on the southwestern side of the source fault. The conductor is attributed to latent magma and related fluids.

Earthquake faulting is one of the most important factors affecting the long-term stability of a geological disposal system, because it could cause a dynamic destruction of basement rocks. Recently, some large earthquakes with no noticeable surface expression of earthquake faulting have occurred, implying the existence of concealed active faults. Therefore, we developed a geochemical approach based on helium isotopes to detect concealed active faults.

The helium isotope ratios ($^3He/^4He$) observed in volcanic regions are usually similar to those of mantle-derived helium, which is several times higher than atmospheric value. These ratios should allow us to determine migration pathways, such as active faults, from the subcrustal mantle. We mapped the distribution of the helium isotope ratio around the active faults of the Itoigawa-Shizuoka tectonic line (ISTL) and of the seismic source region of the western Tottori earthquake by using helium isotope data from groundwater samples from hot springs and drinking water wells.

The spatial variation of the helium isotope ratio along the ISTL revealed that there is a high helium isotope ratio that occurs along the active faults (Fig.8-22), which can be interpreted as the leakage of mantle helium within the crust migrating upward through active faults.

An inland earthquake (M 7.3) occurred in the western Tottori in 2000 where no active fault was related to the earthquake. Groundwater samples collected in the aftershock area are characterized by helium isotope ratios several times higher than the atmospheric value. The helium isotope ratios decrease with distance from the inferred fault segments (Fig.8-23). In addition, magnetotelluric soundings were taken in the aftershock area in order to image subsurface electrical resistivity structure and detected an anomalous conductive body, which may be attributed to latent magma and related fluids, on the southwestern side of the source fault (Fig.8-24). These findings indicate mantle helium leaking from latent magma through the concealed faults. Moreover, the upwelling of fluids to the crust could contribute to triggering a large earthquake by weakening the shear strength of the source fault.

Reference

Umeda, K., Asamori, K. et al., Release of Mantle and Crustal Helium from a Fault Following an Inland Earthquake, Applied Geochemistry, vol.37, 2013, p.134–141.

8–10 Prediction of Radionuclide Speciation in Groundwater

— Determination of Standard Thermodynamic Data of Se(VI)/(IV) Couple —

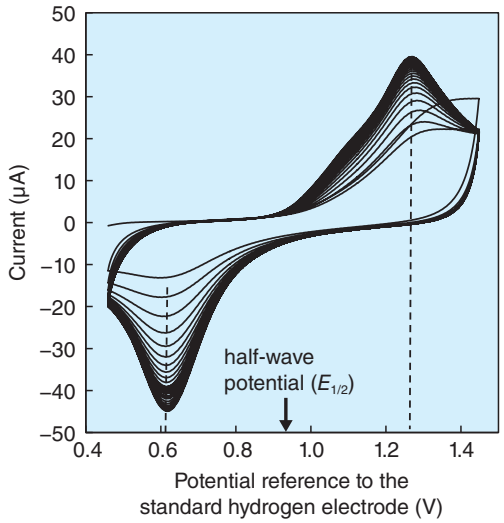

Fig.8-25 Cyclic voltammogram of Se(VI)/(IV) couple
The growth of the redox wave indicates the increase in the active electrode area where electron transfer is possible due to the removal of the passivating layer by repetitive potential cycling. The anodic and cathodic peaks correspond to the oxidation of Se(IV) and the reduction of Se(VI), respectively.

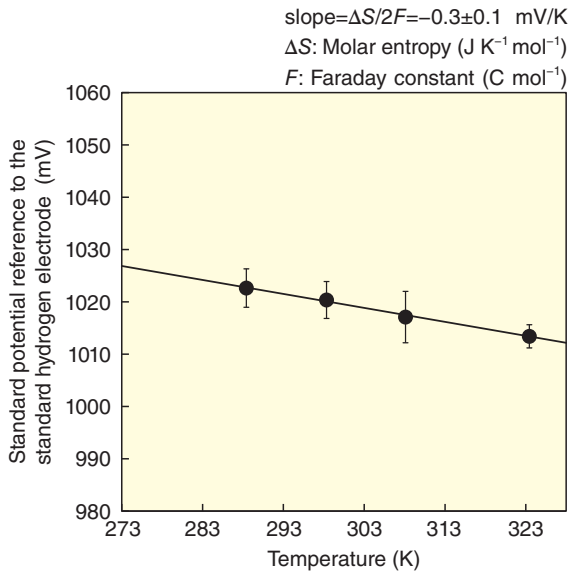

Fig.8-26 Molar entropy of Se(VI)/(IV) couple
$HSeO_4^-/H_2SeO_3$ standard redox potential as a function of temperature. The solid line is a weighted linear regression of the data. ΔS is derived from the slope of this line.

We assess the safety of the geological disposal based on the assumption that the radionuclides contained in vitrified waste are transported to the biosphere by flowing groundwater. We obtained the necessary data for this assessment.

Selenium-79(^{79}Se) is a long-lived fission product. Se species vary, depending on the oxidation/reduction potential E. Radionuclides are transported through the buffer material and host rocks and are retarded by sorption onto them. Because each species has unique sorption characteristics, the migration of Se depends strongly on E. Therefore, we accounted for the oxidation of the original reducing groundwater due to a decrease in the depth of repositories and/or the presence of an oxidizing agent, such as H_2O_2 that radiolysis of groundwater generates. The oxidation state of Se is Se(IV) or Se(VI) in oxidized groundwater. Because the sorption characteristics of Se(IV) differ from those of Se(VI), the accurate prediction of the ratio Se(VI) to Se(IV) is crucial for understanding the migration of Se. The standard redox potential E^0 of the Se(VI)/(IV) couple determines Se(VI) to Se(IV) ratios at 298.15 K in calculating the Se speciation. This potential is difficult to determine because the equilibrium of the Se(VI)/(IV) couple, whose reaction rate is slow, is not rapidly established, and the experimentally determined E is not affected by the Se(VI) to Se(IV) ratio in solution. We therefore chose to use cyclic voltammetry CV, which is a common method used to measure the half-wave potential $E_{1/2}$. The potential $E_{1/2}$ is where the concentration of an oxidant equals that of a reductant. Even for the redox reaction with a slow rate, CV allows us to measure $E_{1/2}$. Fig.8-25 shows the cyclic voltammogram of the Se(VI)/(IV) couple, where $E_{1/2}$ is midway between the anodic and cathodic peak potentials. The value of E^0 is derived from the concentration dependence of $E_{1/2}$.

In the geological environment, temperatures exceed 298 K. Because the molar entropy of the reaction ΔS yields the temperature derivatives of E^0, ΔS of the Se(VI)/(IV) couple is also required to predict the Se(VI) to Se(IV) ratio at a temperature above 298 K. We therefore obtained ΔS for this couple from the temperature dependence of E^0 (Fig.8-26). The results for E^0 and ΔS, which agree with published values of the molar enthalpy of the Se(VI)/(IV) couple, will contribute to a more reliable prediction of Se speciation under various environments and will be input in the JAEA thermodynamic database.

References

Doi, R., Determination of the Selenium (VI)/(IV) Standard Redox Potential by Cyclic Voltammetry, Journal of Nuclear Science and Technology, vol.51, issue 1, 2014, p.56–63.

Doi, R., Molar Entropy of the Selenium (VI)/(IV) Couple Obtained by Cyclic Voltammetry, Journal of Nuclear Science and Technology, vol.51, issue 3, 2014, p.359–368.

8–11 Prediction of Long-Term Alteration Characteristics of HFSC
— Clarification of Decreasing pH and Development of Alteration Model —

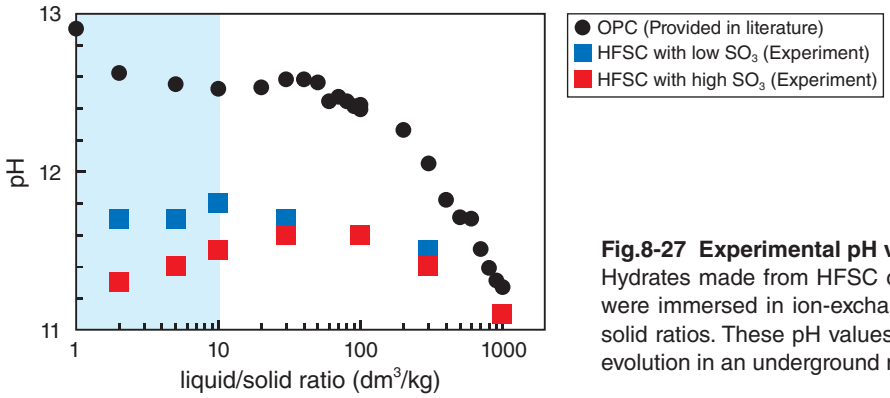

Fig.8-27 Experimental pH value in dissolution experiments
Hydrates made from HFSC containing different amount of SO_3 were immersed in ion-exchanged water with differing liquid-to-solid ratios. These pH values reflect a possible scenario for pH evolution in an underground repository.

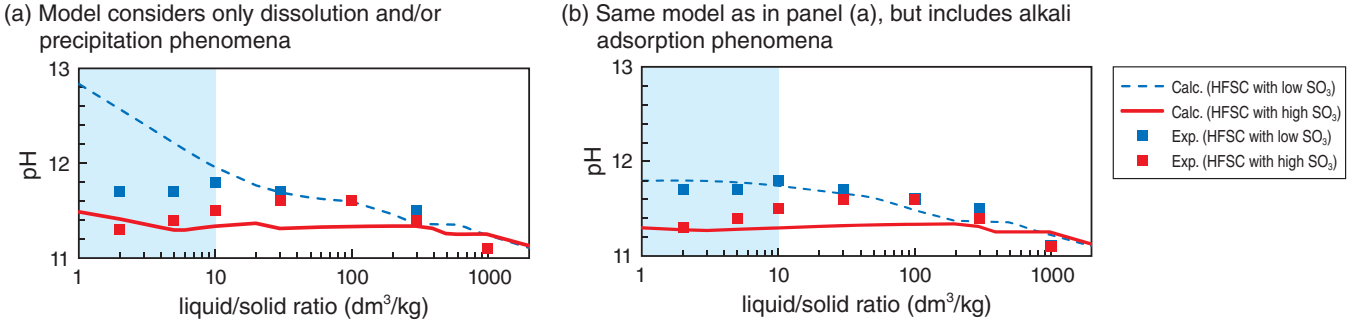

Fig.8-28 Comparison between experimental and calculated pH
Differences between experimental and calculated values (a) can be improved by including alkali adsorption in the model (b).

Cementitious materials are expected to be used to construct an underground repository for the geological disposal of radioactive wastes. Degradation of ordinary Portland cement (OPC) by the ingress of groundwater can generate a high-pH plume ($\geq$ 12.5), which would probably affect the performance of the bentonite buffer used to contain the radioactive wastes and the transport properties of the host rock. Therefore, a new type of high-volume fly ash silica fume cement (HFSC) is being developed that will lead to a lower plume than for OPC.

The long-term alteration characteristics of HFSC need to be predicted to assist in demonstrating the safety of a geological disposal system. The prediction should be made based on an understanding of the mechanisms responsible for alteration phenomena. In this study, dissolution experiments were used with geochemical equilibrium calculations to make a preliminary assessment of the pH-lowering mechanism in HFSC and to predict the long-term alteration characteristics.

These calculations, based on the understanding that pH decreases only when $Ca(OH)_2$ is absent and the molar Ca/Si ratio in the calcium silicate hydrate (C–S–H) gel is lowered, did not satisfactorily reproduce the experimental results. Dissolution experiments were performed with HFSC containing different amount of SO_3, with the focus being on SO_4^{2-} as a counter ion and on the response of the alkali elements (i.e., Na and K). HFSC containing either high or low SO_3 wt% was immersed in ion-exchanged water at various liquid-to-solid ratios, and the resulting pH and liquid composition were measured. At lower liquid-to-solid ratios ($\leq$ 10), the pH was higher for HFSC with low SO_3 than for HFSC with high SO_3 (Fig.8-27). However, the pH calculated with models that only consider dissolution and/or precipitation phenomena differs significantly from the experimental values for HFSC with low SO_3 (Fig.8-28(a)) and so could not be explained by the SO_3 content alone.

An improved chemical equilibrium model was developed by including Na and K adsorption on the C–S–H gel along with the dissolution and/or precipitation phenomena. The pH calculated with the improved model agrees well with the experimental results (Fig.8-28(b)). The model thus developed is expected to help improve our understanding of the mechanisms responsible for lowering pH in HFSC and can be used to predict possible scenarios of pH evolution in a geological disposal system.

Part of this study was sponsored by the Ministry of Economy, Trade and Industry of Japan (METI) through the program “Advanced Assessment Technology Development for Impact of Cement on Geological Disposal System for Long-lived Radioactive Waste” in FY 2011 and 2012.

Reference

Hoshino, S., Honda, A. et al., Mechanism of Alkalinity Lowering and Chemical Equilibrium Model of High Fly Ash Silica Fume Cement, Konkurito Kogaku Ronbunshu (Concrete Research and Technology), vol.25, 2014, p.97-107 (in Japanese).

8–12 Evaluation of Long-Term Geological Evolution

— Study of the Safety of Geological Disposal Considering Uplift and Erosion —

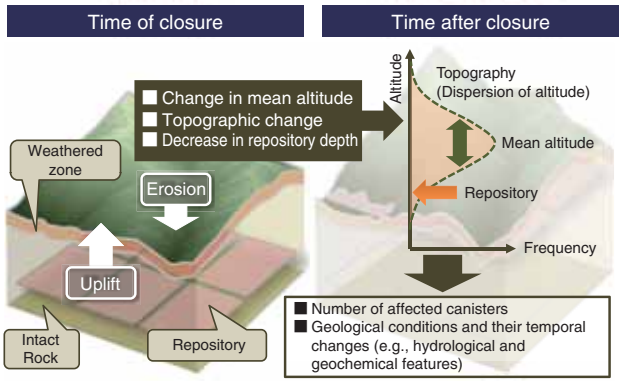

Fig.8-29 Conceptual uplift erosion model for repository and evolution of topography over time
Uplift, erosion, and changes in topography are evaluated using a landscape evolution model, which helps in estimating the time required for a repository to reach the surface of the ground and the number of waste packages eroded as a function of time.

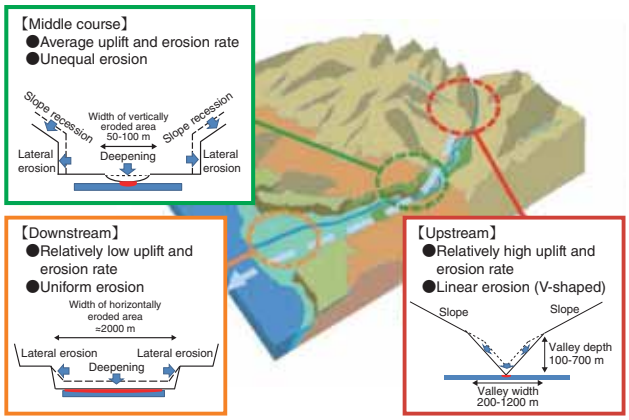

Fig.8-30 Conceptual erosion model

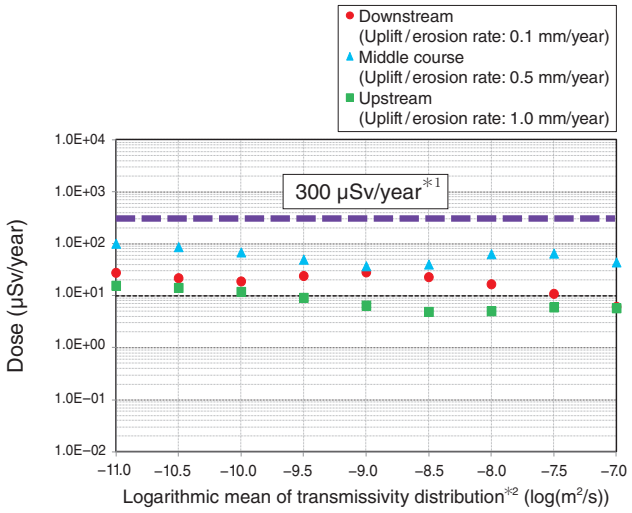

*1 The maximum permitted dose has not yet been decided in Japan and so the dose = 300 μSv/year is adopted from Publication 81 by the ICRP.
*2 The transmissivity (hydraulic conductivity × aperture) distribution expresses a characteristic of the hydrogeologic environment in view of its hydraulic heterogeneity.

Fig.8-31 Results of safety assessment assuming that repository reaches ground surface by uplift and erosion
The effect on humans due to repository is evaluated by considering the uncertainty of transmissivity to examine the various conditions of the geological environment. The result shows that the effect is less than the targeted criterion suggested by the international organization even if the repository reaches the ground surface.

Japan is tectonically active, so a site for the geological disposal of high-level radioactive waste (HLW) must be demonstrated to be stable over the long term. Areas identified by geological investigation that are more likely to experience catastrophic natural events should be avoided (e.g., areas with major fault movements or volcanic activity). More widespread phenomena identified on regional and global scales, however, are more difficult to avoid (e.g., uplift or erosion and changes in sea level). For uplift and erosion, the distance between a 300-m-deep repository and the biosphere can be reduced, and in the worst case, the repository could become exposed at the ground surface. The present study provides a method to evaluate the effects of uplift and erosion on the safety of the geological disposal of HLW.

In previous safety assessments, the rate of erosion was assumed equal to the rate of uplift, so the repository would approach the ground surface at a constant velocity. After reaching the ground surface, the repository was then assumed to erode uniformly. In reality, there are many areas with different rates of uplift and erosion. A systematic method to identify and express the parameters for safety assessments has been developed by using more realistic rates of uplift and erosion (Fig.8-29).

Fluvial erosion is the main erosion process in Japan; so to evaluate the subaerial exposure of a repository, the present study models erosion depending on the precise locations along a river's course (Fig.8-30). The effect on human health is evaluated based on the assumption that radionuclides are released in the biosphere by erosion. In all cases considered, the dose rates are below the target value suggested by the International Commission on Radiation Protection (ICRP) (Fig.8-31). These results can be explained by the low amount of erosion because of the localized upstream deepening, the longer downstream decay time due to the slow rate of uplift and erosion, even considering the large amount of erosion due to uniform deepening, and the average of these two conditions in the middle course.

Reference

Wakasugi, K. et al., Bounding Analysis of Uplift and Erosion Scenario for an HLW Repository, Proceedings of 21st International Conference on Nuclear Engineering (ICONE 21), Chengdu, China, 2013, ICONE21-16724, 9p., in DVD-ROM.

8–13 Improvement of Ruthenium Removal Rate by Electrochemical Oxidation

— Improvement of Stable Operation for Vitrification Process —

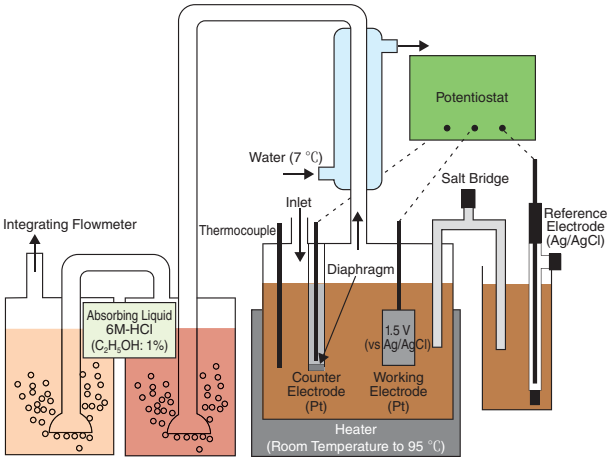

Fig.8-32 Schematic diagram of oxidation cell

Table 8-2 Experimental conditions for electrochemical oxidation

	Temperature (℃)	Ce concentration (mg/ℓ)	Reflux/ Evaporation	Diaphragm
A	95	0	Reflux	○
B	50	0	Reflux	○
C	95	3.0×10^3	Reflux	○
D	95	0	Evaporation	○
E	95	0	Reflux	×

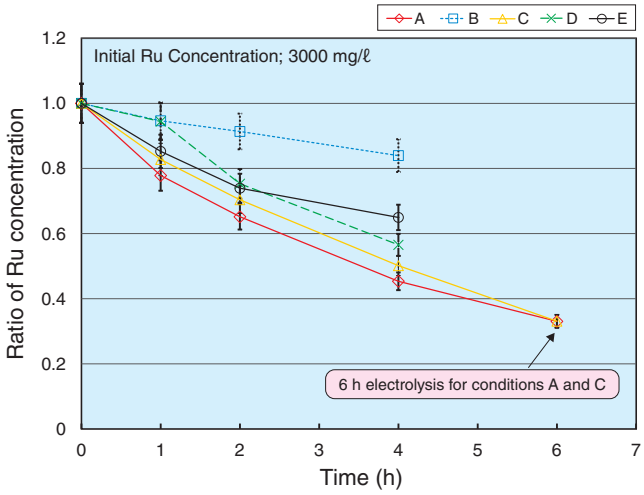

Fig.8-33 Decreasing ratio of Ru concentration, $[Ru]_t/[Ru]_0$, with time

Experimental results showing decreasing rate of Ru concentration ratio, i.e., $[Ru]_t/[Ru]_0$. Electrical oxidation under the conditions A and C are appropriate for fast oxidation.

One of the platinum group elements, i.e., ruthenium (Ru), is a major fission product in high-level liquid waste (HLLW), which is to be disposed as vitrified waste. Platinum group elements precipitate in a glass fusing furnace. These precipitates influence the flow characteristics and electrical conductivity of a melting glass, which complicates the vitrification process. To stabilize the process, these platinum group elements should be removed from the solution before feeding it in the glass fusing furnace.

Ru tetraoxide (RuO_4) has a high vapor pressure, which is sufficiently high to run off from the solution even at room temperature. If Ru ions in the solution could be oxidized to tetraoxide, Ru could be removed from the liquid phase.

We studied an electrochemical oxidation method to oxidize Ru ions in solution to separate Ru as tetraoxide (Fig.8-32). The advantage of this method is that it does not require additional oxidizing or extraction reagents. Electrical oxidation, however, is necessary for long oxidation times. To increase the oxidation rate, we conducted experiments to clarify how the following four fundamental conditions (Table 8-2) influence electrochemical oxidation. Results of experiments involving a decreasing rate of Ru concentration are shown in Fig.8-33.

(1) Electrolyte temperature

When the electrolyte reaches a high temperature, Ru ions easily migrate in the solution, so the oxidation rate can be increased.

(2) Presence of promoter elements

Cerium ions are reported to promote the Ru oxidation rate. We confirmed that Ru migrates to the gas phase effectively with cerium. Cerium ions are electrically oxidized to tetravalent ions, i.e., Ce(IV), which stabilize oxidized octavalent Ru, preventing a back reaction, in the solution. Therefore, the removal of RuO_4 to gas phase becomes more efficient.

(3) Evaporation or reflux of condensed phase

We were concerned about the possible absorption of gaseous tetraoxide Ru into the condensed water in the condenser and its return in the water to the electrolyte cell as reduced Ru dioxide. But the evaporation or reflux conditions do not directly affect the electrochemical oxidation efficiency.

(4) Diaphragm for counter electrode

Simple electrical oxidation system that is easy to maintain should be designed considering the HLLW treatment. If the diaphragm at the counter electrode is not necessary, it can be eliminated to simplify maintenance. However, the diaphragm is necessary for efficient oxidation.

We obtained the following conditions for fast electrochemical oxidation: (1) higher temperature (95 °C), (2) Ce coexistence at 3000 mg/ℓ, and (3) use of a diaphragm for counter electrode. The oxidation rate achieved should be three times faster under these optimized conditions.

The present study was partly supported by “Development of High-level Liquid Waste Conditioning Technology for Advanced Nuclear Fuel Cycle” from the Ministry of Education, Culture, Sports, Science and Technology of Japan (MEXT).

Reference

Sato, S. et al., Optimization for Removal of Ruthenium from Nitric Acid Solution by Volatilizing with Electrochemical Oxidation, Journal of Nuclear Science and Technology, vol.49, issue 2, 2012, p.182–188.

Toward the Practical Use of Fusion Energy

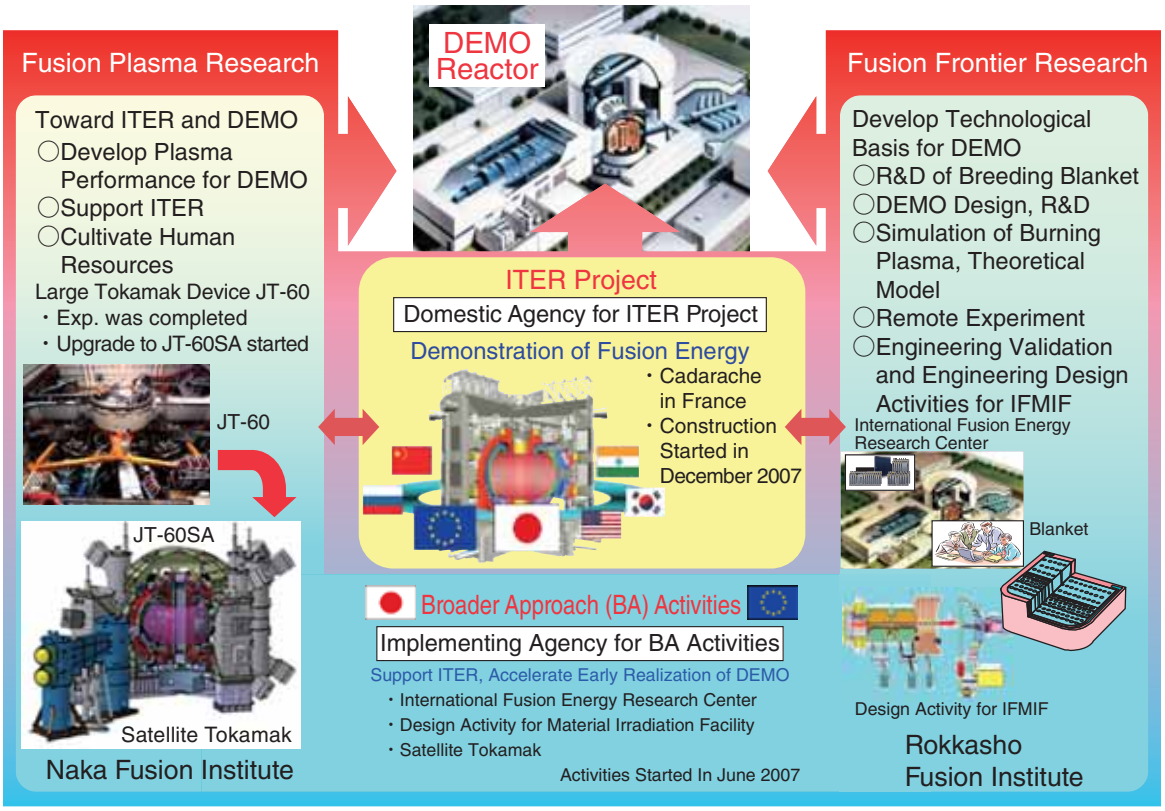

Fig.9-1 Steps involved in the development of the fusion DEMO reactor
Fusion plasma research and fusion frontier research are being pursued for the development of a DEMO reactor, aimed at an early realization of fusion energy.

Crucial developments toward the practical use of fusion energy in the fields of fusion plasma research and fusion frontier research are being pursued through intensive international cooperation. The International Thermonuclear Experimental Reactor (ITER) project, Broader Approach (BA) activities, and other collaborations (Fig.9-1) are aimed at the early realization of a fusion demonstration power plant (DEMO) reactor. Fusion plasma research is mainly being advanced by the Naka Fusion Institute, and fusion frontier research is mainly being advanced by the Rokkasho Fusion Institute.

ITER Project

The ITER project is an international cooperative project to demonstrate the scientific and technological feasibility of fusion energy through the construction and operation of an experimental reactor. The ITER agreement came into force in October 2007, and the Japan Atomic Energy Agency (JAEA) was designated as the domestic agency fronting the ITER project in Japan. JAEA has proceeded with the preparation of the equipment that Japan agreed to provide, and has achieved various results in terms of technological development (Topics 9-1 and 9-2). In particular, JAEA began producing a superconducting coil for the actual machine ahead of any other country participating in ITER.

BA Activities

The Broader Approach (BA) activities are joint projects by Japan and the European Union to conduct supporting research for ITER and research and development (R&D) for a DEMO reactor, which is the next step of ITER, aimed at the early realization of fusion energy. The BA agreement came into force in June 2007, and JAEA was designated as the agency in charge of implementing the BA activities in Japan.

The BA activities comprise three components: projects at the International Fusion Energy Research Center (IFERC), the International Fusion Materials Irradiation Facility/Engineering Validation and Engineering Design Activities (IFMIF/EVEDA) project, and the Satellite Tokamak Program (STP). Topic 9-3 describes the results achieved in the R&D activities toward a DEMO reactor at IFERC. Topic 9-4 describes the results obtained by IFMIF/EVEDA. Topics 9-5 and 9-6 outline the progress toward the construction of the Japan Torus-60 Super Advanced (JT-60SA) fusion reactor by STP. Topic 9-7 also presents results related to JT-60SA.

Fusion Plasma Research

Analysis of JT-60 experimental data was promoted, and inter-machine experiments were conducted for the purpose of achieving high economic efficiency in a fusion reactor by means of attaining a high plasma pressure. Topic 9-8 is a result that indicates the guidelines for overcoming instabilities that hinder the formation of a high plasma pressure.

Fusion Frontier Research

Various R&D activities have been executed at the Rokkasho Fusion Institute, aimed at the construction of the technological basis for a DEMO reactor. Topic 9-9 describes theoretical simulation research that uses the high-performance computer at IFERC; the result can provide a basis for developing a secure shutdown procedure for a DEMO reactor. Topics 9-10 and 9-11 are results that are indispensable for the development of a breeding blanket.

9–1 Lifetime Extension of Beam Dump by Dispersing the Deposition of Laser Energy

— A High Laser Energy-Resistant Beam Dump for Thomson Scattering in ITER —

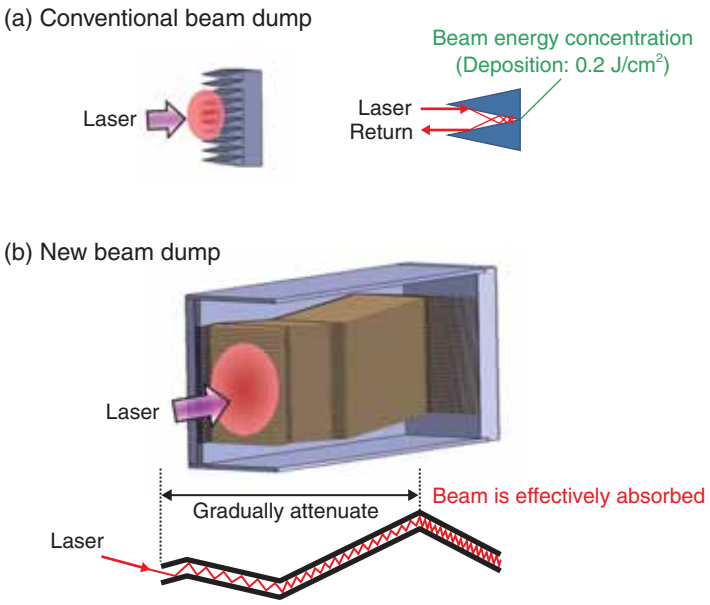

Fig.9-2 Beam dump structures
(a) The conventional beam dump has a relatively small area for beam absorption, which induces damage; (b) the new beam dump has a number of sheets aligned parallel to one another which can gradually absorb the beam energy.

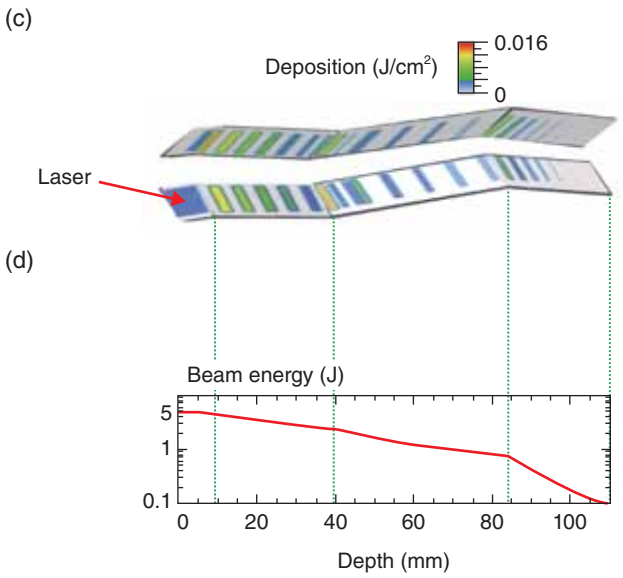

Fig.9-3 Beam energy deposition profile
(c) Beam energy deposition profile on two of the sheets; (d) to use the limited depth effectively, beam energy attenuation of the latter sections is larger than that of the front sections.

When a laser beam is injected into plasma, a very small fraction of the light is scattered by electrons in the plasma. This phenomenon is called Thomson scattering. The electron temperature and density of the ITER plasma are measured from the spectrum and intensity of the scattered light, respectively. Since the proportion of incident photons that are scattered and detected as a signal in ITER is 10^{-14}, it is very important to inject intense laser beams, to collect the scattered light effectively and to reduce the stray light of the laser beam in the Thomson scattering measurement, so that the electron temperature and density can be accurately measured with a high signal to noise ratio (S/N).

Laser beam dumps are designed to terminate intense laser beams and reduce the stray light of the laser beams. Since 10^9 laser pulses with a 5-J energy are to be injected throughout the 20 year operation of ITER, the concentrated laser energy in the valley of a conventional beam dump will cause serious damages to the surface (Fig.9-2(a)). The accuracy of the Thomson scattering measurement significantly degrades if the laser beam dump is damaged, since the stray light from the damaged surface of the beam dump increases. A key concept of the new beam dump is to reduce laser energy absorption per unit area on the surface and to gradually absorb the energy of the laser beam, so that the stray light will be reduced at the same time.

We have applied the idea that the absorption ratio depends on the angle of incidence and the polarization of the laser beam to the design of a new beam dump. Fig.9-2(b) shows the schematic of the newly proposed beam dump. To gradually absorb the beam energy, the laser beam is injected into the beam dump with a large angle of incidence and is polarized parallel to the beam-exposed area (S-polarization). In general, the depth should be sufficiently large to gradually absorb the beam energy. However, the allocated depth for the beam dump in ITER is up to 125 mm. The new beam dump has a number of thin molybdenum sheets with thicknesses of 0.5 mm, which are aligned parallel to each other with a separation of 1 mm. We optimized the angle and position of bending on the sheets to disperse the deposition of the beam energy (Fig.9-3).

While conventional beam dump cannot withstand more than 10^4 laser pulses, the new beam dump would withstand more than 10^9 pulses. In addition, compatibility with ITER's thermal and electromagnetic loads was confirmed through thermo-structural analysis. We have proposed the first detailed beam dump structure in the world that complies with the severe conditions of use, installation environment, and space limitations of ITER.

Reference

Yatsuka, E., Hatae, T. et al., Chevron Beam Dump for ITER Edge Thomson Scattering System, Review of Scientific Instruments, vol.84, no.10, 2013, p.103503-1-103503-6.

9–2 Investigation of Strain Using Neutron Diffraction
— A Foundation for Improvement of ITER Conductor Performance —

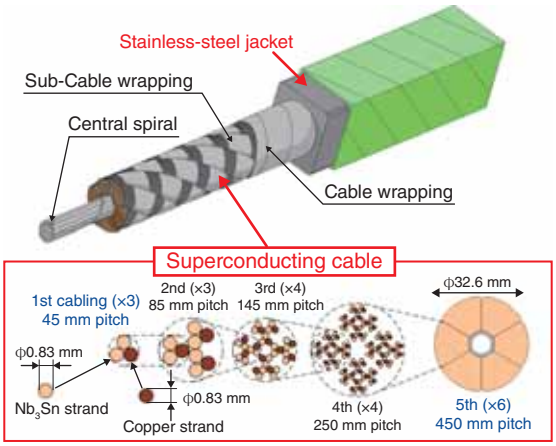

Fig.9-4 Schematics of the ITER CS conductor
The conductor comprises a superconducting cable and a jacket. Strands are cabled 5 times.

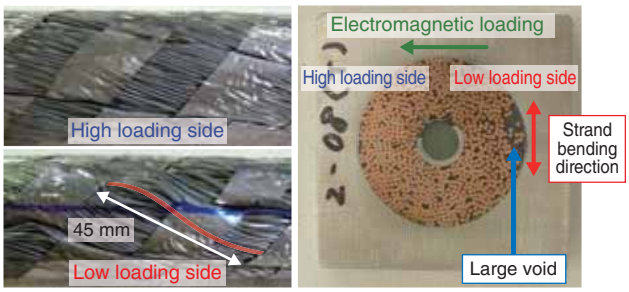

Fig.9-5 Deformation of strands in the cable after testing
The cable was disassembled and visually inspected after testing.

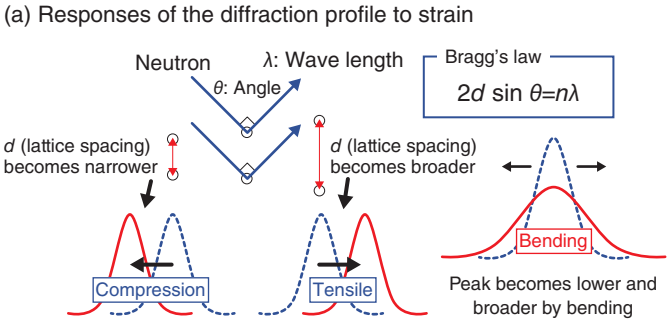

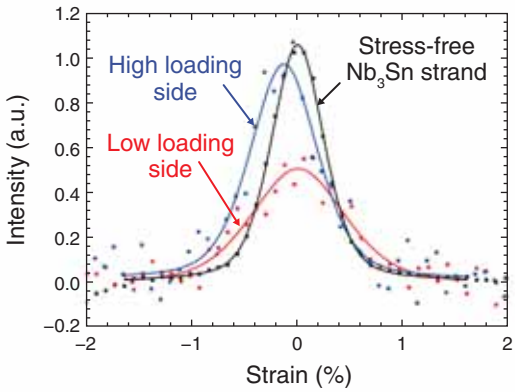

Fig.9-6 Internal strain evaluated by neutron diffraction
Neutrons are diffracted in accordance with Bragg's law. The internal strain in the conductor can be evaluated from neutron diffraction, since the wavelength is changed by the variation of the lattice spacing.

The central solenoid (CS) conductor for ITER, shown in Fig.9-4, is operated at 45 kA and 13 T. The conductor is required to withstand a 60000 cyclic electromagnetic loading of 50 t/m. Short sample tests found that the superconducting performance gradually degraded during these cycles. A clarification of this degradation mechanism is needed.

The performance of the Nb_3Sn strands in the CS conductor is sensitive to strain. Thus, transverse electromagnetic loading has been considered a major cause of the degradation of conductors. Namely, the electromagnetic loading bends the strand at a short pitch (around 5 mm) through contact with adjacent strands in the high loading side (HLS). However, observation of the cable showed that the deflection of strands on the low loading side (LLS) was larger than that on the HLS, as shown in Fig.9-5.

The mechanism behind the strain was reconsidered. Since the fixture of the strand in the cable is relaxed by a large void, the buckling of the strand occurs due to the axial compressive force caused by different amounts of thermal contraction between the cable and the jacket.

The visual observation showed a bending strain of around 0.6% in the LLS. Since the bending strain in the HLS could not be evaluated by visual observation, a quantitative method was needed to evaluate it. Hence, a neutron diffraction measurement using the engineering materials diffractometer in the Japan Proton Accelerator Research Complex (J-PARC) was conducted to evaluate the bending strain. The average bending strains evaluated from the variation of the profile (Fig.9-6) were 0.32% in the HLS and 0.63% in the LLS. Consequently, bending with short pitch in the HLS was not dominant. The bending strains in the LLS that were evaluated by visual inspection and neutron diffraction were in agreement.

The strands' deformation can be prevented by the optimization of cabling, since the strand withstands buckling by shortening the bending pitch. An optimized CS conductor could satisfy the requirement for 60000 operation cycles.

Reference
Hemmi, T. et al., Neutron Diffraction Measurement of Internal Strain in the First Japanese ITER CS Conductor Sample, Superconductor Science and Technology, vol.26, no.8, 2013, p.084002–1–084002–6.

9–3 Failure Behavior of the Hot Isostatic Pressed Joint in the Fusion Blanket

— The Latest Highlight of Research and Development of Reduced Activation Ferritic/Martensitic Steel for Use in the Fusion DEMO Reactor —

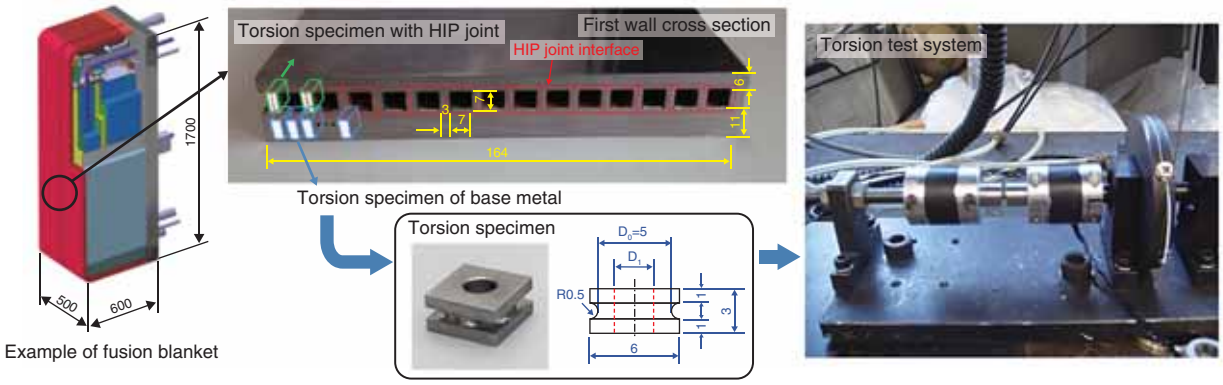

Fig.9-7 Schematic of miniature torsion test method (unit: mm)
The torsion test method is a brand new test technique for evaluating the HIP joint for the thin-walled fusion blanket first wall.

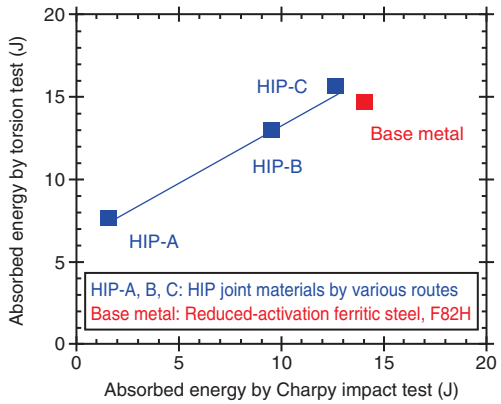

Fig.9-8 Comparison between torsion and Charpy impact tests
Similar to the conventional Charpy impact test method, the torsion test technique enabled us to adequately evaluate the key characteristics of HIP joints produced by various processing routes.

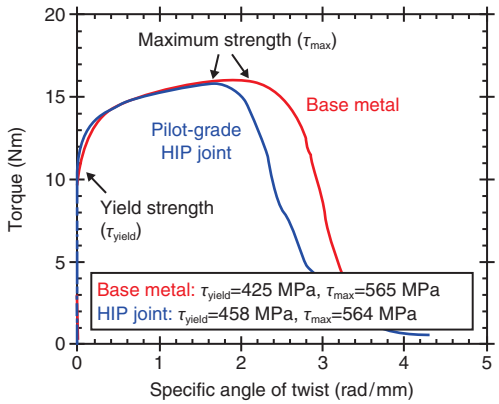

Fig.9-9 Evaluation of HIP joint components as parts of the fusion blanket structure
The torsion test was the first, to our knowledge, to demonstrate that both the yield shear stress and the maximum shear strength of the HIP joint components were equivalent to those of the base metal.

Reduced activation ferritic/martensitic (RAFM) steel is one of the leading structural materials for use in the fusion DEMO reactor, and hot isostatic pressed (HIP) RAFM joints are one of the primary technologies for fabricating the cooling channels in the blanket first wall (FW). For practical application, it is very important to identify the stability and damage tolerance of the HIP joints exposed to harsh environments, such as high-energy neutron exposure and heat from the burning plasma.

The Charpy impact test is an established method for gauging damage tolerance with many perceived advantages. However, it is hard to apply this technique to the thin-walled cooling channels of the blanket FW, due to limitations on the specimen size required in testing.

We therefore developed a brand new torsion test method using a miniature specimen to evaluate HIP joints (Fig.9-7). There has so far been good agreement between the fracture energy obtained by the Charpy test and the estimated energy obtained by the developed torsion test (Fig.9-8). We have also introduced fracture parameters specific to torsion and identified the effects that specimen size and geometry had on them. Eventually, we provided a reasonable solution for the HIP joints of the practical components.

In this study, we first applied the torsion technique to the HIP joint components as parts of the blanket structure and demonstrated good agreement with the properties of the base metal (Fig.9-9).

With this achievement, we have a powerful tool that enables us to directly evaluate the HIP joints of the fusion blanket structure. Establishing this test technique is undoubtedly viable in the establishment of design codes and standards for the DEMO reactor.

Reference

Nozawa, T. et al., Determining the Shear Fracture Properties of HIP Joints of Reduced-Activation Ferritic/Martensitic Steel by a Torsion Test, Journal of Nuclear Materials, vol.427, issues 1-3, 2012, p.282-289.

9–4 Toward the Construction of an Intense Neutron Source that Produces Fusion Reactor Conditions
— Engineering Validation Research and Engineering Design of the Lithium Facility —

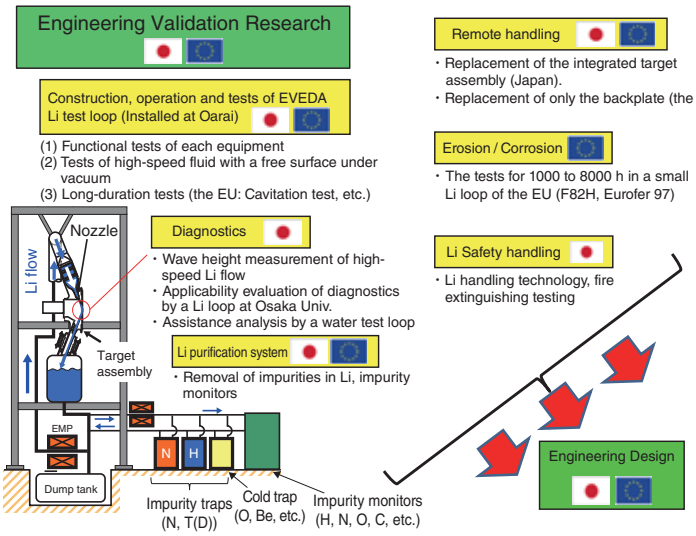

Fig.9-10 Contents of engineering validation and engineering design activities of the lithium facility of IFMIF/EVEDA
For engineering validation of IFMIF, a prototype Li test loop was constructed, operated, and tested. Based on some of the engineering validation tests, an intermediate engineering design report for IFMIF was created.

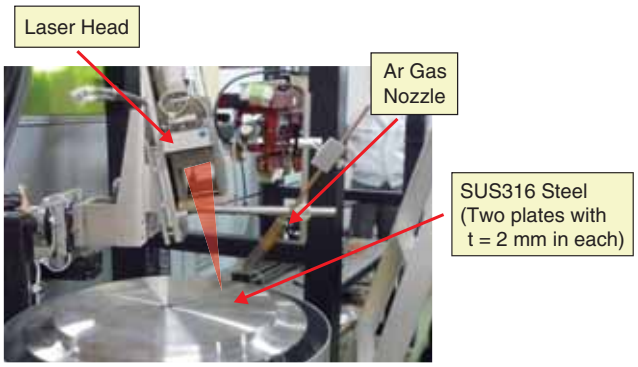

Fig.9-12 Validation tests of the welding and cutting by a fiber laser
The photo shows a validation test of fiber laser welding with the co-operation of the Joining and Welding Research Institute of Osaka University. The laser output and a welding speed were maintained at 5 kW and 3 m/min, respectively.

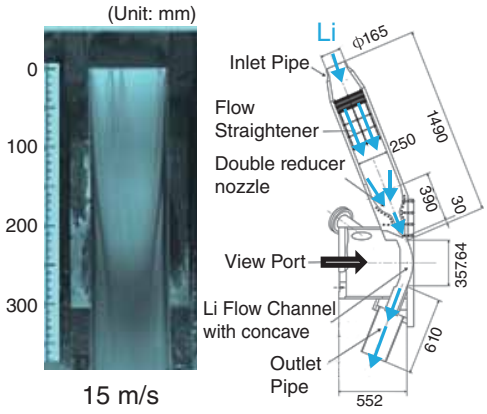

Fig.9-11 An image of high-speed Li flow with a free surface (left) and the flow channel (right)
Stable high-speed lithium flows are shown as the most important validation tests conducted by the Li test loop with the world's largest flow rate of 3000 ℓ/min (250 °C in a vacuum of about 370 Pa).

In fusion reactors, the phenomena of irradiation hardening and irradiation embrittlement of materials occurs due to the displacement damage and nuclear transformation products (e.g., H and He) in materials caused by 14 MeV neutrons produced by the fusion reaction (D–T reaction). The amount of neutron irradiation of materials in ITER, whose construction is currently underway, is several percentage points below the goal for fusion DEMO reactors, and is therefore not sufficient for the evaluation of materials developed for use in DEMO reactors. Therefore, it is essential to evaluate the dependency of the irradiation dose on the materials and components in the irradiation environment for 14 MeV neutrons with a high-intensity like that at IFMIF.

In IFMIF, two deuteron beams of 125 mA at 40 MeV (beam Size: 200 mm width and 50 mm height) were injected into a liquid lithium target (260 mm width, 50 mm height, 25 mm thickness) at 250 °C, having a free surface in a vacuum (10^{-3} Pa), and neutrons were generated. At present, EVEDA are being conducted at IFMIF as one of the BA activities in collaboration between Japan and the EU.

We are conducting engineering validation tests and design of the Li facility in IFMIF, as shown in Fig.9-10. We constructed and are operating the EVEDA Li test loop with the world's largest flow rate (3000 ℓ/min), which is a prototype for the IFMIF Li facility, and we are acquiring the validation test data required to determine the construction of IFMIF. In the evaluation of this high-speed Li flow, observation by a video camera (Fig.9-11) and measurement by a developed noncontact wave-height laser meter revealed that a stable flow could be formed not only at positive pressures but also at negative pressures. As an engineering validation test of remote-control technology, adaptability tests of cutting and welding using a fiber laser were conducted to replace the equipment (called a target assembly) in the Li facility, and some of good results were obtained (Fig.9-12). The 6500-page intermediate engineering design report for the entire IFMIF facility was created in FY 2013, and was based on these engineering validation tests.

Reference

Wakai, E. et al., Engineering Validation and Engineering Design of Lithium Target Facility in IFMIF/EVEDA Project, Fusion Science and Technology, vol.66, no.1, 2014, p.46–56.

9–5 Disassembly of the Japan Torus-60 Tokamak Device for the Japan Torus-60 Super Advanced Project
— Disassembly of Large Radioactivated Structures —

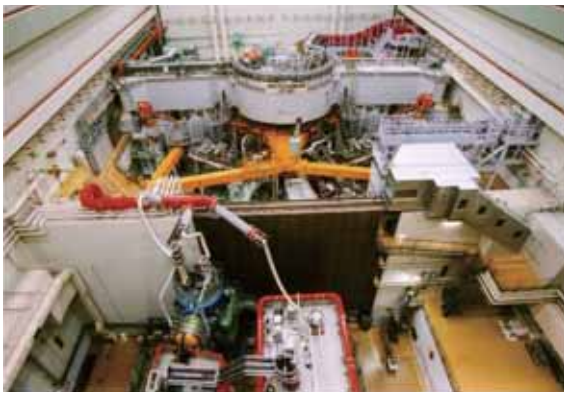

Fig.9-13 JT-60 Torus hall before disassembly
The JT-60 Torus hall was an complex narrow space. There was the JT-60 tokamak device with auxiliary tokamak facilities, diagnostics, and heating system.

Fig.9-14 JT-60 Torus hall after disassembly
Disassembly of the JT-60 tokamak was completed without accidents in October 2012. Assembly of JT-60SA started in January 2013.

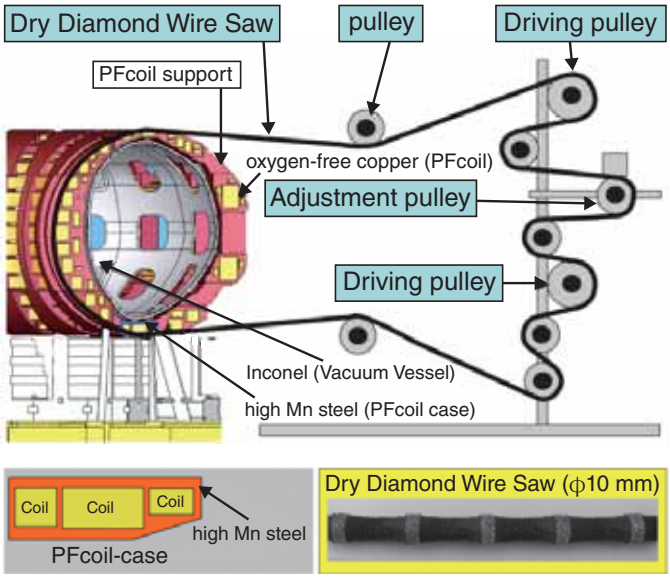

Fig.9-15 Diamond wire-saw system
The diamond wire saw is an embedded diamond chip. It can efficiently cut dissimilar metals without cooling water.

The disassembly of the JT-60 tokamak device (Fig.9-13) was required for the construction of the JT-60SA tokamak as part of the Satellite Tokamak program conducted in collaboration between Japan and the EU. The JT-60 tokamak was a unique fusion device regulated by the Radiation Hazard Prevention Act. This device had been radioactivated by neutrons during deuterium operations between 1991 and 2008. This disassembly was the first such experience with a large, radioactivated fusion device in Japan, and represented a new approach in consideration of the application of clearance level regulations in the future. The disassembly started in 2009 and was completed in October, 2012. The total weight of the dismantled components reached up to 5400 tons (Fig.9-14).

One of the main issues facing this disassembly was the need to cut the several large assembled structures, such as the reinforced points between the toroidal magnetic field coils (TFCs) and the vacuum vessel (VV) with poloidal magnetic field coils (PFCs).

Both TFCs were weld-jointed at the narrow tops and bottoms of their cases (high Mn steel) to reinforce against electromagnetic forces. A portable milling machine was developed to be mounted at the narrow space for cutting the high Mn steel, which is a difficult-to-machine material. Thus, the TFCs could be dismantled one by one.

After removing the TFCs, the main residual components were the vacuum vessel and the PFCs. Their total weight was about 320 tons, which was beyond the building crane capacity (250 tons). The residual component was to be separated into two parts for lifting. The materials of the VV and the PFCs were Inconel and oxygen-free copper supported with high-Mn steel, respectively. In this case, matrix structures were to be simultaneously cut. In the mock-up test, it was found that a dry diamond wire saw could cut those materials without cooling water. Finally, the application of the dry diamond wire saw to the separation was successfully conducted (Fig.9-15).

The JT-60 disassembly was efficiently completed by employing new dismantling technologies, and has provided valuable data, which will be useful for the disassembly of nuclear facilities as well as the other fusion devices.

Reference

Ikeda, Y., Okano, F. et al., Safe Disassembly and Storage of Radioactive Components of JT-60U Torus, Fusion Engineering and Design, vol.89, issues 9–10, 2014, p.2018–2023.

9–6 Accurate Winding of a Nb_3Sn Superconducting Magnet

— Development of JT-60SA Central Solenoid for Precise Plasma Control —

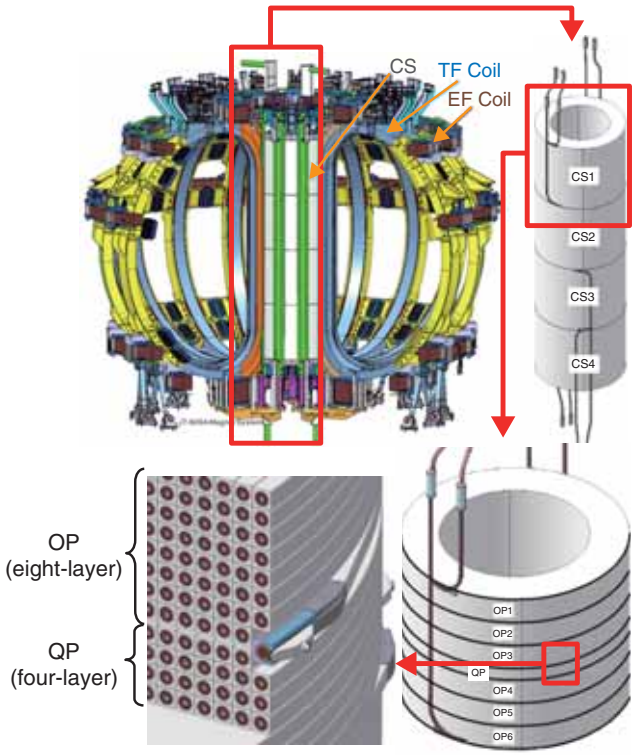

Fig.9-16 Central Solenoid for JT-60SA
The CS of JT-60SA is to comprise four electrically independent modules (CS1-CS4). Each CS module contains 6 eight-layer pancakes (OP1-OP6) and a four-layer pancake (QP).

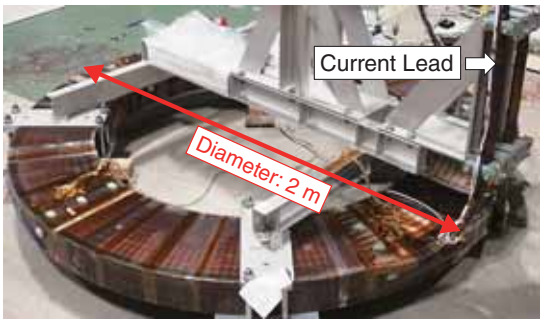

Fig.9-17 CS Model Coil
A prototype CS model coil was manufactured with the full-sized four-layer pancake for the verification test.

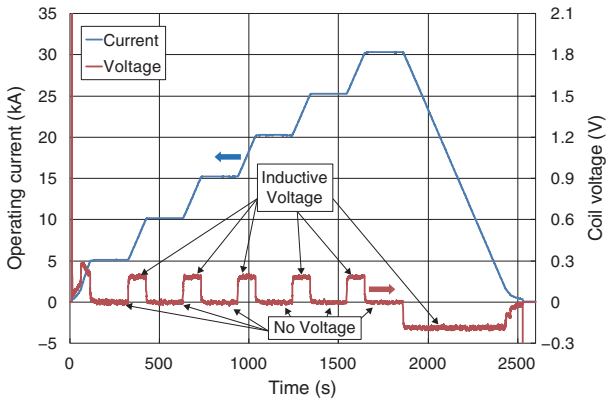

Fig.9-18 Voltage Measurement of the CS Model Coil
Only inductive voltage was measured. A superconducting state was maintained during the performance verification test.

The manufacture of superconducting magnets is in progress as one of the components of the JT-60SA project. The JT-60SA is to comprise 18 TFCs, a CS and 6 equilibrium field (EF) coils, as shown in Fig.9-16. The TFCs are being manufactured by the EU, and the CS and EF coils are being manufactured by Japan.

A NbTi conductor is used for the TFCs and EF coils because of its low magnetic field of under 6 T. The NbTi has a high mechanical workability, but cannot be used for high magnetic field applications. Thus, the Nb_3Sn conductor was selected for the CS since the magnetic field reaches 9 T during the operation.

The heat-treated Nb_3Sn conductor cannot be bent or wound into a coil configuration because Nb_3Sn is very brittle and loses superconductivity easily by deformation. Therefore, the conductor is wound into the final shape before combining Nb with Sn, and then the shaped conductor is heat-treated to manufacture Nb_3Sn. For precise plasma control, the circularity of the CS is required to be less than 4 mm per 2 m in diameter. The technical capabilities to handle the Nb_3Sn conductor and the coil winding with a high accuracy are required for CS manufacturing.

We developed a winding machine that controls the deformation amount from the bending radius and the conductor stiffness. A feedback sequence is added to the winding process to cancel-out the variation of the bending stiffness of the conductor. In addition, the winding accuracy was maintained after the insulation process by appropriate control of the insulation thickness. The winding accuracy of the preproduction was 1.6 mm, which met the minimum requirement of 4 mm. The CS model coil shown in Fig.9-17 was manufactured using the developed winding method and was used for the performance verification test.

The test result shows that the superconducting state was successfully maintained up to 30 kA (Fig.9-18). This means that the CS can be well manufactured using the developed winding method. The manufacturing of the real CS was commenced as a result of this achievement.

Reference

Murakami, H. et al., Development and Test of JT-60SA Central Solenoid Model Coil, IEEE Transactions on Applied Superconductivity, vol.24, no.3, 2014, p.4200205-1-4200205-5.

9–7 World Record-Setting Dual-frequency Gyrotron

— The Development for Electron Cyclotron Resonance Heating in JT-60SA —

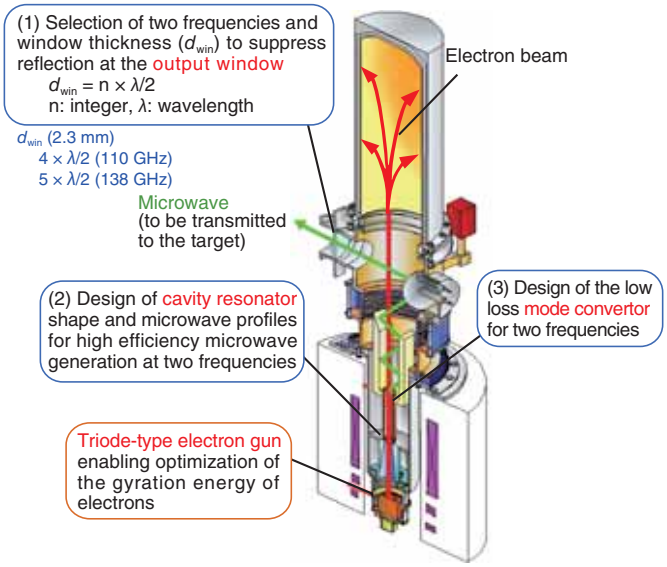

Fig.9-19 Key points of the gyrotron design for obtaining high performance at two frequencies
High efficiency and low loss were achieved by three key points (▭), and the optimum energy of electron gyration was obtained with a triode electron gun.

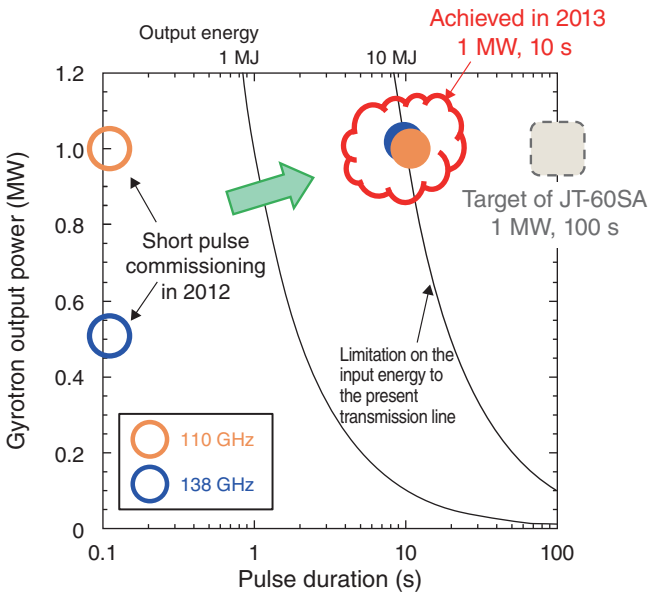

Fig.9-20 Progress in high-power, long-pulse development and its target value
A gyrotron output power of 1 MW for 10 s, which is a world record for a dual-frequency gyrotron, was demonstrated.

An electron cyclotron heating (ECH) system will generate or sustain high-performance plasma in JT-60SA through the injection of high-powered microwaves. ECH enables the plasma to be heated locally where the magnetic field strength corresponds to the microwave frequency. However, long-pulse operation of a gyrotron, which is a source of high-powered microwave, was previously obtained only at a single frequency. Consequently, it was not capable of heating the desired position in the plasma when the magnetic field was changed. To solve this issue, a dual-frequency gyrotron, which can independently be operated at two frequencies, is being developed.

Three key points of the dual frequency gyrotron design (Fig.9-19) are as follows. (1) The thickness of the output window was required to be a multiple of one half of the wavelength for complete suppression of the reflection at the window. (2) A desired set of operating frequencies and microwave profiles in a cavity resonator was required to obtain high conversion efficiency from the energy of the beam from the electron gun to the microwave energy. These conditions have been satisfied simultaneously with a window thickness of 2.3 mm and frequencies of 110 GHz and 138 GHz. Moreover, (3) the shape of the mode convertor, which converts the microwave profile oscillating in the cavity resonator to one suitable for transmission, has been designed to reduce internal loss. A gyrotron design that was sufficient for high-power, long-pulse operations without overheating of the gyrotron internal components was obtained.

To obtain high efficiency in practical operation, an optimized condition of the gyration energy of the electrons in the electron beam was required. The developed gyrotron was equipped with a triode-type electron gun, whereby the gyration energy of the electrons could be controlled. This characteristic enabled us to obtain high efficiency at both frequencies as expected, which was not possible with a diode-type electron gun (e.g., 0.95 MW/140 GHz, 0.85 MW/105 GHz in Russia). The developed gyrotron successfully operated at a nominal output power of 1 MW for 10 s (Fig.9-20). This result set a world record for dual-frequency gyrotrons.

Moreover, we confirmed that the internal loss at the mode convertor and the temperature increases of the components were sufficiently low, as was expected. Although the cooling capability of the transmission line for transmitting the microwave from the window to the target to be heated limited the pulse length this year, it should be possible to expand the pulse length toward the target (1 MW/100 s) by improving the transmission line for JT-60SA.

Reference

Kobayashi, T. et al., Dual Frequency ECRF System Development for JT-60SA, Transaction of Fusion Science and Technology, vol.63, 2013, p.160–163.

9–8 Improvement of the Stability Analysis Model for Rotating Plasmas

— Introducing Rotation Effects into the Kinetic-Magnetohydrodynamic Model —

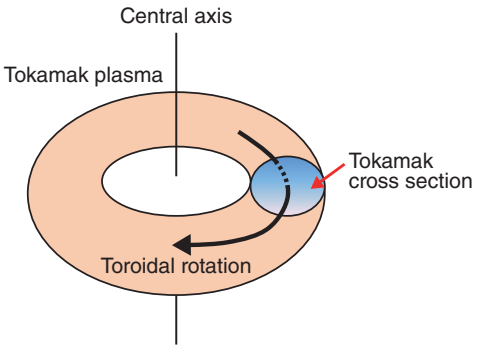

Fig.9-21 Schematic of the tokamak plasma and toroidal rotation
A tokamak plasma rotating in the toroidal (azimuthal) direction is schematically shown. Since the tokamak is axisymmetric, the cross section is focused.

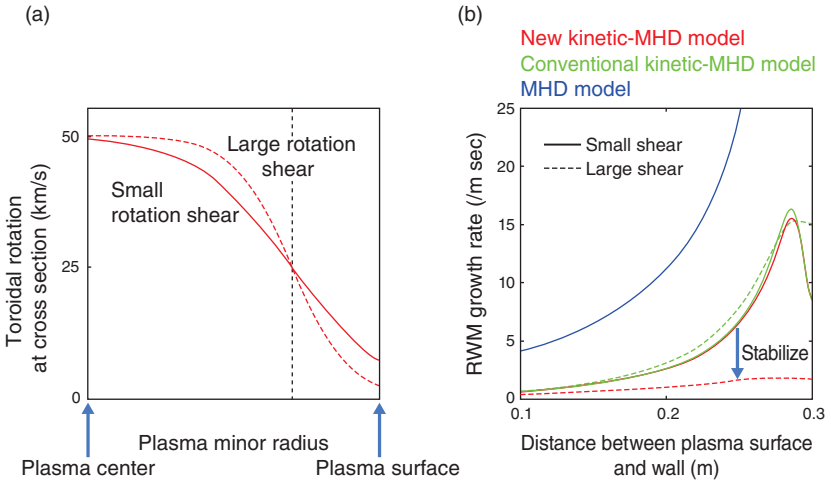

Fig.9-22 (a) Rotation profile in a tokamak cross section (b) RWM growth rate
RWM growth rates by various models. In the new kinetic-MHD model, the RWM growth rate is reduced by the increase of rotation shear.

The JT-60SA tokamak device, which is being constructed at the Naka site of JAEA, is designed to complement ITER research and establish a foundation for a tokamak DEMO reactor. In particular, the JT-60SA device aims to confine a high-pressure plasma, because fusion output increases with the plasma pressure. However, when the plasma pressure increases, a macroscopic instability known as a resistive wall mode (RWM) becomes unstable, limiting the achievable pressure value. Toroidal rotation (Fig.9-21) is known to stabilize RWM. Interaction between the RWM and the constituent particles' motion has also been revealed to be important for the stabilization of RWMs.

To analyze the interaction between the RWMs and the particles' motion, the kinetic-magnetohydrodynamic (MHD) model, which analyzes energy exchange between macroscopic MHD modes (such as RWMs) and constituent particles, has been formulated. In the conventional kinetic-MHD model, the background plasma is assumed to be static (no rotation). In this study, we shed new light on the fact that the constituent particles' motion is affected by plasma rotation. For example, particle motion is affected by the Coriolis force, which is an inertial force appearing in a rotating frame working in the direction perpendicular to the rotational direction. In the rotating frame, another inertial force, the centrifugal force, additionally affects the particle motion. Considering these effects, we reformulated the kinetic-MHD model. The energy of RWMs was found to be strongly damped by resonance with the particles' motion affected by Coriolis and centrifugal effects. Note that these effects were overlooked in the conventional model.

Based on the newly derived kinetic-MHD model, we have investigated RWM stability. Fig.9-22(a) indicates the rotation profile in a tokamak cross section, and shows that the rotation shear (gradient) is increased in keeping with the rotation amplitude at the location where the energy interaction between RWMs and particle motion is large. Fig.9-22(b) shows computation results of the RWM growth rate as functions of distance between the plasma surface and the wall. Since the arrow in Fig.9-22(b) indicates the increased rotation shear, we find that the RWM growth rates are decreased (stabilized) by the rotation shear. This result indicates that the control of the rotation profile is beneficial for stabilizing RWMs, which can contribute to the design of tokamaks with high-pressure plasma confinement.

The present study was partly supported by Japan Society for the Promotion of Science (JSPS) KAKENHI Grant-in-Aid for Young Scientists (B) (No.24760708).

Reference

Shiraishi, J. et al., On Kinetic Resistive Wall Mode Theory with Sheared Rotation, Plasma and Fusion Research, vol.9, 2014, p.3403027–1–3403027–4.

9–9 Safe Shutdown Scenarios for Fusion Reactors
— The Development of a High-Energy Runaway Electron Simulation Code —

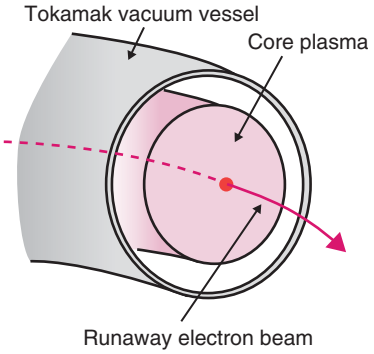

Fig.9-23 Schematic of core plasmas and the runaway electron beam
During disruptions of tokamak operation, the voltage induced in the core plasma accelerates electrons and yields the formation of a high-energy electron beam, which we call “runaway electrons (REs).”

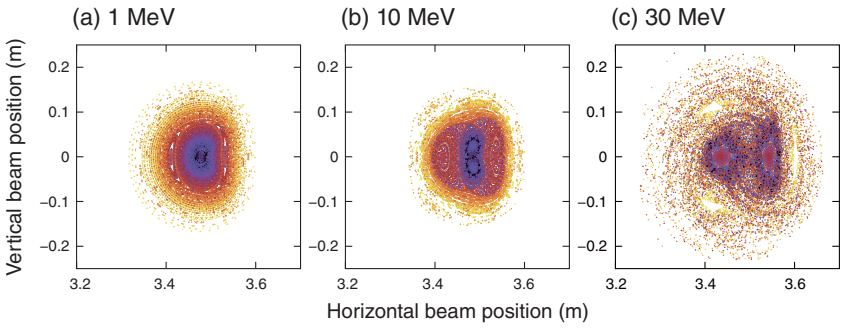

Fig.9-24 Simulation of a high-energy electron orbit with magnetic perturbations
Points in the figures represent the positions at which electrons pass through a tokamak minor cross section; the color of each point indicates the distance between electrons and the beam axis. (a) A concentric circular structure indicates well-confined electron orbits with a negligible radial excursion. (b) Magnetic perturbations cause unstable electron orbits. (c) At high energy, the unstable orbit becomes chaotic, exhibiting random and large radial excursion.

During tokamak operation, a quench of the plasma current, being inherent to the confinement of core plasmas, often occurs due to various internal and external causes, which we call “disruptions.” In future DEMO and commercial reactors, the operation regime must carefully be chosen to avoid such disruptions. On the other hand, in present machines aimed at extending the operational regime so that high-performance tokamaks realize fusion energy, uncontrollable disruptions often occur in experiments.

It is important to understand the physical phenomena involved in disruptions, which are not observed in normal plasma operation. Particularly, the generation of a beam of energetic electrons (Fig.9-23), which is called as “runaway electrons (REs),” is one of the most important topics for the disruption study. REs often attain energies of several tens of MeV through the conversion of magnetic to kinetic energy, which can cause serious damages to the in-vessel components. However, detailed mechanisms of RE generation during tokamak disruptions have not yet been elucidated. To improve our understanding of the interaction between REs and magnetic perturbations, which has been conventionally investigated using relatively simple models, we have developed a new simulation code for analyzing high-energy electron orbits while considering the detailed structure of magnetic perturbations during disruptions.

Using the developed code, we have analyzed the RE orbit for JT-60U scale disruptions and found a novel mechanism such that only high-energy REs above 10 MeV exhibit unstable trajectories and significant radial transport (Fig.9-24). In previous studies, the confinement of such high-energy REs was considered to improve because high-energy REs deviate from magnetic field lines owing to the centrifugal force, and tend not to feel magnetic perturbations. The present calculation has clarified the possibility that high-energy REs exhibit strongly disturbed trajectories compared with low-energy ones. Our simulation shows that such energy dependence is explained by the interference between the magnetic perturbation and the periodic motion of high-energy REs, which occurs if their own characteristic frequencies satisfy a certain condition.

The findings obtained in this study provide a clue toward understanding the RE generation mechanism and offers a physical basis for the control of disruptions and REs in ITER and DEMO reactors.

Reference

Matsuyama, A., Yagi, M. et al., Stochastic Transport of Runaway Electrons due to Low-Order Perturbations in Tokamak Disruption, JPS Conference Proceedings, vol.1, 2014, p.015037-1-015037-4.

9–10 Removing Fuel from the Nuclear Fusion Blanket

— Investigation of Tritium Recovery from a Future Fusion Blanket —

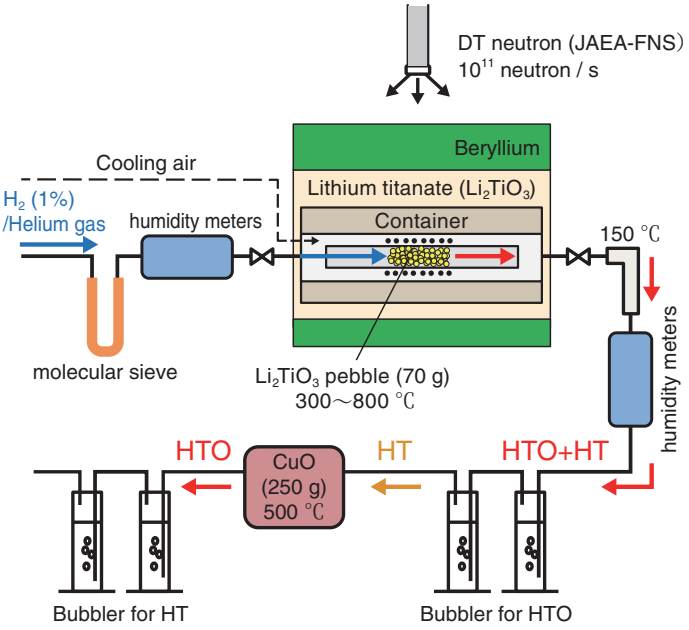

Fig.9-25 JAEA-FNS tritium recovery experiment apparatus
Li_2TIO_3 pebbles were installed in the blanket container in an experimental mock-up. During DT neutron irradiation, tritium produced in the pebbles was recovered with sweeping gas.

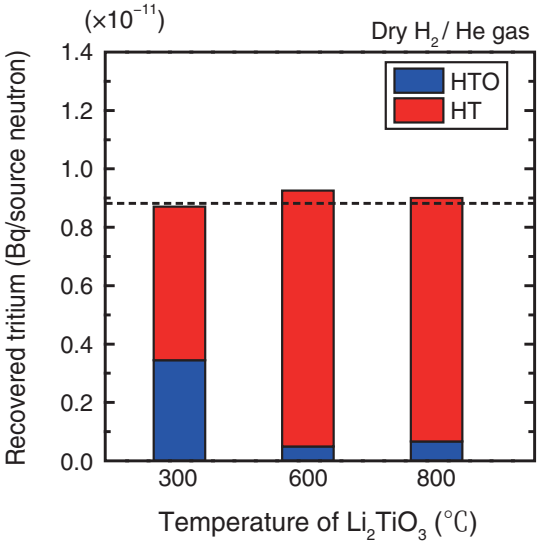

Fig.9-26 Result of the JAEA-FNS tritium recovery experiment
JAEA-FNS conducted the first tritium recovery experiment with DT neutron source. Our quantitative measurement of the recovered tritium indicated that the recovered tritium corresponded to calculated tritium production.

Tritium used as fuel in fusion reactors will be produced by nuclear reactions between lithium and neutrons generated by DT fusion reactions, like ^{6}Li (n, α)^{3}T. It is important to investigate methods to recover the tritium produced in the "blanket," which is a key part for the development of a fusion reactor. To investigate the recovery of the tritium produced, we have conducted a series of tritium recovery *in situ* experiments using the DT neutron source at JAEA's Fusion Neutronics Source facility (FNS).

We irradiated an experimental assembly that simulated a fusion blanket (Fig.9-25) and recovered the tritium produced in the Li_2TiO_3 pebbles that filled the assembly by sweeping with helium gas mixed with a small amount of hydrogen (H_2, 1%). During the neutron irradiation, the Li_2TiO_3 pebbles were heated to temperatures ranging from 300 °C to 800 °C by a heater set near the pebbles.

To remove water moisture from the gas emerging from the gas cylinder, a molecular sieve (MS) was inserted in the line to the inlet of the assembly. Among the tritium (HT and HTO) produced in the Li_2TiO_3 pebbles and swept in the gas, only the tritiated water (HTO) was collected to the first bubblers. A copper oxide bed was set upstream of the second bubblers to oxidize the tritium gas (HT) component to HTO, since the second bubblers could collect only the HT component generated in and released from Li_2TiO_3 pebbles. The recovered tritium was measured with a liquid scintillation counter.

As shown in Fig.9-26, for the first time, the total amount of tritium recovered from the Li_2TiO_3 pebbles was found to be almost the same regardless of the temperature and in good agreement with the tritium production amount calculated. This means that the tritium produced in the blanket can be recovered by sweeping with the helium-hydrogen (H_2, 1%) gas mixture. The percentage of tritium released into the sweeping gas in the form of HT was only 40% at 300 °C, but increased up to 95% at higher temperatures. The HT ratio at 800 °C was almost the same as that at 600 °C.

Reference

Ochiai, K. et al., DT Neutron Irradiation Experiment for Evaluation of Tritium Recovery from WCCB Blanket, Fusion Engineering and Design, vol.89, issues 7–8, 2014, p.1464–1468.

9–11 Stably Supplying Fuel Tritium to Fusion Reactors

— Establishment of a New Pebble Fabrication Technology for an Advanced Tritium Breeder —

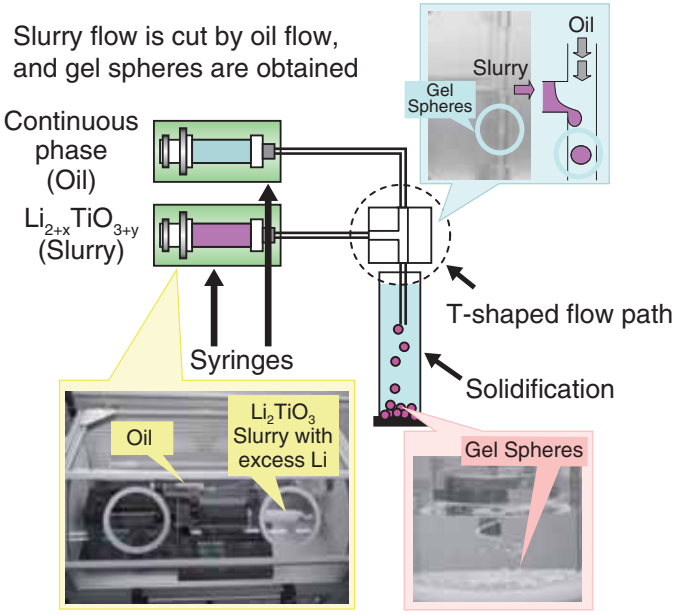

Fig.9-27 Pebble fabrication of tritium breeders using an emulsion method
The flow of the Li_2TiO_3 slurry with excess Li ($Li_{2+x}TiO_{3+y}$) is cut by an oil flow from an oil-filled syringe. The emulsion method is suitable for mass production of $Li_{2+x}TiO_{3+y}$ pebbles.

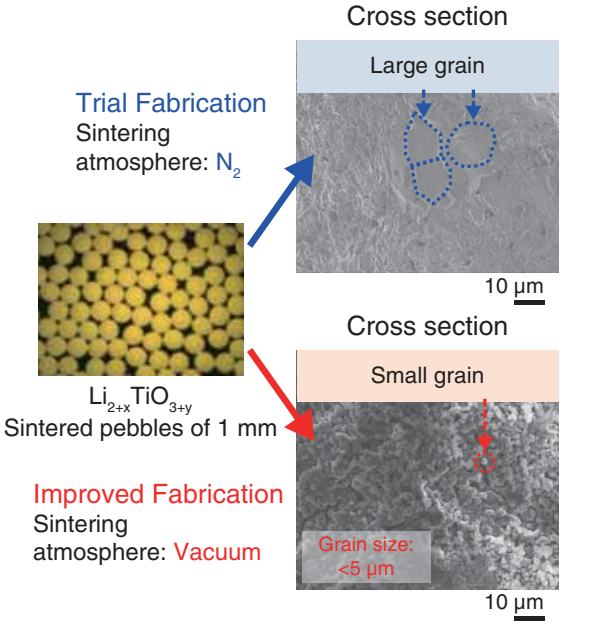

Fig.9-28 Improvement of the grain size of tritium breeder pebbles
To prevent grain growth, $Li_{2+x}TiO_{3+y}$ gel spheres were sintered in vacuum. The average grain size of the sintered $Li_{2+x}TiO_{3+y}$ pebbles was less than 5 μm.

Fusion reactors need deuterium (D) and tritium (T) as their fuel. Since tritium does not exist in nature, it is necessary to produce tritium in a reactor by neutron irradiation of lithium (Li). Lithium titanate (Li_2TiO_3) is one of the most promising candidates among tritium breeders because of its tritium release characteristics. However, the mass of Li in the breeders decreases in a hydrogen atmosphere because of Li evaporation and Li burn-up.

To prevent the mass decrease of Li at high temperatures, Li_2TiO_3 with excess Li ($Li_{2+x}TiO_{3+y}$) has been developed as an advanced tritium breeder. The emulsion method as a pebble fabrication technique for $Li_{2+x}TiO_{3+y}$ was developed under the IFERC program of BA activities. The emulsion method can easily produce large volumes of uniform submicron particles. For fusion reactors, tritium breeder pebbles of 1 mm are needed. To examine whether the emulsion method is suitable for pebble fabrication, we used the granulator shown in Fig.9-27.

This granulator comprised two syringes arranged in a T-shaped flow path. One syringe was filled with oil and the other with a $Li_{2+x}TiO_{3+y}$ slurry. The two flow lines from the syringes were connected perpendicular to one another. This arrangement allowed us to cut the $Li_{2+x}TiO_{3+y}$ slurry flow with an oil flow from the oil-filled syringe. The size of the tritium breeder gel spheres was controlled by the flow speeds of the oil and the slurry. The gel spheres were placed in an oil-filled container.

In a series of fabrication trials, the average grain size on the surface and cross section of the sintered $Li_{2+x}TiO_{3+y}$ pebbles was 2–10 μm. Considering the tritium release characteristics, the optimum grain size after sintering should be less than 5 μm. The grain growth factor was assumed to be the presence of binder in the gel spheres. The remaining binder reacted with the Li in $Li_{2+x}TiO_{3+y}$ and generated Li_2CO_3. To prevent this reaction, the $Li_{2+x}TiO_{3+y}$ pebbles were sintered in a vacuum atmosphere (Fig.9-28). The average grain size on the surfaces and cross sections of the sintered $Li_{2+x}TiO_{3+y}$ pebbles was thus less than 5 μm.

The results suggest that the Li_2CO_3 generated by the remaining binder affects grain growth and that sintering under vacuum improves the grain size of the pebbles.

Reference

Hoshino, T. et al., Development of Fabrication Technologies for Advanced Breeding Functional Materials for DEMO Reactors, Fusion Engineering and Design, vol.87, issues 5–6, 2012, p.486–492.

Advanced Computing and Simulation Technology to Support Nuclear Research and Development

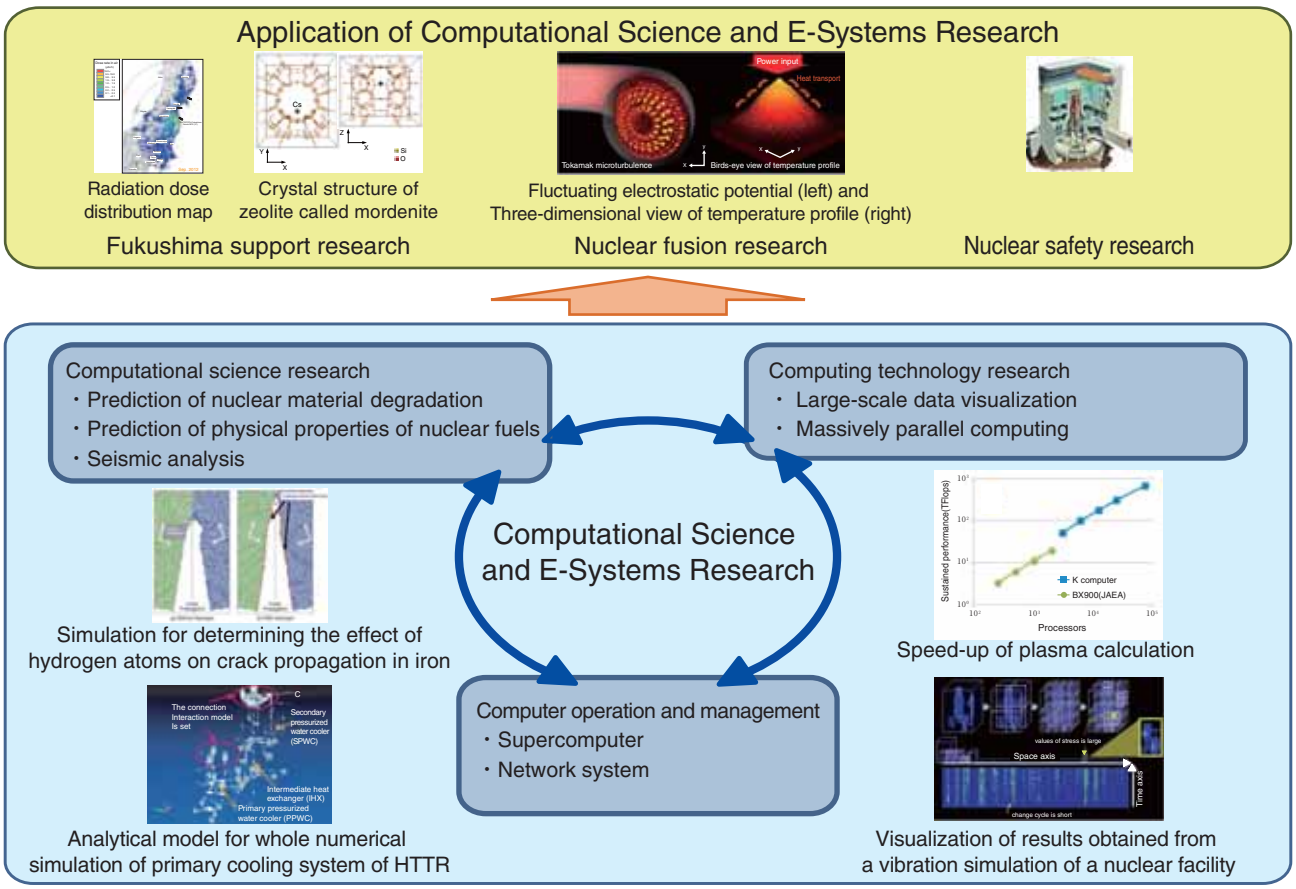

Fig.10-1 Advanced computing and simulation technology and its application to current nuclear research
Computational science research, computing technology research, and computer operations and management are jointly promoted, and the results are applied to research that supports efforts to resolve the problems in Fukushima and atomic energy research.

Computational science is now widely regarded as the third research methodology, following theoretical and experimental research methods. Computational science is indispensable for the elucidation and prediction of phenomena that are difficult to observe or replicate experimentally.

The Center for Computational Science and E-Systems promotes important research in nuclear energy fields, such as prediction of nuclear material degradation, prediction of physical properties of nuclear fuels, and seismic analysis. As a computing technology research, we promote large scale data visualization and massively parallel computing. Additionally, computer operation, management of supercomputers, and network maintenance are promoted in conjunction with our core research areas. Furthermore, our research results are developed further in the domains of Fukushima support research, nuclear fusion research, nuclear safety research, and so forth, through cooperation with organizations both inside and outside JAEA (Fig.10-1).

First, we introduce the research Topics that have been developed for Fukushima support. In Chapter 1 Topic 1-5, we build a system that manages radiation dose measurement results by environmental monitoring and make them available to the public and administrative personnel. In Chapter 1 Topic 1-7, for more efficient decontamination, we clarify the Cs adsorption-desorption mechanism on clay minerals through supercomputer simulations.

Second, we introduce computational science research that has been undertaken. In Topic 10-1, the new knowledge obtained by applying computational science to the analysis of nuclear material degradation is shown. Topic 10-2 introduces research and development toward a new earthquake risk evaluation technique for a nuclear installation based on Monte Carlo simulation. Computing technology research that succeeds in the development of a high-speed computation technique is shown in Topics 10-3 and 10-4. In Topic 10-3, a full-scale simulation of the thermal conductivity behavior exhibited by a superconductor is presented. This was previously impossible because it required a large computing time in general. In Topic 10-4, we show how a multi-scale simulation for evaluating and forecasting plasma turbulence is made achievable by maximizing parallel computing performance.

We work on nuclear research and development using computer science and technology, engage in computer technology research and development that supports nuclear research and development, and have promoted the application of research results to various fields. In the future, we will continue to work diligently on nuclear research and development utilizing advanced computational science.

10–1 Helium Induces Grain Boundary Fracture of Iron

— Finding a Universal Law of Grain Boundary Strength Loss Using a Supercomputer —

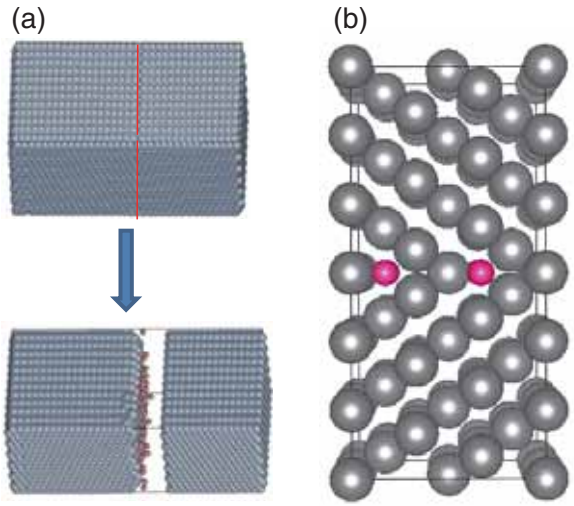

Fig.10-2 Calculation method for GB cohesive energy
GB cohesive energy is defined as the total energy increase per unit area after separating the system at the GB, as shown in (a). The GB used for the present study is symmetrical at the boundary, as seen in (b), being called the symmetrical tilt GB.

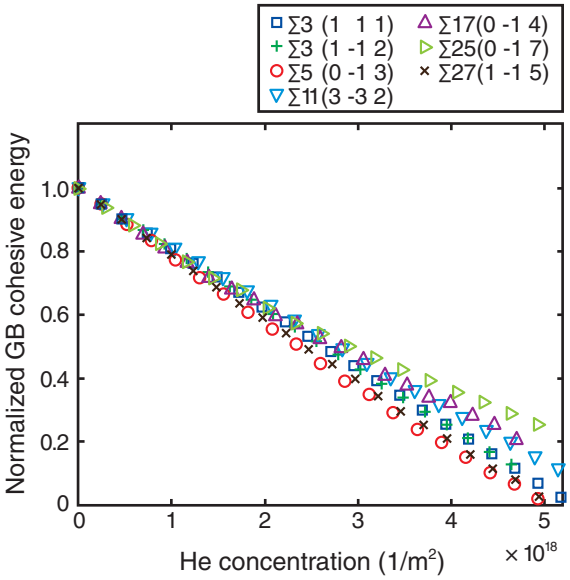

Fig.10-3 The universal relationship between GB cohesive energy and He concentration
GB cohesive energy decreases as He is accumulated. The above value is normalized to the cohesive energy without He accumulation.

Reduced activation ferritic steels are being considered as structural materials of future nuclear fusion reactors. However, it is expected that these steels will become brittle after long-term exposure to a fusion reactor's environment. This may be caused by a decrease in the strength of the grain boundaries (GBs), which are surfaces between two adjacent grains. We suspect that loss of the strength may be caused by helium (He) accumulation at the GBs, which is generated by nuclear transmutation reactions under fast neutron irradiation.

He is accumulated either in the form of bubbles or in an atomic form without forming bubbles. The former occurs under high temperatures and can be observed by electron microscopes. The latter is supposed to occur at low temperatures, but it is difficult to determine the locations or the amount of He involved using experimental means; therefore, the relationship between the GB cohesive energy and the amount of accumulated He is not easily known. For this reason, we particularly focused on the application of computational methodology to He embrittlement without bubble formation under low temperatures.

In the present study, we defined GB cohesive energy as the total system energy increase due to ideal fracture (Fig.10-2) at the GB divided by its area. If this total energy increases, the cohesive energy is positive and a fracture is not expected; otherwise, the fracture is more likely to occur. We evaluated this energy using an atomistic modeling method.

Note that there are plenty types of GBs. In the current study, symmetrical tilt GBs (Fig.10-2(b)), which are suitable for our atomistic modeling, were considered. We searched for He accumulation positions for various GBs and found that these varied with the type of GBs. We artificially inserted He atoms at these positions (in Fig.10-2(b)) and calculated GB cohesive energy as a function of He concentration on the GB. The results for many types of GBs are shown in Fig.10-3. It is known that GB cohesive energy is significantly influenced by He formation energy, which is GB-dependent; however, we found that GB cohesive energy was not dependent on the type of GBs, and was almost uniquely determined by He concentration. This result is critical, because it suggests that investigations on a single GB are sufficient to gauge GB embrittlement caused by He accumulation. As there exist an infinite number of GBs, the benefit gained by this result could significantly increase the efficiency of these types of investigations for other materials.

Reference

Suzudo, T. et al., Atomistic Modeling of He Embrittlement at Grain Boundaries of α-Fe: a Common Feature over Different Grain Boundaries, Modelling and Simulation in Materials Science and Engineering, vol.21, no.8, 2013, p.085013-1-085013-8.

10–2 Toward Reliability Enhancement of Seismic Risk Assessment of NPP
— Proposal for a Ground Motion Generation Method that Combines a Fault Model and Frequency Prediction —

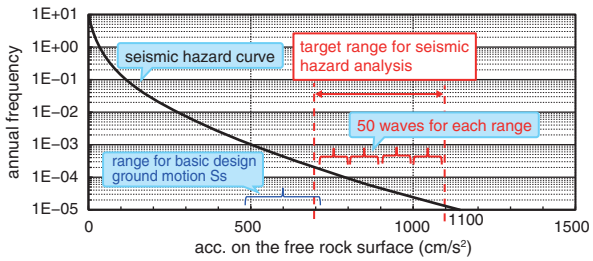

Fig.10-4 SH curve based on the attenuation relationship
The index of the GM intensity is the maximum acceleration on the free rock surface. In this study, the target of the GM reproduction is an annual exceedance probability of 10^{-5}, which is the safety target for the reactor containment vessel, and corresponds to a maximum acceleration of 1100 cm/s^2.

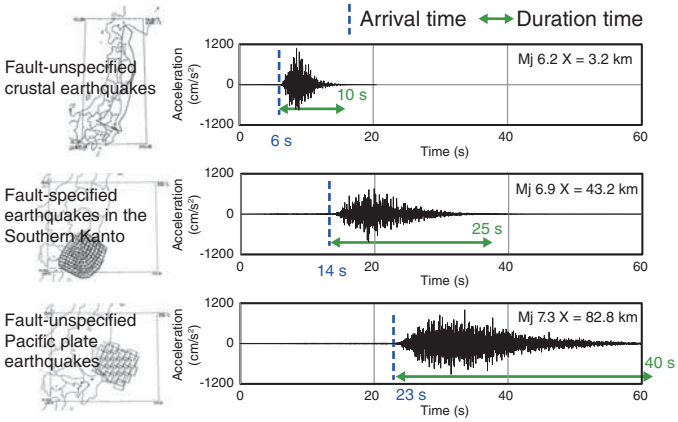

Fig.10-5 Example time histories of reproduced GMs
The GMs in this figure are for the same hazard level; however, it can be seen that GMs reproduced from different faults show different GM properties. (Mj: Magnitude of earthquake, X: Distance from seismic source)

Table 10-1 SSC, considering the uncertainty
MCS was performed by setting the sizes of the uncertainties for stress drop, high-frequency cutoff filter, among others; these parameters were confirmed to have a large impact on maximum acceleration by sensitivity analysis.

Stress drop	$\Delta\sigma$
Rise time coefficient	α_{rr}
Freq. for high-cut filter	f_{max}
Q-value coefficient	C_{Qc}, C_{Qp}
Asperity area ratio	C_{Sa}
Location of the asperity	aspX, aspY
Rupture starting points	startX

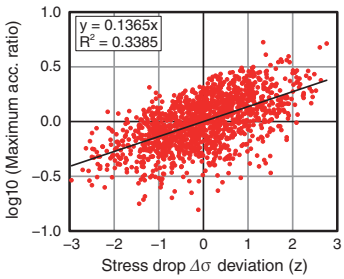

Fig.10-6 Example of the relationship between maximum acceleration ratio and SSC (stress drop)
The horizontal axis is the deviation of SSC, and the vertical axis is the logarithm of the ratio of median acceleration to maximum acceleration for each seismic GM.

Seismic risk assessment (SRA) of nuclear facilities is effective for the consideration of possible ground motions (GMs) that are beyond design assumptions, allowing measures to be reinforced to ensure better safety. Recently, we have embarked on a trial of an enhancement to the SRA method, utilizing a three-dimensional detailed analysis technology that we have developed, with the objective of developing an SRA method using the Monte Carlo simulation (MCS). Instead of the conventional separated evaluation method, potential damage to equipment is assessed by a response simulation using the GM of each item. The advantages of this technique are that it identifies the seismic source characteristics (SSC) that are likely to damage equipment of interest, and that it directly evaluates the correlations between equipment damage.

We began by considering the generation method of the GM as an input. The GM generation methods in conventional SRA are divided into two types: the empirical approach based on the seismic hazard (SH) and an attenuation relationship, and the physical approach based on a fault model. We encountered problems that defeated both methods: the SSC of the GM could not be fully treated in the empirical approach, and the frequency of the GM could not be considered in the physical approach. Therefore, to solve these problems, we devised a technique that combines the two approaches. We proposed a methodology based on MCS to generate a set of GMs that are consistent with the SH, and to consider the differences in the source characteristics using a fault model. Fig.10-4 shows the SH curve at the site. Fig.10-5 shows some examples of time histories of the reproduced GMs.

To date, a trial was conducted at the Oarai site of JAEA to generate GMs by MCS and extract the seismic GMs according to the frequency. Table 10-1 shows the SSC, considering the uncertainty. Consequently, it was found that the SSC (such as high frequency cut-off filter and stress drop) had a large impact on the maximum acceleration of the input, as shown in Fig.10-6. The generation of seismic GM with known SSC enables the analysis of seismic GM characteristics and SSC that affect the damage to nuclear facilities.

Reference

Nishida, A. et al., Characteristics of Simulated Ground Motions Consistent with Seismic Hazard, Transactions of 22nd International Conference on Structural Mechanics in Reactor Technology (SMiRT-22), San Francisco, California, USA, 2013, 10p., in CD-ROM.

10–3 Simulations for Superconductors with High-Performance Eigenvalue Solver
— Toward Real-Size Scale Simulations —

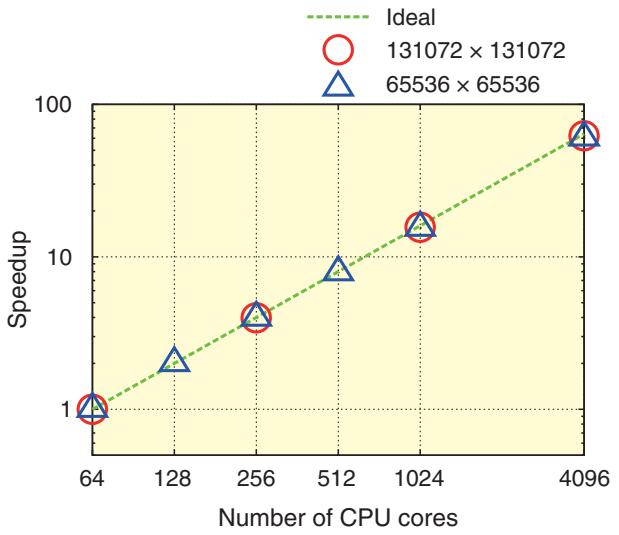

Fig.10-7 Strong scaling plot
Our method shows a perfect strong scaling even with 4096 CPU cores.

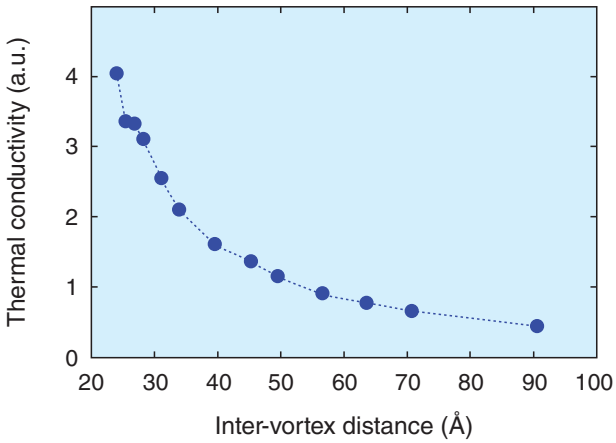

Fig.10-8 Magnetic field dependence of the thermal conductivity in a superconductor
Thermal conductivity increases with increasing magnetic fields.

Superconductivity is one of the most remarkable phenomena in condensed matter systems. A typical behavior is the sudden disappearance of electrical resistance below the superconducting transition temperature. Presently, in the nuclear R&D field, potential applications of the superconductors are being intensively studied. In fact, a superconducting coil will be indispensable for a nuclear fusion reactor. The superconductors are also applicable for the device in the strong radiation such as that with the space probes.

Nano-superconductors are the candidates for replacing the silicon-based semi-conductors. There are various kinds of applications such as the micro SQUID and single photon detectors. Thus, the simulation technique dealing with quantum phenomena in superconductors is very important. In the simulations for superconductors, the superconducting order parameter has to be self-consistently determined by solving the eigenvalue problems of the Hamiltonian matrix. However, the size of the matrix for the nano-superconductors with real-size scale is too huge to calculate with the previous numerical methods. Thus, we developed the simulation technique with the high-performance eigenvalue solver specialized in the massively-parallel supercomputers.

By using the massively-parallel Chebyshev polynomial expansion method for the self-consistently calculations and Sakurai-Sugiura method for calculating physical quantities, we performed the simulations for superconductors with the largest size in the world. Our method has the high-performance even with 4096 CPU cores as shown in Fig.10-7. With the use of our method, we calculated the magnetic field dependence of the thermal conductivity, which is difficult to calculate in the previous methods (Fig.10-8).

We revealed that Sakurai-Sugiura method, that the eigenvalues in a given domain can be obtained very fast, is efficient for calculating the physical quantities in the nano-superconductors. Our high-performance simulations code might be efficient even in the exa-scale supercomputers.

By combining our code with supercomputers, the real-size scale simulations for superconducting devices can be performed and novel functional materials and devices can be constructed in the future.

The present study was partly supported by Japan Society for the Promotion of Science (JSPS) KAKENHI Grant-in-Aid for Scientific Research (B) (No.24340079).

Reference

Nagai, Y. et al., Numerical Construction of a Low-Energy Effective Hamiltonian in a Self-Consistent Bogoliubov-de Gennes Approach of Superconductivity, Journal of the Physical Society of Japan, vol.82, no.9, 2013, p.094701-1-094701-10.

10–4 Massively Parallel Techniques for Realizing 10^5 Times Higher Spatio-Temporal Resolutions
— The K Computer Sheds Light on Multi-Scale Turbulence in Fusion Plasma —

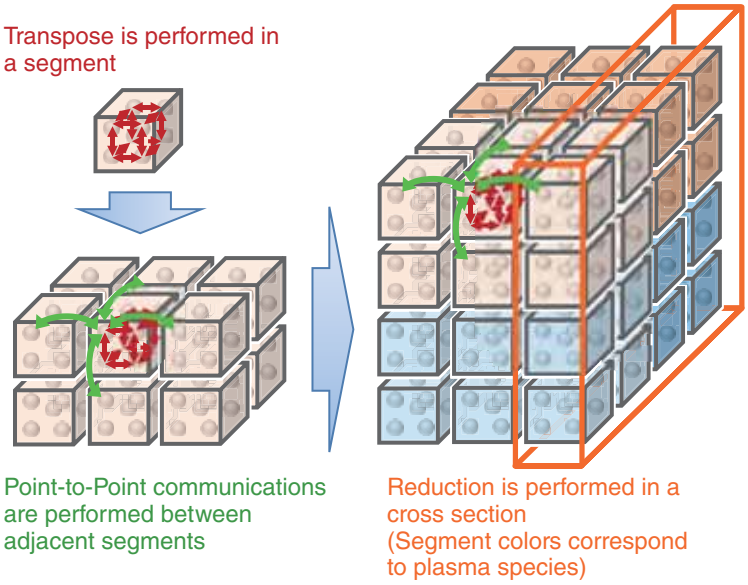

Fig.10-9 Optimized inter-node communication on 3D torus network
The 5D phase space in fusion plasma turbulence is split into small segments, which are allocated on a 3D torus network so as to minimize the required inter-node communications (transpose, point-to-point, and reduction). Thanks to this segmented process mapping, the communication cost is significantly reduced.

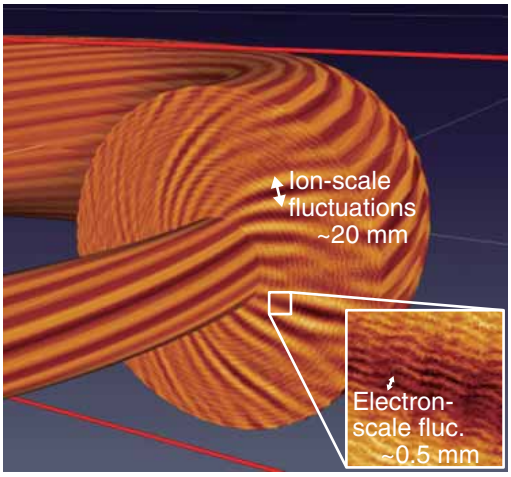

Fig.10-10 Electrostatic potential fluctuations in multi-scale fusion plasma turbulence
We realize multi-scale turbulence simulations that resolve both electron-scale (shown in the magnified view) and ion-scale fluctuations (shown in overall view) consistently, and enable analysis of their cross-scale interactions.

The analysis of turbulent transport is one of the central areas in magnetic fusion research, as the transport caused by electromagnetic turbulent fluctuations has significant impacts on the confinements of fusion fuel in the form of plasma. Numerical simulations of plasma turbulence require significant computation to solve the time evolution of the plasma distributions in a 5-dimensional (5D; three spatial and two velocity coordinates) phase space.

Most of the previous studies have treated the electron-scale turbulence (wavelengths ~0.5 mm, frequencies ~400 kHz) and the ion-scale turbulence (wavelengths ~20 mm, frequencies ~10 kHz) individually by assuming scale separation. The assumption, however, is not obvious. Hence, it is an important issue to reveal whether there are cross-scale interactions or not. Multi-scale simulations resolving their wavelengths and frequencies require 10^5 times higher resolutions than those in single-scale simulations. To realize their large computational requirements, we had to wait for the appearance of petascale supercomputers, such as the K computer (K).

K is a distributed parallel computer, which connects a number of computation nodes with an inter-node network. Therefore, inter-node communications often become a bottleneck for performance. Investigating various types of inter-node communications in the 5D phase space problem, we have developed an optimized communication algorithm on K. The key idea is the segmented mapping of the communication processes, so that communications are performed locally and independently on a 3D torus network (Fig.10-9). This significantly reduces the communication cost by ~60%. Thanks to the optimizations, we have achieved 0.78 PFLOPS using ~600000 cores on K, and realized multi-scale fusion plasma turbulence simulations (Fig.10-10). The simulation result reveals the existence of cross-scale interactions between the electron and ion scales and the change of the turbulent spectrum from those in single-scale simulations. These achievements were internationally appreciated with the Best Poster Award in International Conference for High Performance Computing, Networking, Storage and Analysis: SC13 among other awards.

The present study was supported by HPCI Strategic Program Field 4 and G8 Research Council Initiative NuFuSE.

Reference

Maeyama, S., Idomura, Y. et al., Computation–Communication Overlap Techniques for Parallel Spectral Calculations in Gyrokinetic Vlasov Simulations, Plasma and Fusion Research, vol.8, 2013, p.1403150–1–1403150–8.

Development of Technology and Human Resources in the Area of Nuclear Nonproliferation and Security to Support the Peaceful Use of Nuclear Energy

The Japan Atomic Energy Agency (JAEA) has been conducting the following technological and human resource development activities related to nuclear nonproliferation and security, in cooperation with relevant domestic and overseas organizations (Fig.11-1).

Development of Nuclear Nonproliferation Technology for Japanese and International Applications

We have been examining the concept of nuclear proliferation resistance and evaluation methods by participating in an international project on innovative reactors and the nuclear fuel cycle, as well as the Generation IV International Forum (GIF).

We have been conducting joint research toward advanced nuclear nonproliferation and security with the U.S. Department of Energy (DOE). We also ratified the new project and discussed the new research themes during the 26th permanent coordinating group meeting in March 2014. We have been developing nondestructive assay technology for material accountancy of molten fuels in the Tokyo Electric Power Company, Incorporated Fukushima Daiichi Nuclear Power Station (1F). The technology is based on measurement of passive γ-ray emission from fission products coexisting with nuclear materials. We analyzed the properties of γ-rays leaking from a canister storing molten fuels. From the securing broad options perspective for final disposal, we have initiated a program to develop the safeguard technology that will be applied to the spent fuel direct repository facilities as an alternative option for high-level radioactive waste disposal.

Contributions to the International Community Based on Our Expertise and Experience

To establish a global verification regime for nuclear tests, we have been provisionally operating facilities of the international monitoring system of the Comprehensive Nuclear-Test-Ban Treaty (CTBT) and the National Data Center (NDC). In April 2013, when the Takasaki radionuclide monitoring station detected xenon isotopes that were thought to have originated from a North Korean nuclear test announced two months earlier, we contributed to the government's evaluation using Japan's CTBT national operation system by conducting analysis using the NDC's own methods.

Support for Government Policy Formulation Based on Our Expertise

As a think tank in this area, we conduct research on measures to ensure nuclear nonproliferation and security on the backend of the nuclear fuel cycle. In particular, for the direct disposal of spent nuclear fuel, we conducted the literature review and the site survey for the disposal plan in Finland, and for the safeguards and nuclear security measures of the International Atomic Energy Agency (IAEA). Moreover, we have examined institutional measures such as safeguards to be reviewed in the final disposal site.

Support for JAEA's Transportation and Duties to Research Reactor Fuels

We offer support to the nuclear transportation conducted by JAEA R&D Institutes/Centers, and we have coordinated the procurement of fresh fuels and disposal measures for the spent fuel for our research reactors. Through these activities, we contribute to the Global Threat Reduction Initiative (GTRI), which has strengthened global nuclear security by promoting the systematic return of highly enriched uranium to the United States.

New Efforts on Nuclear Security

On the basis of commitments made by the Japanese government at the Nuclear Security Summit in April 2010, we established the Integrated Support Center for Nuclear nonproliferation and Nuclear Security (ISCN). ISCN conducts capacity building and infrastructure development, focusing on the Asian region. There were approximately 500 participants (approximately 320 of whom were from Asian states) in the training courses on nuclear security and safeguards and other activities in FY 2013.

Furthermore, we have been conducting the research and development of technologies for the measurement to improve nuclear material accountancy, detection of nuclear materials and nuclear forensics in cooperation with the United States, and will continue to contribute to international efforts by establishing highly precise and reliable technologies. Topic 11-1 is one of the results of the research on nuclear security.

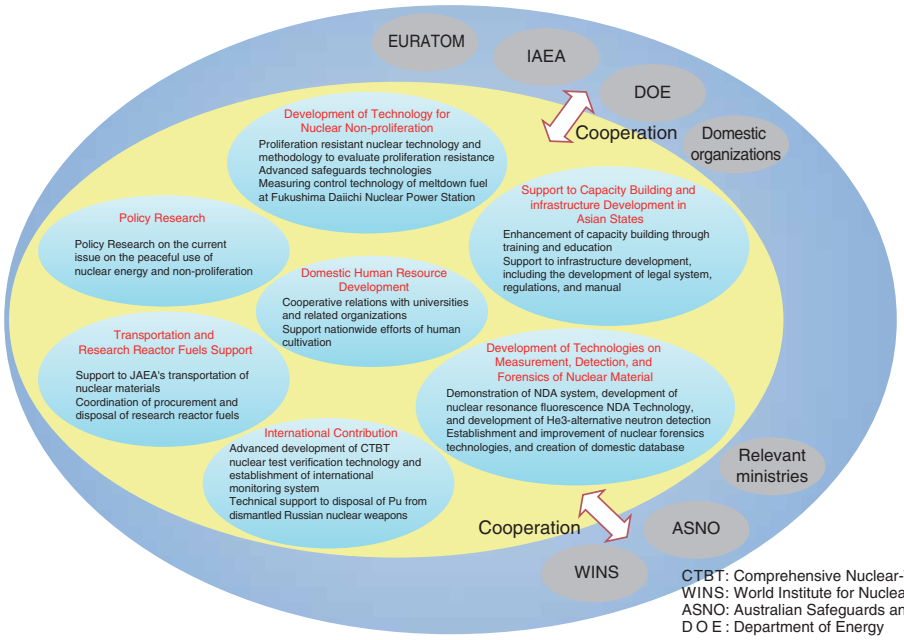

CTBT: Comprehensive Nuclear-Test-Ban Treaty
WINS: World Institute for Nuclear Security
ASNO: Australian Safeguards and Non-Proliferation Office
D O E : Department of Energy

Fig.11-1 JAEA activities toward the development of science and technology for nuclear nonproliferation
We are going to contribute even more to the reinforcement of nuclear nonproliferation and security through the development of technologies for safeguards, nuclear forensics, and the detection of nuclear materials. We are also going to engage in policy research and analysis, and support the capacity building of human resources and infrastructure development in the Asian region, as well as provisional operation of the CTBT international monitoring system, among other initiatives.

11–1 A Probabilistic Expression for Physical Protection Performance in a Nuclear Facility
— A Quantification Method for Physical Protection Performance —

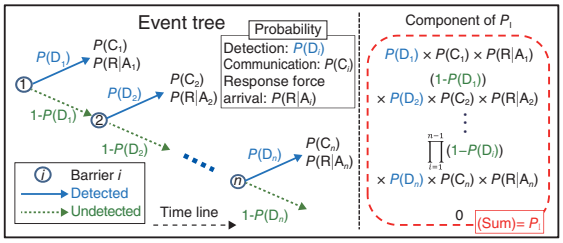

Fig.11-2 Schematic of the EASI method
The left side indicates a simplified event tree diagram at the *i* point barriers, and the right side indicates the calculation components of P_I. P_I is the total probability of these calculation components.

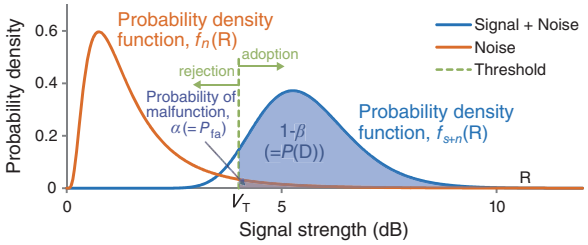

Fig.11-3 Probability distribution functions *P*(D)
Sensors operate in an expected fashion when a signal of strength greater than V_T appears. The type II error, β, is the distribution function of the signal plus the noise from zero to the threshold.

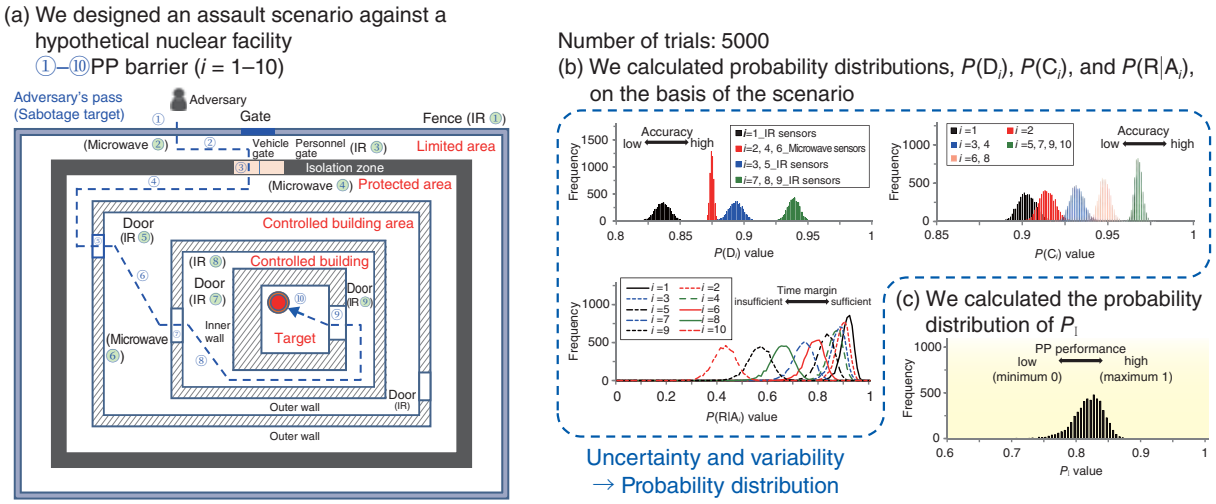

Fig.11-4 Example of P_I assessment in an assault scenario
This figure shows (a) an assault scenario against a hypothetical facility, (b) the performance of each component of P_I ($P(D_i)$, $P(C_i)$, $P(R|A_i)$) at all barriers (*i*=1–10), and (c) the probability distribution of P_I, including the data's uncertainty and variability.

Since the September 11, 2001 attacks, it has become increasingly necessary to consider the physical protection (PP) of nuclear materials against adversarial attacks, i.e., sabotage against a nuclear facility. It is important to assess PP performance when one is designing or implementing PP measures. In general, this is qualitatively evaluated; however, if it is quantitatively assessed, including its uncertainty and variability, it might be possible to provide better PP measures.

In this study, we focus on establishing a quantitative expression for the probability of an adversary being interrupted, P_I, to assess PP performance. A simple calculation describing P_I in an Estimate of Adversary Sequence Interruption (EASI) is shown in Fig.11-2. The left side of this figure indicates a simplified event tree diagram for the P_I calculation at the *i* point barriers, and the right side indicates the calculation components of P_I. $P(D)$ is the probability of a detection alarm (e.g., infrared (IR) sensors) being triggered; $P(C)$ is the probability that the facility guard successfully interprets the alarm condition using the PP equipment and successfully communicates with the response force; and $P(R|A)$ is the conditional probability that the response force arrives prior to the completion of the adversary's action sequence by recognizing the alarm.

In the EASI calculation, both $P(D)$ and $P(C)$ values are considered as the evaluated values without uncertainty and variability, and the $P(R|A)$ value is calculated using a normal distribution. To assess the PP performance more realistically, we develop a new quantification method for P_I that expands EASI by expressing the influence of uncertainty and variability as a probability distribution.

First, we express $P(D)$, as shown in Fig.11-3, using the statistical type II error (β). $P(D)$ is the distribution function area where the probability density function of the signal and noise (f_{s+n}) exceeds a threshold value (V_T). Second, we express the human error affecting $P(C)$ using a log-normal distribution. Third, we re-define $P(R|A)$ using the Poisson distribution to show the margin of error in the response force arrival caused by uncertainty and variability.

We design a hypothetical assault scenario and assess P_I, as shown in Fig.11-4. Furthermore, all components of P_I are calculated from data based on the scenario. Moreover, the data's uncertainty and variability are expressed by normal random numbers. Consequently, we can quantitatively assess P_I using our new method.

Reference

Terao, N., Suzuki, M., A Probabilistic Extension of the EASI Model, Journal of Physical Security, vol.7, issue 2, 2014, p.12–29.

Promotion of Collaboration

To make the technologies, patents and other research results, and facilities and equipment of the Japan Atomic Energy Agency (JAEA) widely available to society, we are promoting activities in three areas: "academia-industry collaboration," "utilization of intellectual property," and "facility usage." We are also creating a database of patents and intellectual property information held by the JAEA.

The following table is a list of intellectual property (patents in foreign countries) in the fiscal year 2013.

Intellectual Property Held by JAEA

Patent Information

No.	Registered Country (Representative Applicant Country)	Title	Department	R&D Institutes and Centers	Publication Number	Date of Registration
1	France	PROCESS FOR PRODUCING METHYLIMINOBISDIALKYLACETAMIDE	Nuclear Science and Engineering Directorate	Nuclear Science Research Institute	1250176	Feb.8, 2013
2	UK	DECLADDING METHOD AND DECLADDING DEVICE FOR SPENT NUCLEAR FUEL REPROCESSING	Nuclear Cycle Engineering Department	Nuclear Fuel Cycle Engineering Laboratories	1496520	Sep.11, 2013
3	France	DECLADDING METHOD AND DECLADDING DEVICE FOR SPENT NUCLEAR FUEL REPROCESSING	Nuclear Cycle Engineering Department	Nuclear Fuel Cycle Engineering Laboratories	1496520	Sep.11, 2013
4	France	MULTIPLAYER FILM COATED DIFFRACTION GRATINGS	Quantum Beam Science Directorate	Kansai Photon Science Institute	2009470	Jan.23, 2013
5	UK	AUSTENITIC STAINLESS STEEL EXCELLENT IN INTERGRANULAR CORROSION RESISTANCE AND STRESS CORROSION CRACKING RESISTANCE	Nuclear Science and Engineering Directorate	Nuclear Science Research Institute	2143815	Jan.8, 2014
6	France	AUSTENITIC STAINLESS STEEL EXCELLENT IN INTERGRANULAR COLLOSION RESISTANCE AND STRESS CORROSION CRACKING RESISTANCE, AND METHOD FOR PRODUCING AUSTENITIC STAINLESS STEEL	Nuclear Science and Engineering Directorate	Nuclear Science Research Institute	2143815	Jan.8, 2014
7	Russia	HYDROGEN COMBUSTION CATALYST AND PROCESS FOR PRODUCTION THEREOF, AND HYDROGEN COMBUSTION METHOD	Fusion Research and Development Directorate	Naka Fusion Institute	2494811	Oct.10, 2013
8	USA	PROCESSES FOR PRODUCING NANO-SPACE CONTROLLED POLYMER ION-EXCHANGE MEMBRANES	Quantum Beam Science Directorate	Takasaki Advanced Radiation Research Institute	8232353	Jul.31, 2012
9	USA	HIGHLY PROTON-CONDUCTIVE POLYMER ELECTROLYTE MEMBRANES THAT EXCEL IN MECHANICAL STRENGTH AND A PROCESS FOR PRODUCING THE SAME	Quantum Beam Science Directorate	Takasaki Advanced Radiation Research Institute	8372558	Feb.12, 2013
10	USA	POWER FEEDING CONTROL APPARATUS AND CHARGING SYSTEM	Safety Administration Department	Head Office (Project Promotion Sector)	8421278	Apr.16, 2013
11	USA	METHOD OF SYNTHESIZING ZIRCONIUM-LOADED FIBROUS ADSORBENT MATERIALS HAVING PHOSPHORYL GROUPS AND REMOVAL OF OBJECTIONABLE SUBSTANCES USING THE ADSORBENTS	Quantum Beam Science Directorate	Takasaki Advanced Radiation Research Institute	8445404	May 21, 2013
12	USA	POLYMER ELECTROLYTE MEMBRANE COMPRISING ALKYLETHER GRAFT CHAIN AND METHOD OF PRODUCING THE SAME	Quantum Beam Science Directorate	Takasaki Advanced Radiation Research Institute	8470895	Jun.25, 2013
13	USA	CLOTH-LIKE RADIOACTIVE MATERIAL ADSORBENT AND ITS MANUFACTURING METHOD	Quantum Beam Science Directorate	Takasaki Advanced Radiation Research Institute	8476188	Jul.2, 2013
14	USA	METHOD OF MANUFACTURING GEL USING POLYSACCHARIDES AS RAW MATERIALS	Quantum Beam Science Directorate	Takasaki Advanced Radiation Research Institute	8481718	Jul.9, 2013
15	USA	METHOD OF MANUFACTURING GEL USING POLYSACCHARIDES AS RAW MATERIALS	Quantum Beam Science Directorate	Takasaki Advanced Radiation Research Institute	8481719	Jul.9, 2013
16	USA	APPARATUS FOR DECONTAMINATING RADIOISOTOPE-CONTAMINATED SURFACE VICINITY REGION BY USE OF NONTHERMAL LASER PEELING	Quantum Beam Science Directorate	Kansai Photon Science Institute	8518331	Aug.27, 2013
17	USA	IMAGE SENSOR, SEMICONDUCTOR DEVICE AND IMAGE SENSING METHOD	Nuclear Science and Engineering Directorate	Nuclear Science Research Institute	8576319	Nov.5, 2013
18	USA	GEL FOR RADIATION DOSIMETER AND RADIATION DOSIMETER WHICH USES THE SAME	Quantum Beam Science Directorate	Takasaki Advanced Radiation Research Institute	8586366	Nov.19, 2013
19	USA	HYDROGEN GAS DETECTING MEMBRANE	Quantum Beam Science Directorate	Takasaki Advanced Radiation Research Institute	8591828	Nov.26, 2013
20	USA	PREPARATION OF GELS DERIVED FROM CARBOXYMETHYL CELLULOSE ALKALI METAL SALT	Quantum Beam Science Directorate	Takasaki Advanced Radiation Research Institute	8633254	Jan.21, 2014
21	USA	METHOD FOR SEPARATING RADIOACTIVE COPPER USING CHELATING-ION EXCHANGE RESIN	Quantum Beam Science Directorate	Takasaki Advanced Radiation Research Institute	8647595	Feb.11, 2014

About the Design of the Cover

The cover is designed to envisage a hopeful future shining in the sky, which is a clear blue color resembling the color of the JAEA logo. This is accompanied by white hexagons similar to the pattern on a tortoise shell, an ancient Japanese symbol of peoples' wishes for longer lives. Coincidentally, this shape is the same as that of the core fuel assemblies of both the prototype fast breeder reactor "MONJU" and the high temperature engineering test reactor "HTTR."

The images on the cover show radiation measurement from the sky using the Unmanned Airplane for Radiation Monitoring System (top left) and results of simplified simulations on the relocation behavior of simulated molten materials (bottom right).

The top left image shows the radiation monitoring system consisting of the radiation detector that we developed and the airplane that was developed by JAXA. The remote operational range of the system is up to approximately 100 km from the ground station, and the flight time can reach approximately six hours. We tested the system and confirmed its capability to map the air dose rate on the ground (Topic Chapter 1 introduction, p.10).

The bottom right image shows the results of simplified simulations on the relocation and accumulation behavior of the lower plenum of simulated core melts comprising fuels and core structural materials (Topic 4-2, p.50).

JAEA R&D Review 2014

Published by
Japan Atomic Energy Agency in February 2015

This publication is issued by Japan Atomic Energy Agency (JAEA) on a yearly basis.
Inquiries about availability and/or copyright of the contents in this publication should be addressed to Institutional Repository Section, Intellectual Resources Management and R&D Collaboration Department, Japan Atomic Energy Agency (JAEA).

Address: 2-4 Shirane, Shirakata, Tokai-mura, Naka-gun, Ibaraki-ken 319-1195, Japan
Phone: +81-29-282-6387, **Facsimile:** +81-29-282-5920, **e-mail:** ird-seika_shi@jaea.go.jp